AERODYNAMIC INTERFERENCE AND LATERAL STABILITY AND CONTROL DURING AIR-TO-AIR REFUELLING

A THESIS SUBMITTED TO THE UNIVERSITY OF MANCHESTER

FOR THE DEGREE OF DOCTOR OF PHILOSOPHY

IN THE FACULTY OF SCIENCE

By

Mohamed Jouma'a

School of Engineering

December 1995

Contents

List of Figures

List of tables

Abstract

UNIVERSITY OF MANCHESTER

ABSTRACT OF THESIS submitted by **Mohamed Jouma'a** for the Degree of Doctor of Philosophy and entitled **Aerodynamic Interference and Lateral Stability and Control During Air-to-Air Refuelling**

Month and Year of Submission: November 1995

An investigation of the aerodynamic interference and the lateral stability and control of a Hercules receiver aircraft refuelling in flight from a KC10 tanker has been carried out. Theoretical models have been developed in order to determine the aerodynamic forces and moments acting on the receiver due to its position and attitude within the tanker wake. The tanker aircraft is represented by its main wing with the wake modelled by a three-dimensional roll-up method. The vortex lattice method and approximate expressions for the receiver fuselage effect are used to determine the tanker induced loads on the receiver. The theoretical models are

validated by comparing with existing experimental data obtained in a low speed wind tunnel.

The tanker induced loads on the receiver are found to depend strongly on the vertical position of the receiver relative to the tanker wing wake. In the case of steady sideslip there is a large decrease in the directional stability of the receiver as quantified by the gradient of the rudder angle versus sideslip. Minimum directional stability corresponds to the tip of the receiver fin intersecting the tanker wing wake. The associated aileron angle is two to three times the value in free air in agreement with flight test data. Solution of the linearised equations of motion of the Hercules receiver reveals a divergent oscillation involving mainly bank and side displacements.

Typical aerodynamic data of the interference between the KC10 tanker and Hercules receiver are obtained over an envelope of the receiver positions and attitudes required for flight simulation. The tanker induced forces and moments on the receiver are assessed relative to the receiver's aerodynamic characteristics in free air. Large changes in lift, drag and pitching moment occur near the tanker wake centre line. As the receiver is displaced sideways towards the tanker wing tip vortices it experiences large side force and yawing moment and particularly high rolling moment. The most significant term due to the receiver attitude is the rolling moment due to bank.

Declaration

No portion of the work referred to in this thesis has been submitted in support of an application for another degree or qualification of this or any other university or other institution of learning.

Copyright

Acknowledgements

I wish to express my gratitude to my supervisor Dr. A.W. Bloy whose guidance and advice made possible the completion of this thesis.

The financial support of the SSRC of Syria is gratefully acknowledged.

Finally I would like to thank Mr R. Maziat, research student, for use of his VLM computer program.

Nomenclature

It should be noted that all the aerodynamic coefficients and their derivatives, used in this thesis, are defined using the American system of notation.

b	Wing span
C_{D_i}	Induced drag coefficient, $D_i/q_\infty S$
C_l	Rolling moment coefficient, $L/q_\infty Sb$
$C_{l_{y/b,\theta,\phi,\psi,\beta,\hat{p},\hat{r},\delta_a,\delta_r}}$	Rolling moment derivatives, in non-dimensional form; $\frac{\partial C_l}{\partial(y/b)}$, $\frac{\partial C_l}{\partial\theta}$, $\frac{\partial C_l}{\partial\phi}$, $\frac{\partial C_l}{\partial\psi}$, $\frac{\partial C_l}{\partial\beta}$, $\frac{\partial C_l}{\partial\hat{p}}$, $\frac{\partial C_l}{\partial\hat{r}}$, $\frac{\partial C_l}{\partial\delta_a}$, $\frac{\partial C_l}{\partial\delta_r}$
C_L	Lift coefficient, $L/q_\infty S$
C_m	Pitching moment coefficient, $M/q_\infty S\bar{c}$
$C_{m_{\theta,\phi,\psi,\alpha,\delta_e}}$	Pitching moment derivatives, in non-dimensional form; $\frac{\partial C_m}{\partial\theta}$, $\frac{\partial C_m}{\partial\phi}$, $\frac{\partial C_m}{\partial\psi}$, $\frac{\partial C_m}{\partial\alpha}$, $\frac{\partial C_m}{\partial\delta_e}$
C_n	Yawing moment coefficient, $N/q_\infty Sb$
$C_{n_{y/b,\theta,\phi,\psi,\beta,\hat{p},\hat{r},\delta_a,\delta_r}}$	Yawing moment derivatives, in non-dimensional form; $\frac{\partial C_n}{\partial(y/b)}$, $\frac{\partial C_n}{\partial\theta}$, $\frac{\partial C_n}{\partial\phi}$, $\frac{\partial C_n}{\partial\psi}$, $\frac{\partial C_n}{\partial\beta}$, $\frac{\partial C_n}{\partial\hat{p}}$, $\frac{\partial C_n}{\partial\hat{r}}$, $\frac{\partial C_n}{\partial\delta_a}$, $\frac{\partial C_n}{\partial\delta_r}$
C_X	Force coefficient, $X/q_\infty S$
$C_{X_{\theta,\phi,\psi,\alpha}}$	Force derivatives, in non-dimensional form;

	$\frac{\partial C_X}{\partial \theta}$, $\frac{\partial C_X}{\partial \phi}$, $\frac{\partial C_X}{\partial \psi}$, $\frac{\partial C_X}{\partial \alpha}$
C_Y	Side force coefficient, $Y/q_\infty S$
$C_{Y_{y/b,\theta,\phi,\psi,\beta,p,r,\delta_a,\delta_r}}$	Side force derivatives, in non-dimensional form;
	$\frac{\partial C_Y}{\partial (y/b)}$, $\frac{\partial C_Y}{\partial \theta}$, $\frac{\partial C_Y}{\partial \phi}$, $\frac{\partial C_Y}{\partial \psi}$, $\frac{\partial C_Y}{\partial \beta}$, $\frac{\partial C_Y}{\partial \hat{p}}$, $\frac{\partial C_Y}{\partial \hat{r}}$, $\frac{\partial C_Y}{\partial \delta_a}$, $\frac{\partial C_Y}{\partial \delta_r}$
C_Z	Force coefficient, $Z/q_\infty S$
$C_{Z_{\theta,\phi,\psi,\alpha,\delta_e}}$	Force derivatives, in non-dimensional form;
	$\frac{\partial C_Z}{\partial \theta}$, $\frac{\partial C_Z}{\partial \phi}$, $\frac{\partial C_Z}{\partial \psi}$, $\frac{\partial C_Z}{\partial \alpha}$, $\frac{\partial C_Z}{\partial \delta_e}$
$\bar{c}$	Wing aerodynamic mean chord
D	Differential operator, $(s/V_\infty)d/dt$
D_i	Induced drag
d_i	Induced drag generated by an elemental panel
h	Perpendicular distance to vortex line
i_A	Inertia parameter, $I_A/\rho S s^3$
i_C	Inertia parameter, $I_C/\rho S s^3$
i_E	Product of inertia parameter, $I_E/\rho S s^3$
I_A	Moment of inertia about Ox
I_C	Moment of inertia about Oz
I_E	Product of inertia about Ox and Oz
J_W	Wing-fin interference factor
L	Rolling moment about Ox
L	Lift
$\tilde{l}$	Lift per unit length of span
l	Lift generated by an elemental panel

M	Pitching moment about Oy
m	Aircraft mass
M	Number of panels on the wing
M_∞	Free-stream Mach number
N	Yawing moment about Oz
$Oxyz$	Axes fixed in aircraft
p	Aircraft angular velocity in roll
$\hat{p}$	ps/V_∞
q	Aircraft angular velocity in pitch
q_∞	Free-stream dynamic pressure
r	Aircraft angular velocity in yaw
$\hat{r}$	rs/V_∞
s	Wing semi-span
S	Wing area
$\bar{s}$	Horseshoe width in plane of horseshoe vortex
t	Leading-edge thrust generated by an elemental panel
t	Time
TSD	Test Section Data
u	Component of induced velocity along Ox
$\hat{u}$	Component of induced velocity along $\hat{X}$-axis
V_∞	Free-stream velocity
v	Component of induced velocity along Oy
$\hat{v}$	Component of induced velocity along $\hat{Y}$-axis

VLM	Vortex Lattice Method
w	Component of induced velocity along Oz
$\hat{w}$	Component of induced velocity along $\hat{Z}$-axis
$\hat{X}, \hat{Y}, \hat{Z}$	Axis system used in VLM
$\hat{x}, \hat{y}, \hat{z}$	Distances along $\hat{X}$, $\hat{Y}$ and $\hat{Z}$
X	Force component along Ox
Y	Force component along Oy
y	Sideways displacement from the plane of symmetry of tanker wing, positive to starboard
Z	Force component along Oz
z	Vertical separation between datum points of tanker and receiver aircraft
Γ	Vortex strength
Δy	Length of a spanwise vortex filament, measured parallel to y-axis
Δx	Length of a spanwise vortex filament, measured parallel to x-axis
α	Angle of attack
β	Sideslip angle
δ_a	Aileron deflection angle
δ_k	Krasny's smoothing factor
δ_r	Rudder deflection angle
ϵ	Downwash angle

θ	Pitch angle
$\lambda = Re\lambda + iIm\lambda$	Characteristic root
μ	Relative density parameter, $m/\rho Ss$
ρ	Air density
σ	Sidewash angle
ϕ	Bank angle
φ	Dihedral angle
ψ	Yaw angle
Λ	Quarter-chord sweep angle of elemental panel

Subscripts

c	Chordwise bound vortex element
f	Fin
Fus	Fuselage
Nac	Nacelles
Pro	Propellers
P	Port wing
R	Receiver aircraft
s	Spanwise bound vortex element
S	Starboard wing
T	Tanker aircraft
t	Tailplane
W	Wing
∞	Free air conditions

Chapter 1

Introduction

1.1 The History of Air-To-Air Refuelling

The first air-to-air refuelling took place in America in 1923 at Rockwell Field, San Diego, California, using two D.H. 4B aircraft [1, 2]. The tanker aircraft trailed a 50-foot refuelling hose terminating in a nozzle which was caught by the observer in the receiver. After insertion of the hose end in the receiver's fuel tank by the observer, fuel was transfered by gravity. Using this technique a record-breaking endurance flight of 37 hours 15 minutes was achieved on 27th August 1923.

Further experiments were conducted in America and France to improve the endurance record leading to a flight of $653\frac{1}{2}$ hours. This record was achieved by the Key brothers in a Curtiss Robin and still stands for atmospheric flight endurance [3, 4]. After Sqd. Ldr. R. Atcherley, a flying officer in the RAF, had

witnessed some of the duration flights taking place in the U.S.A. in 1930, he realised the great civil and military advantages to be achieved by refuelling in flight. As soon as Atcherley returned to his squadron he started work to develop a safer and more reliable method of refuelling in flight. His work resulted in devising a new method of making contact known as the cross-over contact. This method involved trailing from the tail of the receiver a horizontal line terminating in a grapnel. The tanker trailed a weighted line which was contacted by the receiver's grapnel as the tanker was flown from side to side and above and astern of the receiver. Then the hose was passed from tanker to receiver by hauling in the receiver's line.

After two years of testing and organising the flight, Sir Alan Cobham and his refuelling operator Sqn Ldr W Helmore attempted a non-stop flight from England to India in 1934. The receiver aircraft was an Airspeed Courier which was refuelled by Handley Page W.10 tankers. However this attempt had to be discontinued following the disconnection of the Courier's throttle linkage over Malta. In the same year Sir Alan Cobham founded the company Flight Refuelling Limited to develop flight refuelling techniques and equipment. During 1935 Flight Refuelling Ltd was awarded a contract by the Imperial Airways to use flight refuelling on trans-Atlantic routes using Short 'C' class flying boats as receiver aircraft refuelled by Handley Page 'Harrows'. The refuelled trans-Atlantic service began on 5th August, 1939 and sixteen successful crossings of the Atlantic made before the service was stopped due to the outbreak of the war.

During the war, refuelling trials were carried out by the U.S.A.F. at Eglin Field using a Flying Fortress receiver and a Liberator tanker. In 1944 Flight Refuelling

Ltd was authorised to develop refuelling equipment for a large force of Lancasters for the bombing of Japan, but the progress of the war caused the development work to be cancelled. In 1948 a team of B-29's and B-50's were converted to act as tanker and receiver aircraft for the U.S.A.F. using loop-hose equipment supplied by Flight Refuelling Ltd. Using the 'looped hose' system, a B-29 receiver performed the first refuelling in flight in 1949.

All the methods of refuelling in flight, which were based on the looped hose system, were unsuitable for receiver aircraft such as a single seater jet fighter in which an operator could not be employed. This problem led to the development of a new method of refuelling known as the 'probe and drogue' which was introduced by Flight Refuelling Ltd in 1949. Today the 'probe and drogue' method of refuelling is the standard of all the world's air forces who use refuelling in flight, apart from the U.S.A.F. who use the flying boom which was introduced by Boeing in 1948.

1.2 The Probe and Drogue Method of Refuelling

The probe and drogue method of refuelling is shown in figure 1.1 where a Hercules MK1 receiver aircraft is refuelling in flight from a Hercules MK1 tanker aircraft. The equipment required by the receiver is only a nozzle fitted to a probe on the nose or wing leading edge of the receiver. The tanker's equipment consists of a drogue, a flexible hose and a drum. The drogue is a lightweight conical receptacle attached to the hose which in turn is stored in the drum. The hose and drum form

the hose-drum unit which trails the hose and rewinds it in again. The hose-drum unit also contains breaking equipment for emergency disconnect.

A typical probe and drogue refuelling manoeuvre for large receiver aircraft is described by Bradley [5]. The receiver aircraft joins with the tanker in the echelon position with the tanker fuel hose fully trailed to a length of 25 m. The receiver moves from the echelon position to the starting position which is about 15 to 30 m behind and below the drogue. While approaching the starting position, the receiver pilot must ensure that his aircraft is well below the trailing vortex system of the tanker wing. From the starting position the receiver begins to climb along the line of the hose at an over taking speed of 1 to 2 m/s relative to the tanker. At this stage the receiver aircraft is strongly affected by the vortex system of the tanker. Thus buffet and noise may increase, more power is required to maintain the closure rate and the longitudinal and lateral trim changes may be required. The receiver pilot continues to close to the tanker to a position of 3 to 5 m behind the drogue. This position is called the precontact position where the receiver is stabilised and ready to make contact. When the drogue is reasonably steady, the receiver pilot applies more power and the probe flies into the drogue. In going from the precontact to the contact position, the receiver pilot should concentrate on using visual references on the tanker until contact is made. If the contact is not achieved, the receiver pilot should move back to the precontact position and begin a new attempt. When contact has been achieved, the receiver continues to overtake the tanker, applying more power due to the additional drag from the drogue. When about 2.5 m of the hose has been pushed back to the drum, the fuel is automatically pumped to the

receiver. The receiver is continued to close on the tanker until about 10 to 15 m of the hose remains trailed. By using visual references on the tanker, the optimum refuelling position is maintained throughout the refuelling process. On completion of fuel transfer, the receiver pilot starts to move back slowly until the hose reaches its full trail position where probe is pulled out of the drogue. As mentioned above the drum is provided with an emergency break which allows the probe to pull out of the drogue without the hose being fully trailed.

1.3 The Flying Boom Method of Refuelling

The flying boom method of refuelling is illustrated in figure 1.2 where a Lockheed SR-71 receiver aircraft is refuelling in flight from a KC10 tanker aircraft. The separation between tanker and receiver aircraft is less than that for the probe and drogue method. The boom system consists of a semi-rigid telescopic boom which is connected to the tanker's fuel system at one end, and it is fitted with a small conical receptacle at the trailing end. Two aerodynamic control surfaces are placed about 1.2 m inboard of the boom receptacle.

A typical flying boom refuelling manoeuvre is described in detail by Hoganson [6]. This manoeuvre differs from the probe and drogue refuelling manoeuvre in that the control of the refuelling operation is mainly done by the tanker crew. When the receiver is ready to make contact, the boom operator who is situated under the tail unit of the tanker, flies the boom into the receiver's refuelling receptacle using the aerodynamic control surfaces and the telescopic action. Then the operator locks

the coupling between the boom and receiver receptacles and starts the fuel flow.

The disconnection between tanker and receiver can be achieved in three ways [4]. The boom is unlocked and retracted by the operator, the receiver is slowed down by the receiver pilot causing the boom to unlock and fuel flow to stop automatically, or a fully automatic high fuel pressure disconnecting switch is used.

1.4 Review of Other Work

In the past decade there has been a considerable increase in the ability to refuel large aircraft in flight. Flight tests of 43 combinations of tanker and large receiver aircraft were carried out at the Aeroplane and Armament Experimental Establishment [7]. Although refuelling was possible with any of the combinations tested, some handling and performance difficulties were found which led to restrictions in airspeed, altitude and weight. For example, two large receiver aircraft, the Hercules and the Nimrod, experienced lateral and directional handling difficulty behind tankers such as the Tristar particularly at high tanker weight and low airspeed. The Hercules was found to be susceptible to a directional wandering or lateral oscillation that required considerable rudder activity to maintain the amplitude of the yawing oscillation at a low level. The effect of the Tristar tanker wake on the Hercules receiver was given by measurements taken in steady sideslip. When tested both in free air and behind the tanker, the Hercules was found to experience a loss of directional stability quantified by the gradient of the rudder angle versus sideslip, which increased as the tanker lift coefficient increased. At

the same time the aileron deflection required to achieve a specified bank angle was considerably increased and has led to extremely high forces when manoeuvring behind the tanker particularly when following it into or out of a turn. In the case of the Nimrod, it was necessary to both modify the yaw damper and increase the effective fin area in order to produce acceptable handling characteristics. Other handling problems described by Bradley [5, 7] include the tendency of the receiver to enter a short period pitching oscillation when making contact or in the refuelling position. Both the VC10 and Victor aircraft exhibited this tendency.

In air-to-air refuelling the trailing vortices from large tanker aircraft can produce substantial effects on the control of receiver aircraft. For example Bradley [5] has described an exploratory test in which a Hercules aircraft made an approach to a typical refuelling position on the starboard wing of a Tristar tanker aircraft. As the Hercules approached the refuelling position it was necessary to apply progressively more right aileron and rudder. Eventually at a point behind the tanker and well short of a typical drogue position full aileron travel was required to hold the wings level and the approach was terminated. Also the performance of the receiver aircraft is strongly affected by the tanker trailing vortex wake. The receiver lift vector is inclined backwards due to the tanker downwash effectively increasing the induced drag. As an example Bradley [7] has given data which indicates that the effective drag of the Hercules receiver aircraft is nearly doubled when in the normal refuelling position behind a Tristar tanker. In some cases the receiver has insufficient power to make or maintain contact with the tanker in horizontal flight. Therefore, refuelling takes place in descending flight.

Research into air-to-air refuelling began in the Aeronautical Engineering Department at Manchester University following a suggestion from British Aerospace, Woodford which was interested in an air-to-air refuelling flight simulator of the Nimrod receiver aircraft. The initial work by Abu-Assaf [8] and Bloy et al [9] considered the lateral stability and control of a large receiver aircraft, since this problem was of particular interest to British Aerospace. At the horizontal separation distance between tanker and receiver aircraft during contact, which is at least one wing span, the tanker wing trailing vortices were assumed to be fully rolled up and represented by a horseshoe vortex with a spanwise spacing of $\frac{\pi}{4}$ times the wing span. Lifting line theory was used to estimate the aerodynamic loads on the receiver which was only represented by the wing and fin. Kucheman's method [10] was also used to account for sweep and compressibility effects. The major aerodynamic interference terms were found to be the rolling moments due to bank and sideways displacements of the receiver. These moments were found to act in a statically stable sense, tending to restore the receiver to its datum position.

The dynamic stability of the receiver was determined using the linearised equations of motion modified to include the additional aerodynamic derivatives due to the effect of the tanker wake (see appendix A). The solution of these equations was found to give three characteristic modes: an almost neutral Dutch roll oscillation and damped and undamped oscillations involving mainly bank and sideways displacements.

Next, Bloy et al [11] investigated the longitudinal dynamic stability and control of a large receiver aircraft. A simple horseshoe vortex was again used to model

the tanker wing wake. The aerodynamic loads acting on the receiver wing and tailplane were estimated using an approximate method described in reference [12]. The most important additional aerodynamic terms were found to be the normal force and pitching moment due to vertical displacement relative to the tanker wake. The pitching moment was found to depend on the difference between the mean downwash at the wing and at the tailplane. The dynamic stability modes were determined using the longitudinal linearised equations of motion given in appendix A. These modes were found to consist of a longitudinal short period oscillation, similar to that in normal flight, a subsidence involving mainly vertical displacement and two divergent modes.

For more representative theoretical modelling of the aerodynamic interference between tanker and receiver aircraft during air-to-air refuelling, the vortex lattice method of Margason and Lamar [13] was used by Trochalidis and Bloy and Trochalidis [14, 15] to determine the tanker wing loading and the forces and moments acting on the receiver wing and tailplane. The tanker wake was modelled by a simple horseshoe vortex with the wing loading assumed to be elliptic. The self induced downward displacement of the trailing vortices and the viscous effects in the trailing vortex cores were neglected together with jet efflux, tanker fuselage and fuel hose effects. The Hercules and VC10 aircraft were considered refuelling from different tanker aircraft. A significant increase in receiver drag was predicted which compared favourably with the flight test data given by Bradley [5]. A pitching moment was produced on the receiver due mainly to the difference between the mean downwash at the wing and tailplane which was strongly affected by the

tailplane position. At the normal refuelling position the high T-tail VC10 receiver was found to be statically stable with respect to vertical displacement since an upward displacement of the receiver resulted in both less lift and a nose-down pitching moment and vice versa for a downward displacement. However dynamic stability analysis of this receiver using the longitudinal linearised equations of motion revealed a divergent oscillation consistent with flight test observations of the tendency of the VC10 to oscillate in pitch.

In order to evaluate the theoretical models mentioned above, wind-tunnel tests were carried out by Bloy et al [16, 17], using the open return wind tunnel of the Goldstein Laboratories which is described in chapter 3. Similar rectangular wings of aspect ratio 5 with and without flaps were used to represent the tanker wing. This wing was supported on a traverse which allowed bank, pitch, spanwise and vertical displacements relative to a receiver aircraft model which consisted of a main wing identical to the tanker wing together with a rectangular fin and tailplane. A horizontal separation less than one wing span was used between the tanker wing and receiver aircraft model.

In the theoretical model of the wind-tunnel experiments, the tanker wing loading was estimated using vortex lattice method [13] with the flap deflection modelled by an appropriate twist distribution. The wake of the plain wing was modelled by a simple horseshoe vortex with a vortex span of $\frac{\pi}{4}$ times the wing span whereas the wake of the flapped wing was modelled by a pair of horseshoe vortices from both the wing and flap tips. The strength and spanwise position of the horseshoe vortices of the flapped wing were determined using Donaldson's method [18]. The

self-induced vertical displacement of the trailing vortices of the flapped wing was taken into account at the receiver aircraft model position. Either lifting-line theory or vortex lattice method was used to estimate the loads on the receiver aircraft model.

In the experiment, the longitudinal aerodynamic interference was determined at different vertical separations between the tanker wing and receiver aircraft model. The lateral aerodynamic interference was also determined at different vertical positions by banking the tanker wing and displacing it sideways and by yawing the receiver aircraft model. For the flapped tanker wing, data were obtained from open and closed test sections in order to estimate the wind tunnel boundary interference effect. Large differences were found between theory and experiment due mainly to the wind-tunnel boundary interference and incomplete rollup of the trailing vortices. However the overall theoretical and experimental trends with varying vertical separation were found to be similar.

A more realistic wind-tunnel tanker/receiver aircraft model was considered by Bloy et al [19] to investigate both theoretically and experimentally the lateral aerodynamic interference between tanker and receiver aircraft. The tanker was modelled in the experiments by an unswept, tapered wing of an aspect ratio 5.5 and a span identical to that of the receiver aircraft model which was similar to that used previously by Bloy et al [16, 17]. The vortex lattice method of Jouma'a [20], which is explained in chapter 2, was used to determine the tanker wing loading and the forces and moments on the receiver wing and fin/tailplane combination allowing for the aerodynamic interference between the fin and tailplane. The tanker wing

wake was modelled as a flat vortex sheet, with an allowance made for the vertical displacement of the wake in the estimation of the forces on the fin and tailplane.

Significant side forces were produced due to sidewash on the fin from the tanker and receiver wings and, when displaced in yaw, the receiver experienced a loss in directional stability. The overall theoretical results compared favourably with the experimental data obtained from the open and closed test sections.

In the theoretical models described in the above work [8, 9, 11, 12, 14, 15, 16, 17, 19, 20] the tanker wing wake was modelled by either a horseshoe vortex or a flat vortex sheet. Both models are approximations to the actual trailing vortex wake which leaves the wing trailing edge as a flat sheet and eventually rolls up into two distinct trailing vortices. The horseshoe vortex model, which represents the fully rolled up wake, is applicable far downstream; and the flat (i.e. non-rolled up) vortex sheet is only valid near the wing as shown theoretically by Spreiter [21] and experimentally by El-Ramly [22] and Grow [23]. In order to allow more accurate representation of the tanker wing wake, a three-dimensional steady inviscid model of wake roll-up was developed by West [24]. This model is described in chapter 2. Bloy and West [24, 25] applied this model to the tanker/receiver aircraft models which were tested previously by Bloy et al [16, 17]. The tanker wing loading was determined using the vortex lattice method of Mendenhall et al [26, 27] described in chapter 2. The linear VLM of Jouma'a [20] was again used to estimate the aerodynamic loads induced on the receiver aircraft model. The wake roll-up model of the tapered tanker wing showed that at the position of the receiver wing, the tip vortex strength was only 42.5% of the root circulation. The predictions from

the roll-up model of the tapered wing wake indicated significantly higher values of the receiver rolling moment due to sideways displacement, compared with the predictions from a flat vortex sheet model, since the spanwise gradient of downwash was significantly higher in magnitude for the wake model with roll-up than for the flat vortex sheet model. The roll-up effect on the receiver rolling moment due to bank displacement was negligible. Application of the wake roll-up model to the flapped wing showed that the flap and wing tip vortices at one wing span downstream contained 75% of the total circulation. At a typical vertical separation of 0.131 times the wing span, the effect of the roll-up model of the flapped wing was to reduce the receiver rolling moment due to sideways displacement, compared with the horseshoe vortex model giving closer agreement between experiment and theory.

Apart from the above work little previous work appears to have been published on the aerodynamics and the stability and control of the receiver aircraft during air-to-air refuelling. Hoganson [6] evaluated the longitudinal aerodynamic interference between the KC10 tanker and a B52 receiver. At the contact position the horizontal separation was 38 m or 0.76 times the tanker wing span. The tanker wing wake was represented by a flat vortex sheet, and the vortex lattice method was used to evaluate the interference effects. Results were given for the induced downwash distribution and the corresponding lift force and pitching moment. Both the upstream influence of the receiver on the tanker and the effect of the tanker tailplane on the receiver were found to be small.

Other work related to air-to-air refuelling is concerned with the aerodynamic loads

on a wing in the trailing vortex wake of another wing and with formation flying. Smith and Lazzeroni [28] measured the induced lift distribution on a rectangular wing of aspect ratio 4 at 3.25 chord lengths downstream of a similar rectangular wing. Reasonable agreement was obtained between experiment and theory in which the leading wing was replaced by a horseshoe vortex trailing back from the wing tips. From measurements of the downwash behind the leading wing, the spanwise position of the trailing vortices was found to be closer to the wing tip than the predicted value. McMillan et al [29] measured the pressure distribution and overall loads on a wing in close proximity to a tip vortex generated by a larger, upstream semispan wing. Both strip and vortex-lattice theories were used to predict the loads on the following wing. Good results were obtained for overall coefficients and loading distribution using vortex-lattice theory. Strip theory was found to give poor results for loading distribution although predictions of overall loads were acceptable. Barrows [30] evaluated the rolling moments on aircraft encountering wake vortices using two computational methods, viz. the strip theory and the reciprocal theorem of Heaslet and Spreiter [31]. It was shown that the rolling moments on the encountering aircraft were significantly affected by the ratio of the spans of the generating and encountering aircraft. Iversen and Bernstein [32, 33] considered the simulation of trailing vortex effects on aircraft in close formation. A fully rolled up trailing vortex model was used for the C-130 and C-5A aircraft to simulate the effect on a C-130 aircraft. Only the induced lift and rolling moment increments were calculated. These loads varied with the position of the following aircraft in the trailing vortex wake and were dependent on the downwash distribution due to

the lead aircraft. Yates [34] investigated the effect of the trailing vortex wake on the control of aircraft in close formation. Only the induced rolling moment experienced by the following aircraft was considered with the trailing vortex system of the lead aircraft assumed to be fully rolled up.

1.5 Present Work

The purpose of the work presented in this thesis was to develop theoretical models to represent any combination of tanker wing and receiver aircraft during air-to-air refuelling. These models have been used to carry out the following research:

- The application of the theoretical models to an existing wind-tunnel model in order to justify the use of these models to study full-scale tanker and receiver aircraft combinations of practical interest.
- The estimation of the aerodynamic derivatives of a Hercules receiver aircraft in free air which are required prior to analysing the stability and control characteristics of the Hercules behind a KC10 tanker.
- The estimation of the lateral aerodynamic interference; trim in steady sideslip and dynamic stability characteristics of a Hercules receiver refuelling in flight from a KC10 tanker aircraft.
- The generation of typical aerodynamic data of the interference between the KC10 tanker and Hercules receiver aircraft for use in flight simulation.

First, descriptions of individual theories such as linear vortex lattice method, flat vortex sheet model and 3D roll-up method are given. Then, the combinations of the individual theories, used to represent the tanker and receiver aircraft in an air-to-air refuelling configuration, are discussed.

The next chapter is concerned with the application of the theoretical models of the tanker/receiver combination to the wind-tunnel model tested previously by Bloy et al [19]. First, the experimental hardware and software used in the experiments are described. The experimental set-up is discussed next and the experimental data are compared with corresponding theoretical predictions.

Chapter 4 describes the procedures used to estimate the stability and control derivatives of the Hercules aircraft in free air.

In the next chapter the lateral aerodynamic interference and the stability and control characteristics of the KC10 tanker and Hercules receiver aircraft combination is analysed. Aerodynamic results at constant receiver lift coefficient are obtained. The trim of the Hercules in steady sideslip is then predicted and compared with flight test data. Finally, the dynamic stability characteristics of the receiver are determined in both free air and air-to-air refuelling.

In chapter 6 typical aerodynamic data of the interference between the KC10 tanker and Hercules receiver aircraft are obtained over an envelope of the receiver positions and attitudes which covers that required for flight simulation. The aerodynamic loads on the receiver due to both its position and attitude are compared with the aerodynamic characteristics of the receiver in free air, and presented by contour

plots in the y, z plane at a typical downstream position.

Finally, the conclusions of this research work are given together with suggestions for future investigations of the aerodynamic interference between tanker and receiver aircraft during air-to-air refuelling.

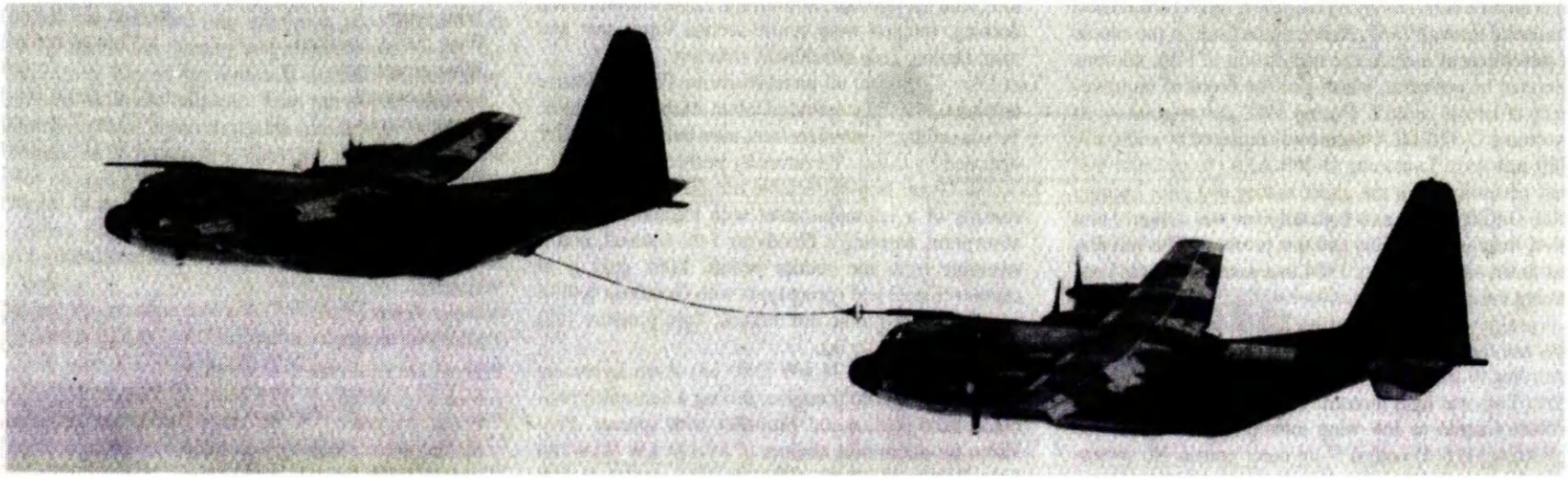

Figure 1.1: Hercules MK1 receiver refuelling in flight from Hercules MK1 tanker, using the probe and drogue method.

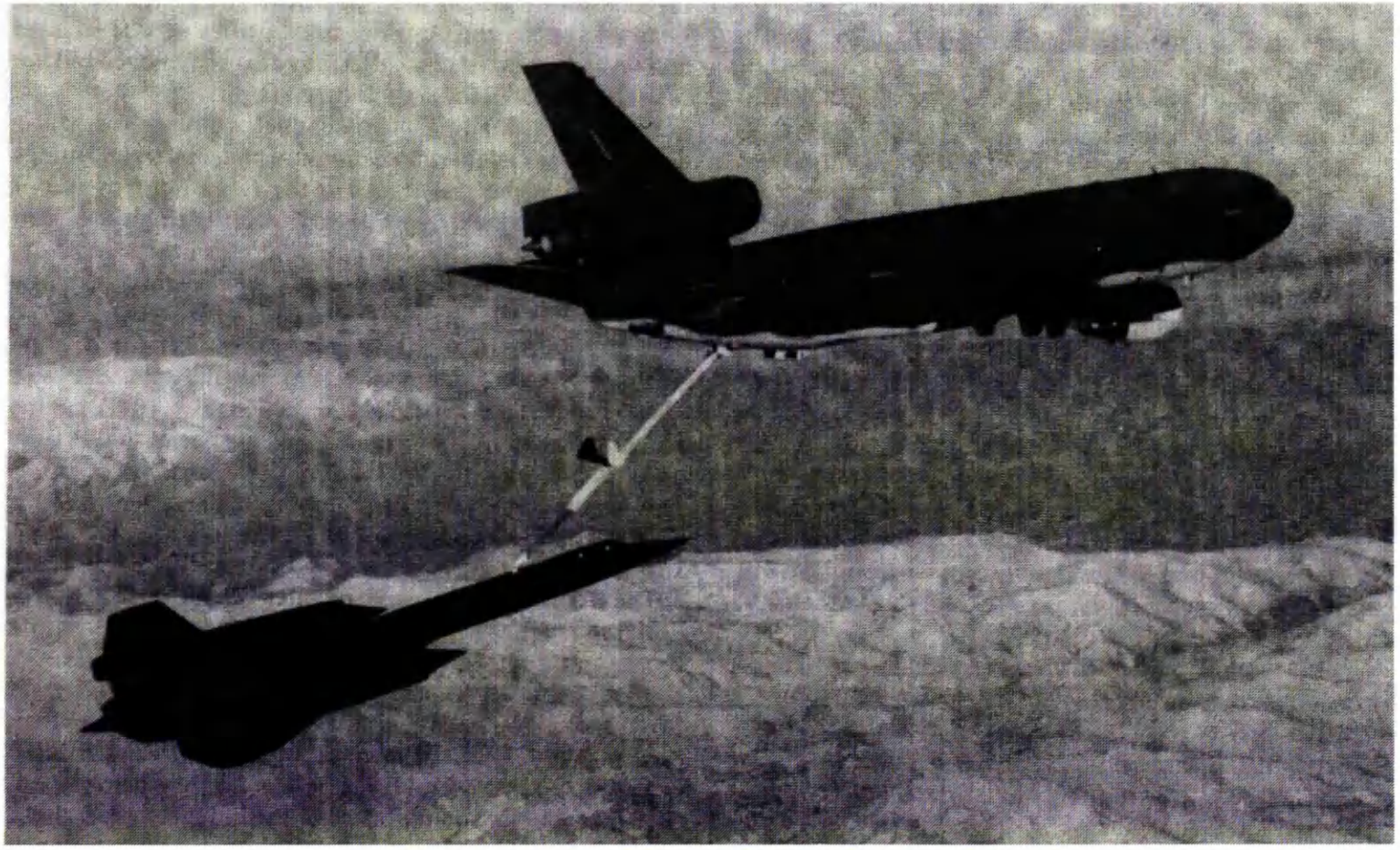

Figure 1.2: KC-10A Extender tanker refuelling a Lockheed SR-71, using the flying boom method.

Chapter 2

Theoretical Modelling of the Aerodynamic Interference Between Tanker and Receiver Aircraft

During air-to-air refuelling, the receiver aircraft flies in the sidewash and downwash field of the tanker aircraft as illustrated in figure 2.1. Therefore aerodynamic forces and moments, additional to those in normal flight, are produced on the receiver. These forces and moments depend on the position and attitude of the receiver aircraft relative to the tanker aircraft. The estimation of the receiver additional loads requires an aerodynamic model capable of predicting the aerodynamic characteristics of both tanker and receiver aircraft including the mutual aerodynamic

interference effects.

This chapter describes the theoretical models used to estimate the aerodynamic interference between tanker and receiver aircraft during air-to-air refuelling.

First, the linear vortex lattice method used to calculate the forces and moments acting on the receiver is explained. This is followed by a description of the application of linear VLM to the receiver tailplane-fin combination. Then, a flat vortex sheet model used to represent the receiver wing wake is described. In the following section an existing three-dimensional steady roll-up model used to model the tanker wing wake is discussed. For comparison with the wake roll-up model, the tanker wing wake was also modelled using the flat vortex sheet model. Finally, the combinations of the aerodynamic models of tanker and receiver, used to model both aircraft in an air-to-air refuelling configuration, are introduced.

2.1 Linear Vortex Lattice Method (VLM)

VLM is a numerical method in which the continuous distribution of bound vorticity over the wing surface is approximated by a finite number of discrete horseshoe vortices as shown in figure 2.2. The wing surface is divided into trapezoidal elemental panels. Each panel is replaced by a horseshoe vortex. The bound vortex lies along the quarter chord of the panel, and the two trailing vortices, one on each side of the panel, starting at the quarter chord and extending downstream to infinity in the free-stream direction. A control point is defined for each panel at the midspan three-quarter panel chord line. The flow tangency boundary condition (i.e. there is

no flow through the wing surface) is satisfied at these control points. Applying the flow tangency boundary condition at all the control points provides a set of simultaneous equations whose solution leads to the required horseshoe vortex strengths. The Kutta-Joukowski theorem for aerodynamic forces on a vortex filament is used to calculate the aerodynamic loads acting on each elemental panel, with the induced velocities calculated from the Biot-Savart law. The total aerodynamic forces are then determined by summing up the forces from each individual panel.

The linear VLM used assumes steady, irrotational, inviscid, incompressible, attached flow. Compressibility effects are accounted for by applying the Prandtl-Glauert rule to modify the planform geometry. This involves dividing the x-coordinates by $\left(\sqrt{1-M_\infty^2}\right)$ [13].

2.1.1 Vortex Strength Calculation

The strengths of the horseshoe vortices, which represent the flow field of the wing, are determined by satisfying the flow tangency boundary condition at all the wing control points. At each control point, the tangent flow boundary condition is satisfied by equating the component of the induced velocity normal to the wing surface to the normal component of the free stream velocity. The application of the tangent flow boundary condition at all the control points results in a set of simultaneous equations which can be expressed in matrix form as

$$[C]\{\Gamma\} = \{B\} \tag{2.1}$$

where $[C]$ is the influence function matrix, a typical element of $[C]$, c_{ij} represents the geometrical function of the normal velocity at the control point of ith panel induced by a horseshoe vortex at jth panel, $\{\Gamma\}$ represents the unknown circulation matrix, where the jth element of this matrix is the circulation at the jth panel and $\{B\}$ is the tangent flow boundary condition matrix, with the ith element of this matrix represents the boundary condition at the control point of ith panel. The vortex strengths are then obtained by inverting the influence function matrix

$$\{\Gamma\} = [C]^{-1}\{B\}$$

As described by the author [20] the boundary condition for flat wings with dihedral at small angles of attack is given by the following equation

$$\hat{w} - \hat{v}\tan\varphi \approx -V_\infty \alpha \tag{2.2}$$

The induced velocity components are calculated using the Biot-Savart law. Hence, the sidewash and downwash velocities at any point $(\hat{x}, \hat{y}, \hat{z})$ induced by the horseshoe vortex shown in figure 2.3, can be written as

$$\hat{v}(\hat{x}, \hat{y}, \hat{z}) = \frac{\Gamma}{4\pi} F_v\left(\hat{x}, \hat{y}, \hat{z}, \hat{x}_1, \hat{y}_1, \hat{z}_1, \hat{x}_2, \hat{y}_2, \hat{z}_2\right) \tag{2.3}$$

$$\hat{w}(\hat{x}, \hat{y}, \hat{z}) = \frac{\Gamma}{4\pi} F_w\left(\hat{x}, \hat{y}, \hat{z}, \hat{x}_1, \hat{y}_1, \hat{z}_1, \hat{x}_2, \hat{y}_2, \hat{z}_2\right) \tag{2.4}$$

where F_v and F_w are the sidewash and downwash influence functions, respectively. These functions are given by the following equations which are derived in reference [35].

$$F_v = -\left[\left(xx_1\right)\left(zz_2\right) - \left(xx_2\right)\left(zz_1\right)\right]\frac{B_1}{B_2}$$

$$+ \frac{zz_1}{(zz_1)^2 + (y_1y)^2}\left(1 + \frac{xx_1}{r_1}\right)$$
$$- \frac{zz_2}{(zz_2)^2 + (y_2y)^2}\left(1 + \frac{xx_2}{r_2}\right) \tag{2.5}$$

$$F_w = [(xx_1)(yy_2) - (xx_2)(yy_1)]\frac{B_1}{B_2}$$
$$+ \frac{y_1y}{(zz_1)^2 + (y_1y)^2}\left(1 + \frac{xx_1}{r_1}\right)$$
$$- \frac{y_2y}{(zz_2)^2 + (y_2y)^2}\left(1 + \frac{xx_2}{r_2}\right) \tag{2.6}$$

where

$$B_1 = \frac{(x_2x_1)(xx_1) + (y_2y_1)(yy_1) + (z_2z_1)(zz_1)}{r_1}$$
$$- \frac{(x_2x_1)(xx_2) + (y_2y_1)(yy_2) + (z_2z_1)(zz_2)}{r_2} \tag{2.7}$$

$$B_2 = [(yy_1)(zz_2) - (yy_2)(zz_1)]^2$$
$$+ [(xx_1)(zz_2) - (xx_2)(zz_1)]^2$$
$$+ [(xx_1)(yy_2) - (xx_2)(yy_1)]^2 \tag{2.8}$$

$$r_1 = \sqrt{(xx_1)^2 + (yy_1)^2 + (zz_1)^2}$$

$$r_2 = \sqrt{(xx_2)^2 + (yy_2)^2 + (zz_2)^2}$$

$$xx_1 = (\hat{x} - \hat{x}_1),\ yy_1 = (\hat{y} - \hat{y}_1),\ zz_1 = (\hat{z} - \hat{z}_1),\ y_1y = (\hat{y}_1 - \hat{y})$$

$$xx_2 = (\hat{x} - \hat{x}_2),\ yy_2 = (\hat{y} - \hat{y}_2),\ zz_2 = (\hat{z} - \hat{z}_2),\ y_2y = (\hat{y}_2 - \hat{y})$$

$$x_2x_1 = (\hat{x}_2 - \hat{x}_1),\ y_2y_1 = (\hat{y}_2 - \hat{y}_1),\ z_2z_1 = (\hat{z}_2 - \hat{z}_1)$$

Then, by using equations 2.3 and 2.4, equation 2.2 can be expressed as

$$\frac{\Gamma}{4\pi}(F_w - F_v \tan\varphi) = -V_\infty \alpha \tag{2.9}$$

For a vortex lattice of M elemental panels, equation 2.9 can be written for a particular control point as

$$\sum_{m=1}^{M} \left(F_{w,m} - F_{v,m} \tan \varphi_m\right) \frac{\Gamma_m}{V_\infty} = -4\pi\alpha \tag{2.10}$$

Therefore, for this vortex lattice of M elemental panels, the vortex strength in each panel Γ_m can be calculated by solving the following matrix equation which is obtained from the application of equation 2.10 to all the elemental panels.

$$\left[F_{w,m,k} - F_{v,m,k} \tan \varphi_m\right] \left\{\frac{\Gamma_m}{V_\infty}\right\} = -4\pi \left\{\alpha_k\right\} \tag{2.11}$$

where α_k is the local angle of attack at the kth control point.

2.1.2 Aerodynamic Forces and Moments of Receiver Wing

Two different procedures are used to estimate the forces and moments for wings with and without dihedral. For zero-dihedral wings, the aerodynamic forces are produced by the interaction of the free-stream velocity with the wing spanwise bound vortices. However, for wings with dihedral, extra sidewash velocity component is produced. The interaction of this component with the spanwise and chordwise bound vortices provides additional forces. Kutta-Joukowski theorem for force per unit length of a vortex filament is used to estimate the aerodynamic forces for wings with and without dihedral. The forces and moments are calculated in the aerodynamic-body axes Oxyz, with the origin is at the aircraft centre of gravity, the x-axis is in the free-stream direction (positive forward), the y and z axes are positive to the starboard and downwards, respectively.

Wings with No Dihedral

Lift Coefficient

Using Kutta-Joukowski theorem, the lift per unit of span is given by

$$\tilde{l} = \rho_\infty V_\infty \Gamma \tag{2.12}$$

The total lift is obtained by integrating equation 2.12 over the wing span as given by

$$L = \rho_\infty V_\infty \int_{-\frac{b}{2}}^{\frac{b}{2}} \Gamma dy \tag{2.13}$$

or approximately by

$$L = \rho_\infty V_\infty^2 \left[\sum_{m=1}^{M/2} \left(\frac{\Gamma_m}{V_\infty} \Delta y_m \right)_S + \sum_{m=1}^{M/2} \left(\frac{\Gamma_m}{V_\infty} \right)_P (\Delta y_m)_S \right] \tag{2.14}$$

Where Δy_m is the width of the mth panel.

Thus the lift coefficient can be written as

$$C_L = \frac{L}{q_\infty S} = \frac{2}{S} \left[\sum_{m=1}^{M/2} \left(\frac{\Gamma_m}{V_\infty} \Delta y_m \right)_S + \sum_{m=1}^{M/2} \left(\frac{\Gamma_m}{V_\infty} \right)_P (\Delta y_m)_S \right] \tag{2.15}$$

If the loading is symmetric, the lift coefficient can be expressed as

$$C_L = \frac{4}{S} \sum_{m=1}^{M/2} \left(\frac{\Gamma_m}{V_\infty} \Delta y_m \right)_S \tag{2.16}$$

Rolling Moment Coefficient

For an mth elemental panel on the port wing, the rolling moment produced about the x-axis can be expressed as

$$(L_m)_P = \rho_\infty V_\infty \left(\Gamma_m \Delta y_m y_m \right)_P \tag{2.17}$$

where L_m is the rolling moment produced by the mth panel and y_m is the rolling moment arm of the elemental lift on the mth panel.

Similarly, the rolling moment generated by the image of mth panel on the starboard wing is given by

$$(L_m)_S = -\rho_\infty V_\infty \left(\Gamma_m \Delta y_m y_m\right)_S \tag{2.18}$$

Thus the total rolling moment about the x-axis is given by

$$L = \rho_\infty V_\infty^2 \left[\sum_{m=1}^{M/2} \left(\frac{\Gamma_m}{V_\infty} \Delta y_m y_m\right)_P - \sum_{m=1}^{M/2} \left(\frac{\Gamma_m}{V_\infty} \Delta y_m y_m\right)_S\right] \tag{2.19}$$

and the rolling moment coefficient is

$$C_l = \frac{L}{q_\infty S b} = \frac{2}{bS} \left[\sum_{m=1}^{M/2} \left(\frac{\Gamma_m}{V_\infty} \Delta y_m y_m\right)_P - \sum_{m=1}^{M/2} \left(\frac{\Gamma_m}{V_\infty} \Delta y_m y_m\right)_S\right] \tag{2.20}$$

Induced Drag Coefficient

The far-field method which is based on the lifting-line concepts and employed by Munk in the Trefftz plane (i.e. yz plane) is used to estimate the induced drag as follows. The total induced drag can be expressed as

$$D_i = \rho_\infty V_\infty \int_{-\frac{b}{2}}^{\frac{b}{2}} \Gamma \epsilon dy \tag{2.21}$$

where ϵ is the downwash angle. Equation 2.21 can be approximated as

$$D_i = \rho_\infty V_\infty^2 \left[\sum_{m=1}^{M/2} \left(\frac{\Gamma_m}{V_\infty} \epsilon_m\right)_P (\Delta y_m)_S + \sum_{m=1}^{M/2} \left(\frac{\Gamma_m}{V_\infty} \epsilon_m \Delta y_m\right)_S\right] \tag{2.22}$$

where ϵ_m is calculated at the quarter-chord of the mth panel. The total induced drag coefficient is then given by

$$C_{D_i} = \frac{D_i}{q_\infty S} = \frac{2}{S} \left[\sum_{m=1}^{M/2} \left(\frac{\Gamma_m}{V_\infty} \epsilon_m\right)_P (\Delta y_m)_S + \sum_{m=1}^{M/2} \left(\frac{\Gamma_m}{V_\infty} \epsilon_m \Delta y_m\right)_S\right] \tag{2.23}$$

If the wing loading is symmetric, the total induced drag coefficient can be expressed as

$$C_{D_i} = \frac{4}{S} \sum_{m=1}^{M/2} \left(\frac{\Gamma_m}{V_\infty} \epsilon_m \Delta y_m \right)_S \tag{2.24}$$

Yawing Moment Coefficient

For an mth elemental panel on the port wing, the yawing moment generated about the z-axis can be expressed as

$$(N_m)_P = -\rho_\infty V_\infty \left(\Gamma_m \epsilon_m \Delta y_m y_m \right)_P \tag{2.25}$$

where N_m is the yawing moment produced by the mth panel and y_m is the yawing moment arm of the elemental induced drag of the mth panel.

Similarly, for the image of mth panel on the starboard wing, the yawing moment is

$$(N_m)_S = \rho_\infty V_\infty \left(\Gamma_m \epsilon_m \Delta y_m y_m \right)_S \tag{2.26}$$

The total yawing moment is obtained by summing equations 2.25 and 2.26 all over the elemental panels as follows

$$N = \rho_\infty V_\infty^2 \left[\sum_{m=1}^{M/2} \left(\frac{\Gamma_m}{V_\infty} \epsilon_m \Delta y_m y_m \right)_S - \sum_{m=1}^{M/2} \left(\frac{\Gamma_m}{V_\infty} \epsilon_m \Delta y_m y_m \right)_P \right] \tag{2.27}$$

and the total yawing moment coefficient is

$$C_n = \frac{N}{q_\infty S b} = \frac{2}{S b} \left[\sum_{m=1}^{M/2} \left(\frac{\Gamma_m}{V_\infty} \epsilon_m \Delta y_m y_m \right)_S - \sum_{m=1}^{M/2} \left(\frac{\Gamma_m}{V_\infty} \epsilon_m \Delta y_m y_m \right)_P \right] \tag{2.28}$$

Pitching Moment coefficient

The elemental lift on the nth panel on the starboard wing produces a pitching moment about the y-axis given by

$$(M_n)_S = \rho_\infty V_\infty (\Gamma_n \Delta y_n x_n)_S \tag{2.29}$$

where M_n is the pitching moment produced by the nth panel and x_n is the pitching moment arm of the elemental lift on the nth panel.

Similarly, for the image of nth panel on the port wing, the pitching moment is

$$(M_n)_P = \rho_\infty V_\infty (\Gamma_n x_n)_P (\Delta y_n)_S \tag{2.30}$$

Therefore the total pitching moment about the y-axis is given by

$$M = \rho_\infty V_\infty^2 \left[\sum_{n=1}^{M/2} \left(\frac{\Gamma_n}{V_\infty} x_n \right)_P (\Delta y_n)_S + \sum_{n=1}^{M/2} \left(\frac{\Gamma_n}{V_\infty} \Delta y_n x_n \right)_S \right] \tag{2.31}$$

and the pitching moment coefficient is

$$C_m = \frac{M}{q_\infty S \bar{c}} = \frac{2}{S\bar{c}} \left[\sum_{n=1}^{M/2} \left(\frac{\Gamma_n}{V_\infty} x_n \right)_P (\Delta y_n)_S + \sum_{n=1}^{M/2} \left(\frac{\Gamma_n}{V_\infty} \Delta y_n x_n \right)_S \right] \tag{2.32}$$

If the wing loading is symmetric, the pitching moment coefficient can be expressed as

$$C_m = \frac{4}{S\bar{c}} \sum_{n=1}^{M/2} \left(\frac{\Gamma_n}{V_\infty} \Delta y_n x_n \right)_S \tag{2.33}$$

Wings with Dihedral

Lift Coefficient

As mentioned in section 2.1.2, for wings with dihedral, a more complicated approach is required to estimate the forces and moments. In this case, the lift is produced by

both the interaction of the backwash and free-stream velocities with the spanwise bound vortices, and the interaction of the sidewash velocity with the spanwise and chordwise bound vortices. The spanwise and chordwise lift components are calculated using Kutta-Joukowski theorem as described below.

The lift generated along the spanwise vortex filament shown in figure 2.4 comes from both the total axial velocity interacting with the component of the vortex filament parallel to the y-axis ($\Delta y = \bar{s}\cos\varphi$) and the sidewash velocity interacting with the component of the vortex filament parallel to the x-axis ($\Delta x = \bar{s}\tan\Lambda\cos\varphi$). The expression for this lift for the mth panel on the starboard wing in non-dimensional form is

$$\left[\left(\frac{l_s}{q_\infty S}\right)_m\right]_S = \frac{2}{S}\left\{\left(\frac{\Gamma_s}{V_\infty}\right)_m\left[\left(1-\frac{u}{V_\infty}\right)\Delta y - \frac{v}{V_\infty}\Delta x\right]_m\right\}_S \tag{2.34}$$

where l_s is the lift generated along the spanwise bound vortex of the mth panel; Δx and Δy are the components of the spanwise bound vortex of the mth panel along the x and y axes, respectively. The sidewash and backwash velocities are evaluated at the quarter-chord of the mth panel. The sidewash velocity, v, is equal to $\hat{v}$ which is given by equation 2.3, and the backwash velocity, u, is equal to minus $\hat{u}$ which is given by

$$\hat{u}(\hat{x},\hat{y},\hat{z}) = \frac{\Gamma}{4\pi}F_u\left(\hat{x},\hat{y},\hat{z},\hat{x}_1,\hat{y}_1,\hat{z}_1,\hat{x}_2,\hat{y}_2,\hat{z}_2\right) \tag{2.35}$$

where the backwash influence function, F_u, is given by

$$F_u = \left[\left(yy_1\right)\left(zz_2\right) - \left(yy_2\right)\left(zz_1\right)\right]\frac{B_1}{B_2} \tag{2.36}$$

Similarly, the lift generated along the spanwise bound vortex of the image of mth

panel on the port wing, in non-dimensional form is

$$\left[\left(\frac{l_s}{q_\infty S}\right)_m\right]_P = \frac{2}{S}\left\{\left(\frac{\Gamma_s}{V_\infty}\right)_m\left[\left(1-\frac{u}{V_\infty}\right)\Delta y + \frac{v}{V_\infty}\Delta x\right]_m\right\}_P \tag{2.37}$$

where Δy is taken as positive on the port wing.

The lift generated along the chordwise bound vortices of an mth panel on the starboard wing, in non-dimensional form, is given by

$$\left[\left(\frac{l_c}{q_\infty S}\right)_m\right]_S = \frac{2}{S}\left\{\left[\frac{\Gamma_c}{V_\infty}\left(\frac{v_i}{V_\infty}c_i - \frac{v_o}{V_\infty}c_o\right)\right]_m\right\}_S \tag{2.38}$$

where c_i and c_o are the lengths of the inboard and outboard chordwise bound vortices of the mth panel, respectively, as shown in figure 2.5 and Γ_c is the strength of chordwise bound vortices of the mth panel which is described as follows. Consider a chordwise row of three elemental panels as shown in figure 2.6. The lift generated along the chordwise bound vortices varies from the leading edge to trailing edge of the wing because of the longitudinal variation of both the sidewash velocity and the local value of circulation. Along the chordwise bound vortices from the wing leading edge to the quarter-chord of the first panel, there is no circulation and consequently no lift can be produced here. Along the chordwise bound vortices from the quarter-chord of the first panel to the quarter-chord of the second panel, there is a constant value of circulation equals that of the first panel and a varying sidewash. From the quarter-chord of the second panel to the quarter-chord of the third panel, the circulation is equal to the sum of the circulation values of the first two panels. Between the quarter-chord of the third panel and the wing trailing edge, the circulation is equal to the sum of the circulation of the third panel and the circulations of the first two panels. The sidewash velocities v_i and v_o are calculated

at the three-quarter of the inboard and outboard chords of each elemental panel, respectively.

Similarly, the lift produced along the chordwise bound vortices of the image of mth panel on the port wing, in non-dimensional form is

$$\left[\left(\frac{l_c}{q_\infty S}\right)_m\right]_P = \frac{2}{S}\left\{\left[\frac{\Gamma_c}{V_\infty}\left(\frac{v_o}{V_\infty}c_o - \frac{v_i}{V_\infty}c_i\right)\right]_m\right\}_P \tag{2.39}$$

Thus, the total lift produced by the mth panel on the starboard wing is

$$\left[\left(\frac{l}{q_\infty S}\right)_m\right]_S = \left[\left(\frac{l_s}{q_\infty S}\right)_m\right]_S + \left[\left(\frac{l_c}{q_\infty S}\right)_m\right]_S \tag{2.40}$$

and on the port wing is

$$\left[\left(\frac{l}{q_\infty S}\right)_m\right]_P = \left[\left(\frac{l_s}{q_\infty S}\right)_m\right]_P + \left[\left(\frac{l_c}{q_\infty S}\right)_m\right]_P \tag{2.41}$$

Hence, the wing lift coefficient is obtained by summing equations 2.40 and 2.41 over all the wing elemental panels

$$C_L = \frac{L}{q_\infty S} = \sum_{m=1}^{M/2}\left[\left(\frac{l}{q_\infty S}\right)_m\right]_S + \sum_{m=1}^{M/2}\left[\left(\frac{l}{q_\infty S}\right)_m\right]_P \tag{2.42}$$

If the wing loading is symmetric, equation 2.42 can be written as

$$C_L = \frac{L}{q_\infty S} = 2\sum_{m=1}^{M/2}\left[\left(\frac{l}{q_\infty S}\right)_m\right]_S \tag{2.43}$$

Rolling Moment Coefficient

The rolling moment produced about the x-axis by the mth panel on the starboard wing can be expressed in non-dimensional form as

$$[(C_l)_m]_S = -\left\{\left(\frac{l_s}{q_\infty S}\frac{y_s}{b}\right)_m + \frac{2}{S}\left[\frac{\Gamma_c}{V_\infty}\left(\frac{v_i}{V_\infty}c_i\frac{y_{c_i}}{b} - \frac{v_o}{V_\infty}c_o\frac{y_{c_o}}{b}\right)\right]_m\right\}_S \tag{2.44}$$

where $\frac{l_s}{q_\infty S}$ is given by equation 2.34; y_s, y_{c_i} and y_{c_o} are the rolling moment arms of the lift components generated along the spanwise, the inboard and outboard chordwise bound vortices of the mth panel, respectively, as shown in figure 2.5. The rolling moment coefficient of the image of mth panel on the port wing is

$$[(C_l)_m]_P = \left\{ \left(\frac{l_s}{q_\infty S} \frac{y_s}{b} \right)_m + \frac{2}{S} \left[\frac{\Gamma_c}{V_\infty} \left(\frac{v_o}{V_\infty} c_o \frac{y_{c_o}}{b} - \frac{v_i}{V_\infty} c_i \frac{y_{c_i}}{b} \right) \right]_m \right\}_P \tag{2.45}$$

where $\frac{l_s}{q_\infty S}$ is given by equation 2.37; y_s, y_{c_i} and y_{c_o} are taken as positive values on the port wing.

Hence the wing rolling moment coefficient can be written as

$$C_l = \frac{L}{q_\infty S b} = \sum_{m=1}^{M/2} [(C_l)_m]_S + \sum_{m=1}^{M/2} [(C_l)_m]_P \tag{2.46}$$

Pitching Moment Coefficient

On the starboard wing, the pitching moment coefficient of the nth panel is given by

$$[(C_m)_n]_S = \left\{ \left(\frac{l_s}{q_\infty S} \frac{x_s}{\bar{c}} \right)_n + \frac{2}{S} \left[\frac{\Gamma_c}{V_\infty} \left(\frac{v_i}{V_\infty} c_i \frac{x_{c_i}}{\bar{c}} - \frac{v_o}{V_\infty} c_o \frac{x_{c_o}}{\bar{c}} \right) \right]_n \right\}_S \tag{2.47}$$

where $\frac{l_s}{q_\infty S}$ is given by equation 2.34; x_s, x_{c_i} and x_{c_o} are the pitching moment arms of the lift components generated along the spanwise, the inboard and outboard chordwise bound vortices of the nth panel, respectively, as shown in figure 2.5. The pitching moment coefficient of the image of the nth panel on the port wing is

$$[(C_m)_n]_P = \left\{ \left(\frac{l_s}{q_\infty S} \frac{x_s}{\bar{c}} \right)_n + \frac{2}{S} \left[\frac{\Gamma_c}{V_\infty} \left(\frac{v_o}{V_\infty} c_o \frac{x_{c_o}}{\bar{c}} - \frac{v_i}{V_\infty} c_i \frac{x_{c_i}}{\bar{c}} \right) \right]_n \right\}_P \tag{2.48}$$

Thus, the total pitching moment coefficient can be expressed as

$$C_m = \frac{M}{q_\infty S \bar{c}} = \sum_{n=1}^{M/2} [(C_m)_n]_S + \sum_{n=1}^{M/2} [(C_m)_n]_P \tag{2.49}$$

If the wing loading is symmetric, the pitching moment coefficient can be expressed as

$$C_m = 2\sum_{n=1}^{M/2}\left[(C_m)_n\right]_S \tag{2.50}$$

Induced Drag Coefficient

The induced drag for wings with dihedral is estimated using the near-field method which takes into account the contribution to the induced drag term from the induced sidewash interacting with the spanwise and chordwise bound vortices. This method is based on combining for each elemental panel the lift and leading-edge thrust as follows. On the starboard wing, the induced drag of the mth panel in non-dimensional form is given by

$$\left[\left(\frac{d_i}{q_\infty S}\right)_m\right]_S = \alpha\left[\left(\frac{l}{q_\infty S}\right)_m\right]_S - \left[\left(\frac{t}{q_\infty S}\right)_m\right]_S \tag{2.51}$$

where $\left[\left(\frac{l}{q_\infty S}\right)_m\right]_S$ is calculated by equation 2.40 and $\left[\left(\frac{t}{q_\infty S}\right)_m\right]_S$ is the non-dimensional leading edge thrust which is calculated by using Kutta-Joukowski theorem where the induced and free-stream velocity components interact with the spanwise bound vortex filament of the mth panel as follows.

$$\left[\left(\frac{t}{q_\infty S}\right)_m\right]_S = -\frac{2}{S}\left\{\frac{\Gamma_m}{V_\infty}\Delta y_m\left[\frac{w_m}{V_\infty} + \frac{v_m}{V_\infty}\tan\varphi - \alpha\right]\right\}_S \tag{2.52}$$

The downwash velocity, w, is equal to minus $\hat{w}$ which is given by equation 2.4.

Similarly, the non-dimensional induced drag of the image of the mth panel on the port wing is

$$\left[\left(\frac{d_i}{q_\infty S}\right)_m\right]_P = \alpha\left[\left(\frac{l}{q_\infty S}\right)_m\right]_P - \left[\left(\frac{t}{q_\infty S}\right)_m\right]_P \tag{2.53}$$

where $\left[\left(\frac{l}{q_\infty S}\right)_m\right]_P$ is calculated by equation 2.41 and $\left[\left(\frac{t}{q_\infty S}\right)_m\right]_P$ is given by

$$\left[\left(\frac{t}{q_\infty S}\right)_m\right]_P = -\frac{2}{S}\left\{\frac{\Gamma_m}{V_\infty}\Delta y_m\left[\frac{w_m}{V_\infty} - \frac{v_m}{V_\infty}\tan\varphi - \alpha\right]\right\}_P \tag{2.54}$$

Hence, the total induced drag coefficient can be expressed as

$$C_{D_i} = \frac{D}{q_\infty S} = \sum_{m=1}^{M/2}\left[\left(\frac{d_i}{q_\infty S}\right)_m\right]_S + \sum_{m=1}^{M/2}\left[\left(\frac{d_i}{q_\infty S}\right)_m\right]_P \tag{2.55}$$

For symmetrical loading, the induced drag coefficient is given by

$$C_{D_i} = 2\sum_{m=1}^{M/2}\left[\left(\frac{d_i}{q_\infty S}\right)_m\right]_S \tag{2.56}$$

Yawing Moment Coefficient

Using equation 2.51, the yawing moment produced about the z-axis by the mth panel on the starboard wing can be written in non-dimensional form as

$$\begin{aligned}[(C_n)_m]_S &= \left\{\alpha\left[\left(\frac{l_s}{q_\infty S}\frac{y_s}{b}\right)_m + \frac{2}{S}\left(\frac{\Gamma_c}{V_\infty}\right)_m\left(\frac{v_i}{V_\infty}c_i\frac{y_{c_i}}{b} - \frac{v_o}{V_\infty}c_o\frac{y_{c_o}}{b}\right)_m\right]\right. \\ &\quad \left. - \left(\frac{t}{q_\infty S}\right)_m\left(\frac{y_s}{b}\right)_m\right\}_S \end{aligned} \tag{2.57}$$

Where $\left[\left(\frac{l_s}{q_\infty S}\right)_m\right]_S$ and $\left[\left(\frac{t}{q_\infty S}\right)_m\right]_S$ are given by equations 2.34 and 2.52, respectively. y_s, y_{c_i} and y_{c_o} are the yawing moment arms of the induced drag components generated along the spanwise, the inboard and outboard chordwise bound vortices of the mth panel, respectively. By using equation 2.53, the yawing moment coefficient of the image of the mth panel on the port wing can be written as

$$\begin{aligned}[(C_n)_m]_P &= -\left\{\alpha\left[\left(\frac{l_s}{q_\infty S}\frac{y_s}{b}\right)_m + \frac{2}{S}\left(\frac{\Gamma_c}{V_\infty}\right)_m\left(\frac{v_o}{V_\infty}c_o\frac{y_{c_o}}{b} - \frac{v_i}{V_\infty}c_i\frac{y_{c_i}}{b}\right)_m\right]\right. \\ &\quad \left. - \left(\frac{t}{q_\infty S}\right)_m\left(\frac{y_s}{b}\right)_m\right\}_P \end{aligned} \tag{2.58}$$

Where $\left[\left(\frac{l_s}{q_\infty S}\right)_m\right]_P$ and $\left[\left(\frac{t}{q_\infty S}\right)_m\right]_P$ are given by equations 2.37 and 2.54 respectively. y_s, y_{c_i} and y_{c_o} are taken as positive values on the port wing.

Thus the total yawing moment coefficient can be expressed as

$$C_n = \frac{N}{q_\infty S b} = \sum_{m=1}^{M/2} [(C_n)_m]_S + \sum_{m=1}^{M/2} [(C_n)_m]_P \tag{2.59}$$

2.1.3 Wing VLM Computer Program

Based on linear VLM described in section 2.1, a computer program was developed by the author to estimate the aerodynamic characteristics of wings of any geometry in both symmetrical and asymmetrical flows. This program was validated by comparison with the linear VLM of Margason and Lamar [13] as described in reference [20]. The calculations carried out in this program are shown in figure 2.7. First, the wing geometry and the horseshoe vortex lattice parameters are read in. This is followed by the calculations required to represent the wing planform by a system of horseshoe vortices. Then, the influence function and boundary condition matrices are calculated, which represent, respectively, the left and right hand sides of equation 2.1. Solving this matrix equation using an appropriate NAG subroutine, viz. F04ATF, provides the values for the circulation strengths of each horseshoe vortex describing the wing flow field. Given the circulation strengths and the induced velocities, the aerodynamic loads on each elemental panel and hence the total forces and moments can be calculated as described in section 2.1.2. Finally, the calculation of the induced velocity field at specified field points can be carried out, which is required to determine the effect of tanker flow field on the

receiver aircraft.

Vortex Lattice Arrangement

The geometric description of the wing planform is based on the axis-system shown in figure 2.8, with the origin at the wing root chord leading edge and the $\hat{X}$-axis in the free-stream direction. The positive directions of the $\hat{X}$, $\hat{Y}$ and $\hat{Z}$ axes are forward, to the starboard and upwards, respectively. The wing characteristics considered by the wing VLM computer program are

- Both leading and trailing edges may have constant or variable sweep angles across the semispan.
- Taper ratio is determined from leading and trailing edge shapes.
- Any dihedral angle is allowed, constant or variable across the semispan.
- Any twist distribution is allowed across the span.
- Wing camber and thickness are assumed to be zero.

The geometrical parameters required to represent the wing planform by a lattice of horseshoe vortices are shown in figure 2.8, and explained in appendix B. Figure 2.9 illustrates the parameters used to describe the geometry of an elemental panel.

The spanwise locations of the elemental panels are adjusted so that there is always a trailing vortex filament at the locations of the points where there is change in the sweep angle of either the leading or trailing edges of the wing. In the spanwise

direction, the widths of the elemental panels can be constant or may be varied to fit loading situations, i.e. in regions of large spanwise loading gradients, the panels widths may be reduced to allow closer spacing and more detailed load predictions. In the chordwise direction, the elemental panels are distributed uniformly. The effect of the number of spanwise and chordwise panels on the circulation distribution over the Hercules wing is shown in figures 2.10a and b, respectively.

2.1.4 Tailplane-Fin Combination Model

The linear VLM used to estimate the wing span loadings is applied to fin and tailplane combination in sideslip. Figure 2.11 shows the vortex lattice arrangement used to represent the tailplane and fin in sideslip. The flow tangency boundary condition is satisfied at each control point by equating the normal velocity arising from the complete vortex system of fin and tailplane to the component of the free-stream velocity normal to the surface. The normal velocity component at any control point resulting from a system of horseshoe vortices representing two intersecting surfaces consists of the downwash contributed by all horseshoe vortices contained in the same plane as the control point plus the sidewash generated by all horseshoe vortices located in the intersecting plane. Expressions for the downwash and sidewash velocity components due to a single horseshoe vortex are given by equations 2.3 and 2.4, respectively. The tailplane-fin combination is considered at an angle of attack α and sideslip angle β, with the dihedral angle of the tailplane denoted by φ. If the circulation strengths Γ_m are assumed to be positive for the representation shown in figure 2.11, the boundary condition for a control point on

the tailplane is

$$\sum_{m=1}^{M_t/2}\left[\left(F_{w,m}-F_{v,m}\tan\varphi\right)\frac{\Gamma_m}{V_\infty}\right]_S - \sum_{m=1}^{M_t/2}\left[\left(F_{w,m}-F_{v,m}\tan\varphi\right)\frac{\Gamma_m}{V_\infty}\right]_P - \sum_{m=1}^{M_f}\left(F_{w,m}-F_{v,m}\tan\varphi\right)\frac{\Gamma_m}{V_\infty} = -4\pi\alpha \tag{2.60}$$

and for a control point on the fin is

$$\sum_{m=1}^{M_t/2}\left(F_{v,m}\frac{\Gamma_m}{V_\infty}\right)_S - \sum_{m=1}^{M_t/2}\left(F_{v,m}\frac{\Gamma_m}{V_\infty}\right)_p - \sum_{m=1}^{M_f}\left(F_{v,m}\frac{\Gamma_m}{V_\infty}\right) = 4\pi\beta \tag{2.61}$$

The first and second summations in equations 2.60 and 2.61 are the normal velocities induced by horseshoe vortices on the starboard and port halves of the tailplane, respectively. The third summation in equations 2.60 and 2.61 represent the normal velocities induced by horseshoe vortices on the fin. F_v and F_w are the sidewash and downwash influence functions for a single horseshoe vortex, respectively. Expressions for these functions are given by equations 2.5 and 2.6, respectively. The angles α and β are assumed to be sufficiently small so that $\cos\alpha = \cos\beta \approx 1$, $\sin\alpha \approx \alpha$ and $\sin\beta \approx \beta$. The Kutta-Joukowski theorem is then used to estimate the elemental force produced by each individual panel. This elemental force is then integrated across the tailplane span and over the fin height in order to obtain the total forces and moments.

2.1.5 Aerodynamic Forces and Moments of Receiver Tailplane and Fin

The forces and moments acting on the tailplane can be calculated using the equations developed for wings as described in section 2.1.2. The forces and moments acting on the fin are estimated as follows.

Fin Side Force Coefficient

Using Kutta-Joukowski theorem, the side force produced by an elemental panel, mth, on the fin due to sideslip is given by

$$(\Delta Y)_m = \rho_\infty V_\infty (\Gamma \Delta z_f)_m \tag{2.62}$$

Where Δz_f and Γ are the width and the strength of the spanwise bound vortex of the mth panel, respectively. The total side force is determined by summing equation 2.62 over all the fin elemental panels

$$Y = \rho_\infty V_\infty \sum_{m=1}^{M_f} (\Gamma \Delta z_f)_m \tag{2.63}$$

Thus, the side force coefficient based on the wing area is

$$C_Y = \frac{Y}{\frac{1}{2}\rho_\infty V_\infty^2 S} = \frac{2}{S} \sum_{m=1}^{M_f} \left(\frac{\Gamma}{V_\infty} \Delta z_f\right)_m \tag{2.64}$$

Fin Yawing and Rolling Moment coefficients

The yawing and rolling moments generated about the z and x axes, respectively, by an elemental panel, mth, on the fin can be written as

$$\Delta N = -\rho_\infty V_\infty \left[\Gamma \Delta z_f \left(x_f \cos\alpha + z_f \sin\alpha\right)\right]_m \tag{2.65}$$

and

$$\Delta L = \rho_\infty V_\infty \left[\Gamma \Delta z_f \left(z_f \cos\alpha - x_f \sin\alpha\right)\right]_m \tag{2.66}$$

where x_f and z_f are the distances between the aircraft centre of gravity and the quarter-chord of the mth panel, measured parallel and perpendicular to the longitudinal body axis, respectively, as shown in figure 2.12. The total yawing and rolling moments can be expressed as

$$N = -\rho_\infty V_\infty \sum_{m=1}^{M_f} \left[\Gamma \Delta z_f \left(x_f \cos\alpha + z_f \sin\alpha\right)\right]_m \tag{2.67}$$

and

$$L = \rho_\infty V_\infty \sum_{m=1}^{M_f} \left[\Gamma \Delta z_f \left(z_f \cos\alpha - x_f \sin\alpha\right)\right]_m \tag{2.68}$$

Thus, the yawing and rolling moment coefficients based on the wing span and area are given by

$$C_n = \frac{N}{\frac{1}{2}\rho_\infty V_\infty^2 S b} = -\frac{2}{Sb} \sum_{m=1}^{M_f} \left[\Gamma \Delta z_f \left(x_f \cos\alpha + z_f \sin\alpha\right)\right]_m \tag{2.69}$$

and

$$C_l = \frac{L}{\frac{1}{2}\rho_\infty V_\infty^2 S b} = \frac{2}{Sb} \sum_{m=1}^{M_f} \left[\Gamma \Delta z_f \left(z_f \cos\alpha - x_f \sin\alpha\right)\right]_m \tag{2.70}$$

2.1.6 Tailplane-Fin VLM Computer Program

A computer program was developed to model the tailplane-fin combination of any geometry by linear VLM. This program was validated by comparison with the analytical solution given by Laschka [36] as described by the author in reference [20]. Figure 2.13 shows the calculations carried out in this program. These calculations are similar to those described in the wing VLM computer program. The horseshoe

vortex lattice arrangement considered for wings as described in section 2.1.3 can be applied to the tailplane-fin combinations. The input data required for the tailplane-fin VLM program is given in appendix B.

2.2 Wake Velocity Using Flat Vortex Sheet Model

As was described in section 2.1, all the wing trailing vortices in linear VLM are located in a plane parallel to the free stream as shown in figure 2.14. This arrangement of the wing trailing vortices is equivalent to modelling the wing wake as a flat vortex sheet. Therefore, linear VLM is used to model the wing wake by a flat vortex sheet. The Biot-Savart law is used to calculate the velocity induced at any point in the flow field by a single horseshoe vortex as described in reference [35]. Thus, for a vortex sheet of M horseshoe vortices, the induced velocities can be expressed as

$$\hat{u} = \frac{1}{4\pi} \sum_{i=1}^{m} F_{u_i} \frac{\Gamma_i}{V_\infty}$$

$$\hat{v} = \frac{1}{4\pi} \sum_{i=1}^{m} F_{v_i} \frac{\Gamma_i}{V_\infty}$$

$$\hat{w} = \frac{1}{4\pi} \sum_{i=1}^{m} F_{w_i} \frac{\Gamma_i}{V_\infty}$$

where Γ_i are the horseshoe vortex strengths and F_u, F_v and F_w are the geometric functions associated with a unit horseshoe vortex. The functions F_u, F_v and F_w are given by equations 2.35, 2.5 and 2.6, respectively. Both the horseshoe vortex strengths and the geometric functions are obtained from linear VLM.

The velocities induced by flat vortex sheets representing tapered and swept wings

were examined by West [24] and Alford [37], respectively, at various horizontal , lateral and vertical positions. The results showed that the vortex sheet model predicted the backwash and downwash correctly but it did not produce the correct sidewash close to the vortex sheet given by

$$\hat{v} = \pm\frac{1}{2}\left(\frac{d\Gamma}{d\hat{y}}\right)$$

This is due the fact that the sidewash on the sheet is either zero or infinite depending on whether the point of interest lies between or on the trailing vortices. More realistic values of the sidewash velocity close to the vortex sheet were obtained by Alford [37] by estimating the sidewash in the plane of the wing due to the lateral gradient of the circulation and fairing from this value to the maximum sidewash obtained from the vortex sheet model slightly below the wing.

In air-to-air refuelling, the points of interest on the receiver fin and tailplane must be arranged such that any trailing vortices from either the tanker or receiver wing vortex sheets are prevented from passing very close to these points. However, Bloy et al [19] found that the region in which the sidewash on the fin was incorrect was relatively small and had negligible effect on the fin side force.

2.3 Three-Dimensional Steady Roll-up Model

The roll-up model developed by West [24] is used to calculate the roll-up of the tanker wing wake. The roll-up model uses a steady, inviscid three-dimensional line vortex method based on that of Butter and Hancock [38]. The method includes the effect of both the bound and the trailing vortices. The continuous vortex sheet

from a lifting wing is replaced by discrete trailing vortices whose total vorticity is equal to that of the continuous vortex sheet. Each trailing vortex was divided into finite-length vortex elements, initially aligned with the free-stream direction. The influence on each vortex element due to the wing vortex system (i.e. spanwise and chordwise bound vortices) and all shed vortices except for the vortex element itself was calculated. The downstream end of each vortex element was then allowed to move in order to align the vortex element with the local flow direction. The portion of the trailing vortex between the downstream end of the vortex element and infinity moved with the vortex element to remain attached, but stayed in the free-stream direction. The calculations were continued to a downstream distance sufficient for evaluating the effect of tanker wing wake roll-up on the receiver aircraft (i.e. beyond this distance the tanker wing wake roll-up had no effect on the receiver).

As described by Moore [39], the line vortex method can produce chaotic motion of the vortices due to the very high velocities induced by vortices in close proximity. This chaotic motion was prevented by using the method of Krasny [40] which modifies the induced velocities due to a line vortex so that high velocities near the vortex core are avoided. The smoothing factor is analogous to the introduction of artificial viscosity. For a doubly-infinite line vortex, the modified induced velocity v is given by

$$v = \frac{\Gamma}{2\pi h}\left(\frac{h^2}{h^2 + \delta_k^2 b^2}\right) \tag{2.71}$$

Typical values of the Krasny smoothing factor δ_k lie in the range 0.001 to 0.1. The chaotic motion is reduced as the smoothing factor increases. The optimum value for δ_k depends on step size (i.e. length of vortex elements), number of trailing

vortices, downstream distance and spanwise spacing of vortices.

The calculations required by the wing wake roll-up model are described here briefly and in more detail in reference [24].

2.3.1 The Vortex Lattice Method of Mendenhall et al

Since the roll-up model was originally developed to model flapped wings, the VLM of Mendenhall et al [26, 27] was used to generate the lattice structure on the wing (i.e. the strengths and positions of chordwise and spanwise bound vortices). The VLM of Mendenhall et al was developed to calculate the longitudinal aerodynamic characteristics of wing-flap configurations with externally blown flaps. A horseshoe vortex-lattice is used to represent the wing-flap surfaces and a series of vortex rings to model the jet wake. In this research work, only the wing model was required. This model differs from the linear VLM model in that the trailing vortex legs extend to infinity in the plane of the wing rather than the free-stream direction as illustrated in figures 2.15a and b. For small angles of attack, both models produce the same results as shown in figure 2.16 which gives the lift characteristics of the tapered tanker wing specified in chapter 3. Figure 2.16 indicates that for higher angles of attack, the VLM of Mendenhall et al produces slight non-linearity in the variation of the lift coefficient with incidence.

2.3.2 Discretising the Trailing Vortex Sheet

The continuous trailing vortex sheet is divided into discrete trailing vortices of equal strengths or equal spacings. The positions and strengths of the discrete vortices are determined using cubic spline interpolation in order to ensure that continuous curves are fitted to the circulation distribution over the wing. Figures 2.17a and b show the circulation distribution of the KC10 tanker wing divided into equal strength and equal spacing vortices, respectively. The equal strength vortices were used to give a good representation of the regions of highly concentrated shed vorticity found near the wing tips while the equal spaced vortices were found to give a better representation of the central part of the wing vortex sheet [24].

2.3.3 Wing Vortex Wake Roll-up

The vortex wake roll-up is modelled using elemental steps of the discrete trailing vortices. The roll-up calculations are then carried out one step at a time. In the first step the finite length vortex elements are located between the wing trailing edge and the upstream ends of the semi-infinite trailing vortices as shown for a rectangular wing in figure 2.18. Each finite length vortex element is defined by three points as illustrated in figure 2.19. Initially the coordinates of these points for the first step are given by

$$x, y, z(1, i, j) = \textit{point on wing trailing edge}$$

$$x(2, i, j) = x(1, i, j) + s_f$$

$$y, z(2, i, j) = y, z(1, i, j) \textit{ i.e. no displacements in } y \textit{ or } z \textit{ directions}$$

$$x(3,i,j) = x(1,i,j) + 2s_f$$

$$y,z(3,i,j) = y,z(1,i,j)$$

where s_f is the half step length, i is the downstream step (i.e. the number of the finite length vortex element downstream of the trailing edge, i=1 for the first step) and j is the spanwise vortex number (i.e. specifies which trailing vortex the finite length vortex element belongs to). For each vortex element in the first step, the velocity induced by all other trailing vortex elements and by the wing bound vortices is calculated at the mid point of the finite length vortex element. The wing bound vortices are located at the quarter-chord line of each panel and in the chordwise direction over the wing surface. Each trailing vortex element in the first step is then allowed to follow the local flow direction and the downstream end positions of these trailing vortex elements are calculated with the remaining part of the trailing vortex elements aligned with the freestream. The new coordinates of the vortex elements in the first step are now given by

$$x,y,z(1,i,j) \; \textit{fixed at wing trailing edge}$$

$$x(2,i,j) = x(1,i,j) + \delta x'$$

$$y(2,i,j) = y(1,i,j) + \delta y'$$

$$z(2,i,j) = z(1,i,j) + \delta z'$$

$$x(3,i,j) = x(1,i,j) + 2\delta x'$$

$$y(3,i,j) = y(1,i,j) + 2\delta y'$$

$$z(3,i,j) = z(1,i,j) + 2\delta z'$$

where

$$\delta x' = \frac{s_f + \delta x}{\sqrt{(s_f + \delta x)^2 + \delta y^2 + \delta z^2}} s_f$$

$$\delta y' = \frac{\delta y}{\sqrt{(s_f + \delta x)^2 + \delta y^2 + \delta z^2}} s_f$$

$$\delta z' = \frac{\delta z}{\sqrt{(s_f + \delta x)^2 + \delta y^2 + \delta z^2}} s_f$$

$$\delta x = \frac{u}{U_\infty} s_f, \quad \delta y = \frac{v}{U_\infty} s_f \quad and \quad \delta z = \frac{w}{U_\infty} s_f$$

A second step is made along the trailing vortices as shown in figure 2.20, with the coordinates of the finite length vortex elements initially given by

$$x, y, z(1, i, j) = x, y, z(3, i-1, j)$$

$$x(2, i, j) = x(1, i, j) + s_f$$

$$y, z(2, i, j) = y, z(1, i, j)$$

$$x(3, i, j) = x(1, i, j) + 2s_f$$

$$y, z(3, i, j) = y, z(1, i, j)$$

where i=2 for the second step.

The calculation of the induced velocity due to the wing bound vortices and the trailing vortex system obtained after the first step is then repeated. The finite length vortex elements in the second step are aligned with the local flow and the process repeated to the required distance downstream. The effect of wake roll-up on the wing loading was neglected. This was justified by calculating the circulation distribution of the KC10 tanker wing with and without wake roll-up using the non-linear VLM of Maziat [41]. Results showed that the wake roll-up had negligible

effect on wing circulation distribution. Therefore, the roll-up calculations from the wing trailing edge to the required distance downstream were only carried out once.

2.4 Tanker-Receiver Aerodynamic Models

This section describes the theoretical models used to estimate the longitudinal and lateral aerodynamic interference between tanker and receiver aircraft. The tanker is represented by its main wing with the trailing vortex wake modelled using 3-D roll-up or flat vortex sheet models. The forces and moments acting on the receiver wing are calculated using tanker wing VLM-receiver wing VLM model whereas the aerodynamic loads on the receiver tailplane and fin are estimated using tanker wing VLM-receiver wing, tailplane and fin VLM model. Approximate expressions, based on both ESDU data sheet and the tanker wing sidewash and downwash induced at the receiver centre of gravity, are used to determine the aerodynamic loads on the receiver fuselage.

2.4.1 Tanker Wing VLM-Receiver Wing VLM Model

This theoretical model uses the VLM to model the tanker and receiver wings. A computer program was developed to apply this model to any tanker and receiver wings. The calculations carried out in this program are shown in figure 2.21. First, the tanker wing loading is determine using either the VLM of Mendenhall et al described in section 2.3.1 or the linear VLM explained in section 2.1. Next, given

the relative position of the receiver wing, the tanker wing induced velocities on the receiver wing can be calculated using either the 3-D roll-up or the flat vortex sheet models described in sections 2.3 and 2.2, respectively. The linear VLM program described in section 2.1.3 is then applied to the receiver wing with the tanker wing induced velocities modelled as a twist distribution across the receiver wing span. Thus, as was shown in section 2.1.2, the VLM program can provide all the aerodynamic loads on the receiver wing.

2.4.2 Tanker Wing VLM-Receiver Wing, Tailplane and Fin VLM Model

This theoretical model uses again the VLM to model the tanker wing and receiver wing, tailplane and fin. A computer program was also developed to apply this model to any tanker wing and any receiver wing , tailplane and fin. Figure 2.22 illustrates the calculations carried out in this program. First, the tanker and receiver wing loadings are obtained using the tanker wing VLM-receiver wing VLM program as described in section 2.4.1. Next, given the relative position of the receiver tailplane and fin, the tanker wing induced velocities at the receiver tailplane and fin control points can be calculated using either the 3-D roll-up or the flat vortex sheet models. This is followed by the calculation of the receiver wing induced velocities at the receiver tailplane and fin control points using the flat vortex sheet model. In the application of the flat vortex sheet model, The tanker and receiver wing trailing vortices must not pass through or very close to the receiver tailplane and fin control points. This is necessary to ensure that no infinite or very

large velocities are induced on the tailplane and fin. The aerodynamic loads on the receiver tailplane and fin are then estimated using the tailplane-fin VLM program with the tanker and receiver wing induced velocities replaced by twist distributions over the fin height and across the tailplane span.

2.4.3 Longitudinal Aerodynamic Interference

The longitudinal aerodynamic interference between tanker and receiver aircraft is considered by displacing the receiver vertically and horizontally in the z and x directions, respectively, and by varying the receiver pitch angle. Positive vertical and horizontal displacements from the datum position move the receiver in the downwards and downstream directions, respectively, positive pitch displacement moves the receiver nose upward. The vertical and horizontal separations between tanker and receiver aircraft are measured between the root chord leading edge points of the tanker and receiver wings. Using the aerodynamic models described in section 2.4 to estimate the longitudinal interference requires the components of the tanker induced velocity in directions normal and parallel to the receiver wing, tailplane and fin surfaces. Therefore, for receiver wings with dihedral, the components of the tanker induced velocity normal and parallel to the wing surface are determined as shown in figure 2.23a.

2.4.4 Lateral Aerodynamic Interference

The lateral aerodynamic interference between tanker and receiver aircraft is considered by banking and yawing the receiver and displacing it sideways. The arrangements of tanker and receiver aircraft during positive side, bank and yaw displacements are shown in figures 2.24a, b and c, respectively. In the side displacement case, the tanker induced velocities can be used directly in the application of the aerodynamic models described in section 2.4 since tanker axes are parallel to receiver axes. However, for the bank and yaw displacements, the tanker induced velocities along the tanker axes need to be resolved normal and parallel to the receiver wing, tailplane and fin surfaces. Banking the receiver produces the velocity components shown in figure 2.23b while the effect of yawing the receiver is illustrated in figure 2.23c.

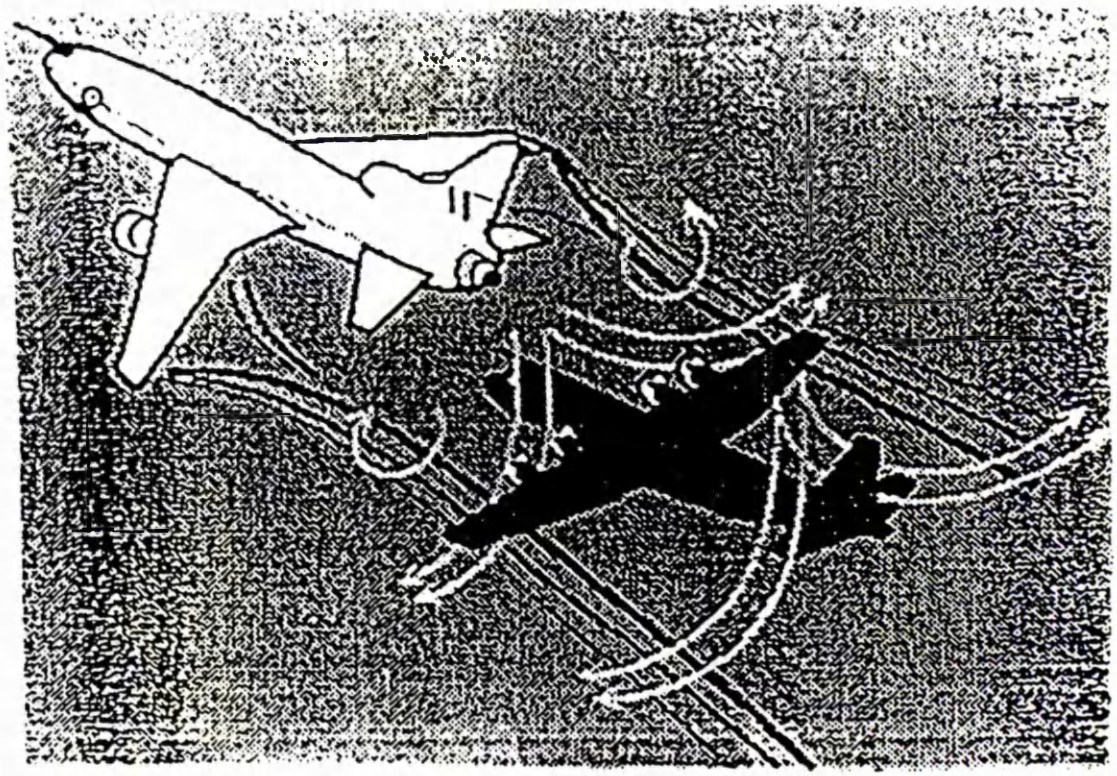

Figure 2.1: Downwash and sidewash flow components over the receiver produced by the tanker wing shed vortices.

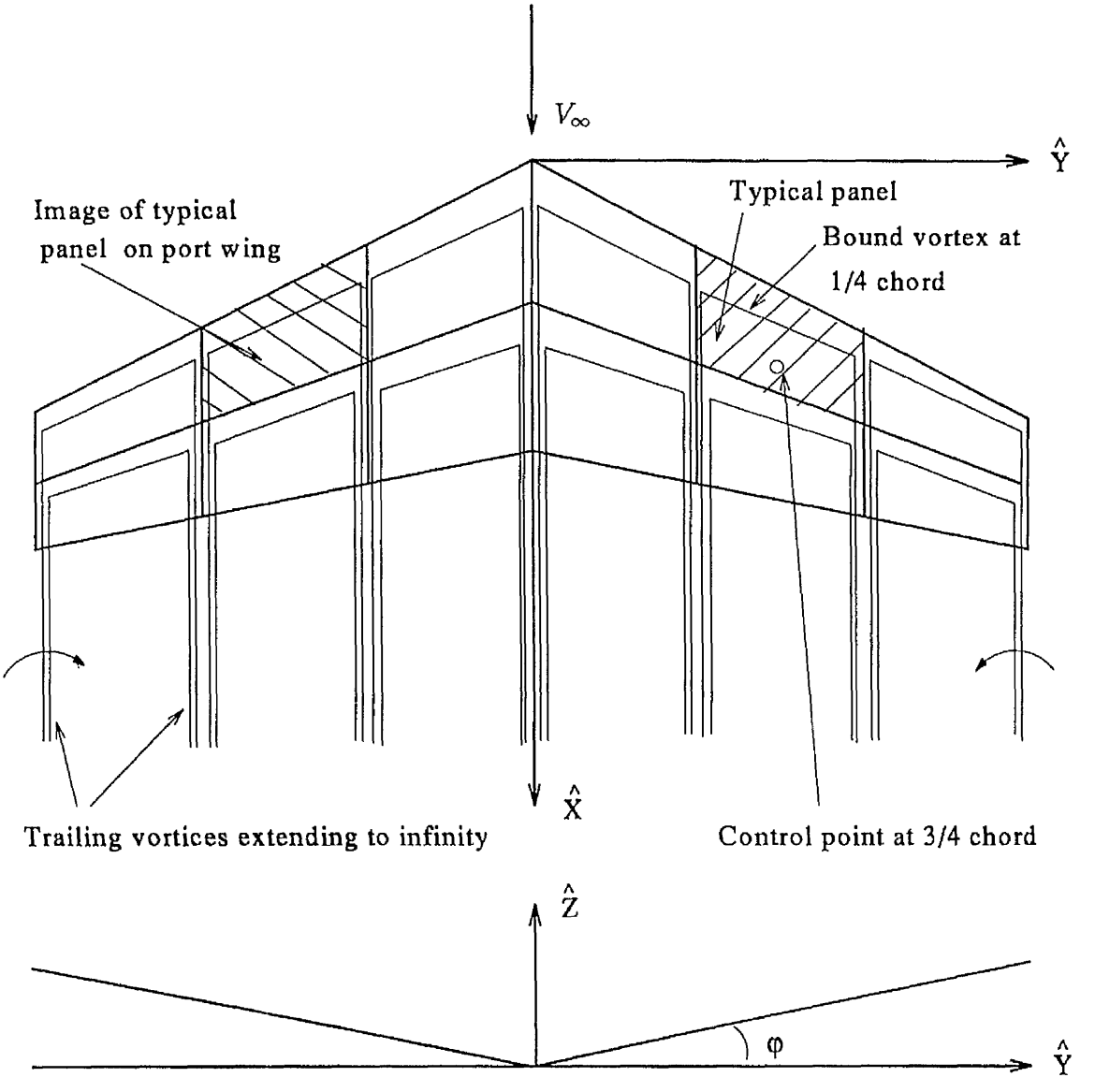

Figure 2.2: Vortex lattice modelling of a typical wing planform showing elemental panels, horseshoe vortices and coordinate system.

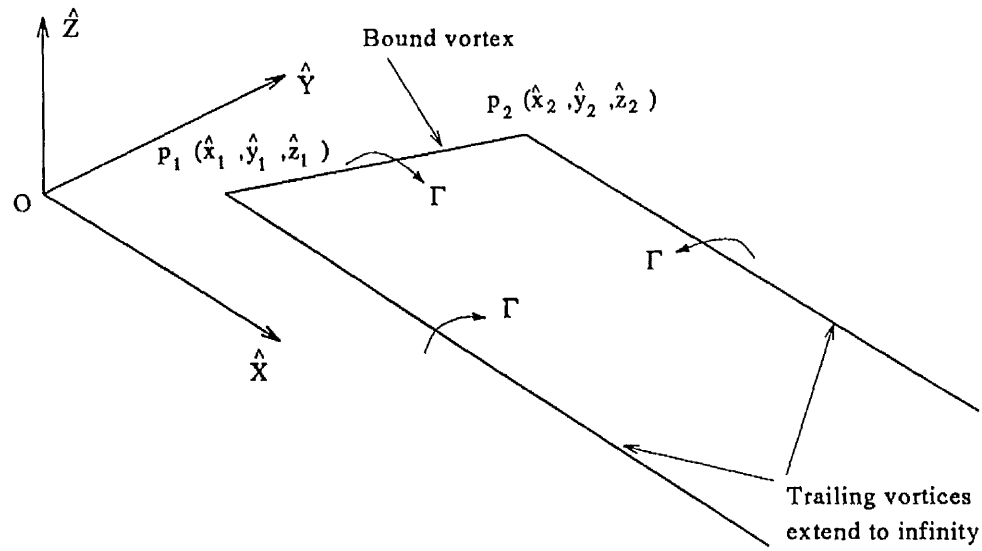

Figure 2.3: Horseshoe vortex showing coordinate system used in linear VLM.

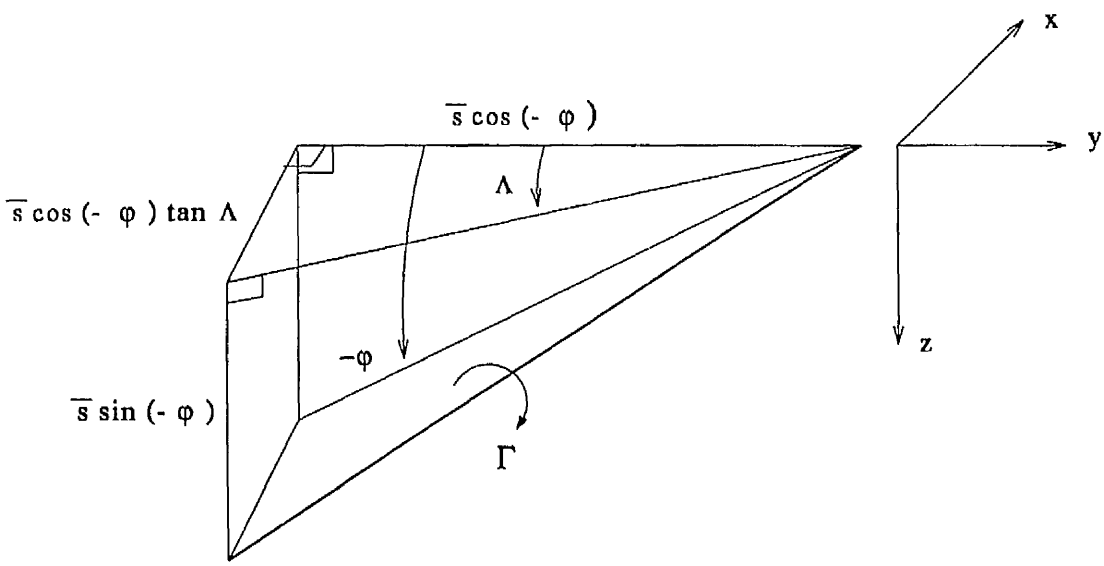

Figure 2.4: Components of a spanwise bound vortex filament at an arbitrary orientation in the flow.

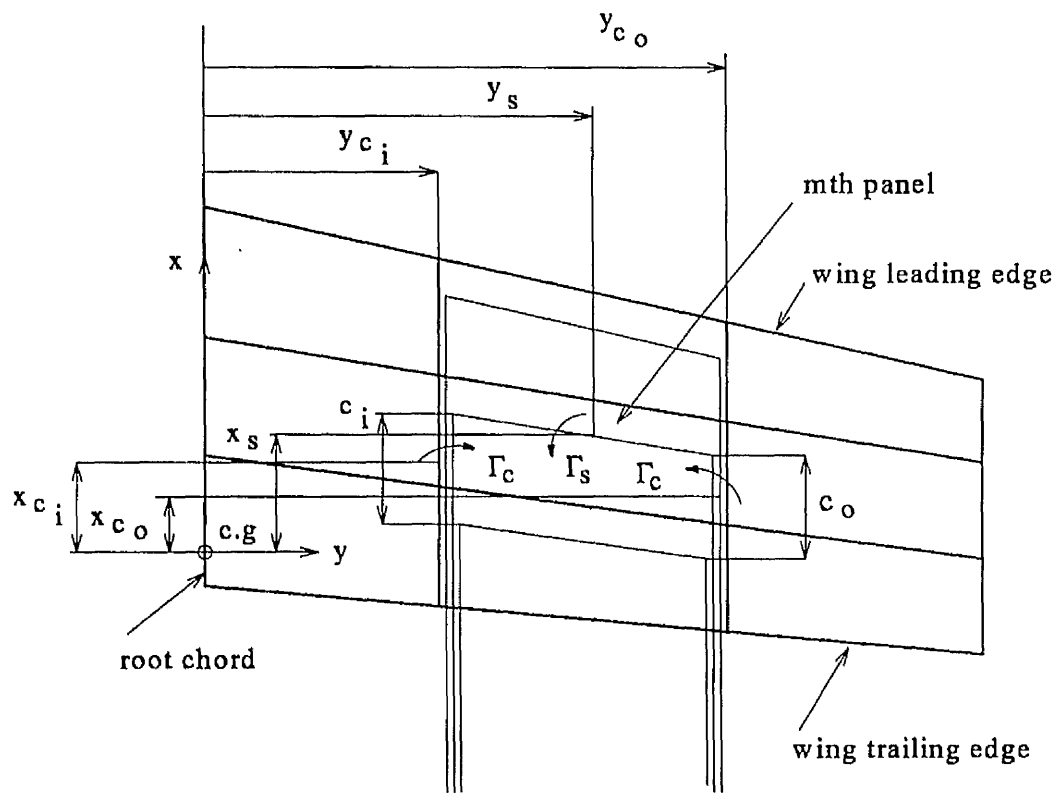

Figure 2.5: Details of mth panel on the starboard wing used to calculate the forces and moments.

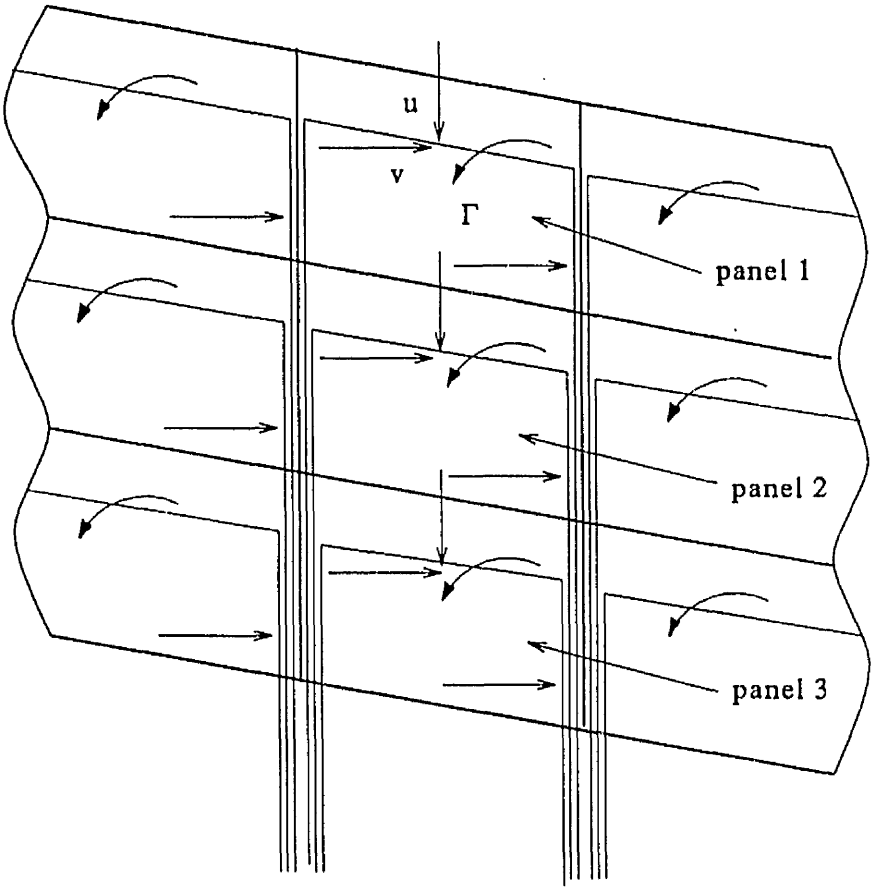

Figure 2.6: Details of chordwise row of horseshoe vortices which illustrate the velocities and circulation used to calculate the forces and moments on the elemental panels of a wing with dihedral.

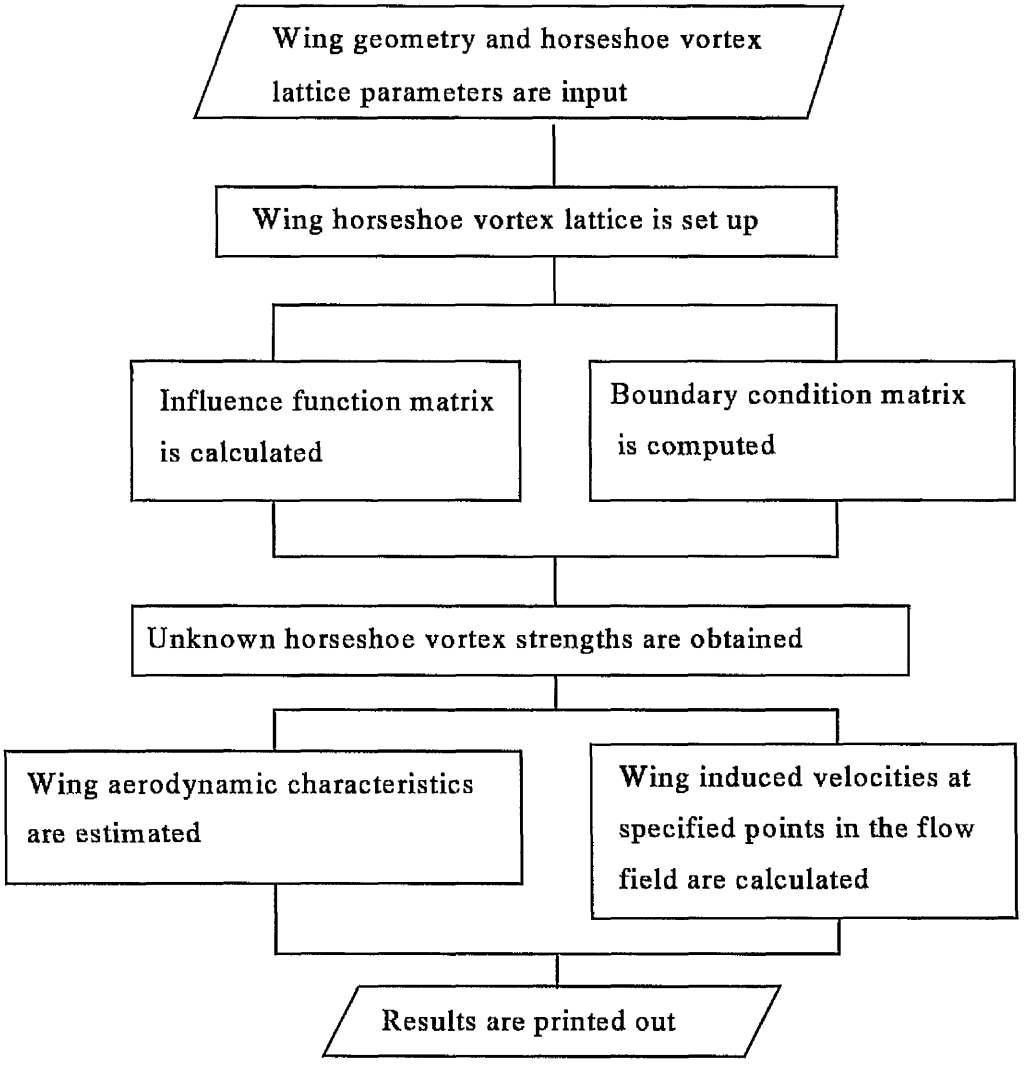

Figure 2.7: General flow chart of wing VLM computer program.

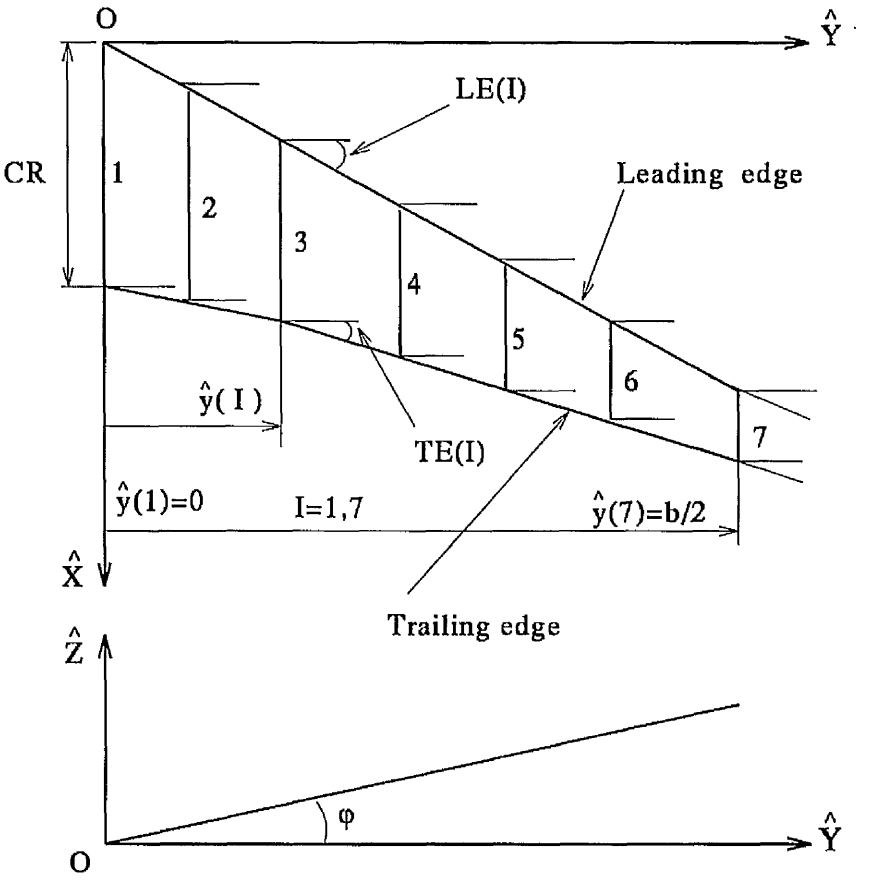

Figure 2.8: Parameters used to describe the wing geometry.

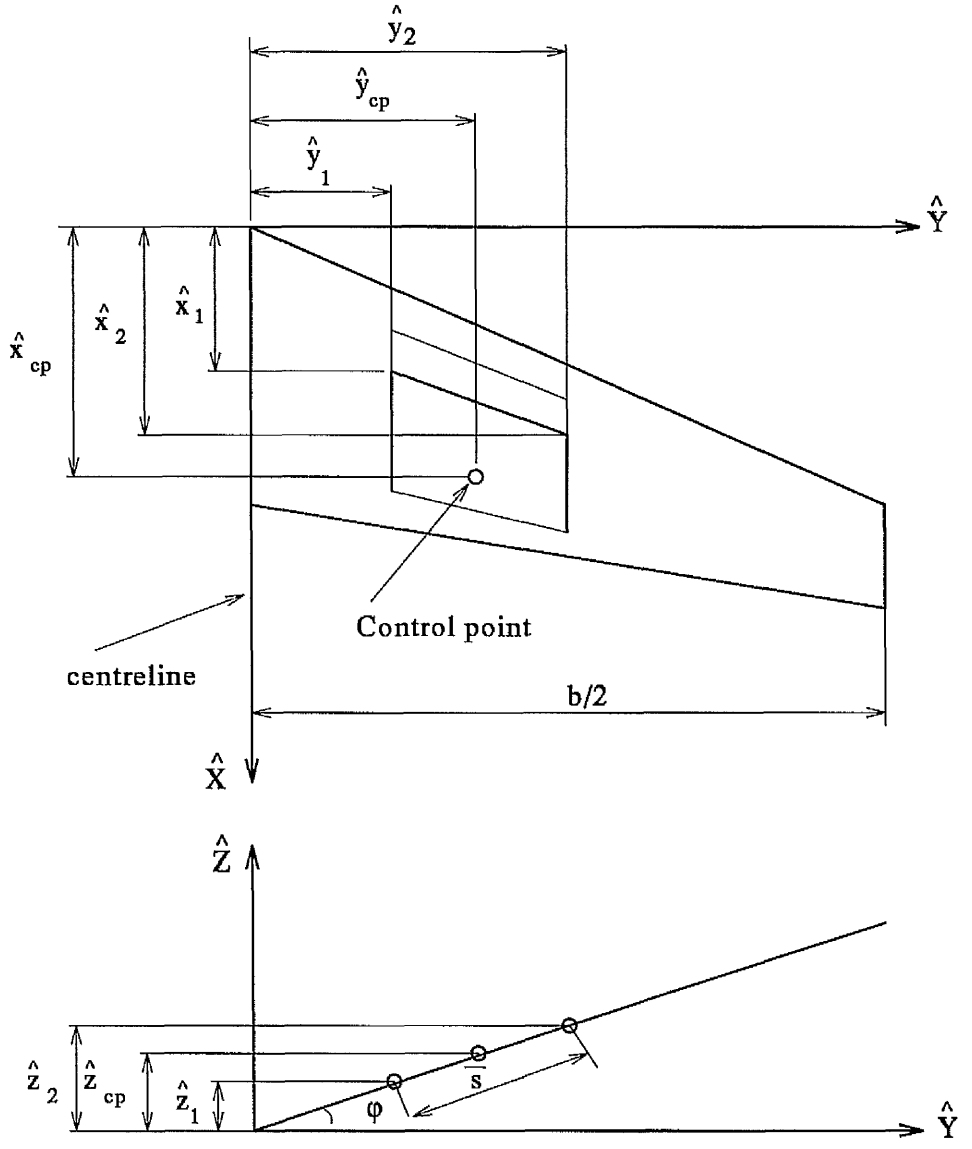

Figure 2.9: Parameters used to describe the geometry of an elemental panel.

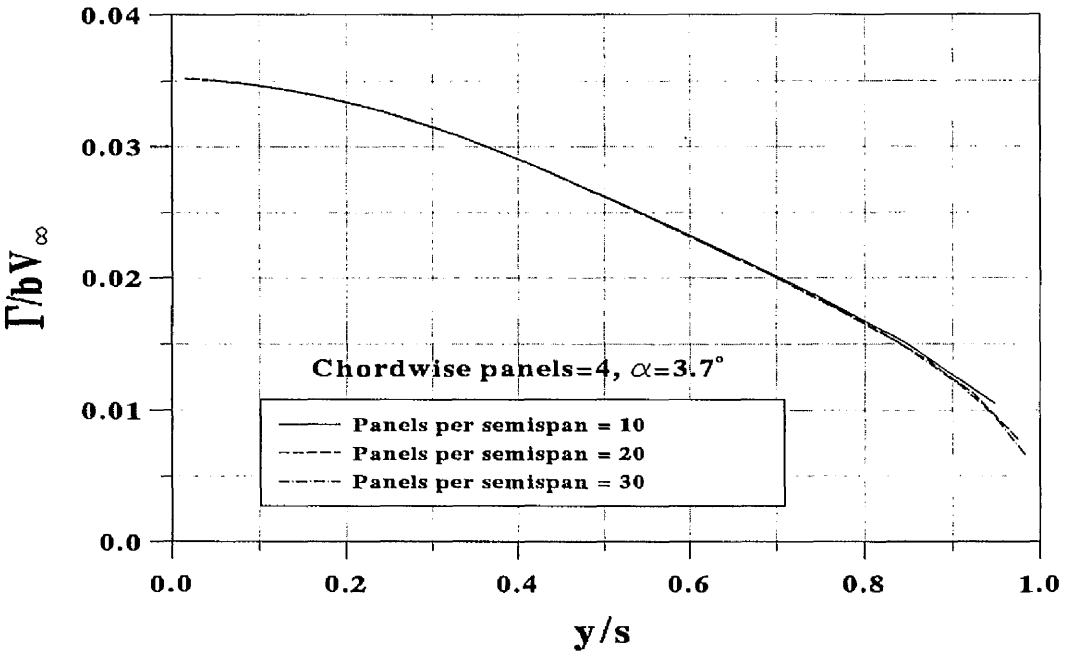

(a) Effect of number of spanwise panels

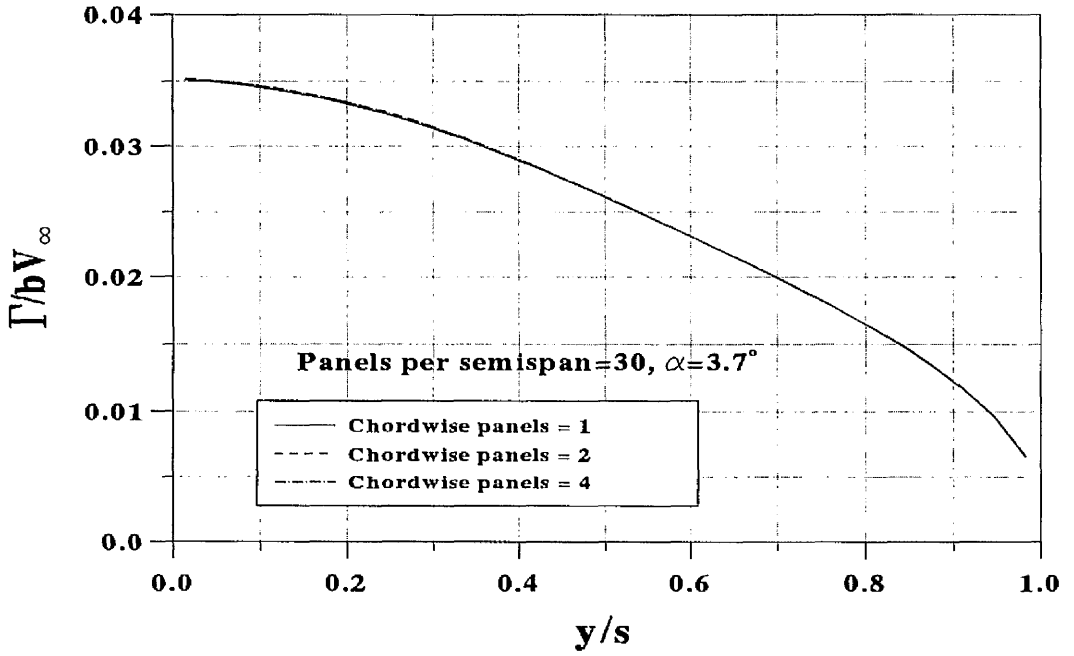

(b) Effect of number of chordwise panels.

Figure 2.10: Effect of number of panels on the circulation distribution over the Hercules wing.

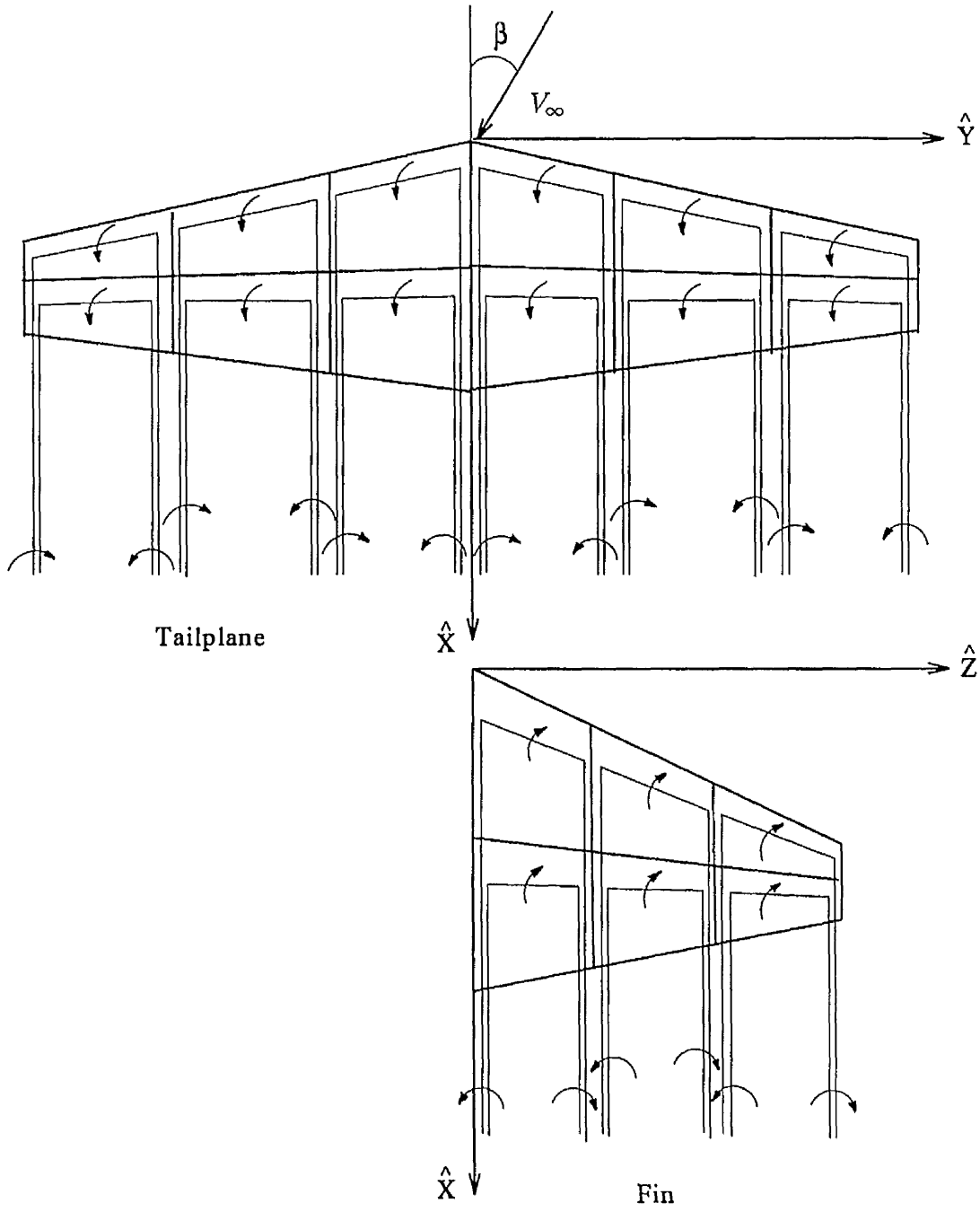

Figure 2.11: Linear VLM modelling of the tailplane and fin.

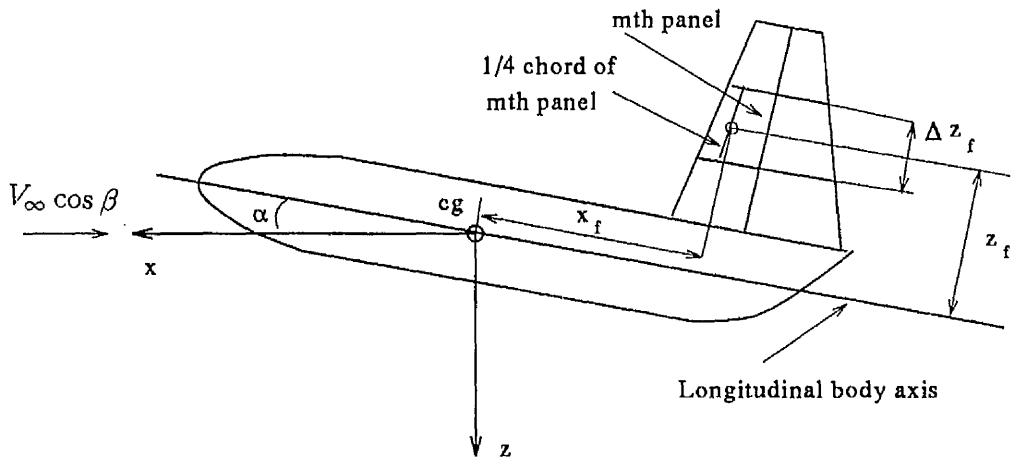

Figure 2.12: Illustration of symbols used in calculating the forces and moments on the fin.

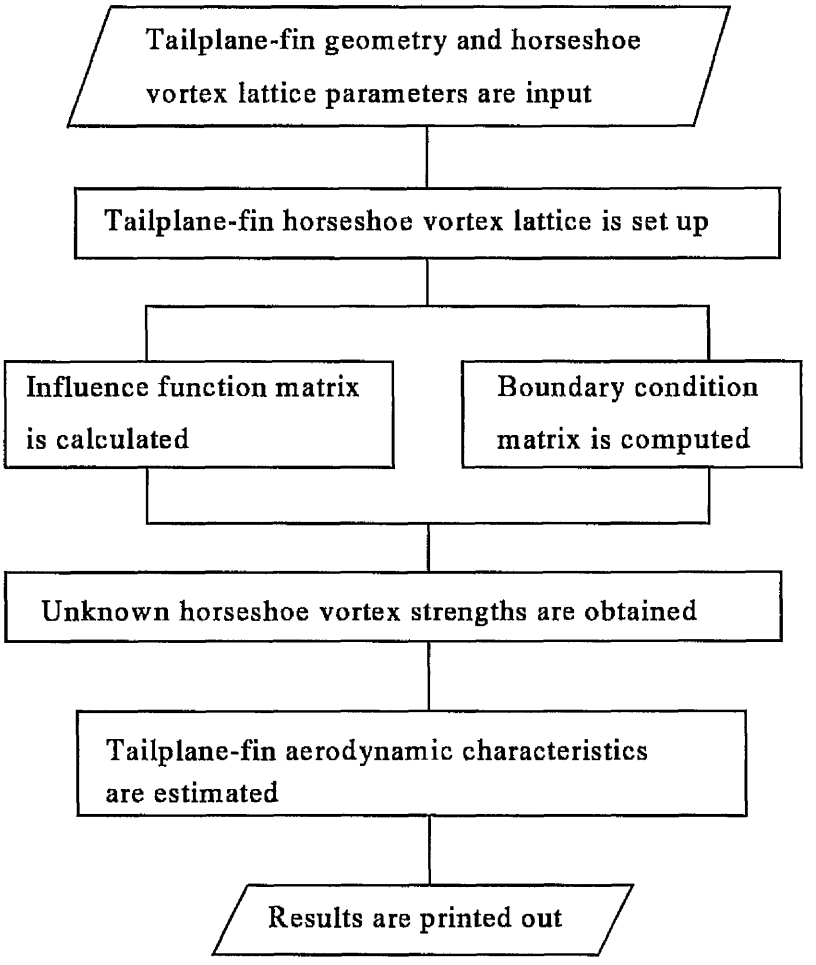

Figure 2.13: General flow chart of tailplane-fin VLM computer program.

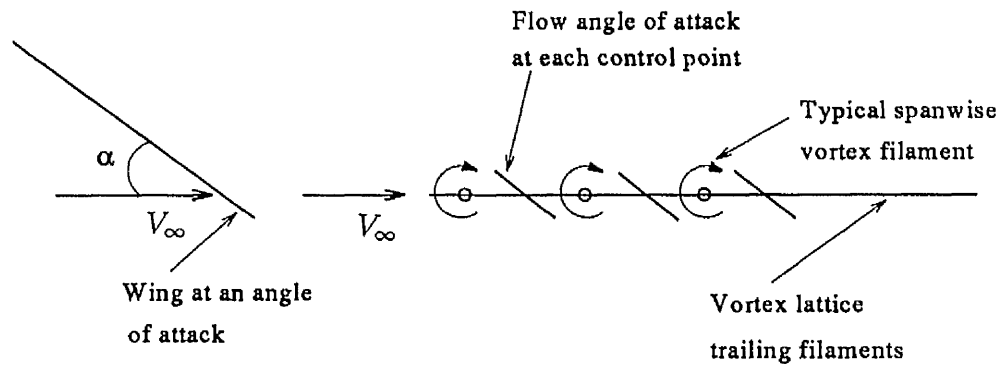

Figure 2.14: Linear VLM model of a wing.

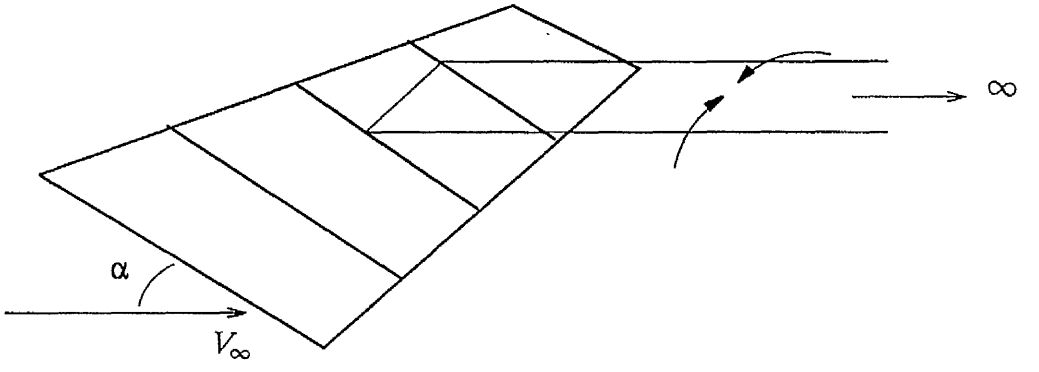

(a) Linear VLM

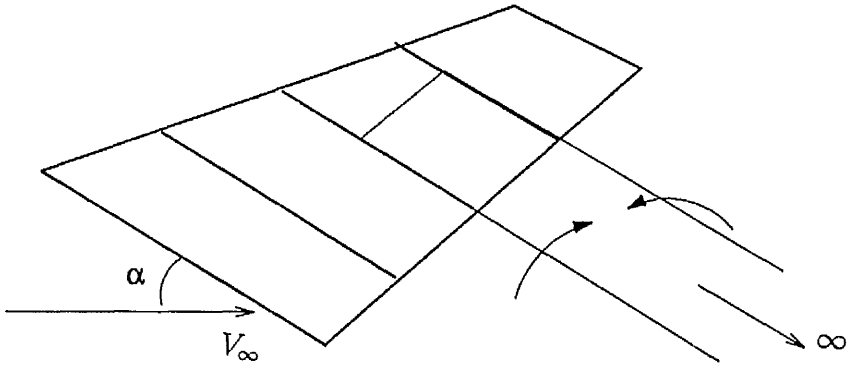

(b) VLM of Mendenhall et al

Figure 2.15: Linear and Mendenhall et al VLM models.

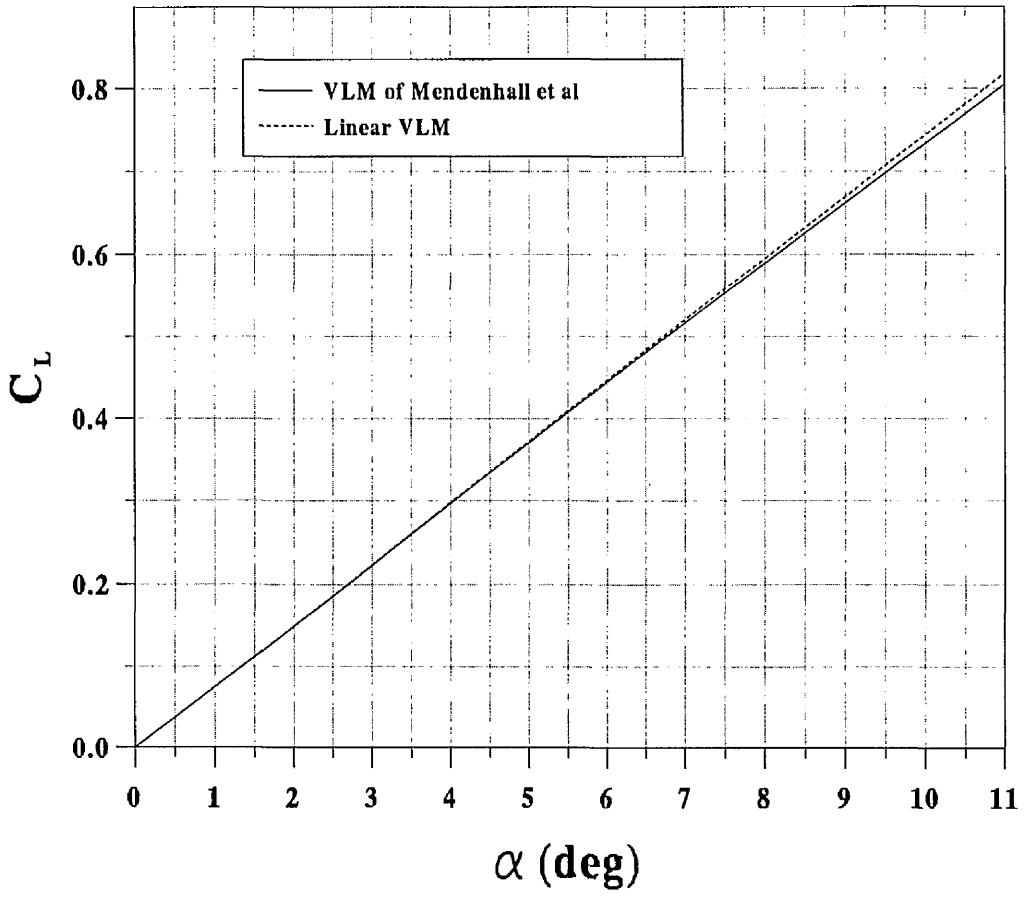

Figure 2.16: Comparison between VLM of Mendenhall et al and linear VLM.

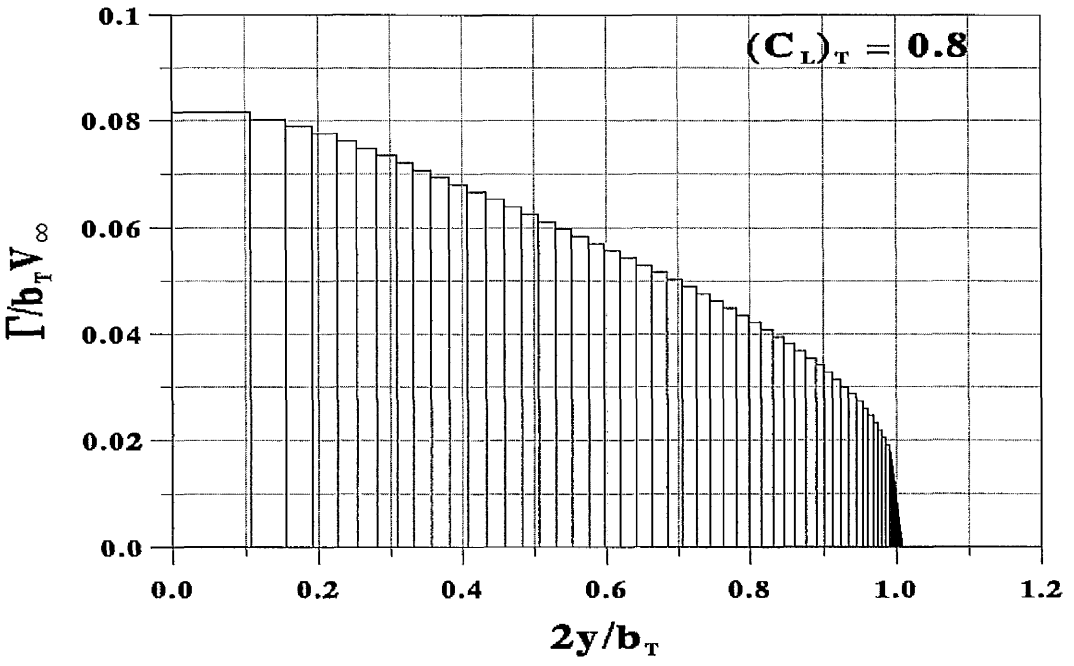

(a) Equal strength

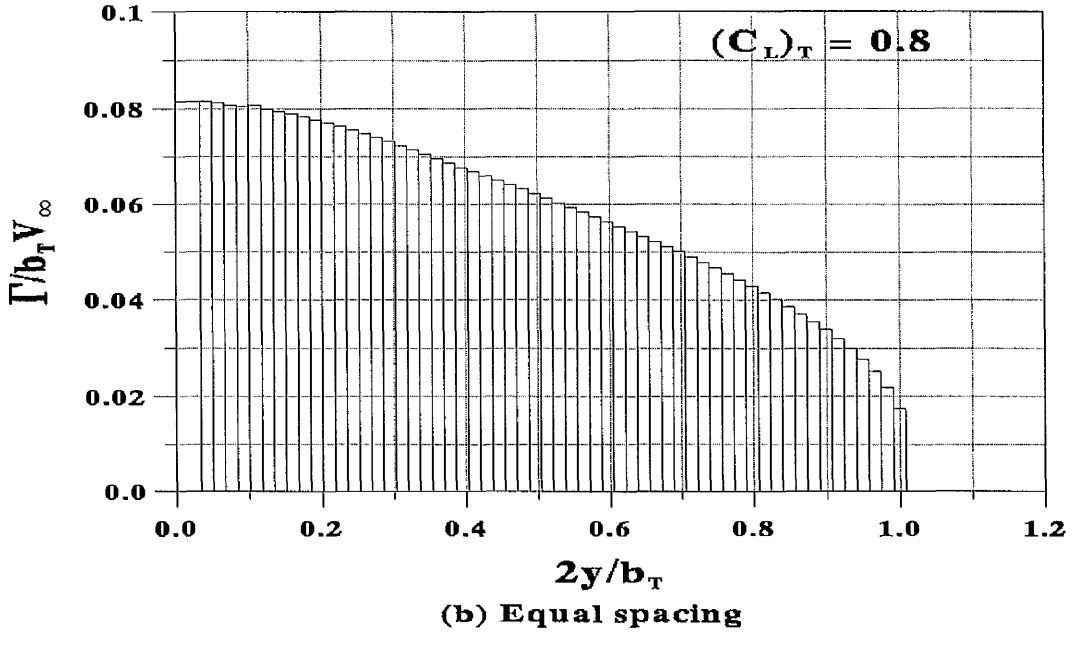

(b) Equal spacing

Figure 2.17: Circulation distribution of KC10 wing divided into equal spacing and equal strength vortices.

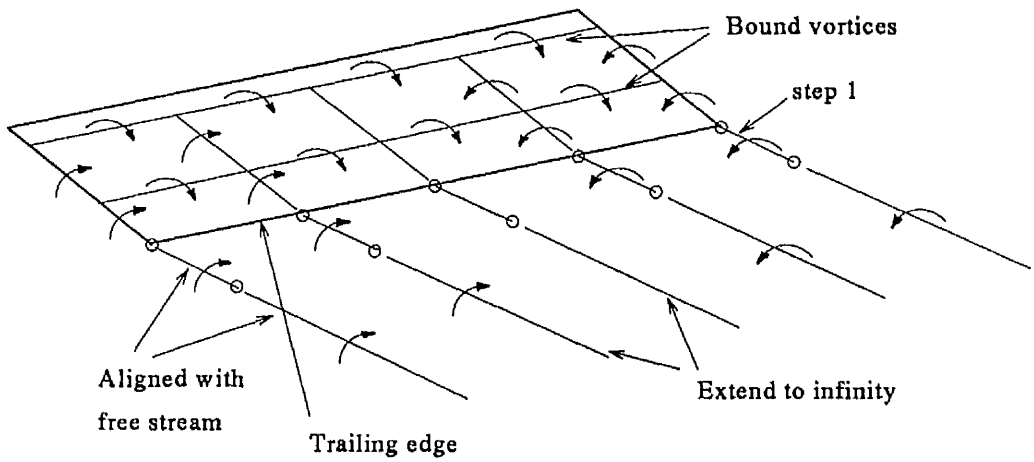

Figure 2.18: Arrangement of shed vortices for step 1.

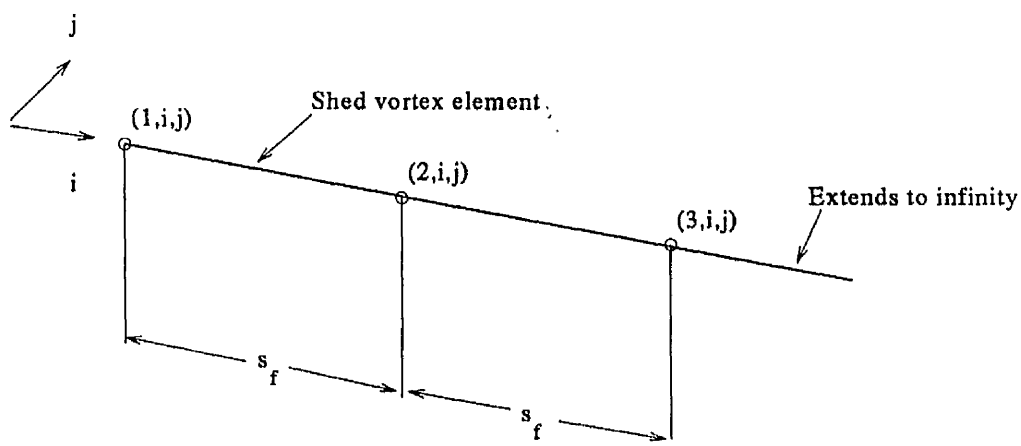

Figure 2.19: Shed vortex elements used in roll-up calculations.

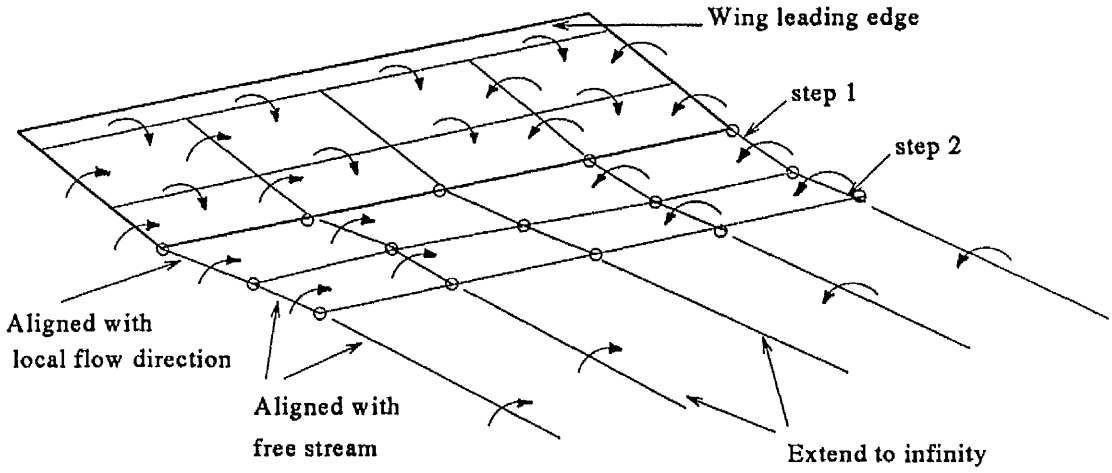

Figure 2.20: Arrangement of shed vortices for step 2.

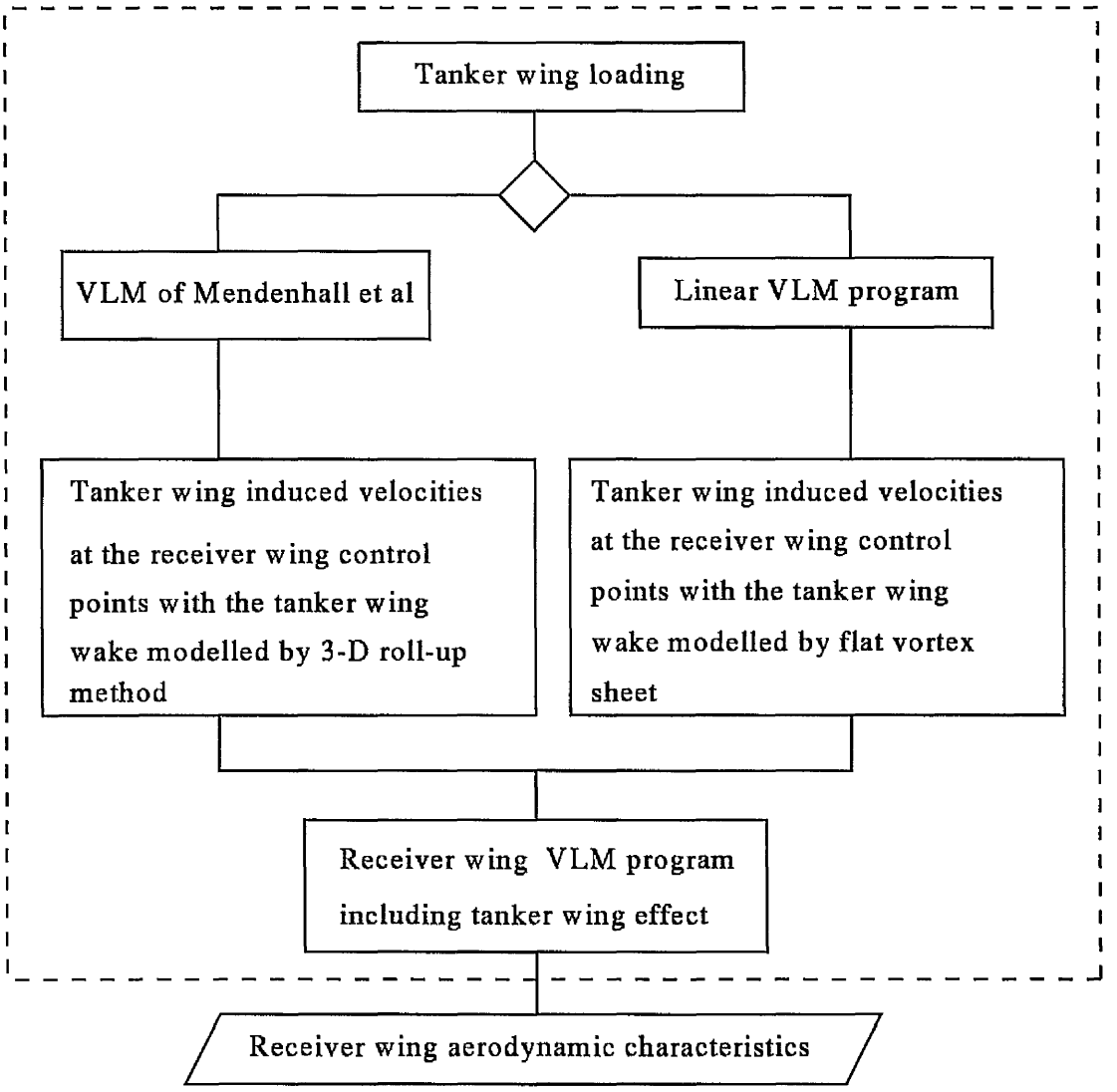

Figure 2.21: General flow chart of tanker wing VLM-receiver wing VLM computer program.

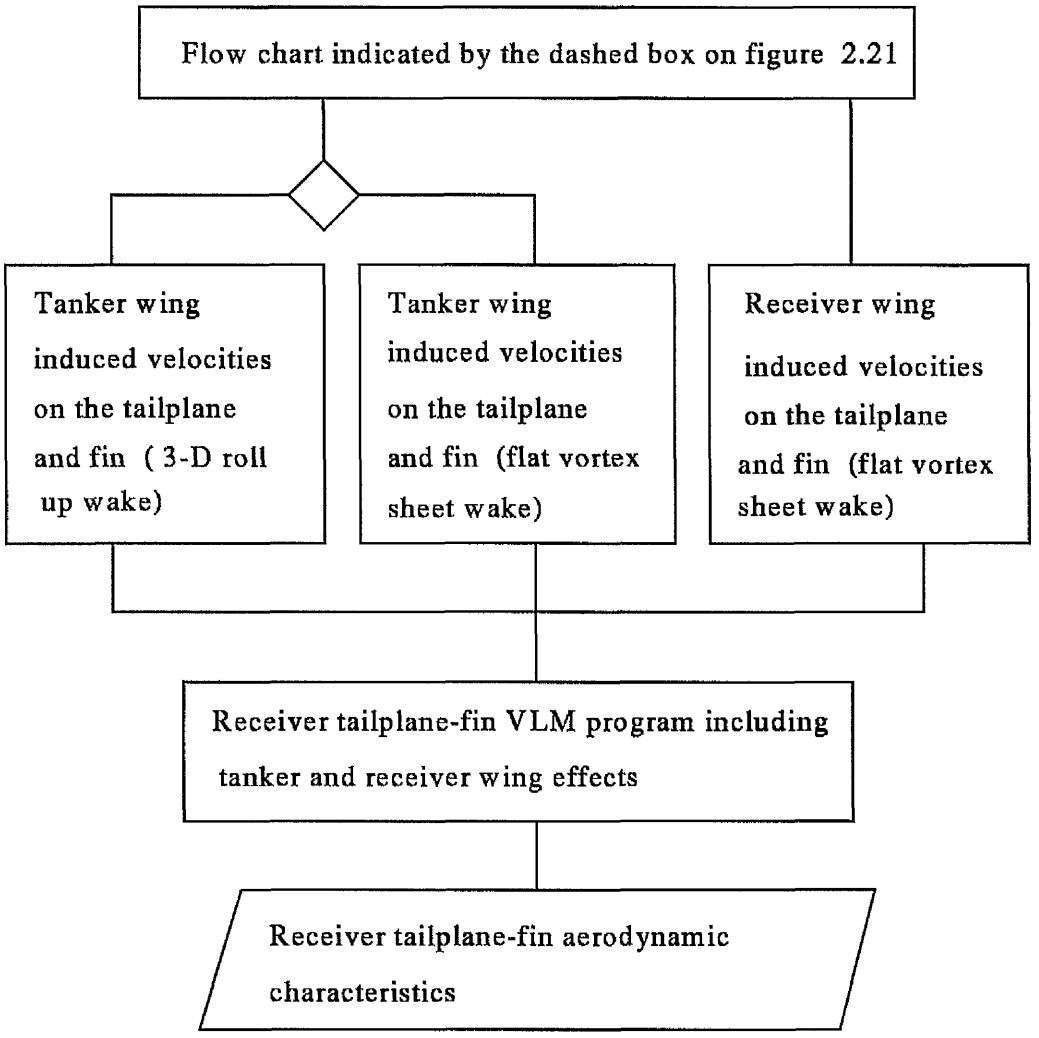

Figure 2.22: General flow chart of tanker wing VLM-receiver wing, tailplane and fin VLM computer program.

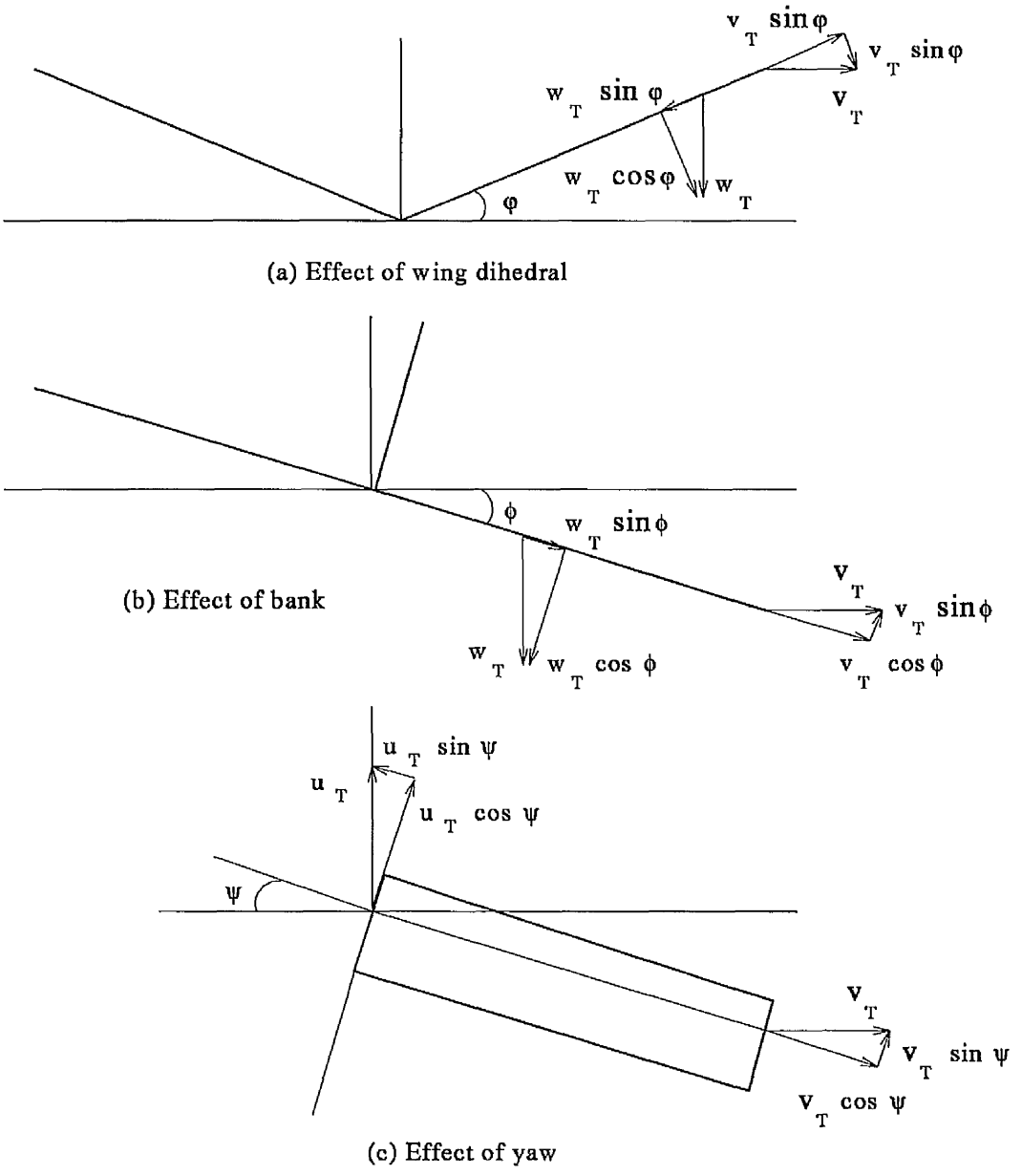

Figure 2.23: Tanker induced velocity components parallel and normal to the receiver wing.

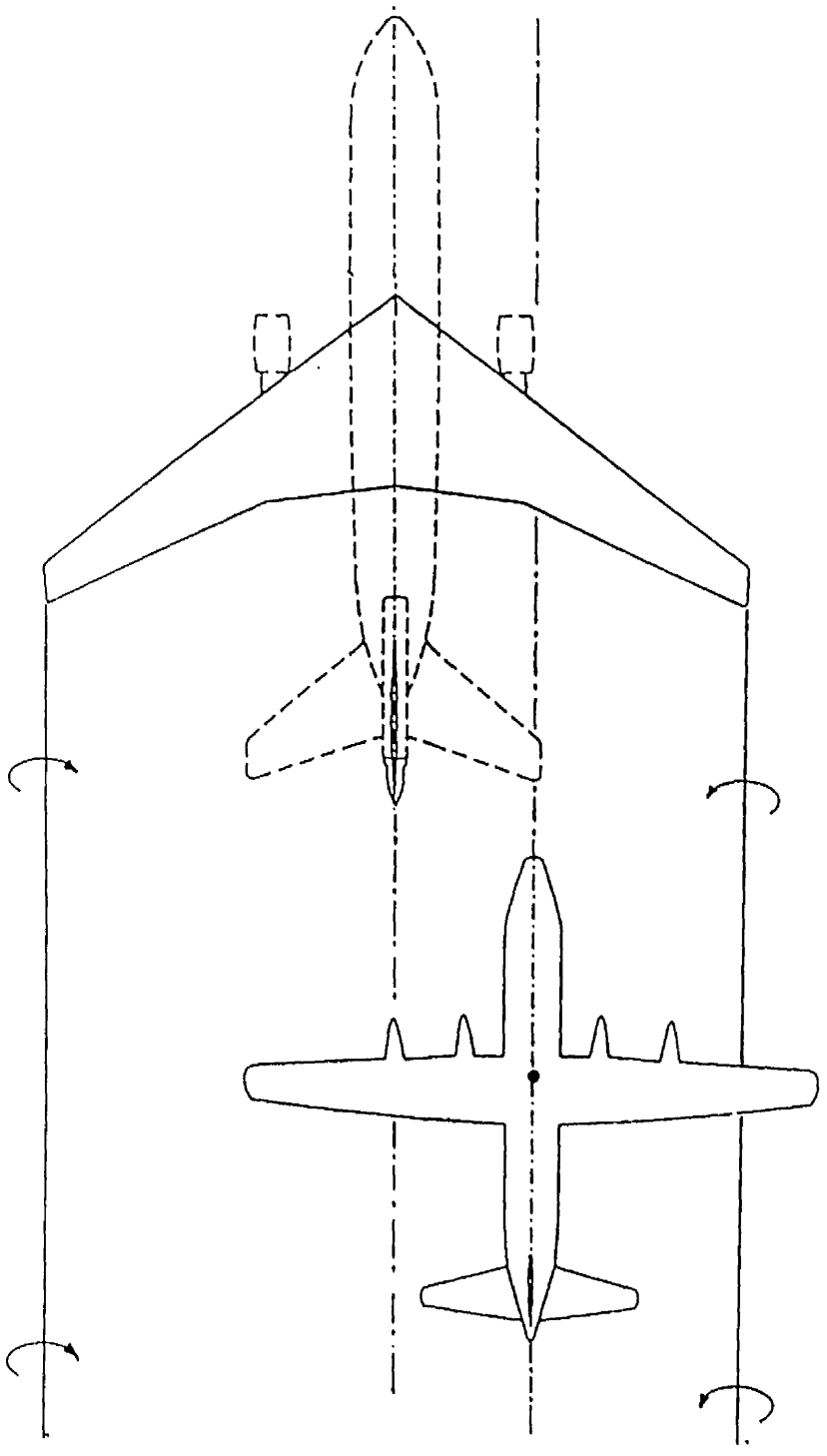

(a) Positive side displacement

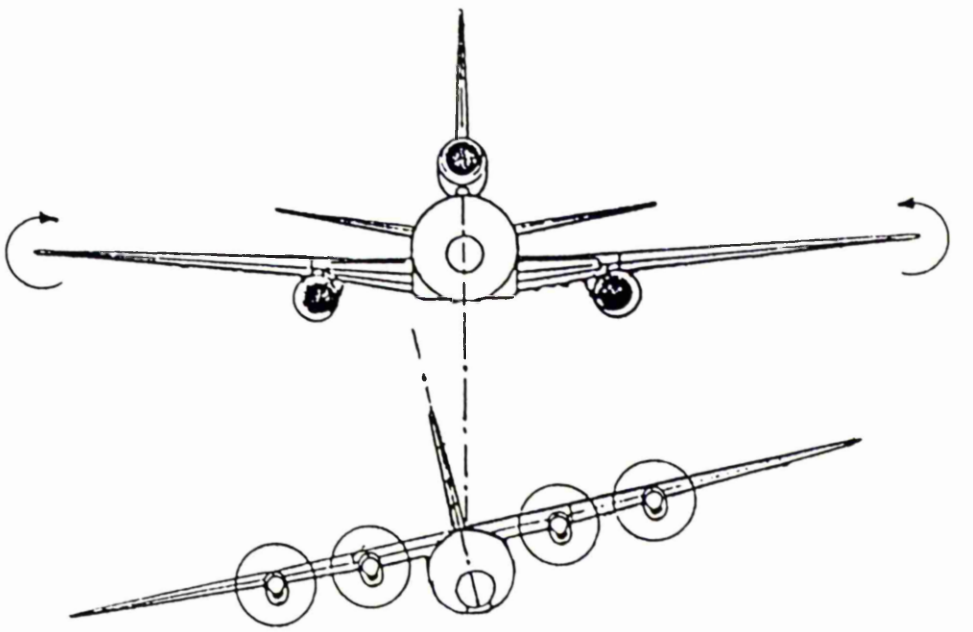

(b) Positive bank displacement

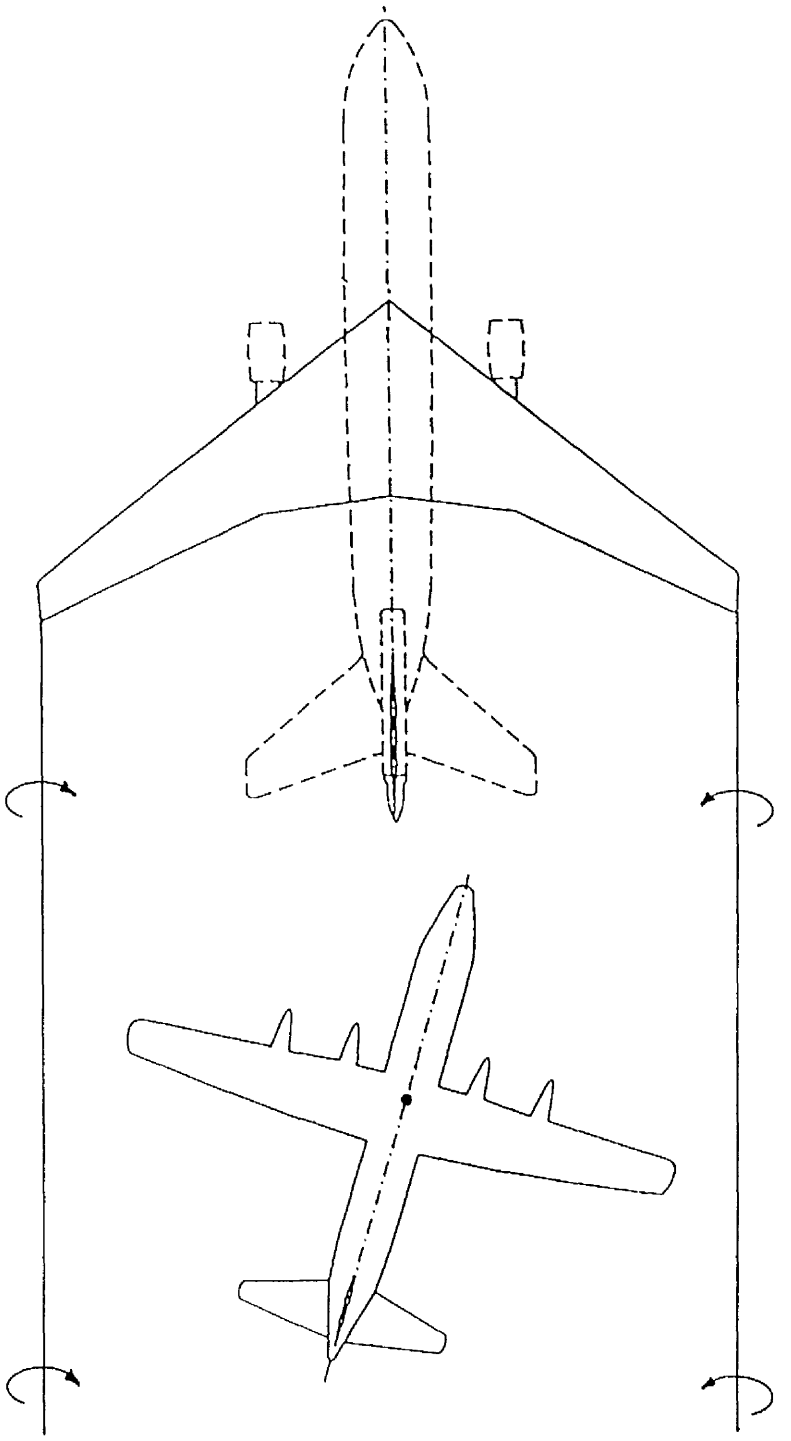

(c) Positive yaw displacement

Figure 2.24: Arrangements of tanker and receiver during positive side, bank and yaw displacements.

Chapter 3

Comparison Between Theory and Experiment

This chapter is concerned with the application of the aerodynamic models, described in chapter 2, to an existing wind tunnel model shown in figure 3.1. This model was tested previously by West [24] to determine the longitudinal and lateral aerodynamic interference between the tanker wing and receiver aircraft model. The experiments were carried out in the open test section.

3.1 Project Wind Tunnel

The experiments were performed in the subsonic wind tunnel at the Goldstein Laboratory of the University of Manchester. This wind tunnel is shown in figure 3.2. The tunnel exit section is octagonal in shape measuring 1.13 m horizontally and

0.87 m vertically. Each corner fillet is set at 45° with a length of 0.287 m. Hence, the total exit area is 0.875 m^2. The overall contraction ratio of the tunnel is 6:1 with four turbulence screens placed upstream of the contraction area. The turbulence level has been measured as 1%. The tunnel is powered by a 75 kW constant speed electric motor which includes a magnetic clutch and a brake which applies additional load at low air speeds (3-5 m/s). The tunnel fan is 1.27 m in diameter and uses blades of Mathew and Yates 1300V aerofoil cross-section. The tunnel operating speed is 37.5 m/s for the open test section.

The forces and moments on a model to be tested are measured using an Elven Precision Ltd Model 158 Six Component Wind Tunnel Balance. The model is mounted inverted on the balance which consists of an earth frame, forces frame and moments frame as shown in figure 3.3. The earth frame is mounted on a support platform which is not connected to the tunnel to minimise the effect of vibration on the test section. From the earth frame are suspended torsion bar coupled lift beams which are connected to four vertical links which carry the forces frame. The moment frame is suspended below the forces frame and is supported from it by a pair of inclined plates whose angle of inclination defines the centre of the balance roll axis. Six electromechanical transducers are used to give measurements of lift, drag, side force, rolling, pitching and yawing moments.

The balance allows the model under test to yaw and pitch. The model is pitched using an electrically driven adjustable pitch arm. The earth frame is allowed to rotate with the model in yaw using a D.C. electric motor.

The data acquisition system used in the experiments consisted of a BBC microcomputer connected to the balance transducers via a 16-channel analogue-to-digital (A/D) converter and an IEEE interface. A BASIC and assembly language program processed the raw data (i.e. the output from the A/D converter) and presented the results in the form of usable physical quantities. The program used the tunnel speed, measured from pressure tappings before and after the tunnel contraction; the model wing span, area and mean chord and applied corrections for the forces and moments on the support struts.

3.2 Experimental Set-up

The tanker was represented by an unswept, straight tapered wing of taper ratio 0.244, mean chord 0.14 m and span 0.765 m. This wing used the NACA 0018 section. The receiver aircraft model consisted of a main rectangular wing with the same span as the tanker wing and a rectangular tailplane and fin mounted on a stick fuselage of length 0.264 m. All the airfoil sections of the receiver aircraft model were NACA 0015 sections and the tailplane was set level with the wing at three positions, low, mid and high on the fin. Only the low tailplane setting was required for the lateral case. The horizontal separation between the quarter-chord points of the tanker and receiver wings is 0.55 m or 0.72 times the wing span. This separation is close to that used in contact between the tanker and receiver aircraft during air-to-air refuelling. Figure 3.1 gives the relevant dimensions of the tanker and receiver models and the positions within the test section.

For the open test section experiments, the tanker wing was supported at each wing tip by a tapered horizontal bar fixed to a traverse which allowed bank, pitch, spanwise and vertical displacements of the wing. The receiver aircraft model was mounted inverted on the wind tunnel balance described in section 3.1. The model was positioned 0.15 m above the centre-line of the wind tunnel and the tanker wing was traversed vertically varying the vertical separation between the tanker and receiver. All the experimental data were presented without any corrections due to wind tunnel boundary interference effects which were significant due to the relatively high ratio of the wing span to tunnel span of 0.7.

3.3 Theoretical Model

3.3.1 Tanker Wing Model

The tanker wing wake was represented by the 3D roll-up model described in section 2.3. Results for the wake roll-up from the tanker wing have been given previously by Bloy and West [25]. In the present work the tanker wing was set at a lift coefficient of 0.544 as used in the experiment. 120 trailing vortices were taken across the wing span with a downstream step size equal to 1/8th of the wing mean chord. The Krasny smoothing factor was taken as 0.025. Calculations of the tanker wing wake roll-up were performed to a distance 4.24 wing-spans downstream.

Figure 3.4 shows slices through the yz plane of the tanker wing wake at various downstream stations. The slices indicate that the emerging wing tip spiral remains

in the same horizontal position as the tanker wing tip trailing edge and the centre of the vortex sheet is deflected downwards. From the flat vortex sheet model, the vertical displacement at the centre line of the tanker wake can be estimated approximately by integrating the tanker downwash angle downstream from the trailing edge of the tanker wing. At the receiver fin position, this displacement was found to be $z/b = 0.1$ compared with $z/b = 0.11$ obtained from the roll-up model.

Figure 3.5 shows plan and side views of the tapered wing vortex wake. Since the strength of every trailing vortex is the same or zero on the centre line, the strength of the tip vortex at any particular downstream station can be determined by counting the vortices in the region between the tip vortex and the centre line of the vortex sheet and subtracting this sum from the total number of trailing vortices. The tip vortex is defined from the tip of the vortex sheet to the point at which the sheet last passes below the centre of the tip vortex. At the position of the receiver wing which is 0.79 times the wing span downstream the tip vortex strength is found to be 43.3% of the tanker wing centre-line circulation. At two wing spans downstream the strength increases to 58.3%. The 3D view of the tanker wing wake is shown in figure 3.6.

Typical downwash distributions at the position of the receiver main wing and sidewash distributions at the position of the receiver fin are shown in figures 3.7 and 3.8, respectively, for various values of the vertical separation z between tanker and receiver wings.

3.3.2 Receiver Aircraft Model

In the longitudinal case, aerodynamic loads are induced on the receiver wing and tailplane due to the downwash only. Upstream influence of the receiver aircraft wing on the tanker wing was neglected since the estimated change in the tanker wing angle of attack due to the receiver is 1.5%. With no dihedral or fuselage effects, the lateral moments on the receiver wing and tailplane depend mainly on the asymmetric distribution of the downwash over the wing and tailplane as the receiver is displaced from the zero sideslip, wings level position on the centre line of the tanker wake although the contribution due to the tailplane, which is in the downwash of both the tanker and receiver, is relatively small. The side load on the fin is due mainly to the tanker sidewash and the component of downwash acting normal to the fin following a bank displacement.

The aerodynamic model described in section 2.4.1 was used to estimate the induced loads on the receiver wing with 60 spanwise and 4 chordwise panels used to represent the receiver wing. The same number of panels was used to represent the tanker wing. The induced loads on the receiver tailplane and fin were determined using the aerodynamic model given in section 2.4.2 with 30 spanwise and 4 chordwise panels used on the fin and each half of the tailplane.

3.4 Longitudinal Tests at Fixed Receiver Lift Coefficient

As described by West [24] The tanker wing was set at a lift coefficient of 0.544. The tunnel airspeed for all of the tests was 37 m/s giving a Reynolds number based on the wing chord of 3.8×10^5. In order to determine the longitudinal aerodynamic interference between the tanker wing and receiver aircraft model, the tanker wing was traversed vertically across the test section varying the vertical separation between tanker and receiver. Test points were taken at different vertical separations. For each test point the receiver pitch angle was adjusted, as in true flight, to maintain a constant lift coefficient of 0.42. Measurements of the receiver pitch angle, drag and pitching moment were taken. In order to eliminate the wind tunnel boundary interference effect due to receiver, the measurements were presented in the form of the difference between the values obtained in air-to-air refuelling (i.e. in the presence of the tanker wing) and in free flight (i.e. in the absence of the tanker wing). However, the more significant interference effect due to the tanker wing remained.

3.4.1 Pitch Angle Increment $(\theta - \theta_\infty)$

Figure 3.9 shows the variation of the receiver pitch angle increment with vertical separation. This increment is equivalent to the mean downwash angle due to the tanker wing. It can be seen that the receiver pitch angle, required to maintain constant lift, increases as the vertical separation reduces. This is due to the increase

in the tanker induced downwash at the receiver wing and tailplane associated with reducing vertical separation.

The difference between the theory and experiment is partly due to the effect of the tanker wing image vortex system associated with the wind-tunnel boundary interference. In the case of the open test section, the interference effect produces an additional downwash which leads to an increase of the receiver pitch angle in order to maintain constant lift. By using the method of images [42], the additional downwash due to the tanker wing image vortex system was estimated to be about 0.8°.

Below the tanker wing wake, the high tailplane, being close to the tanker wake, experiences the highest tanker downwash. Consequently the high tailplane produces the highest pitch angle increment as shown in figure 3.9. At low vertical separations, the high tailplane, being above the tanker wing wake, experiences lower downwash than the low tailplane. Thus, the theory produces slightly higher pitch angle increment for the low tailplane than for the high tailplane.

3.4.2 Induced Drag Coefficient Increment $(C_{D_i} - C_{D_{i_\infty}})$

The variation of the receiver induced drag coefficient increment with vertical separation is shown in figure 3.10. As the vertical separation between tanker and receiver reduces the receiver induced drag increases. This is due to the backwards tilt of the receiver wing and tailplane lift vectors which is due to the increase in tanker downwash as the vertical separation is reduced. As described in section 3.4.1

additional downwash is produced due to the boundary interference effect and consequently the receiver lift vector is tilted further back. This partly accounts for the higher drag coefficient data compared with the theory as shown in figure 3.10.

3.4.3 Pitching Moment Coefficient Increment $(C_m - C_{m_\infty})$

Figure 3.11 shows the changes in the receiver pitching moment coefficient due to the presence of the tanker wing. The theory compares favourably with the experimental data for both high and low tailplane cases. The induced pitching moment on the receiver depends mainly on the difference between the downwash at the wing and at the tailplane due to the tanker. Thus, the receiver trim in pitch is strongly affected by the tailplane position on the fin as shown in figure 3.11. Since the high tailplane is closer to the tanker wing wake than the wing it experiences higher downwash as the vertical separation is reduced. This results in a nose-up pitching moment with the peak value corresponding to the highest downwash on the tailplane. This occurs when the tailplane touches the tanker wing wake. The theoretical and experimental pitching moment peaks occur at $z/b = 0.23$ and $z/b = 0.26$, respectively. As expected the open test section tends to increase the wake deflection due to the additional downwash produced by the tanker wing image vortex system. At low vertical separations, the high tailplane rises above the tanker trailing vortex with the downwash on the tailplane reducing whereas that on the wing increases producing a nose-down pitching moment.

For the low tailplane case, the downwash at the wing and tailplane are similar. Hence, the corresponding changes in pitching moment are small.

3.5 Lateral Tests at Fixed Receiver Pitch Angle

Lateral tests were performed by displacing the tanker wing sideways and in bank on its support frame and by rotating the receiver aircraft model in yaw on the wind tunnel balance. According to the usual convention, sideways displacement is taken as positive when the tanker wing moves to starboard. Positive bank displacement corresponds to the starboard wing moving up since the tanker wing is inverted in the wind tunnel. The effect of banking the tanker wing is to rotate the wing wake and effectively move the receiver aircraft model by a relatively small amount to starboard as shown in figure 3.12. Positive yaw of the receiver rotates the nose of the receiver to starboard inducing negative sideslip in the wind tunnel and displacing the fin to the port side. In all of the lateral tests the low tailplane position on the receiver was used and the receiver aircraft model was tested at 6° pitch angle to the horizontal.

The variations of the aerodynamic loads of the receiver with sideways, bank and yaw displacements are essentially linear over the range of interest as shown in figures 3.13, 3.14 and 3.15, respectively. This allows the aerodynamic data to be presented in derivative form. The derivatives are determined at the datum position which is with zero sideslip and wings level on the centre line of the tanker wing wake.

3.5.1 Side Displacement of the Tanker Wing

Rolling Moment Derivative ($\partial C_{l_R}/\partial(y_T/b)$)

Positive side displacement of the tanker wing increases the downwash on the receiver starboard wing and tailplane and reduces the downwash on the port wing and tailplane. This produces a positive rolling moment tending to roll the receiver and align it parallel to the tanker. Thus, the rolling moment is stabilising. Figure 3.16 gives the rolling moment due to tanker sideways displacement derivative over the range of vertical separation tested. There is good agreement between the theory and the open test section data. The rolling moment derivative is due mainly to the rate of change of tanker downwash across the receiver wing span. Thus higher values occur near the wing tip and at low vertical separation between tanker and receiver. There are small contributions from the tailplane and fin due to the tanker wing downwash and sidewash, respectively. Below the tanker wing wake, the fin contribution acts in a destabilising sense opposite to the contribution from the wing and tailplane.

Side Force Derivative ($\partial C_{Y_R}/\partial(y_T/b)$)

The side force on the receiver aircraft model is mainly due to the effect of tanker wing sidewash on the receiver fin. Figure 3.17 shows the variation of side force derivative with vertical separation. The theory compares favourably with the experimental data. The peak value of the side force occurs when the tip of the receiver fin intersects the vortex wake of the tanker wing. The theoretical peak occurs at

the vertical separation z/b=0.23. Insufficient data were taken to determine the experimental peak position. Below the tanker wing wake, the side force acts in a destabilising sense tending to move the receiver away from the tanker wake centre line.

Yawing Moment Derivative ($\partial C_{n_R}/\partial(y_T/b)$)

This derivative is relatively small compared with the rolling moment derivative. It is due mainly to the effect of tanker sidewash on the receiver fin with a small contribution from the main wing associated with the variation of induced drag across the wing span. Figure 3.18 shows the variation of the yawing moment derivative with vertical separation. The ratio of the side force to yawing moment is approximately equal to the wing span/fin arm which has the value 2. The yawing moment acts in a stabilising sense tending to move the nose of the receiver towards the tanker centre line when the fin is below the tanker wing wake.

3.5.2 Bank Displacement of the Tanker Wing

As described in section 3.5 the bank displacement was produced by rotating the tanker wing on its support frame. This rotation generates a sideways displacement of the receiver aircraft relative to the tanker wing wake which is proportional to the vertical separation. The effect of the sideways displacement is that the measured forces and moments are less than those obtained by banking the receiver aircraft.

Rolling Moment Derivative ($\partial C_{l_R}/\partial \phi_T$)

As in the sideways displacement case, positive bank of the tanker wing gives an increase in the downwash on the receiver starboard wing and a decrease in the downwash on the port wing. The resulting rolling moment acts in the stable sense tending to reduce the relative bank angle between tanker and receiver. The rolling moment depends on the rate of change of the tanker downwash in the vertical direction. Figure 3.19 shows the variation of the rolling moment due to bank derivative with vertical separation. It can be seen than the theory gives very good agreement with the open test section data. The fin and tailplane contributions are small.

Side Force Derivative ($\partial C_{Y_R}/\partial \phi_T$)

The side force derivative shown in figure 3.20 is due to the effect of the tanker wing sidewash and downwash components acting normal to the receiver fin. The major contribution is due to the downwash component which is highest at low vertical separation between tanker and receiver. The side force derivative is destabilising tending to increase the side displacement. The side force derivative data are higher in magnitude than those obtained from the theory due to the additional downwash associated with the tunnel boundary effects.

Yawing Moment Derivative ($\partial C_{n_R}/\partial \phi_T$)

Figure 3.21 shows the variation of yawing moment due to bank derivative with vertical separation between tanker and receiver. The yawing moment is due mainly to side force acting on the fin moment arm with a small contribution from the differential drag on the receiver wing.

3.5.3 Yaw Displacement of the Receiver Model

The forces and moments acting on the receiver aircraft model following a small yaw angle displacement are due mainly to the receiver fin and tailplane. Positive yaw displacement moves the port wing slightly forward while the starboard wing moves equally rearward. Since the tanker wing downwash at the receiver aircraft position changes only slightly in the downstream direction, the downwash distribution over the receiver wing is practically unaffected by yawing the receiver. Thus, the receiver wing experiences no lateral forces or moments due to yaw displacement. However the receiver fin and tailplane produce forces and moments due to the effect of both the tanker and receiver wing wakes. Hence the experimental case shown in figure 3.22a was represented theoretically by the arrangement shown in figure 3.22b with the forces and moments on the receiver fin and tailplane determined using the aerodynamic model described in section 2.4.2.

The effect of yawing the receiver in the tanker wing wake was determined by testing the receiver aircraft model with and without the tanker wing in position. The results are then presented in the form of the difference between the values obtained

from the tanker/receiver combination and the receiver only.

Side Force Derivative Increment $(\partial C_Y/\partial\psi)_R$-$(\partial C_Y/\partial\psi)_{R_\infty}$

Figure 3.23 shows the variation of the side force derivative increment with vertical separation. The side force is entirely due to the effect of the sidewash at the receiver fin which is mainly from the tanker wing and partly from the receiver wing. Below the tanker wing wake, the side force acts in a destabilising sense tending to increase the yaw displacement. As discussed in the side displacement case, the peak value of the side force occurs when the tip of the fin touches the tanker wing wake. In the theory, this occurs at the vertical separation of z/b=0.23 compared with the experimental value of z/b=0.26. The difference between the theoretical and experimental peak positions gives an estimate of the effect of the boundary interference on the displacement of the tanker wing wake.

Yawing Moment Derivative Increment $(\partial C_n/\partial\psi)_R$-$(\partial C_n/\partial\psi)_{R_\infty}$

The yawing moment derivative shown in figure 3.24 is similar in form to the side force derivative since the main contribution is due to the fin. The fin moment arm has approximately a length of b/2 and hence the yawing moment derivative in coefficient form is approximately half the side force derivative in coefficient form. The yawing moment acts in a destabilising sense resulting in a reduction in the directional stability of the receiver aircraft. Figure 3.24 shows that the theoretical peak reduction in stability is almost the same as that obtained from the experiment. The peak reduction represents 12% of the receiver aircraft directional stability

derivative C_{n_β} which is equal to 0.19. Again the theory compares favourably with the experimental data.

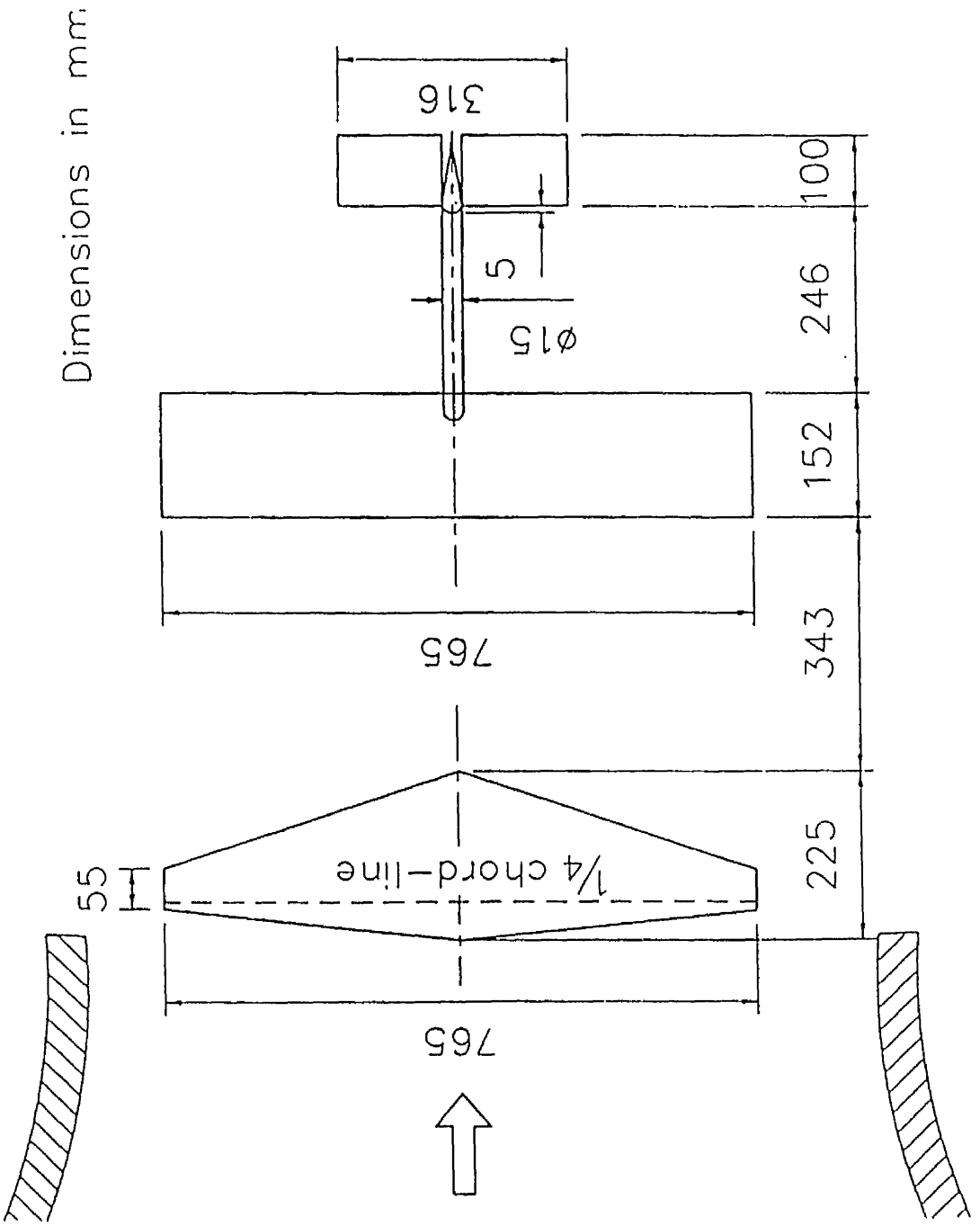

Figure 3.1: Dimensions of tanker wing and receiver aircraft model and position in wind tunnel section.

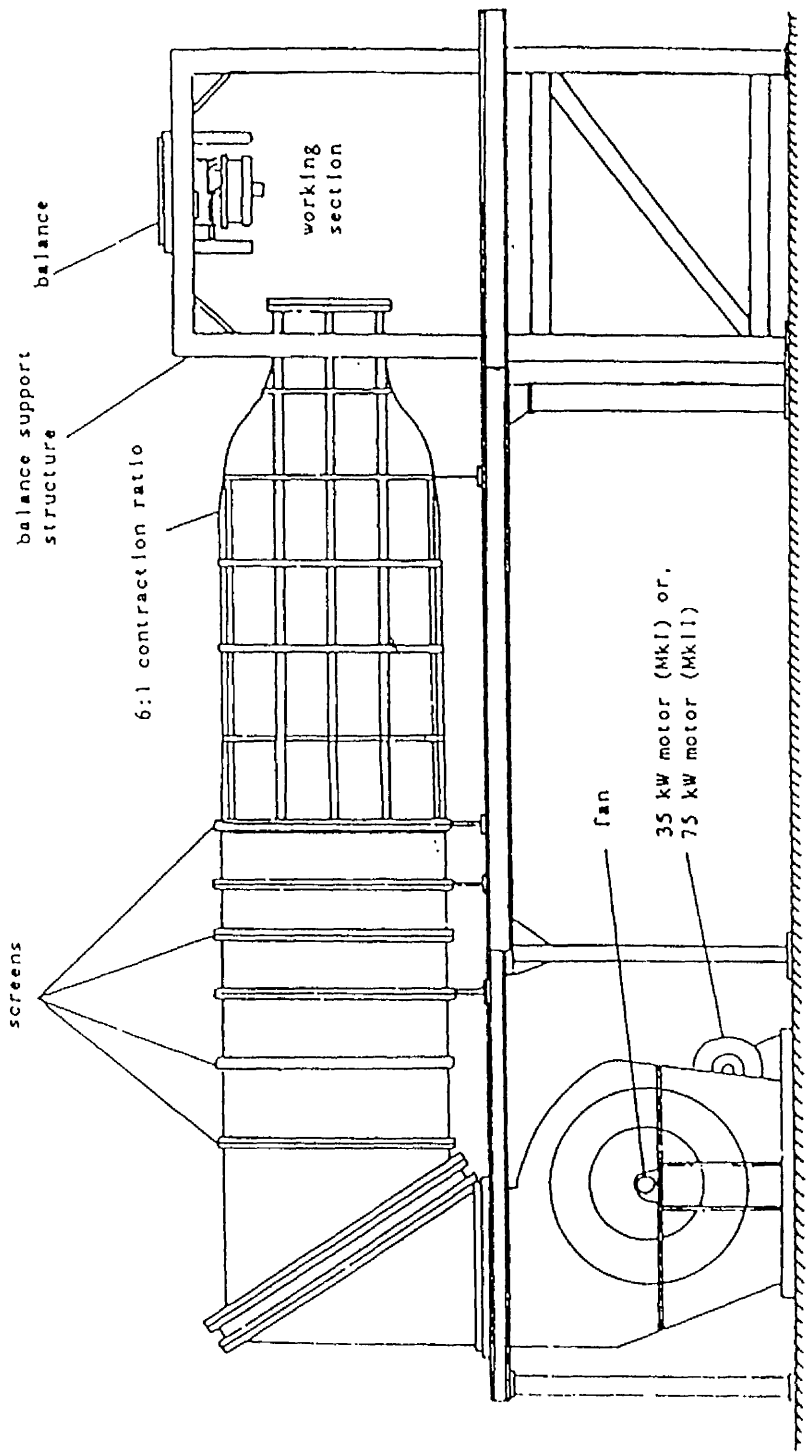

Figure 3.2: General arrangement of project wind tunnel.

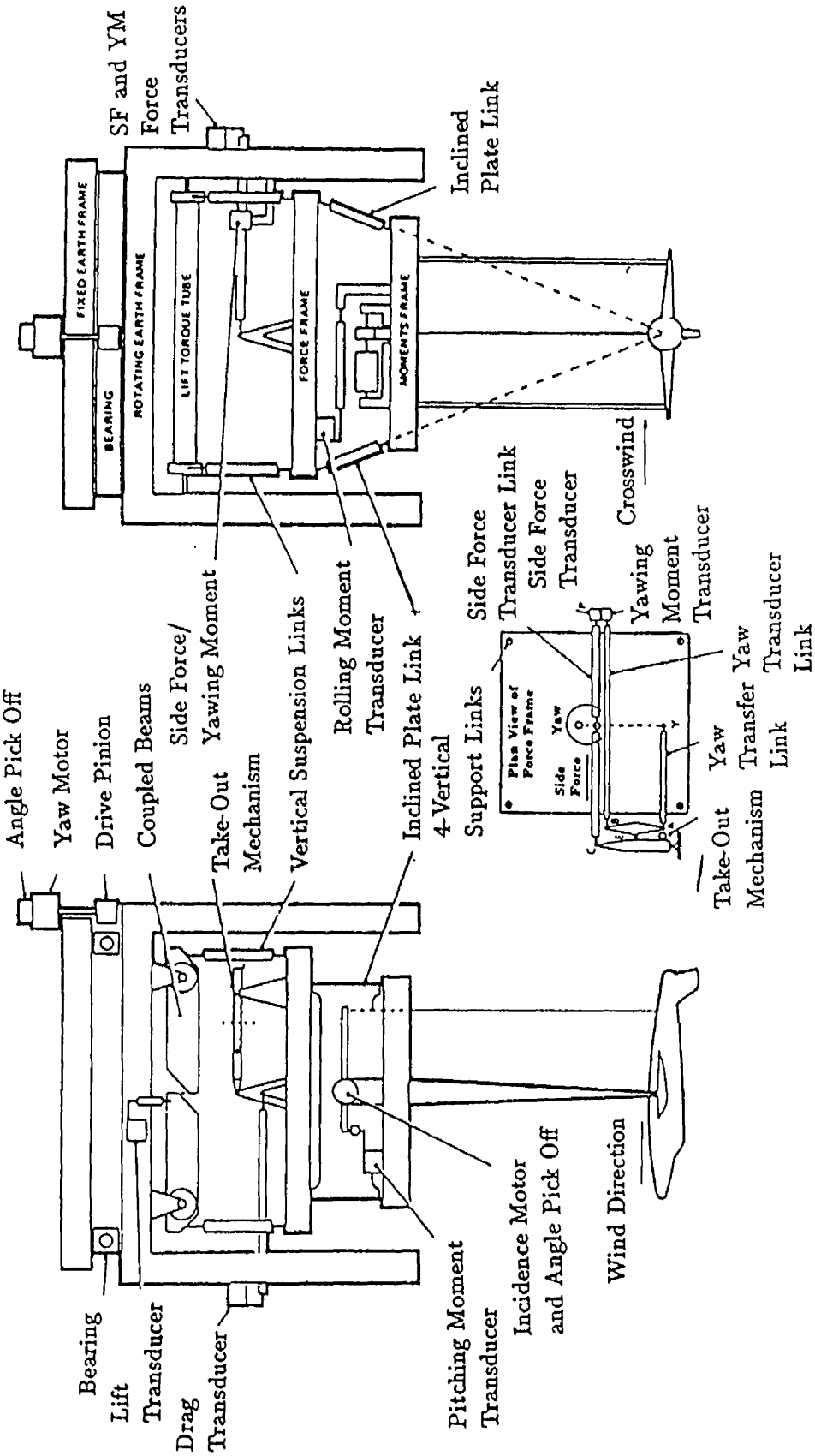

Figure 3.3: Description of wind tunnel balance.

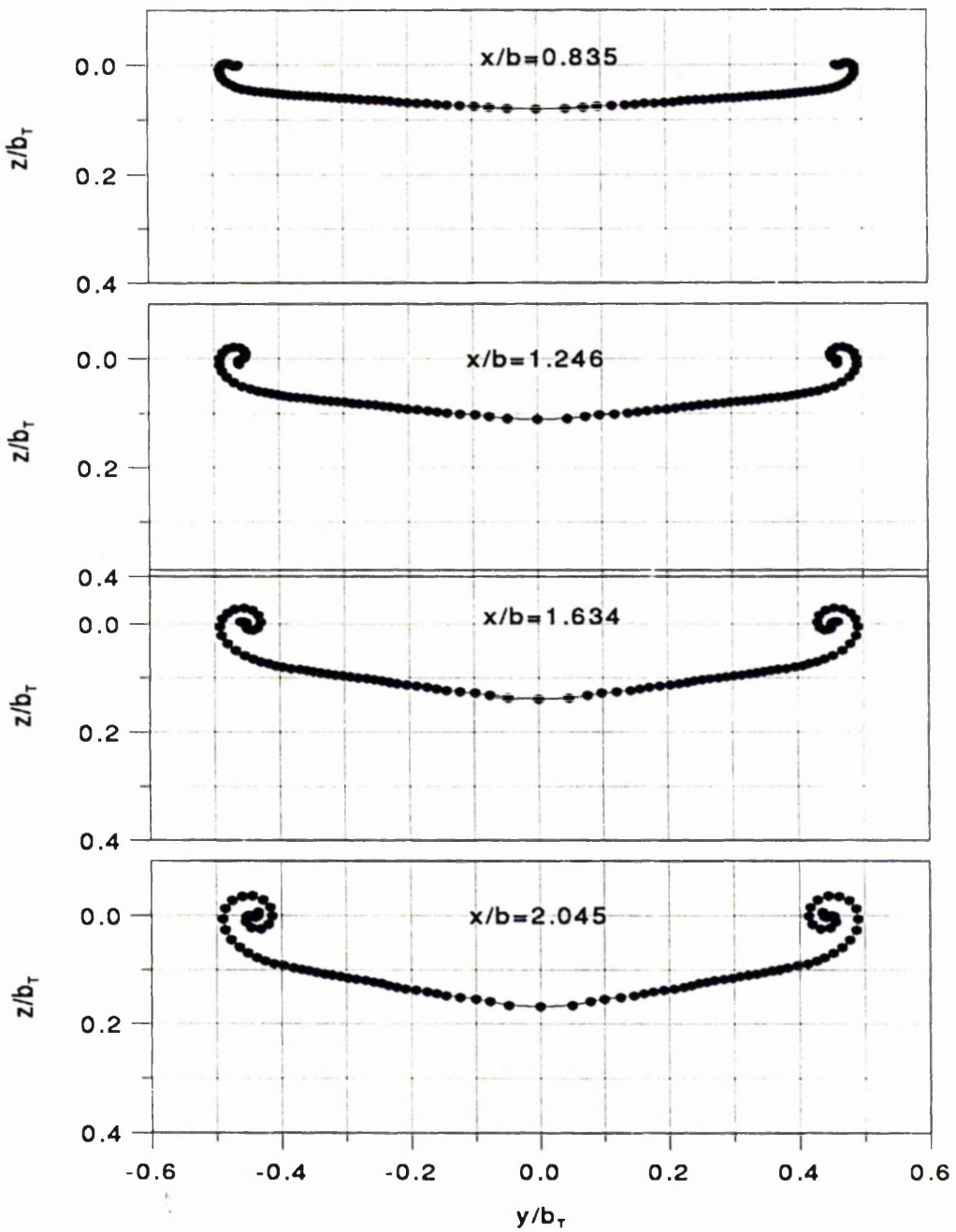

Figure 3.4: Tapered wing wake roll-up development in the downstream direction.

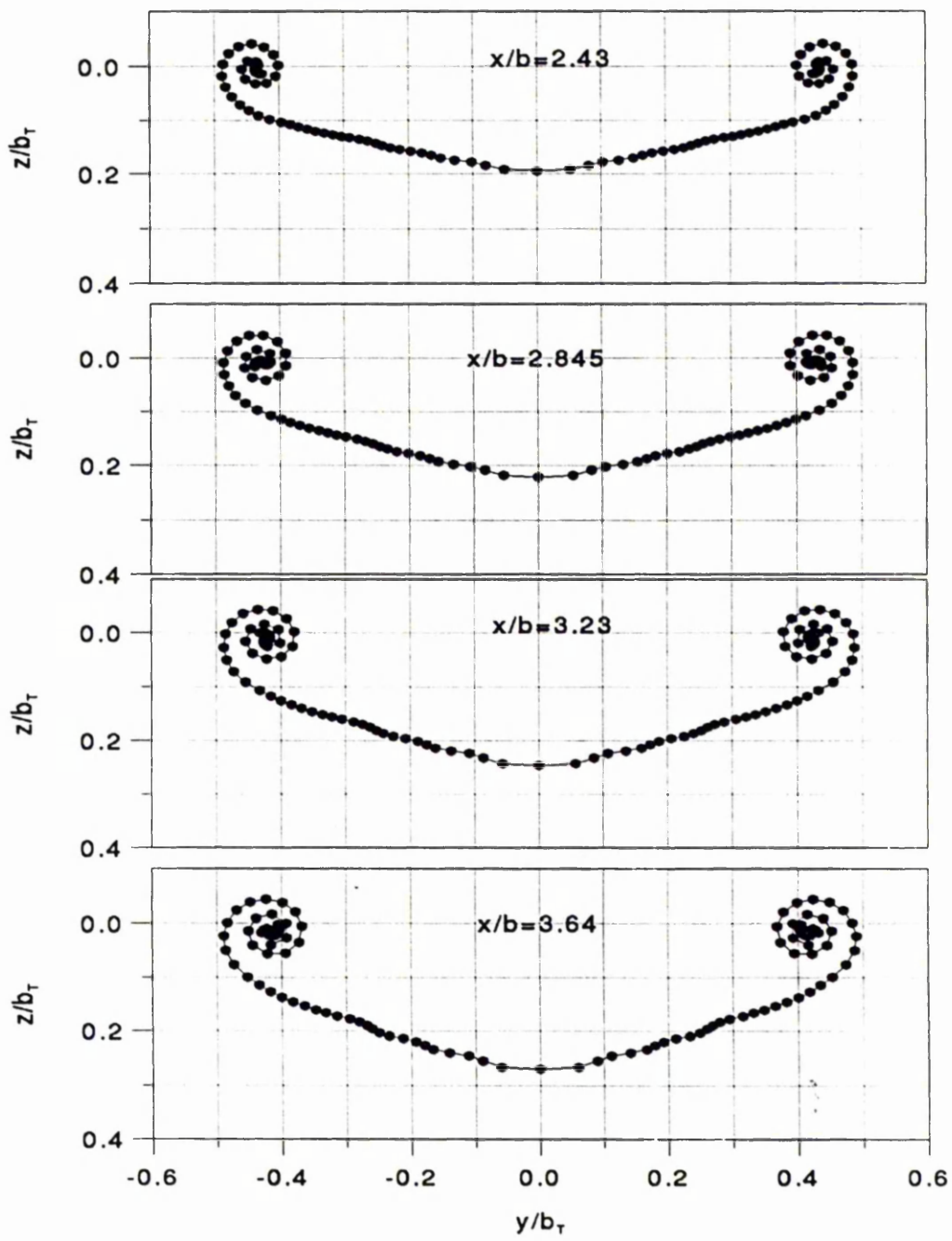

Figure 3.4: Continued

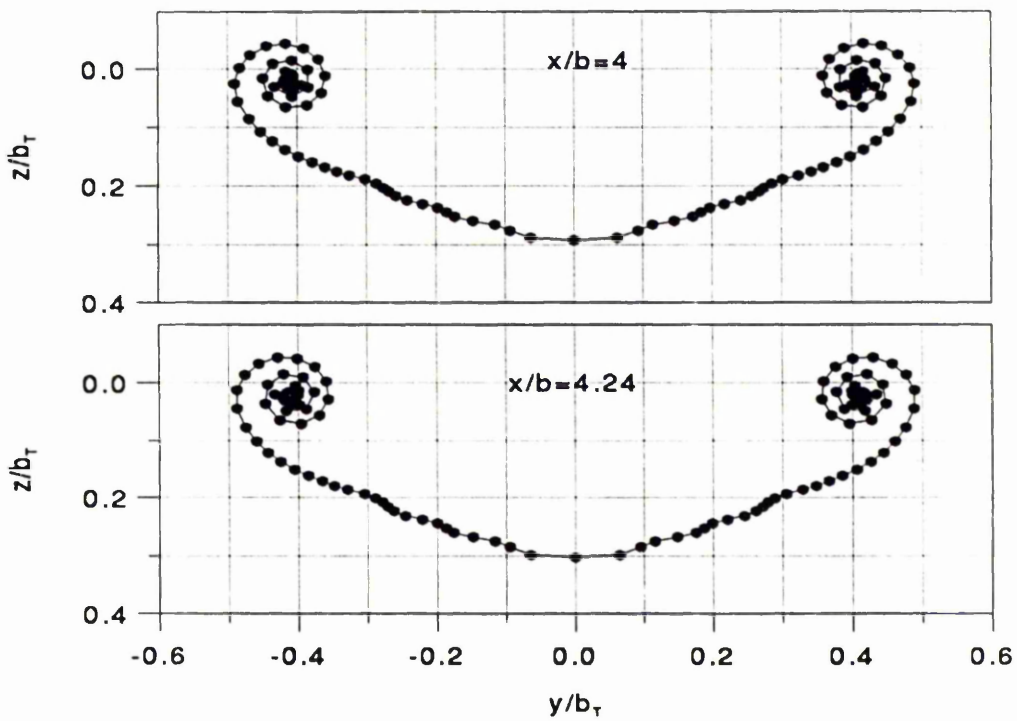

Figure 3.4: Continued

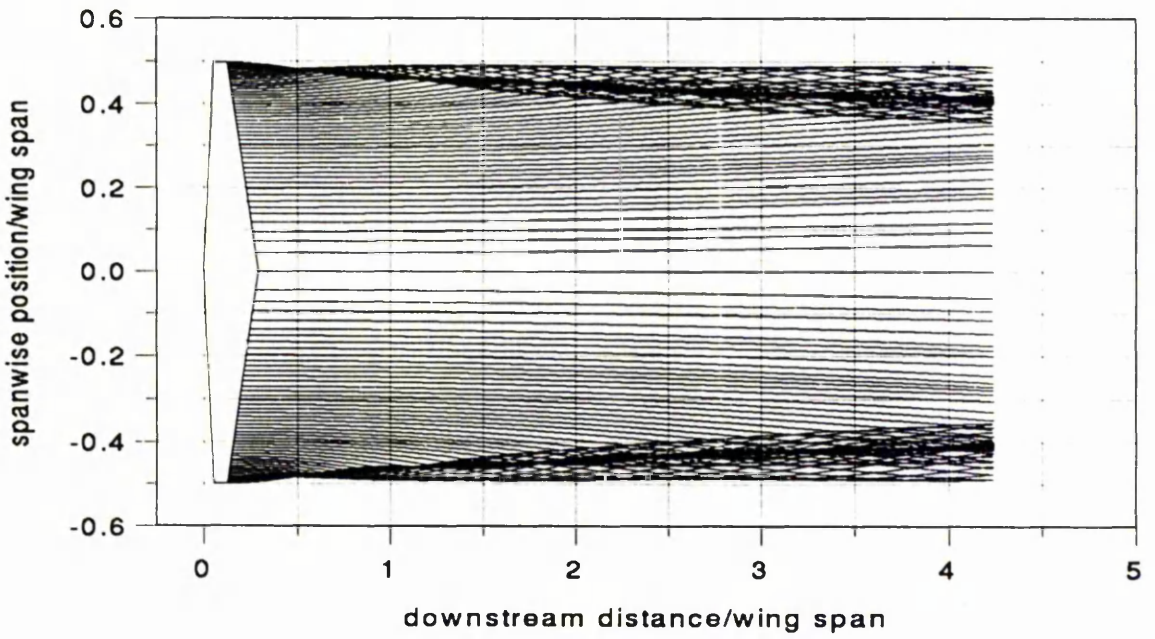

(a) Plan view

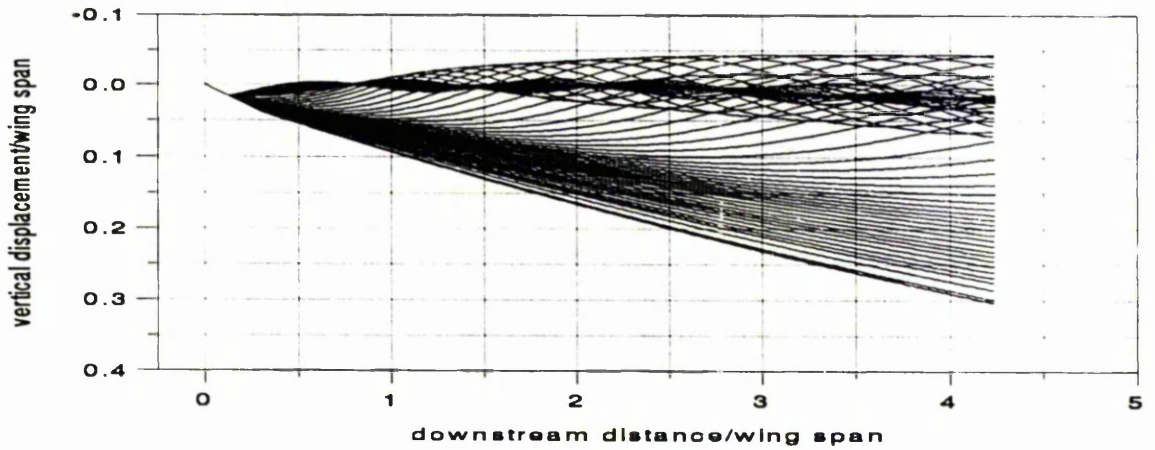

(b) Side view

Figure 3.5: Plan and side views of the tapered wing wake roll-up.

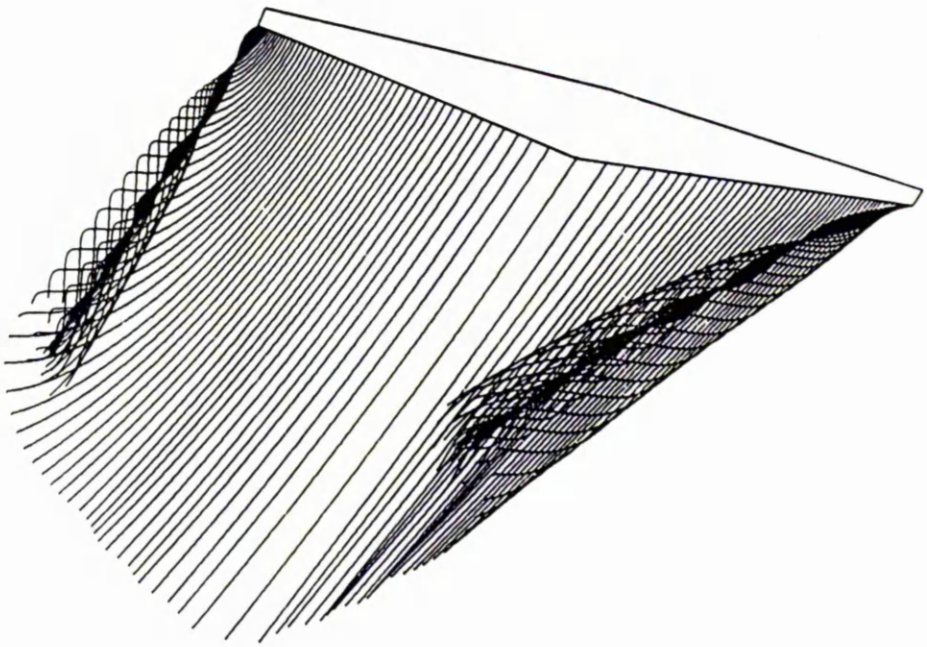

Figure 3.6: 3D view of the tapered wing wake roll-up.

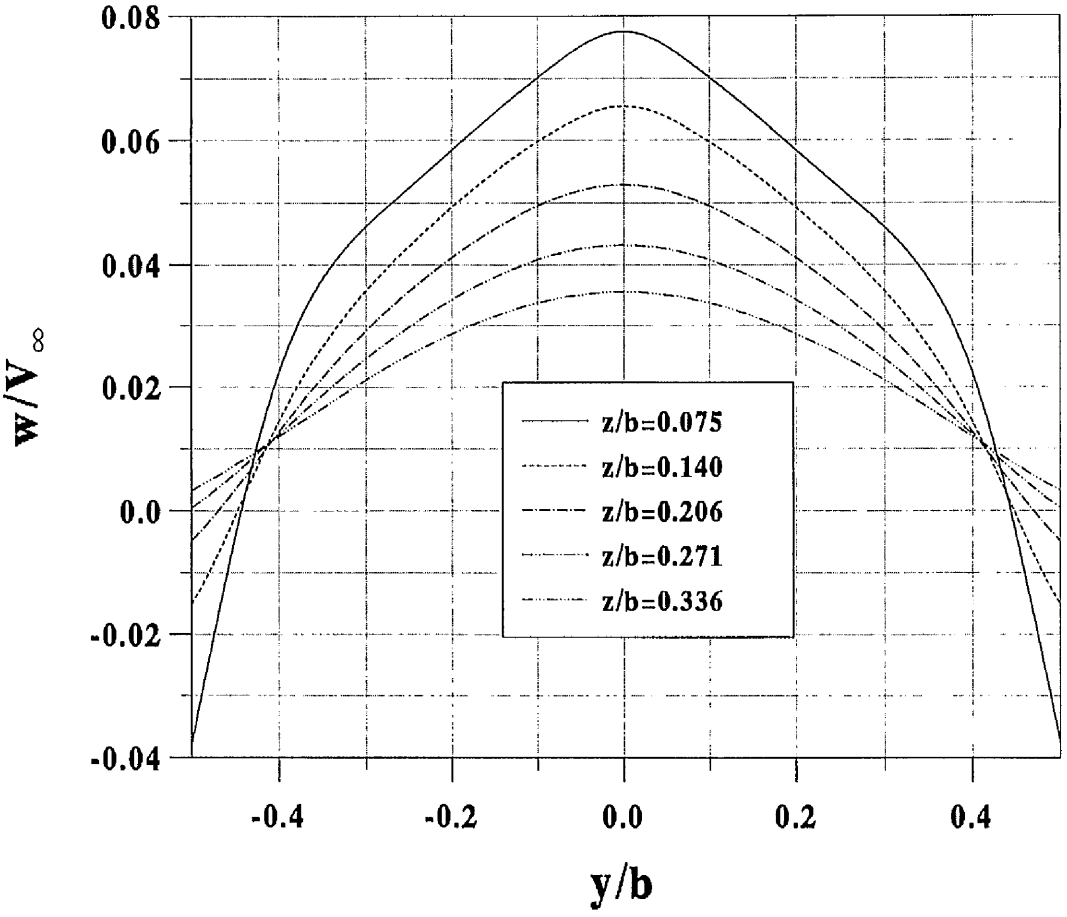

Figure 3.7: Downwash induced by tanker wing at position of receiver wing.

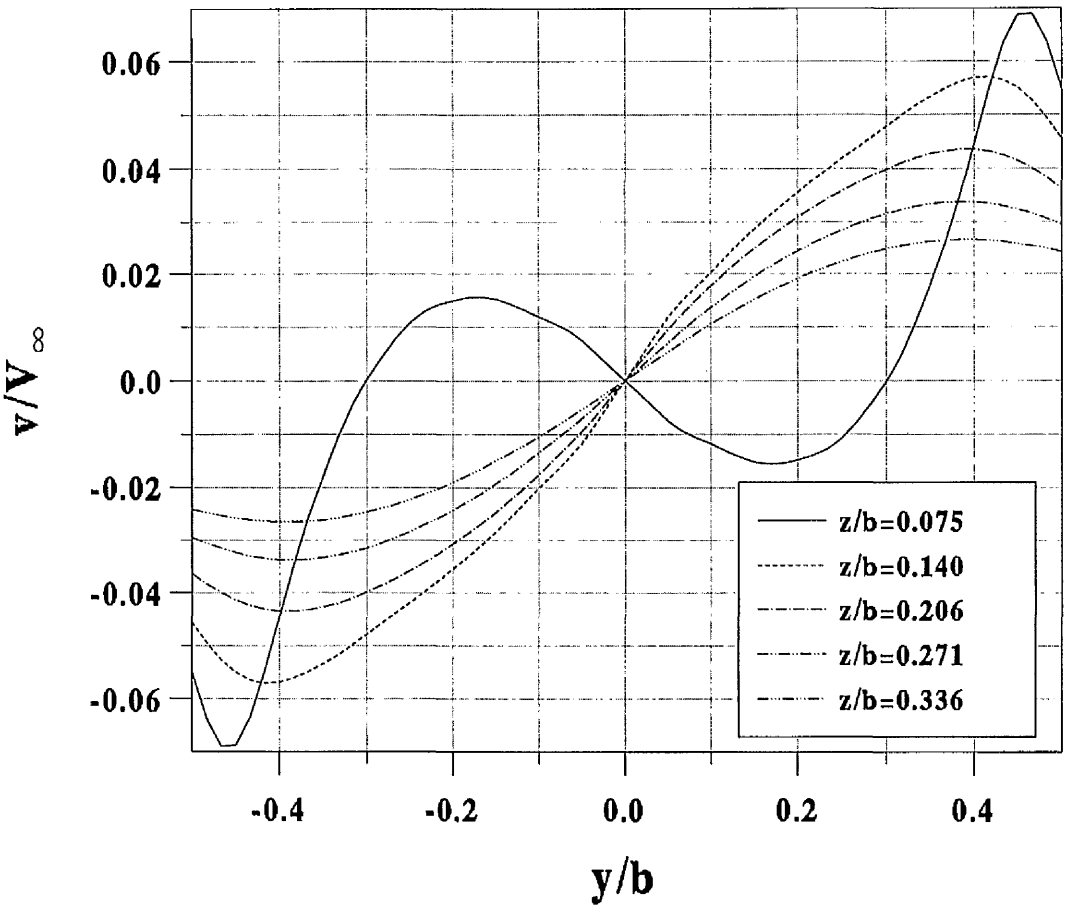

Figure 3.8: Sidewash induced by tanker wing at position of receiver fin.

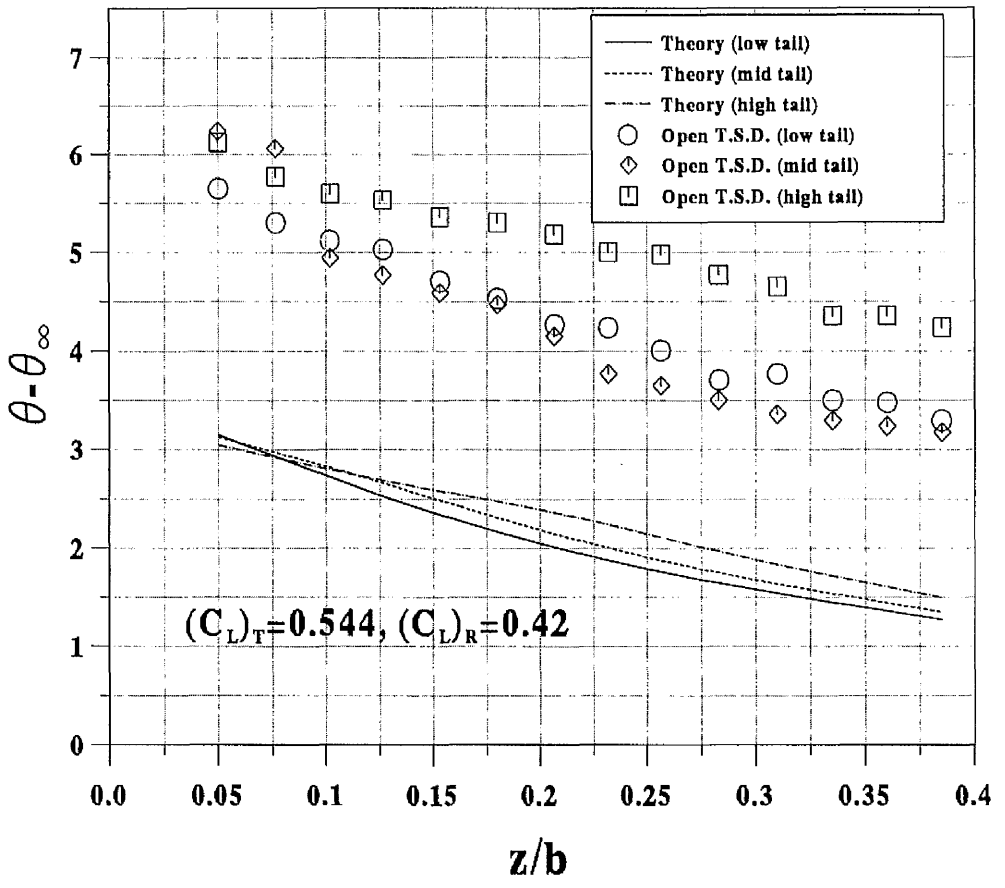

Figure 3.9: Receiver pitch angle increment with varying vertical separation.

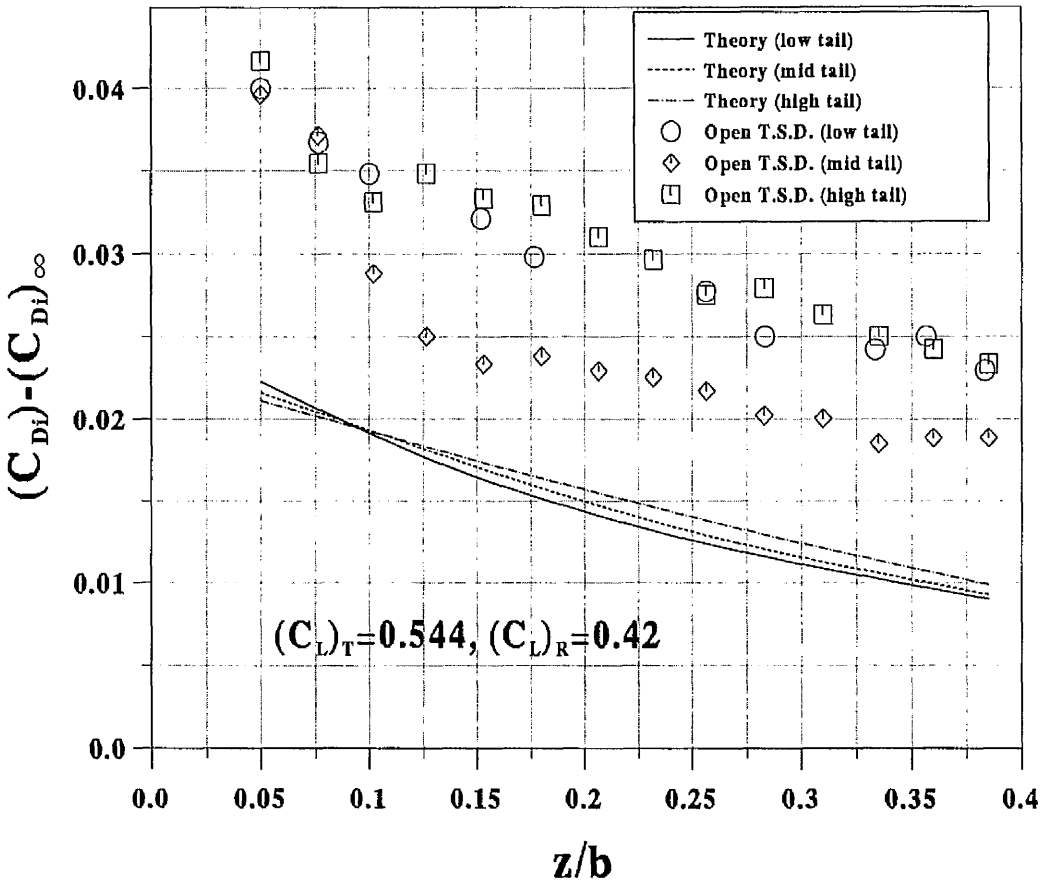

Figure 3.10: Receiver induced drag coefficient increment with varying vertical separation.

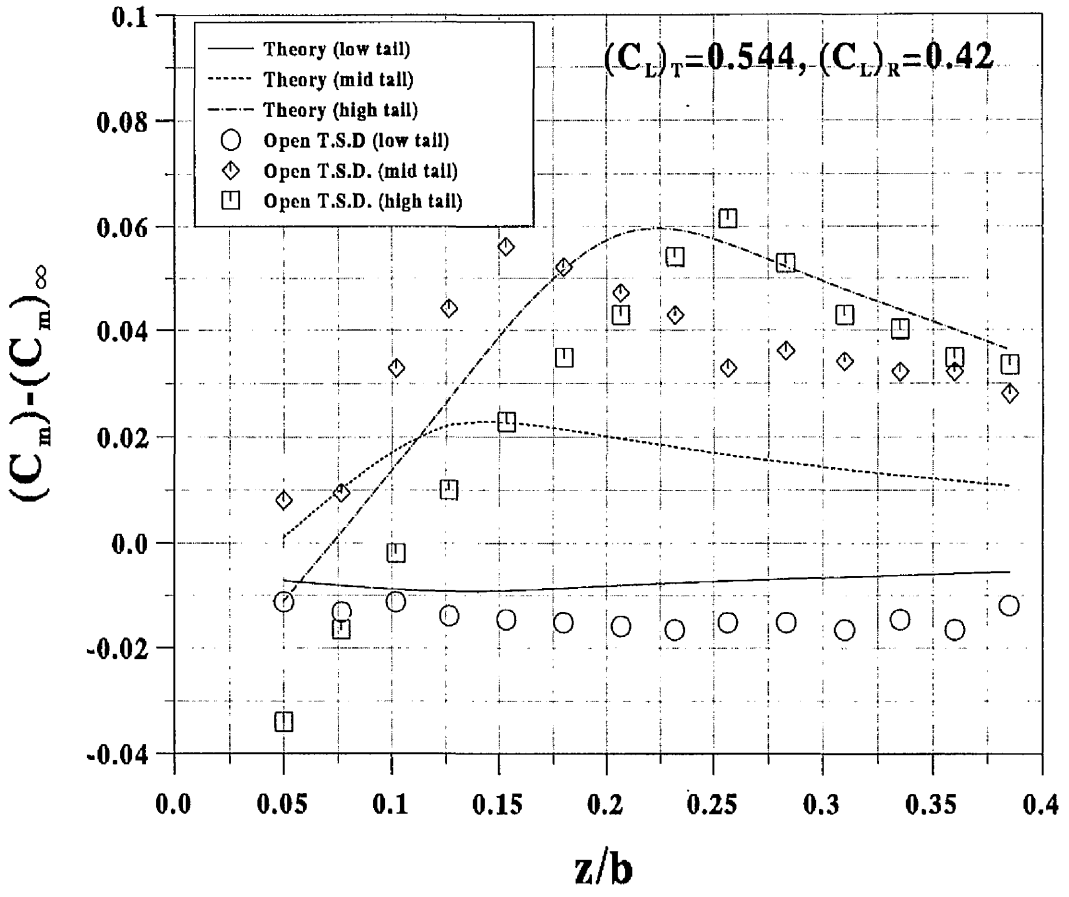

Figure 3.11: Receiver pitching moment coefficient increment with varying vertical separation.

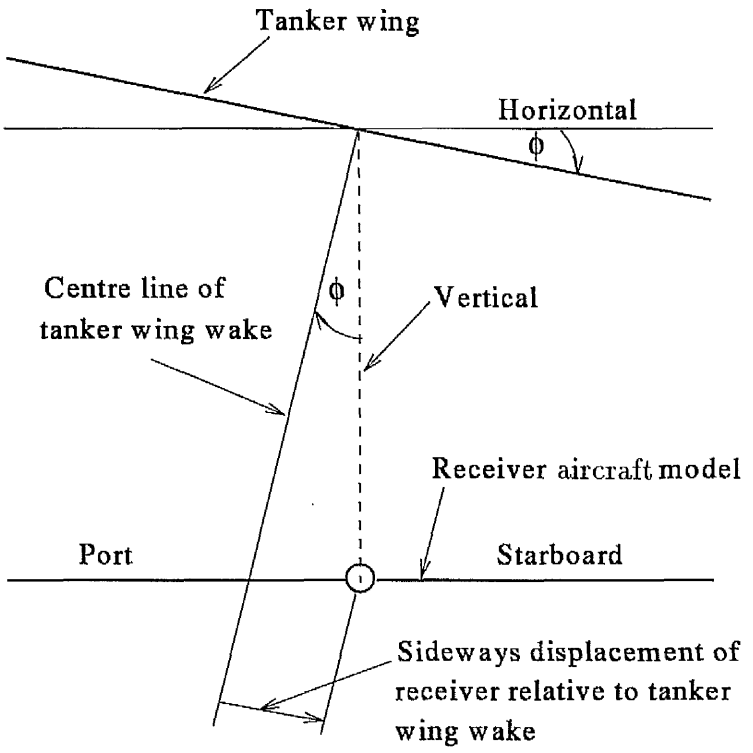

Figure 3.12: Displacement of receiver aircraft model relative to banked tanker wake.

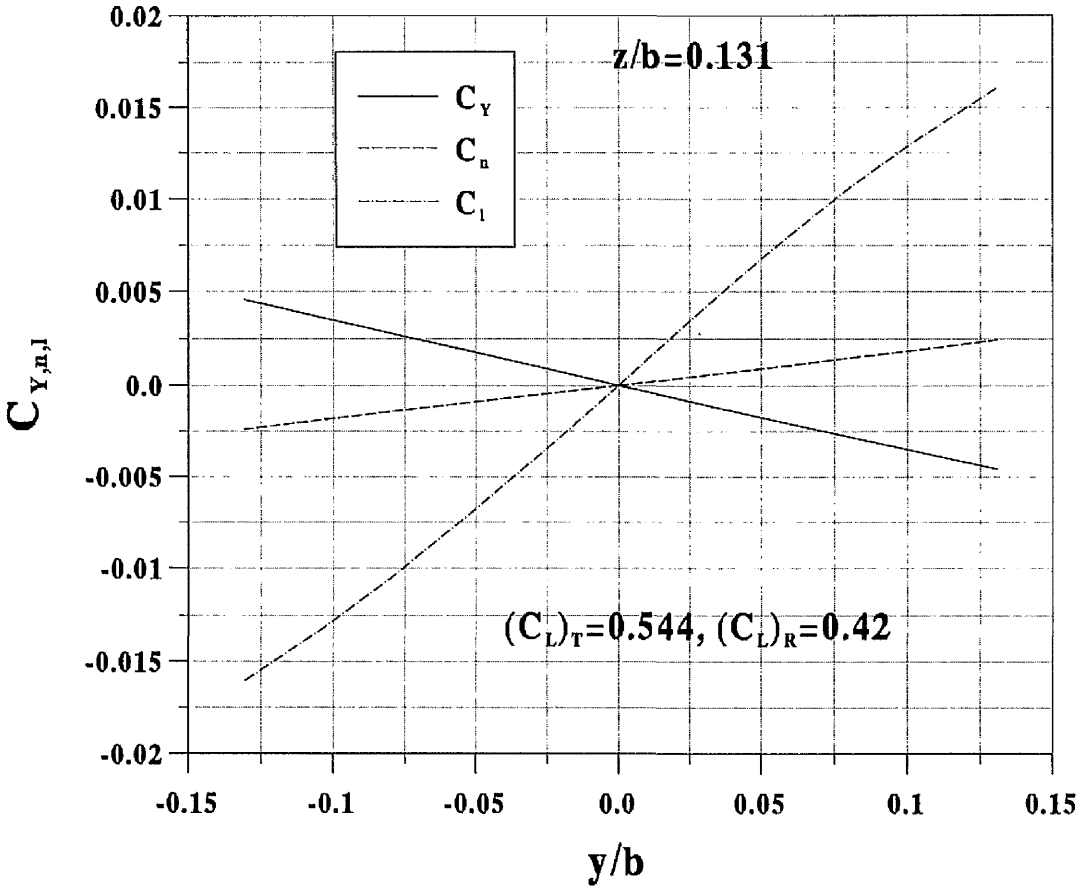

Figure 3.13: Receiver side force, rolling and yawing moments due to tanker wing side displacement.

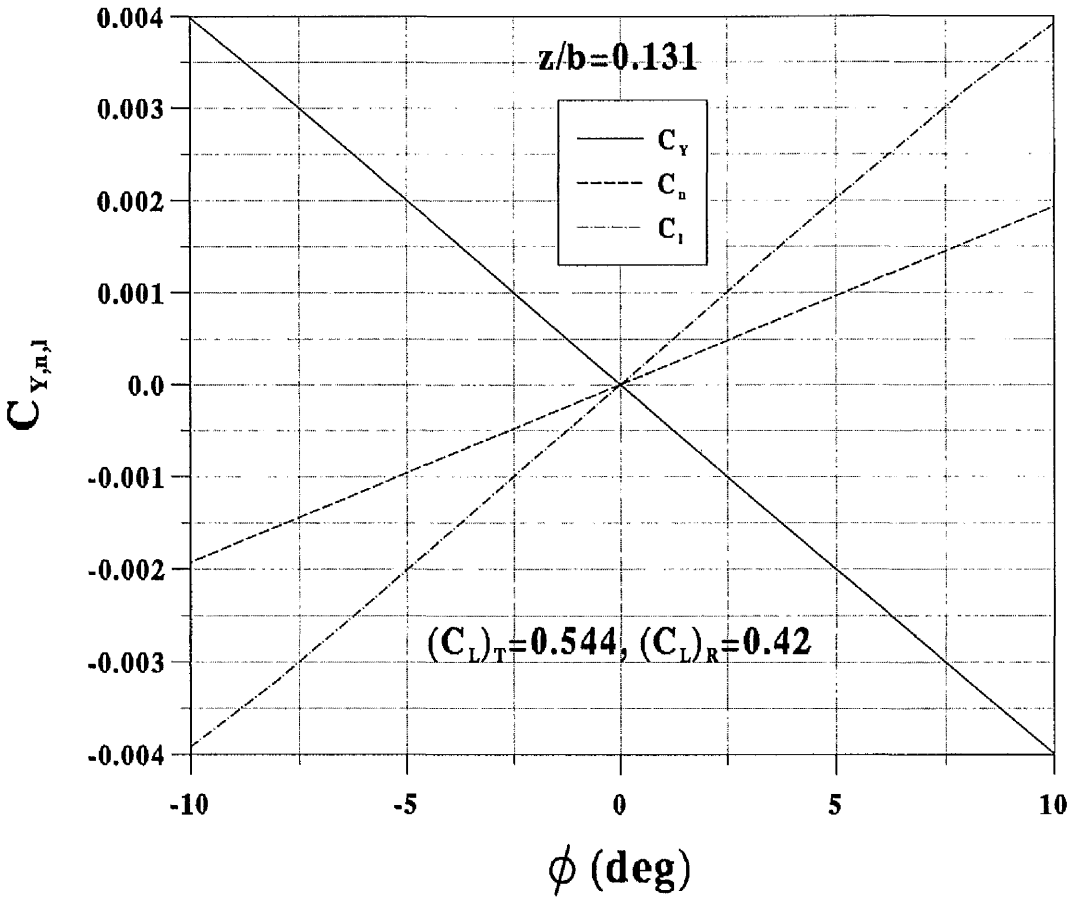

Figure 3.14: Receiver side force, rolling and yawing moments due to tanker wing bank displacement.

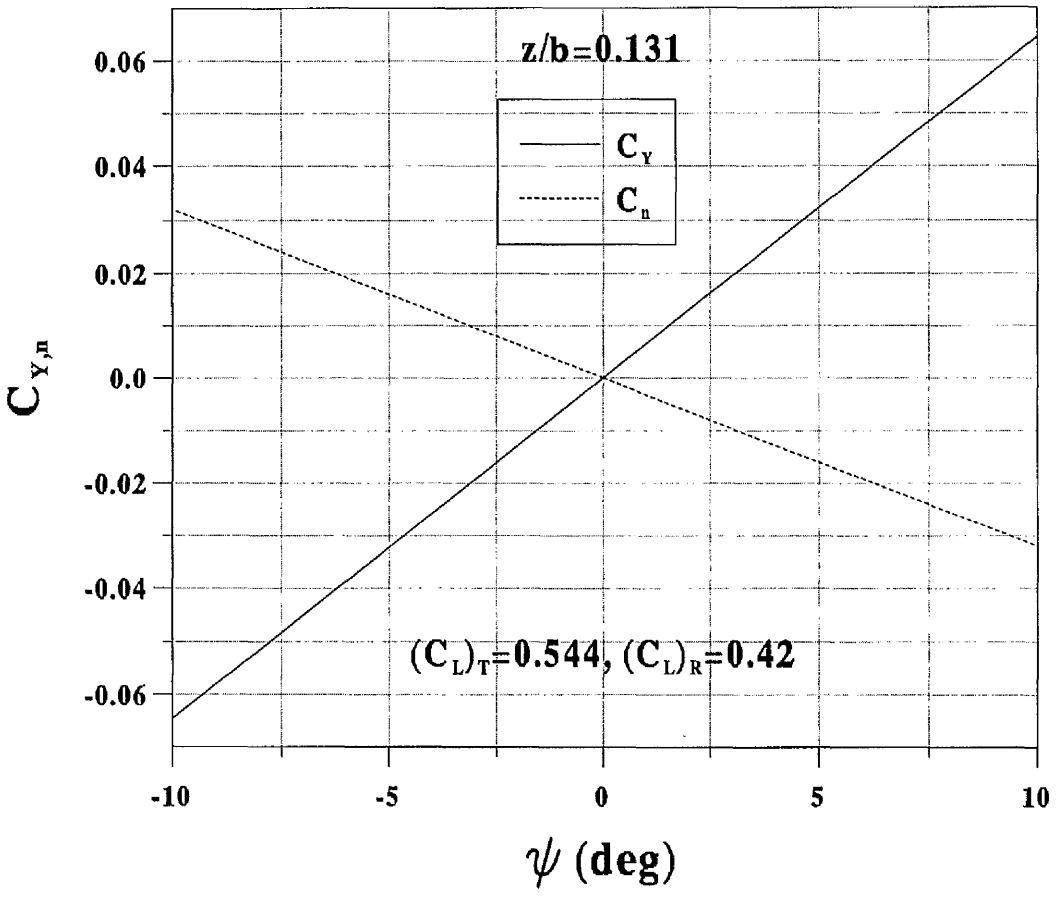

Figure 3.15: Receiver side force and yawing moment due to receiver yaw displacement.

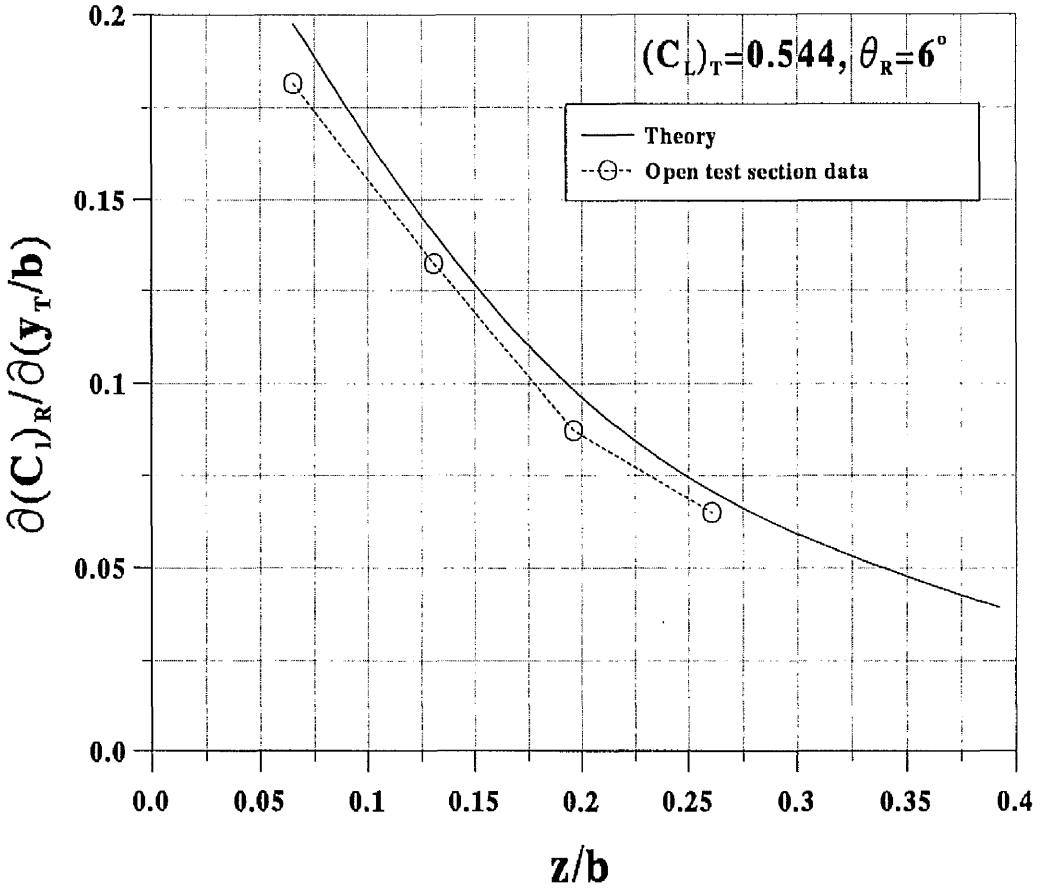

Figure 3.16: Receiver rolling moment due to tanker side displacement derivative.

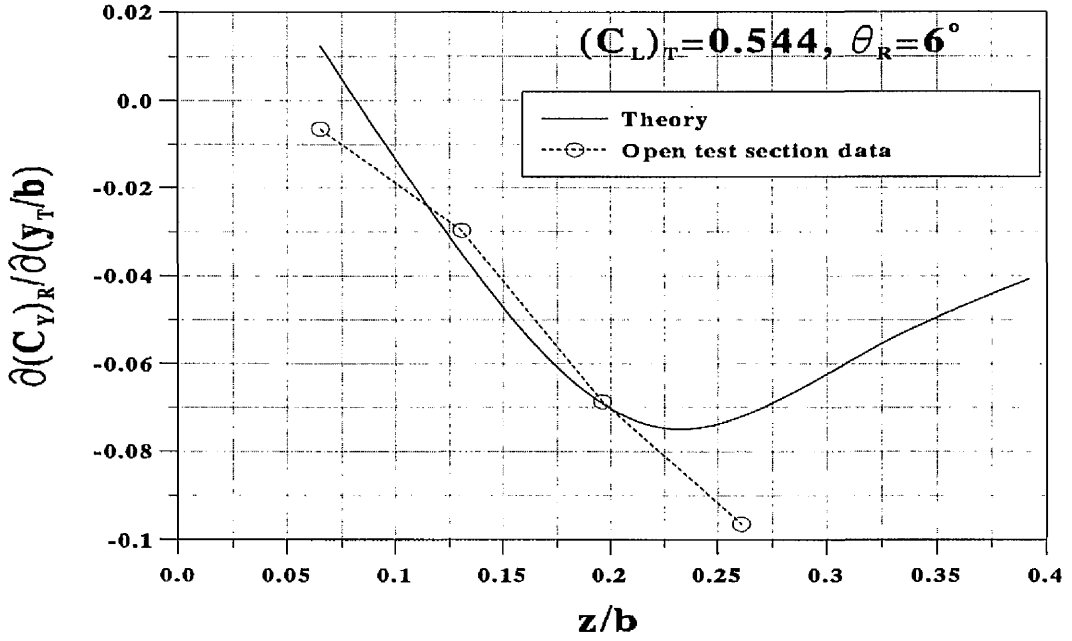

Figure 3.17: Receiver side force due to tanker side displacement derivative.

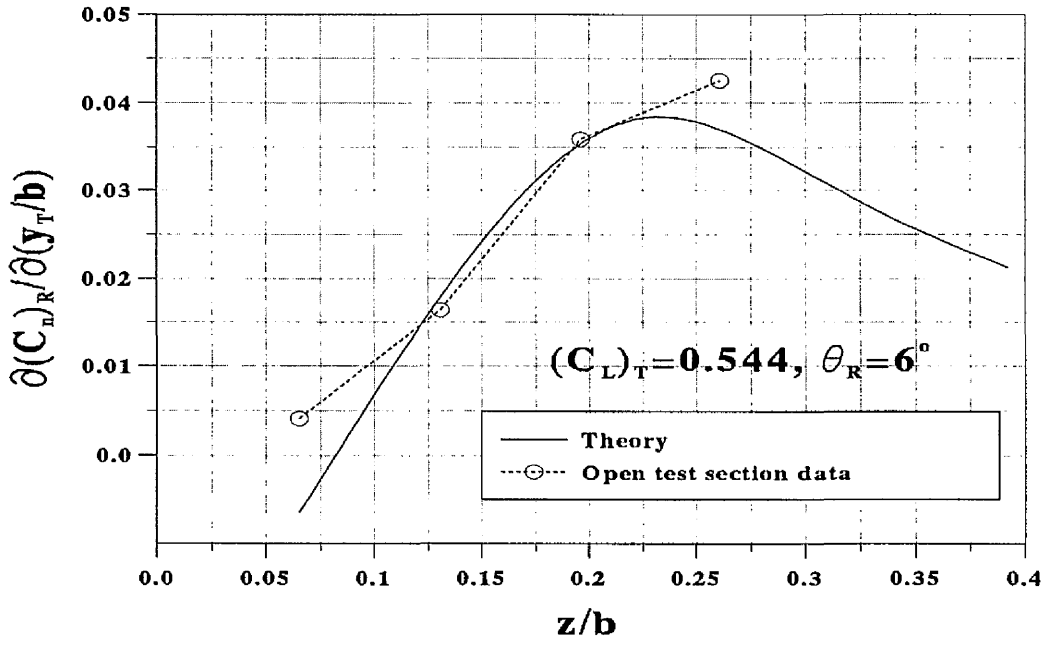

Figure 3.18: Receiver yawing moment due to tanker side displacement derivative.

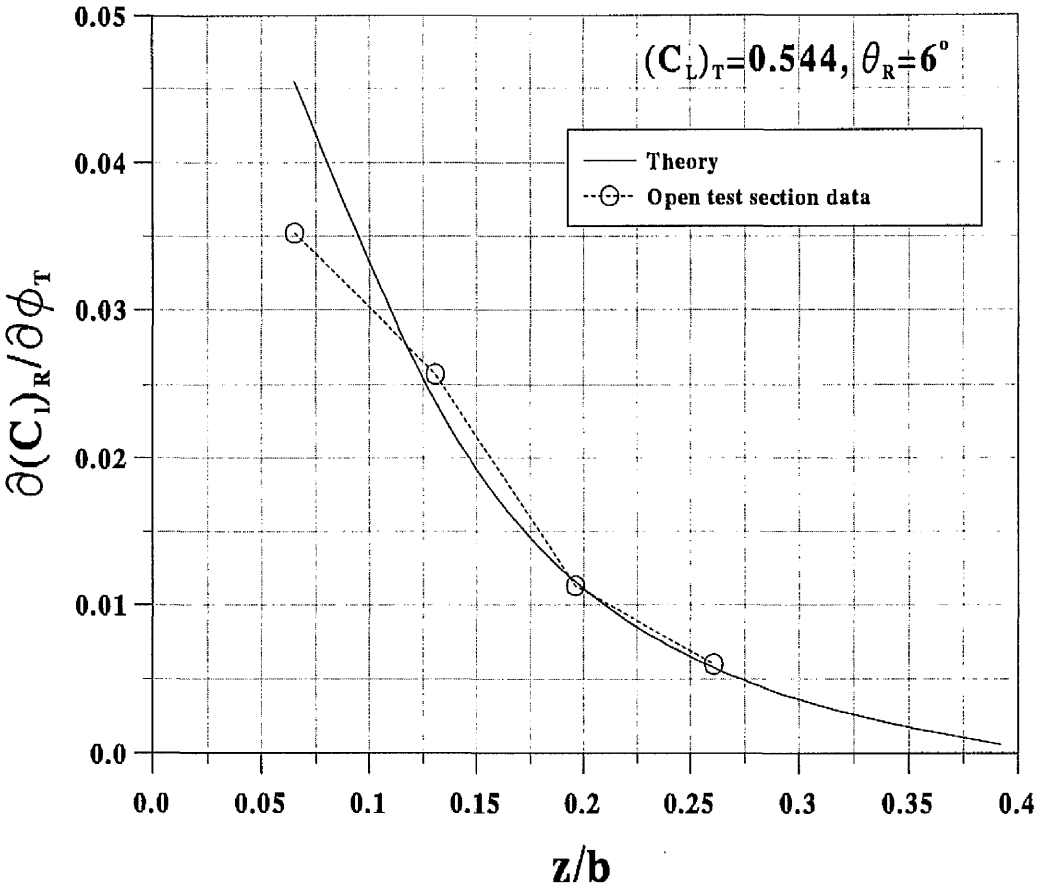

Figure 3.19: Receiver rolling moment due to tanker bank displacement derivative.

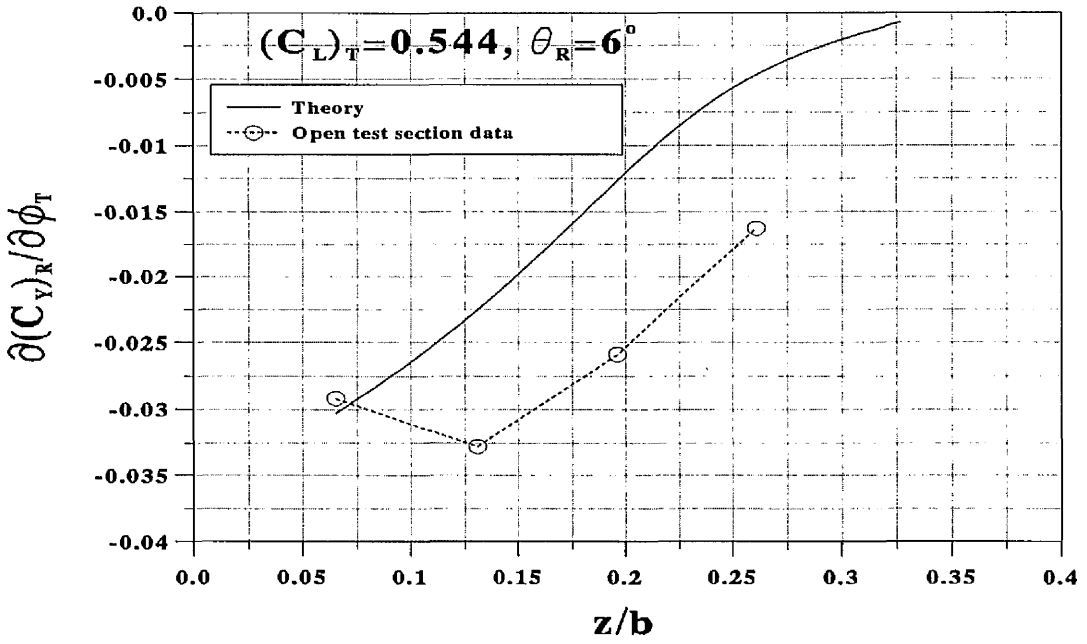

Figure 3.20: Receiver side force due to tanker bank displacement derivative.

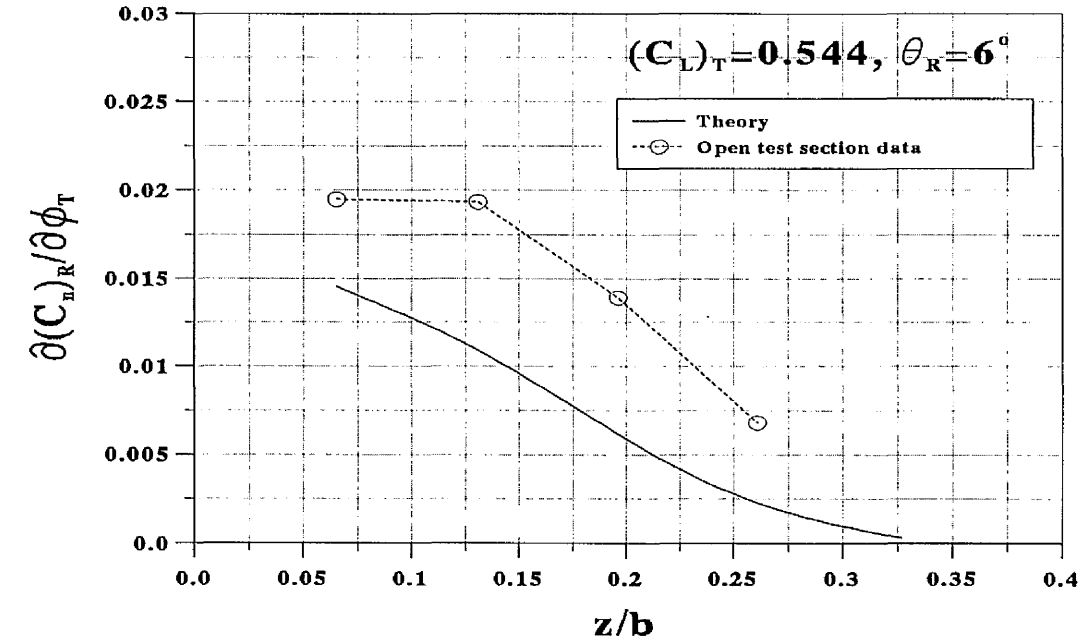

Figure 3.21: Receiver yawing moment due to tanker bank displacement derivative.

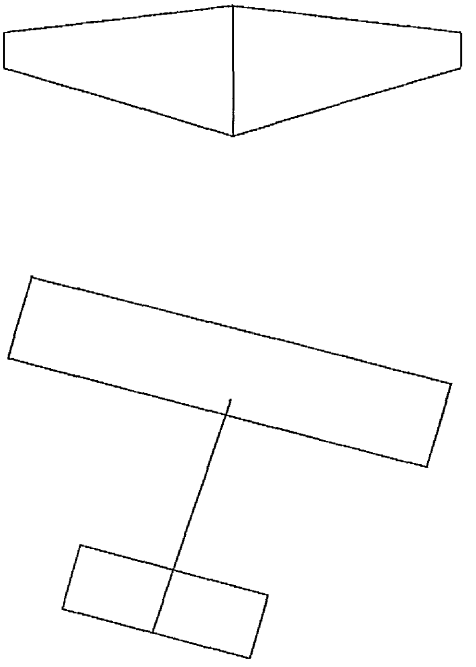

(a) Experimental case.

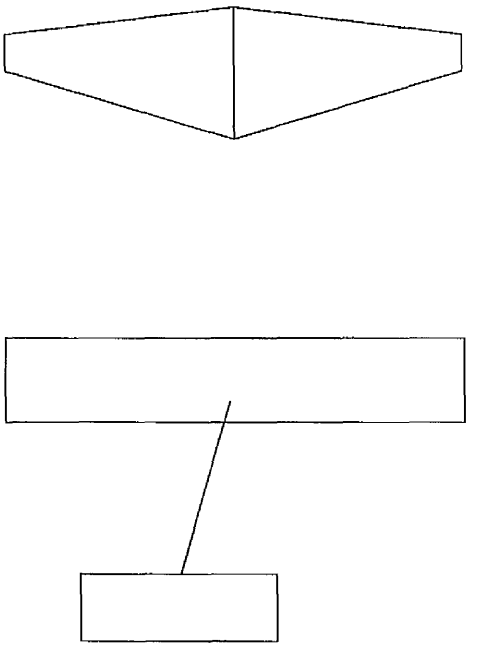

(b) Theoretical model.

Figure 3.22: Representation of the receiver aircraft model in yaw.

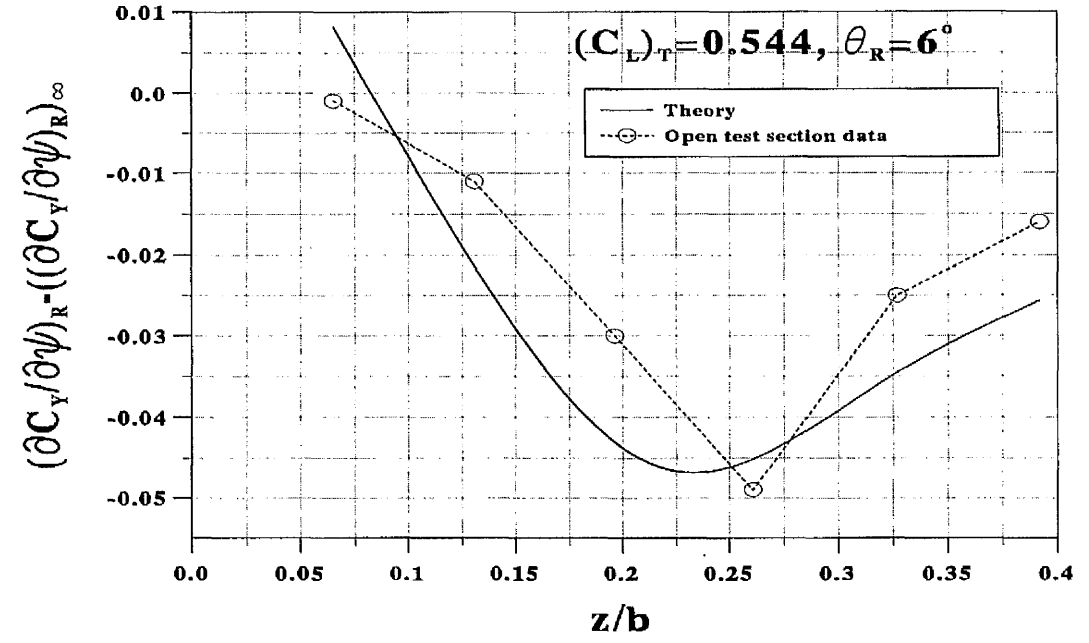

Figure 3.23: Receiver side force due to receiver yaw displacement derivative.

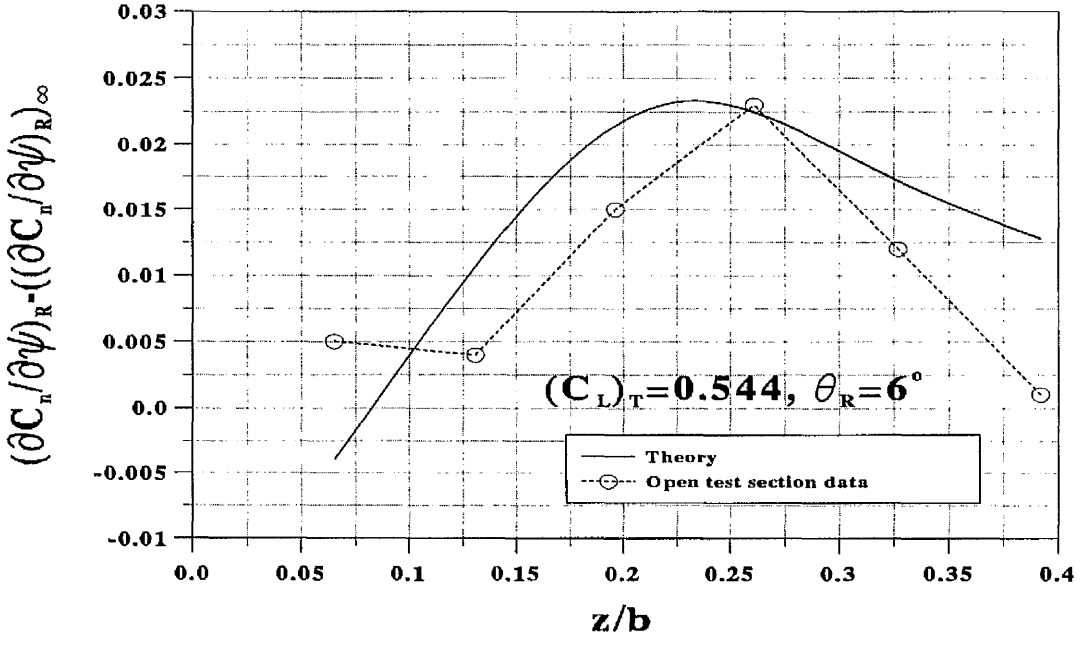

Figure 3.24: Receiver yawing moment due to receiver yaw displacement derivative.

Chapter 4

Estimation of Hercules Aerodynamic Derivatives in Free Air

This chapter describes the procedures used to estimate the aerodynamic derivatives of the Hercules aircraft in free air.

The aerodynamic derivatives of the Hercules receiver aircraft in free air were required in order to analyse the lateral stability and control characteristics of the Hercules receiver refuelling in flight from a KC10 tanker. The derivatives were also used for comparison with the aerodynamic characteristics of the Hercules in air-to-air refuelling. The American system of notation is used to define the aerodynamic derivatives which are divided into those associated with the asymmetric motion of the aircraft (i.e. lateral aerodynamic derivatives) and those associated

with the symmetric motion (i.e. longitudinal aerodynamic derivatives). The lateral aerodynamic derivatives of interest are given in non-dimensional form by C_{Y_β}, C_{n_β}, C_{l_β} due to sideslip, C_{Y_p}, C_{n_p}, C_{l_p} due to rate of roll, C_{Y_r}, C_{n_r}, C_{l_r} due to rate of yaw, $C_{l_{\delta_a}}$, $C_{n_{\delta_a}}$ due to aileron deflection and $C_{Y_{\delta_r}}$, $C_{n_{\delta_r}}$, $C_{l_{\delta_r}}$ due to rudder deflection. In the longitudinal case, the aerodynamic derivatives used are given in non-dimensional form by C_{Z_α}, C_{X_α}, C_{m_α} due to angle of attack and $C_{Z_{\delta_e}}$, $C_{m_{\delta_e}}$ due to elevator deflection. The aerodynamic derivatives due to q and u were not required since the longitudinal dynamic stability characteristics of the Hercules were not analysed. The above derivatives are estimated by considering the contributions from the aircraft wing, tailplane, fin, fuselage, nacelles and propellers. The wing, tailplane and fin contributions are estimated using linear VLM described in chapter 2 while fuselage, nacelles and propellers are calculated using both ESDU data sheet [43, 44, 45] and approximate methods [46, 47]. Tables 4.1 and 4.2 summarise the methods used to estimate the lateral stability and control derivatives of the Hercules aircraft, respectively, while table 4.3 gives the methods used to estimate the longitudinal stability and control derivatives. The aerodynamic derivatives are determined relative to the aerodynamic body axes, Oxyz, with the origin at the centre of gravity and the x-axis coinciding with the direction of the free-stream. The positive directions of the x, y and z axes are forward, to starboard and downwards, respectively.

4.1 Flight Conditions and Aircraft Data

The aerodynamic derivatives of the Hercules aircraft in free air are estimated at a lift coefficient of 0.5 and Mach number of 0.347. The Hercules centre of gravity is taken at the 25% mean chord position. A three-view drawing of the Hercules aircraft is shown in figure 4.1, with the basic data is listed in table 4.4. The planforms of the Hercules receiver wing, tailplane and fin used in the VLM computer program are shown in figure 4.2.

4.2 Hercules Lateral Stability Derivatives

4.2.1 Derivatives due to Sideslip, C_{l_β}, C_{n_β} and C_{Y_β}

The rolling moment derivative, C_{l_β}, is considered to be made up of contributions from the following

- Wing, $\left(C_{l_\beta}\right)_W$.
- Tailplane and fin in the presence of the high wing, $\left(C_{l_\beta}\right)_{t+f}$.
- Fuselage, including high wing-fuselage interference effect, $\left(C_{l_\beta}\right)_{Fus}$.

Therefore, the rolling moment derivative due to sideslip can be expressed as

$$C_{l_\beta} = \left(C_{l_\beta}\right)_W + \left(C_{l_\beta}\right)_{t+f} + \left(C_{l_\beta}\right)_{Fus}$$

The Hercules side force and yawing moment derivatives, C_{Y_β} and C_{n_β}, respectively, are considered to be made up of the following contributions

- Fin, including the interference effects of the wing and tailplane, $\left(C_{Y_\beta}\right)_f$, $\left(C_{n_\beta}\right)_f$.
- Fuselage, including wing-fuselage interference effect, $\left(C_{Y_\beta}\right)_{Fus}$, $\left(C_{n_\beta}\right)_{Fus}$.
- Nacelles, $\left(C_{Y_\beta}\right)_{Nac}$, $\left(C_{n_\beta}\right)_{Nac}$.
- Propellers, $\left(C_{Y_\beta}\right)_{Pro}$, $\left(C_{n_\beta}\right)_{Pro}$.

Thus, the side force and yawing moment derivatives due to sideslip can be expressed as

$$C_{Y_\beta} = \left(C_{Y_\beta}\right)_f + \left(C_{Y_\beta}\right)_{Fus} + \left(C_{Y_\beta}\right)_{Nac} + \left(C_{Y_\beta}\right)_{Pro}$$

$$C_{n_\beta} = \left(C_{n_\beta}\right)_f + \left(C_{n_\beta}\right)_{Fus} + \left(C_{n_\beta}\right)_{Nac} + \left(C_{n_\beta}\right)_{Pro}$$

Wing Contribution to C_{l_β}

The method used to estimate $(C_{l_\beta})_W$ is based on a vortex representation of the wing which was developed by Weissinger for unswept wings and applied to swept wings by Queijo [48]. In reference [48], the wing vortex system was represented by both a modified lifting line theory and horseshoe vortex model as shown in figures 4.3 and 4.4, respectively. Both systems allowed the lift to be produced by the spanwise bound vortex which is placed along the wing quarter-chord line and the chordwise bound vortices which extend from the quarter-chord line to the wing trailing edge. The trailing vortex sheet behind the wing is made up of free vortices which are in the direction of the free-stream and hence develop no lift. The two systems were applied to sideslipping wings by Queijo to predict $(C_{l_\beta})_W$ and the results were in good agreement with the experimental data.

The vortex system used in the present work for the wing in sideslip is based on the horseshoe vortex representation used by Queijo, with 4 chordwise horseshoe vortices used as shown in figure 4.5. Since it was shown in reference [49] that small sideslip angles had a negligible effect on the local circulation, the bound vortex system (i.e. the spanwise and chordwise bound vortices) is the same as that used in linear VLM without sideslip which is described in section 2.1. The trailing vortex sheet is in the free-stream direction. The rolling moment due to sideslip is calculated by considering the interaction of the velocity components with the wing bound vortex system. It is only necessary to carry out the calculations on the starboard wing since an equal and opposite rolling moment is produced on the port wing.

By using equation 2.34, the non-dimensional lift produced by the spanwise bound vortex of an mth elemental panel in sideslip is

$$\left[\left(\frac{l_s}{q_\infty S}\right)_m\right]_S = \frac{2}{S}\left\{\left[\frac{\Gamma_s}{V_\infty}\left(\Delta y\cos\beta + \Delta x\sin\beta\right)\right]_m\right\}_S \tag{4.1}$$

For small sideslip angles such that $\sin\beta \approx \beta$ and $\cos\beta \approx 1$, equation 4.1 can be written as

$$\left[\left(\frac{l_s}{q_\infty S}\right)_m\right]_S = \frac{2}{S}\left\{\left[\frac{\Gamma_s}{V_\infty}\left(\Delta y + \Delta x\beta\right)\right]_m\right\}_S \tag{4.2}$$

where Γ_s, Δx and Δy are the same as described in section 2.1.2.

The non-dimensional lift generated along the chordwise bound vortices of the mth panel in sideslip is given by

$$\left[\left(\frac{l_c}{q_\infty S}\right)_m\right]_S = \frac{2}{S}\left\{\left[\frac{\Gamma_c}{V_\infty}\left(c_o - c_i\right)\right]_m \beta\right\}_S \tag{4.3}$$

where Γ_c, c_i and c_o are the same as described in section 2.1.2. The non-dimensional rolling moment of the mth panel is obtained by summing equations 4.2 and 4.3 after multiplying them by the appropriate rolling moment arms as follows

$$\begin{aligned}[(C_l)_m]_S &= -\frac{2}{S}\left\{\left[\frac{\Gamma_s}{V_\infty}(\Delta y + \Delta x\beta)\frac{y_s}{b}\right]_m \right. \\ &+ \left.\left[\frac{\Gamma_c}{V_\infty}\left(c_o\frac{y_{c_o}}{b} - c_i\frac{y_{c_i}}{b}\right)\right]_m \beta\right\}_S \end{aligned} \tag{4.4}$$

where y_s, y_{c_i} and y_{c_o} are shown in figure 2.5. The rolling moment derivative due to sideslip of the mth panel is obtained by differentiating equation 4.4 with respect to β

$$\left[\left(\frac{\partial C_l}{\partial \beta}\right)_m\right]_S = -\frac{2}{S}\left[\left(\frac{\Gamma_s}{V_\infty}\Delta x\frac{y_s}{b}\right)_m + \left(\frac{\Gamma_c}{V_\infty}\right)_m\left(c_o\frac{y_{c_o}}{b} - c_i\frac{y_{c_i}}{b}\right)_m\right]_S \tag{4.5}$$

The wing rolling moment derivative due to sideslip is determined by summing equation 4.5 over all the elemental panels of the starboard wing and multiplying the result by two

$$\left(C_{l_\beta}\right)_W = \left(\frac{\partial C_l}{\partial \beta}\right)_W = 2\sum_{m=1}^{M/2}\left[\left(\frac{\partial C_l}{\partial \beta}\right)_m\right]_S \tag{4.6}$$

Contribution of Tailplane-Fin combination to C_{l_β}, C_{n_β} and C_{Y_β}

The linear VLM model of the tailplane-fin combination described in section 2.1.4 is used to estimate the tailplane and fin contributions to the side force, rolling and yawing moment derivatives due to sideslip. The VLM model allows for the aerodynamic interference between the tailplane and fin. However, the interference effect of the fuselage is not included. The effect of the Hercules high wing position on the sideslip angle at the fin is accounted for by using a correction factor, J_W,

which is estimated using ESDU data sheet [50]. The induced wing downwash on the tailplane and sidewash on the fin are determined using the flat vortex sheet model as described for the receiver aircraft model in chapter 3.

The circulation due to sideslip of the Hercules tailplane-fin combination with the tailplane at zero lift is shown in figure 4.6. The circulation distribution over the fin produces a negative side force with corresponding positive and negative yawing and rolling moments, respectively. A rolling moment is produced on the tailplane which opposes that of the fin. For small angles of sideslip ($\beta = \pm 5°$), the variations of the side force, rolling and yawing moments with angle of sideslip are linear. Finally, allowing for the wing-fuselage interference, the tailplane and fin contributions to C_{Y_β}, C_{n_β} and C_{l_β} can be expressed as

$$\left(C_{Y_\beta}\right)_f = J_W \left(C_{Y_\beta}\right)_{f,VLM}$$

$$\left(C_{n_\beta}\right)_f = J_W \left(C_{n_\beta}\right)_{f,VLM}$$

$$\left(C_{l_\beta}\right)_{t+f} = J_W \left(C_{l_\beta}\right)_{t+f,VLM}$$

where the side force, rolling and yawing moments acting on the tailplane and fin due to sideslip are calculated as described in section 2.1.5.

Fuselage Contribution to C_{l_β}, C_{n_β} and C_{Y_β}

The contribution of the fuselage alone to C_{l_β} is negligible, however, the wing-fuselage interference effect produces a significant contribution to C_{l_β}. This interference effect is related to the vertical location of the wing on the fuselage.

Figure 4.7 illustrates the cross flow produced by positive sideslip over the fuselage of a high wing aircraft such as the Hercules. The effect of the cross flow due to sideslip on the high wing position is to increase the angle of attack of the starboard wing and decrease that of the port wing resulting in a negative rolling moment. The opposite applies to the low wing position while the midwing position results in essentially zero interference effect. The contributions of the fuselage and wing-fuselage of the Hercules to C_{l_β} are estimated using ESDU data sheet [45] as described in appendix C. Also the cross flow over the fuselage produces a negative side force with a destabilising yawing moment which depend on both the fuselage alone and the wing-fuselage interference. ESDU data sheet [43] is used to estimate the contributions of the fuselage and wing-fuselage of the Hercules to C_{Y_β} and C_{n_β} as shown in appendix C.

Contribution of Propellers and Nacelles to C_{n_β} and C_{Y_β}

The effect of positive sideslip on the Hercules propellers is to produce a negative side force with a destabilising yawing moment. The corresponding side force and yawing moment derivatives due to sideslip are estimated using the method of reference [51] as described in appendix D.

The cross flow due to positive sideslip over the Hercules nacelles generates negative side force and yawing moment. The ESDU data sheet [43] is used to estimate the contribution of the nacelles to the side force and yawing moment derivatives due to sideslip as shown in appendix D.

4.2.2 Derivatives due to Rate of Roll, C_{l_p}, C_{n_p} and C_{Y_p}

The rolling moment derivative, C_{l_p}, of the Hercules is considered to be made up of contributions from the wing, $\left(C_{l_p}\right)_W$; fin, $\left(C_{l_p}\right)_f$, and tailplane, $\left(C_{l_p}\right)_t$ with the interference between the wing and tailplane-fin combination considered in the estimation of the fin and tailplane contributions. Thus, the damping in roll derivative, C_{l_p}, is given by

$$C_{l_p} = \left(C_{l_p}\right)_W + \left(C_{l_p}\right)_f + \left(C_{l_p}\right)_t$$

The fin is the only significant contributor to C_{Y_p}

$$C_{Y_p} = \left(C_{Y_p}\right)_f$$

The yawing moment derivative, C_{n_p}, is considered to be made up of contributions from the wing, $(C_{n_p})_W$, and fin, $(C_{n_p})_f$. Thus C_{n_p} is given by

$$C_{n_p} = \left(C_{n_p}\right)_W + \left(C_{n_p}\right)_f$$

Wing Contribution to C_{l_p} and C_{n_p}

When the wing performs a rolling motion about the x-axis with an angular velocity, p, an additional normal velocity (i.e. in the z direction), which varies linearly in the spanwise direction, is obtained as illustrated in figures 4.8a and b. Due to the normal velocity produced by the rolling motion, the local geometric angle of attack of the starboard wing is increased by $(\Delta\alpha = \frac{py}{V_\infty})$ and that of the port wing is decreased by the same amount as shown in figure 4.8c. Therefore, the circulation of a rolling wing is made up of

- Circulation due to symmetric angle of attack.
- Circulation due to asymmetric angle of attack associated with rolling velocity.

The circulation of the rolling wing is estimated using the linear VLM described in chapter 2 having the rolling motion modelled by a linear twist distribution across the wing span. The twist is zero at the wing centreline and is $(\frac{pb}{2V_\infty})$ and $(-\frac{pb}{2V_\infty})$ at the starboard and port wing tips, respectively. The wing contribution to the rolling moment is then calculated using equation 2.46. The yawing moment of the rolling wing is produced by the interaction of the rolling velocity (py) with the wing spanwise bound vortices as described by Queijo [48]. Thus, the non-dimensional yawing moment of an elemental panel, mth, on the starboard wing due to rate of roll can be expressed as

$$\left[\left(\frac{N}{q_\infty Sb}\right)_m\right]_S = \frac{2}{S}\left\{\left[\frac{\Gamma_s}{V_\infty}\frac{py_s}{V_\infty}\left(\Delta x\frac{x_s}{b} - \Delta y\frac{y_s}{b}\right)\right]_m\right\}_S \tag{4.7}$$

or

$$\left[\left(\frac{N}{q_\infty Sb}\right)_m\right]_S = \frac{2}{S}\frac{pb}{2V_\infty}\left\{\left[\frac{\Gamma_s}{V_\infty}\frac{y_s}{b/2}\left(\Delta x\frac{x_s}{b} - \Delta y\frac{y_s}{b}\right)\right]_m\right\}_S \tag{4.8}$$

where x_s and y_s are the yawing moment arms of the forces produced by the spanwise bound vortex of the mth panel. The elemental yawing moment derivative due to rate of roll in coefficient form of the mth panel is obtained by differentiating equation 4.8 with respect to $\frac{pb}{2V_\infty}$ to give,

$$\left[\left(\frac{\frac{\partial N}{\partial \frac{pb}{2V_\infty}}}{q_\infty Sb}\right)_m\right]_S = \frac{2}{S}\left\{\left[\frac{\Gamma_s}{V_\infty}\frac{y_s}{b/2}\left(\Delta x\frac{x_s}{b} - \Delta y\frac{y_s}{b}\right)\right]_m\right\}_S \tag{4.9}$$

The total wing yawing moment derivative due to rate of roll is determined by summing equation 4.9 over all the starboard wing elemental panels and multiplying

the result by two to give,

$$\left(C_{n_p}\right)_W = \left(\frac{\partial C_n}{\partial \frac{pb}{2V_\infty}}\right)_W = 2\sum_{m=1}^{M/2}\left[\left(\frac{\frac{\partial N}{\partial \frac{pb}{2V_\infty}}}{q_\infty S}\right)_m\right]_S \tag{4.10}$$

Contribution of Tailplane-Fin combination to C_{l_p}, C_{n_p} and C_{Y_p}

The VLM model of the tailplane-fin combination described in chapter 2 is used to estimate the tailplane and fin contributions to the aerodynamic derivatives due to rate of roll. In the rolling motion, the induced velocities on the tailplane and fin consist of two parts:

- The sidewash and downwash velocities induced by the asymmetric load distribution on the rolling wing.
- The velocities induced by the rolling motion of the isolated tailplane-fin combination.

The sidewash and downwash velocities induced by the rolling wing are calculated using the flat vortex sheet model of the wing wake described in section 2.2. The sidewash and downwash velocities induced on the Hercules fin and tailplane by the rolling wing for unit $\frac{pb}{2V_\infty}$ are shown in figures 4.9 and 4.10, respectively. Figure 4.9 shows the change in direction of the sidewash which corresponds to positions on the fin below and above the wing wake.

The rolling motion of the isolated tailplane-fin is proportional to the rate of roll, p, and the perpendicular distances measured from the tailplane-fin surfaces to the axis of roll as shown in figure 4.11. Thus, the induced sidewash, with the aircraft

at an angle of attack α, is given by

$$v = -p\left(m_f \cos\alpha - l_f \sin\alpha\right) = -\frac{pb}{2V_\infty}\frac{V_\infty}{b/2}\left(m_f \cos\alpha - l_f \sin\alpha\right)$$

and the sidewash angle is

$$\frac{v}{V_\infty} = -\frac{pb}{2V_\infty}\frac{m_f \cos\alpha - l_f \sin\alpha}{b/2}$$

where l_f and m_f are the distances between the aircraft centre of gravity and the control point of an elemental panel on the fin, measured parallel and perpendicular to the longitudinal body axis, respectively.

The induced downwash on the tailplane can be expressed as

$$w = \pm p y_t = \pm\frac{pb}{2V_\infty}\frac{V_\infty}{b/2}y_t$$

and the downwash angle is

$$\frac{w}{V_\infty} = \pm\frac{pb}{2V_\infty}\frac{y_t}{b/2}$$

where y_t is the distance between the axis of roll and the control point of an elemental panel on the tailplane, measured parallel to the y-axis. The plus and minus signs are for the starboard and port halves of the tailplane, respectively.

Once the velocities induced by the rolling wing and the rolling motion of the isolated tailplane-fin are determined, the linear VLM can be used to calculate the tailplane-fin loading due to rate of roll. Then, the fin contributions to the side force, rolling and yawing moments and the tailplane contribution to the rolling moment are calculated using the equations given in section 2.1.5.

4.2.3 Derivatives due to Rate of Yaw, C_{l_r}, C_{n_r} and C_{Y_r}

The fin is the major contributor to C_{Y_r} and C_{n_r}. The fuselage contribution is also significant for estimating C_{Y_r} and C_{n_r}. Hence, the damping in yaw derivative, C_{n_r}, is given by

$$C_{n_r} = (C_{n_r})_f + (C_{n_r})_{Fus}$$

and the side force derivative, C_{Y_r}, is

$$C_{Y_r} = (C_{Y_r})_f + (C_{Y_r})_{Fus}$$

The wing and fin are the only components that make significant contributions to the rolling moment derivative due to rate of yaw. Thus, C_{l_r} is given by

$$C_{l_r} = (C_{l_r})_W + (C_{l_r})_f$$

Wing Contribution to C_{l_r}

The yawing motion of the wing with an angular velocity, r, about the z-axis (positive in the clockwise direction) produces additional velocities which are functions of position on the wing as shown in figure 4.12. Therefore, the yawing wing can be considered to be in sideslip, with the angle of sideslip varying over the wing. The assumption used for circulation distribution of the wing in sideslip can be carried over to the yawing wing [48]. Thus, it is assumed that the circulation distribution for a yawing wing is essentially the same as that for a non-yawing wing. The wing yawing moment due to rate of yaw is calculated by considering the interaction of the velocities due to yawing motion with the vortex system of the yawing

wing which is shown in figure 4.13. The bound vortex system is the same as that of sideslipping and rolling wings. The trailing vortex sheet however is curved to match the airflow streamlines [48]. The total velocity due to rate of yaw at any point on the wing (see figure 4.12) is given by

$$V_l = r\frac{y_l}{\cos\delta}$$

On the starboard wing, the velocity components parallel and normal to the wing plane of symmetry are

$$u_l = V_l \cos\delta = r y_l$$

and

$$v_l = -V_l \sin\delta = -r x_l$$

Since the circulation distribution is assumed to be symmetric, the calculations are only carried out on the starboard wing.

By using equation 2.34, the non-dimensional lift generated along the spanwise bound vortex of an elemental panel, mth, due to rate of yaw can be expressed as

$$\left[\left(\frac{l_s}{q_\infty S}\right)_m\right]_S = \frac{2}{S}\left\{\left(\frac{\Gamma_s}{V_\infty}\right)_m\left[\left(1-\frac{r y_s}{V_\infty}\right)\Delta y + \frac{r x_s}{V_\infty}\Delta x\right]_m\right\}_S \tag{4.11}$$

or

$$\left[\left(\frac{l_s}{q_\infty S}\right)_m\right]_S = \frac{2}{S}\left\{\left(\frac{\Gamma_s}{V_\infty}\right)_m\left[\left(1-\frac{rb}{2V_\infty}\frac{y_s}{b/2}\right)\Delta y + \frac{rb}{2V_\infty}\frac{x_s}{b/2}\Delta x\right]_m\right\}_S \tag{4.12}$$

where x_s, y_s and Γ_s are the same as defined in section 2.1.2. ($\Delta x = \bar{s}\tan\Lambda\cos\varphi$) and ($\Delta y = \bar{s}cos\varphi$) are the components of the spanwise vortex filament of the mth panel parallel to the x and y axes, respectively.

Using equation 2.38, the non-dimensional lift generated along the chordwise bound vortices of the mth panel due to rate of yaw can be written as

$$\left[\left(\frac{l_c}{q_\infty S}\right)_m\right]_S = \frac{2}{S}\left\{\left[\frac{\Gamma_c}{V_\infty}\left(\frac{rx_{c_o}}{V_\infty}c_o - \frac{rx_{c_i}}{V_\infty}c_i\right)\right]_m\right\}_S \tag{4.13}$$

or

$$\left[\left(\frac{l_c}{q_\infty S}\right)_m\right]_S = \frac{2}{S}\left\{\left[\frac{\Gamma_c}{V_\infty}\left(\frac{rb}{2V_\infty}\frac{x_{c_o}}{b/2}c_o - \frac{rb}{2V_\infty}\frac{x_{c_i}}{b/2}c_i\right)\right]_m\right\}_S \tag{4.14}$$

where c_i, c_o, x_{c_i}, x_{c_i} and Γ_c are the same as defined in section 2.1.2. By combining the spanwise and chordwise lift components with the appropriate rolling moment arms, the rolling moment coefficient of the mth panel can be expressed as

$$\begin{aligned}[(C_l)_m]_S &= -\frac{2}{S}\left\{\left(\frac{\Gamma_s}{V_\infty}\right)_m\left[\left(1 - \frac{rb}{2V_\infty}\frac{y_s}{b/2}\right)\Delta y - \frac{rb}{2V_\infty}\frac{x_s}{b/2}\Delta x\right]_m\left(\frac{y_s}{b}\right)_m\right. \\ &+ \left.\left[\frac{\Gamma_c}{V_\infty}\left(\frac{rb}{2V_\infty}\frac{x_{c_o}}{b/2}c_o\frac{y_{c_o}}{b} - \frac{rb}{2V_\infty}\frac{x_{c_i}}{b/2}c_i\frac{y_{c_i}}{b}\right)\right]_m\right\}_S \end{aligned} \tag{4.15}$$

The rolling moment derivative due to rate of yaw of the mth panel is obtained by differentiating equation 4.15 with respect to $\frac{rb}{2V_\infty}$ to give,

$$\begin{aligned}\left[\left(\frac{\partial C_l}{\partial\frac{rb}{2V_\infty}}\right)_m\right]_S &= -\frac{2}{S}\left\{\left[\frac{\Gamma_s}{V_\infty}\left(-\frac{y_s}{b/2}\Delta y + \frac{x_s}{b/2}\Delta x\right)\frac{y_s}{b}\right]_m\right. \\ &+ \left.\left[\frac{\Gamma_c}{V_\infty}\left(-\frac{x_{c_i}}{b/2}c_i\frac{y_{c_i}}{b} + \frac{x_{c_o}}{b/2}c_o\frac{y_{c_o}}{b}\right)\right]_m\right\}_S \end{aligned} \tag{4.16}$$

The wing rolling moment derivative due to rate of yaw is obtained by summing equation 4.16 over all the starboard wing elemental panels and multiplying the result by two

$$(C_{l_r})_W = \left(\frac{\partial C_l}{\partial\frac{rb}{2V_\infty}}\right)_W = 2\sum_{m=1}^{M/2}\left[\left(\frac{\partial C_l}{\partial\frac{rb}{2V_\infty}}\right)_m\right]_S \tag{4.17}$$

Fin Contributions to C_{l_r}, C_{n_r} and C_{Y_r}

Since the circulation distribution across the wing span is assumed to be unaffected by the yawing motion [48], the effect of rate of yaw is to produce a local sideslip velocity at the fin that is equal to the product of the rate of yaw and the moment arm of the side force acting on the fin. Thus, the fin can be assumed to be in sideslip, with the angle of sideslip varying over the fin height. The fin contributions to C_{l_r}, C_{Y_r} and C_{n_r} are then calculated using the forces and moments acting on the fin in sideslip with the wing-fuselage interference factor (J_W) is taken equal to one since the effect of wing height is very small for the derivatives due to rate of yaw [52].

For an elemental panel, mth, on the fin, the sideslip angle due to yawing motion at an angle of attack α is

$$-\frac{r}{V_\infty}\left(x_f \cos\alpha + z_f \sin\alpha\right)$$

where x_f and z_f are the same as defined in section 2.1.5. Thus, using the side force produced by the mth panel due to sideslip, the non-dimensional side force due to rate of yaw of the mth panel can be expressed as

$$(C_Y)_m = -\frac{2}{S}\left(\frac{\Gamma}{V_\infty}\Delta z\right)_m \frac{r}{V_\infty}\left(x_f \cos\alpha + z_f \sin\alpha\right)_m$$

or

$$(C_Y)_m = -\frac{2}{S}\left(\frac{\Gamma}{V_\infty}\Delta z\right)_m \frac{rb}{2V_\infty}\left(\frac{x_f \cos\alpha + z_f \sin\alpha}{b/2}\right)_m \tag{4.18}$$

The side force derivative due to rate of yaw of the mth panel is obtained by differentiating equation 4.18 with respect to $\frac{rb}{2V_\infty}$

$$\left(\frac{\partial C_Y}{\partial \frac{rb}{2V_\infty}}\right)_m = -\frac{2}{S}\left(\frac{\Gamma}{V_\infty}\Delta z \frac{x_f \cos\alpha + z_f \sin\alpha}{b/2}\right)_m \tag{4.19}$$

Thus, the fin contribution to the side force derivative due to rate of yaw is obtained by summing equation 4.19 over all the fin elemental panels.

$$(C_{Y_r})_f = \left(\frac{\partial C_Y}{\partial \frac{rb}{2V_\infty}}\right)_f = \sum_{m=1}^{M_f} \left(\frac{\partial C_Y}{\partial \frac{rb}{2V_\infty}}\right)_m$$

The corresponding non-dimensional yawing and rolling moment derivatives due to rate of yaw of the mth panel can be expressed as

$$\left(\frac{\partial C_n}{\partial \frac{rb}{2V_\infty}}\right)_m = \frac{2}{S}\left(\frac{\Gamma}{V_\infty}\Delta z\right)_m \left(\frac{x_f \cos\alpha + z_f \sin\alpha}{b/2} \times \frac{x_f \cos\alpha + z_f \sin\alpha}{b}\right)_m \tag{4.20}$$

and

$$\left(\frac{\partial C_l}{\partial \frac{rb}{2V_\infty}}\right)_m = -\frac{2}{S}\left(\frac{\Gamma}{V_\infty}\Delta z\right)_m \left(\frac{x_f \cos\alpha + z_f \sin\alpha}{b/2} \times \frac{z_f \cos\alpha - x_f \sin\alpha}{b}\right)_m \tag{4.21}$$

respectively.

The fin yawing and rolling moment derivatives due to rate of yaw are obtained by summing equations 4.20 and 4.21 over all the fin elemental panels, respectively.

$$(C_{n_r})_f = \left(\frac{\partial C_n}{\partial \frac{rb}{2V_\infty}}\right)_f = \sum_{m=1}^{M_f} \left(\frac{\partial C_n}{\partial \frac{rb}{2V_\infty}}\right)_m$$

$$(C_{l_r})_f = \left(\frac{\partial C_l}{\partial \frac{rb}{2V_\infty}}\right)_f = \sum_{m=1}^{M_f} \left(\frac{\partial C_l}{\partial \frac{rb}{2V_\infty}}\right)_m$$

Fuselage Contribution to C_{n_r} and C_{Y_r}

As described in appendix C, a purely empirical method is used to estimate the fuselage contributions to the side force and yawing moment due to rate of yaw

derivatives. The Hercules fuselage provides a small contribution to C_{n_r} acting in the same direction as the fin component. However the fuselage contribution to C_{Y_r} is significant and opposes the fin component.

4.3 Hercules Lateral Control Derivatives

4.3.1 Derivatives due to Ailerons, $C_{l_{\delta_a}}$ and $C_{n_{\delta_a}}$

The rolling and yawing moments due to aileron deflection are estimated using the linear VLM which is applied to plain wings as described in chapter 2. The wing and aileron surfaces are replaced by a lattice of horseshoe vortices according to the principles of linear VLM given in section 2.1. The boundary condition, which ensures tangential flow to the wing and aileron surfaces, is satisfied at the control points of the wing and aileron elemental panels. By using equation 2.10, the boundary condition for a control point on the wing can be written as

$$\sum_{m=1}^{M_W+M_a} \left(F_{w,m} - F_{v,m} \tan \varphi_m\right) \frac{\Gamma_m}{V_\infty} = -4\pi\alpha \tag{4.22}$$

and for a control point on the ailerons is

$$\sum_{m=1}^{M_W+M_a} \left(F_{w,m} - F_{v,m} \tan \varphi_m\right) \frac{\Gamma_m}{V_\infty} = -4\pi \left(\alpha \pm \delta_a\right) \tag{4.23}$$

where M_W and M_a are the numbers of panels on the wing and ailerons, respectively. The aileron deflection angle, δ_a, is defined as

$$\delta_a = \frac{(\delta_a)_S + (\delta_a)_P}{2}$$

δ_a is positive when the starboard and port ailerons are deflected downwards and upwards, respectively. Thus, for equation 4.23, $(+\delta_a)$ and $(-\delta_a)$ correspond to the starboard and port ailerons, respectively.

When the boundary equations for all the control points are solved simultaneously, values of the unknown circulations and hence the span loading are obtained. The asymmetric deflection of the ailerons produces asymmetric loading across the wing span as shown in figure 4.14 for the Hercules wing. Having determined the span loading due to aileron deflection, the rolling and yawing moments can be calculated using equations 2.46 and 2.59, respectively.

4.3.2 Derivatives due to Rudder, $C_{l_{\delta_r}}$, $C_{n_{\delta_r}}$ and $C_{Y_{\delta_r}}$

The linear VLM, which is applied to the tailplane-fin combination as shown in chapter 2, is used to estimate the side force, rolling and yawing moments acting on the tailplane and fin due to rudder deflection. By using equations 2.60 and 2.61, the boundary condition of the tailplane-fin combination with the rudder deflected can be expressed as follows.

Firstly, for a control point on the tailplane;

$$\begin{aligned} & \sum_{m=1}^{M_t/2} \left[(F_{w,m} - F_{v,m} \tan\varphi) \frac{\Gamma_m}{V_\infty} \right]_S \\ - & \sum_{m=1}^{M_t/2} \left[(F_{w,m} - F_{v,m} \tan\varphi) \frac{\Gamma_m}{V_\infty} \right]_P \\ - & \sum_{m=1}^{M_f+M_r} (F_{w,m} - F_{v,m} \tan\varphi) \frac{\Gamma_m}{V_\infty} = -4\pi\alpha \end{aligned} \tag{4.24}$$

secondly, for a control point on the fin;

$$\sum_{m=1}^{M_t/2}\left(F_{v,m}\frac{\Gamma_m}{V_\infty}\right)_S - \sum_{m=1}^{M_t/2}\left(F_{v,m}\frac{\Gamma_m}{V_\infty}\right)_p - \sum_{m=1}^{M_f+M_r}\left(F_{v,m}\frac{\Gamma_m}{V_\infty}\right) = 0 \qquad (4.25)$$

and finally, for a control point on the rudder

$$\sum_{m=1}^{M_t/2}\left(F_{v,m}\frac{\Gamma_m}{V_\infty}\right)_S - \sum_{m=1}^{M_t/2}\left(F_{v,m}\frac{\Gamma_m}{V_\infty}\right)_p - \sum_{m=1}^{M_f+M_r}\left(F_{v,m}\frac{\Gamma_m}{V_\infty}\right) = -4\pi\delta_r \qquad (4.26)$$

where M_t, M_f and M_r are the numbers of panels on the tailplane, fin and rudder, respectively. The rudder deflection angle, δ_r, is positive when the rudder is deflected to the port side.

The solution of the boundary equations for all the control points simultaneously leads to the circulation distribution of the tailplane-fin combination, with the rudder deflected. The circulation distribution of the Hercules tailplane-fin combination due to rudder deflection, with the tailplane at zero angle of attack, is shown in figure 4.15. The aerodynamic loads on the tailplane and fin are then calculated as described in section 2.1.5.

4.4 Hercules Longitudinal Stability Derivatives

The aerodynamic force derivatives C_{Z_α} and C_{X_α} are considered to be made up of contributions from the wing, $(C_{Z_\alpha})_W$, $(C_{X_\alpha})_W$, and the tailplane including the wing interference effect, $(C_{Z_\alpha})_t$, $(C_{X_\alpha})_t$. Thus

$$C_{Z_\alpha} = (C_{Z_\alpha})_W + (C_{Z_\alpha})_t$$

$$C_{X_\alpha} = (C_{X_\alpha})_W + (C_{X_\alpha})_t$$

The components considered for estimating the Hercules pitching moment derivative, C_{m_α}, are due to the wing, $(C_{m_\alpha})_W$, the tailplane including the wing interference effect, $(C_{m_\alpha})_t$ and the fuselage, $(C_{m_\alpha})_{Fus}$. Therefore, C_{m_α} is given by

$$C_{m_\alpha} = (C_{m_\alpha})_W + (C_{m_\alpha})_t + (C_{m_\alpha})_{Fus}$$

4.4.1 Wing and Tailplane Contributions to C_{m_α}, C_{X_α} and C_{Z_α}

The wing contributions to C_{Z_α} and C_{X_α} are estimated using equations 2.42 and 2.55, respectively whereas the tailplane contributions to C_{Z_α} and C_{X_α} are calculated using equations 2.15 and 2.23, respectively, with the effect of the wing induced downwash on the tailplane determined using the flat vortex sheet model. The upstream influence of the tailplane on the wing was neglected since the estimated change in the wing lift coefficient due to tailplane is about 1%. For small angles of attack, it is assumed that $C_{Z_\alpha} = -C_{L_\alpha}$ and $C_{X_\alpha} = -C_{D_{i_\alpha}}$ where C_{L_α} and $C_{D_{i_\alpha}}$ are determined as the gradients of the $C_L - \alpha$ and $C_{D_i} - \alpha$ curves, respectively.

The wing contribution to C_{m_α} is estimated using equation 2.49.

The tailplane contribution to C_{m_α} is calculated using linear VLM. The pitching moment generated about the y-axis by an elemental panel, mth, on the tailplane is given by

$$\Delta M = -\rho_\infty V_\infty \left[\Gamma \Delta y \left(l_t \cos\alpha + m_t \sin\alpha\right)\right]_m \tag{4.27}$$

where Γ and Δy are the circulation and the width of the mth panel, respectively. l_t and m_t are the distances between the centre of gravity and the quarter-chord of

the mth panel, measured parallel and perpendicular to the longitudinal body-axis, respectively. The total pitching moment can be expressed as

$$M = -\rho_\infty V_\infty \sum_{m=1}^{M_t} \left[\Gamma \Delta y \left(l_t \cos\alpha + m_t \sin\alpha\right)\right]_m \tag{4.28}$$

where M_t is the number of panels on the tailplane and Δy is taken as positive on the left half of the tailplane. Hence, the pitching moment coefficient based on the wing aerodynamic mean chord and area is

$$C_m = \frac{M}{\frac{1}{2}\rho_\infty V_\infty^2 S\bar{c}} = -\frac{2}{S\bar{c}} \sum_{m=1}^{M_t} \left[\Gamma \Delta y \left(l_t \cos\alpha + m_t \sin\alpha\right)\right]_m \tag{4.29}$$

$(C_{m_\alpha})_t$ is obtained as the gradient of the $C_m - \alpha$ curve of the tailplane.

4.4.2 Fuselage Contribution to C_{m_α}

The fuselage contribution to C_{m_α} is determined using the method of Multhopp [46] which is given in references [53, 54] as described in appendix C. The method requires the change in local flow angle due to the wing upwash or downwash with angle of attack, $\frac{\partial \alpha_l}{\partial \alpha}$, along the fuselage centreline. This is determined using the flat vortex sheet model given in section 2.2.

4.5 Hercules Longitudinal Control Derivatives

The linear VLM, developed for the wing and ailerons as shown in section 4.3.1, is used to calculate the lift and pitching moment generated by the tailplane due to elevator deflection. First, the circulation distribution over the Hercules tailplane

due to elevator deflection is determined. Figure 4.16 shows the change of circulation due to elevator deflection over the Hercules tailplane. Next, the tailplane lift and pitching moment are calculated using equations 2.15 and 4.29, respectively.

Finally, the values of all the contributions to the longitudinal and lateral aerodynamic derivatives of the Hercules aircraft, estimated using the procedures described above and using the flight conditions given in section 4.1, are summarised in tables 4.5 and 4.6, respectively.

Derivatives	Aircraft components					
	Wing	Fin	Tailplane	Fuselage	Nacelles	Propellers
C_{l_β}	VLM	VLM	VLM	ESDU [45]	-	-
C_{n_β}	-	VLM	-	ESDU [43]	ESDU [43]	Reference [51]
C_{Y_β}	-	VLM	-	ESDU [43]	ESDU [43]	Reference [51]
C_{l_p}	VLM	VLM	VLM	-	-	-
C_{n_p}	VLM	VLM	-	-	-	-
C_{Y_p}	-	VLM	-	-	-	-
C_{l_r}	VLM	VLM	-	-	-	-
C_{n_r}	-	VLM	-	ESDU [52]	-	-
C_{Y_r}	-	VLM	-	ESDU [52]	-	-

Table 4.1: Methods used to estimate the lateral stability derivatives of the Hercules aircraft.

Derivatives	Aircraft components	
	Ailerons	Rudder
$C_{l_{\delta_a}}$	VLM	-
$C_{n_{\delta_a}}$	VLM	-
$C_{l_{\delta_r}}$	-	VLM
$C_{n_{\delta_r}}$	-	VLM
$C_{Y_{\delta_r}}$	-	VLM

Table 4.2: Methods used to estimate the lateral control derivatives of the Hercules aircraft.

Derivatives	Aircraft components			
	Wing	Tailplane	Fuselage	Elevator
C_{m_α}	VLM	VLM	Reference [46]	-
C_{X_α}	VLM	VLM	-	-
C_{Z_α}	VLM	VLM	-	-
$C_{m_{\delta_e}}$	-	-	-	VLM
$C_{Z_{\delta_e}}$	-	-	-	VLM

Table 4.3: Methods used to estimate the longitudinal stability and control derivatives of the Hercules aircraft.

Wing span	40.14 m
Wing area	161.84 m^2
Wing twist	3°
Wing dihedral	2.5°
Tailplane span	15.776 m
Tailplane area	48.022 m^2
Fin height	6.71 m
Fin area	25.062 m^2

Table 4.4: Hercules aircraft data.

Aerodynamic derivative	Contributions of aircraft components				
	Wing	Tailplane	Fuselage	Elevator	Total
$C_{D_{i_\alpha}}$	0.16	0.044	-	-	0.204
C_{L_α}	5.329	0.906	-	-	6.235
C_{m_α}	-0.075	-3.308	0.917	-	-2.466
$C_{L_{\delta_e}}$	-	-	-	0.923	0.923
$C_{m_{\delta_e}}$	-	-	-	-3.53	-3.53

Table 4.5: Hercules Longitudinal aerodynamic derivatives (c.g. at $0.25\bar{c}$, all derivatives are per radian).

Aerodynamic derivative	Contributions of aircraft components								
	Wing	Tail	Fin	Fus	Nac	Pro	Rudder	Ailerons	Total
C_{l_β}	-0.03	0.01	-0.04	-0.04	-	-	-	-	-0.10
C_{n_β}	-	-	0.16	-0.07	-0.01	-0.01	-	-	0.07
C_{Y_β}	-	-	-0.47	-0.23	-0.19	-0.08	-	-	-0.97
C_{l_p}	-0.57	-0.01	-0.002	-	-	-	-	-	-0.58
C_{n_p}	-0.06	-	0.01	-	-	-	-	-	-0.05
C_{Y_p}	-	-	-0.02	-	-	-	-	-	-0.02
C_{l_r}	0.06	-	0.03	-	-	-	-	-	0.09
C_{n_r}	-	-	-0.12	-0.01	-	-	-	-	-0.13
C_{Y_r}	-	-	0.36	-0.05	-	-	-	-	0.31
$C_{l_{\delta_a}}$	-	-	-	-	-	-	-	-0.23	-0.23
$C_{n_{\delta_a}}$	-	-	-	-	-	-	-	0.01	0.01
$C_{l_{\delta_r}}$	-	-	-	-	-	-	-	0.02	0.02
$C_{n_{\delta_r}}$	-	-	-	-	-	-	-	-0.12	-0.12
$C_{Y_{\delta_r}}$	-	-	-	-	-	-	-	0.31	0.31

Table 4.6: Hercules lateral aerodynamic derivatives (all derivatives are per radian).

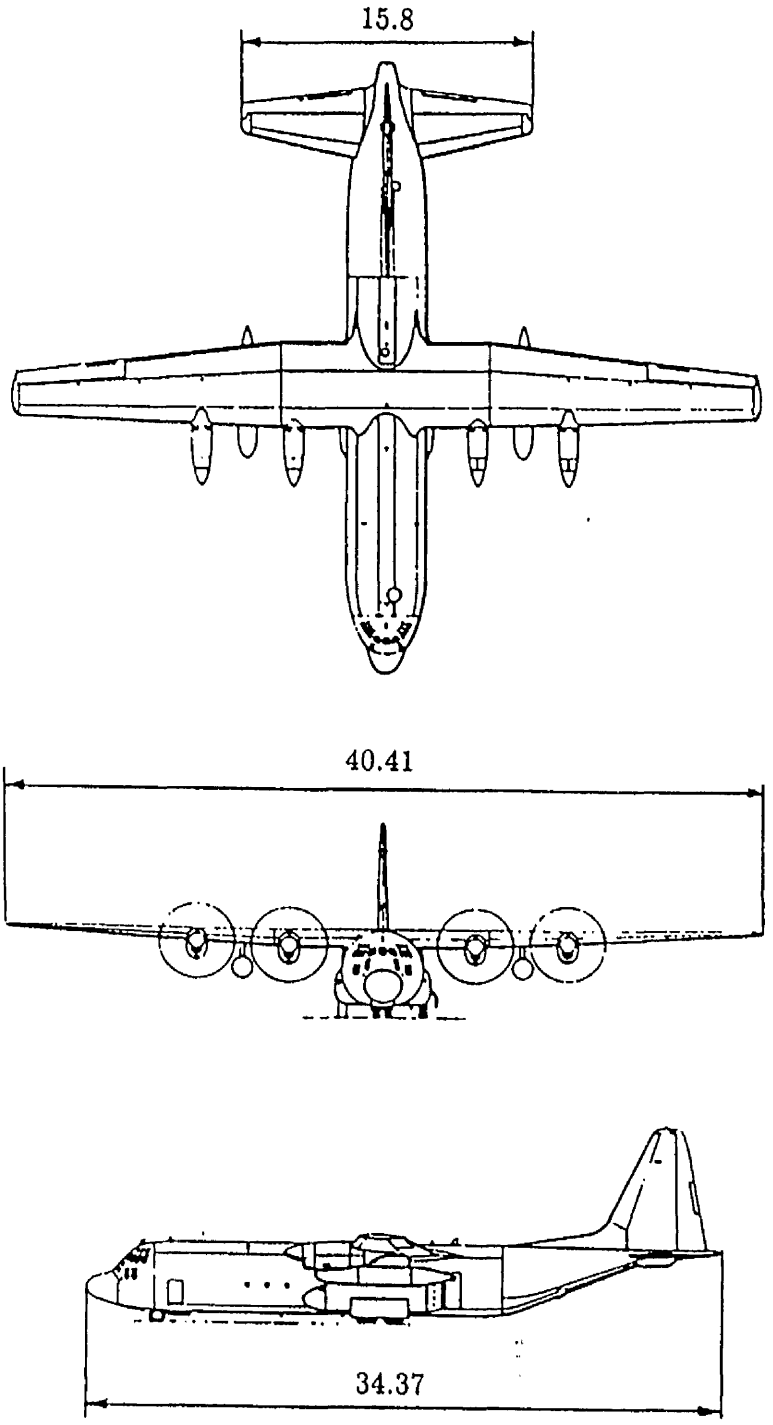

Figure 4.1: 3D view drawing of the Hercules aircraft (all dimensions in m).

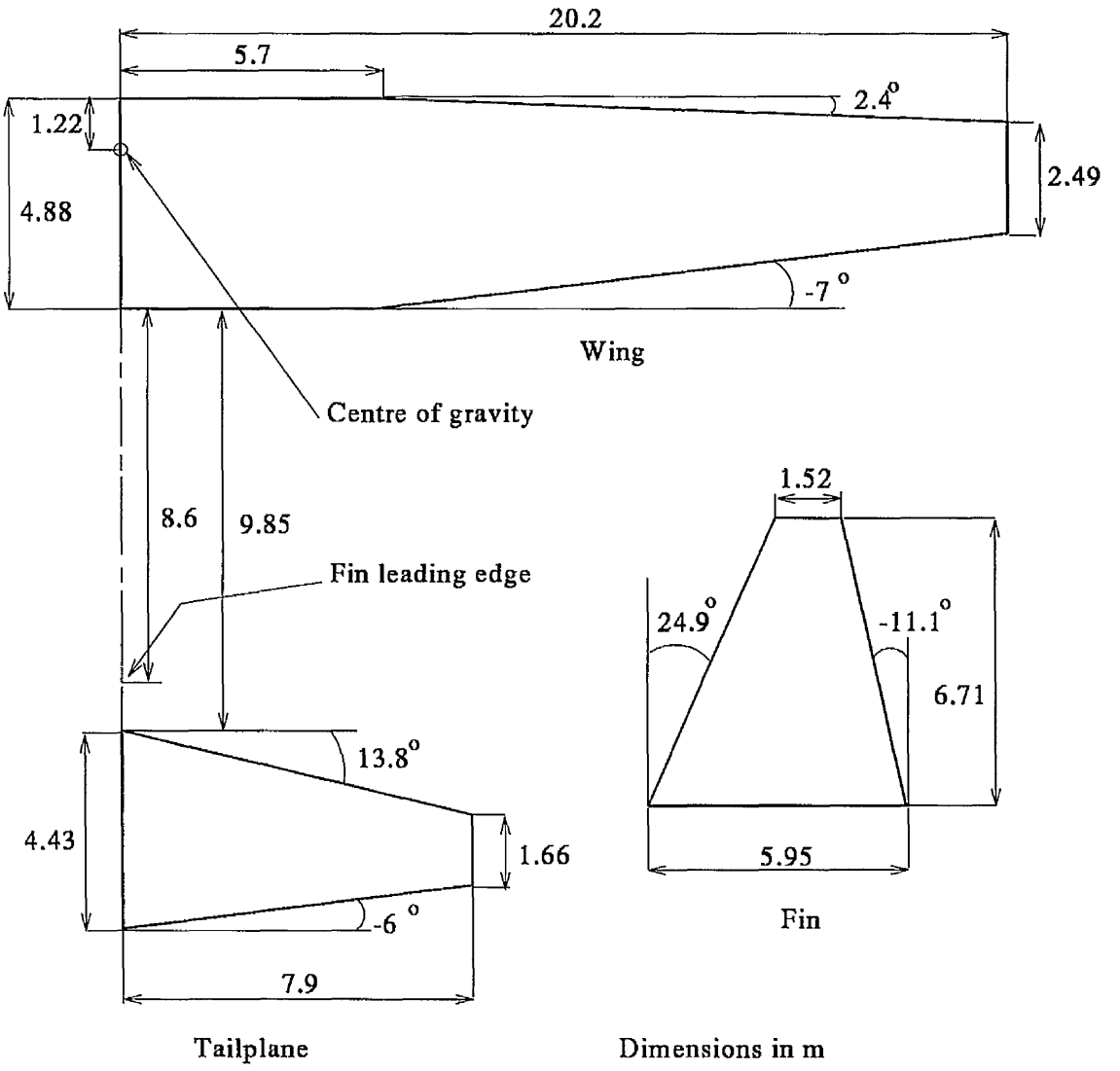

Figure 4.2: Hercules wing, tailplane and fin planforms used in VLM computer program.

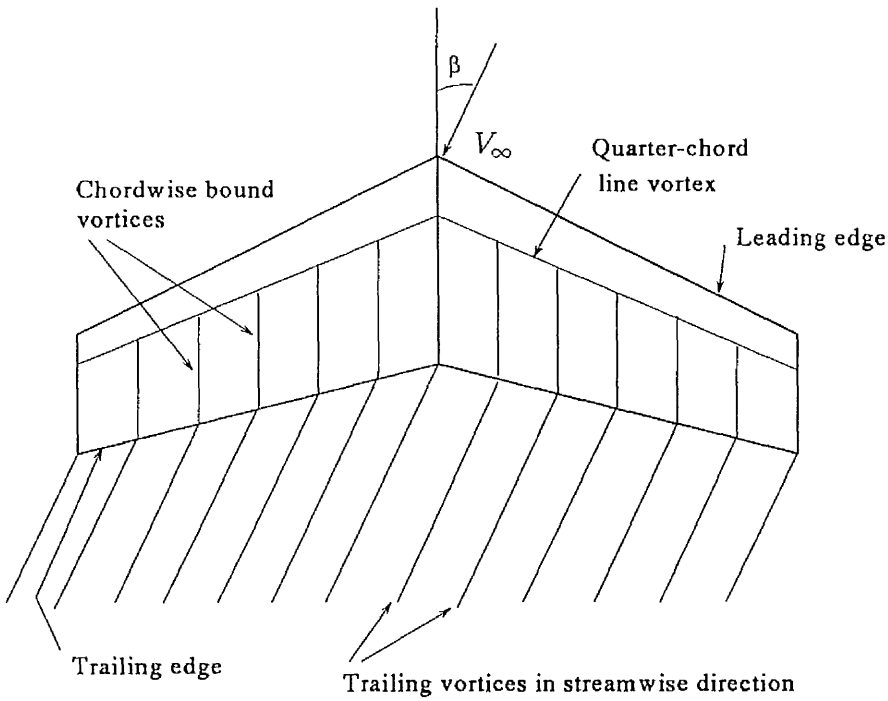

Figure 4.3: Modified lifting-line-theory arrangement for sideslip used by Queijo [48].

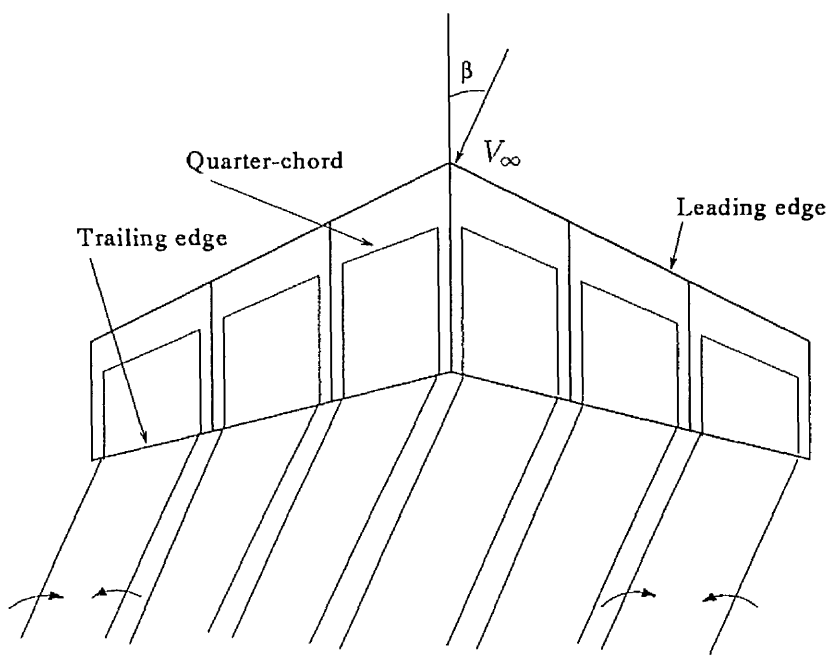

Figure 4.4: Arrangement of one chordwise of horseshoe vortices used for sideslip by Queijo [48].

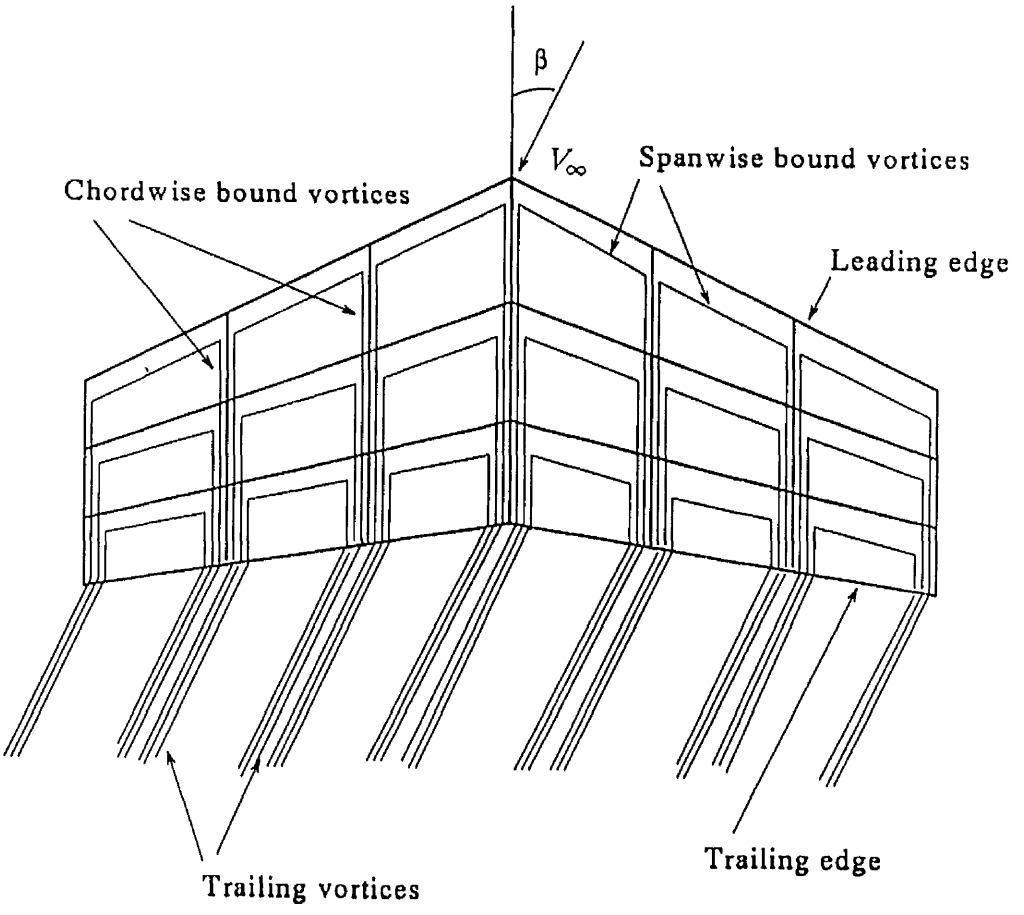

Figure 4.5: VLM representation of wing in sideslip.

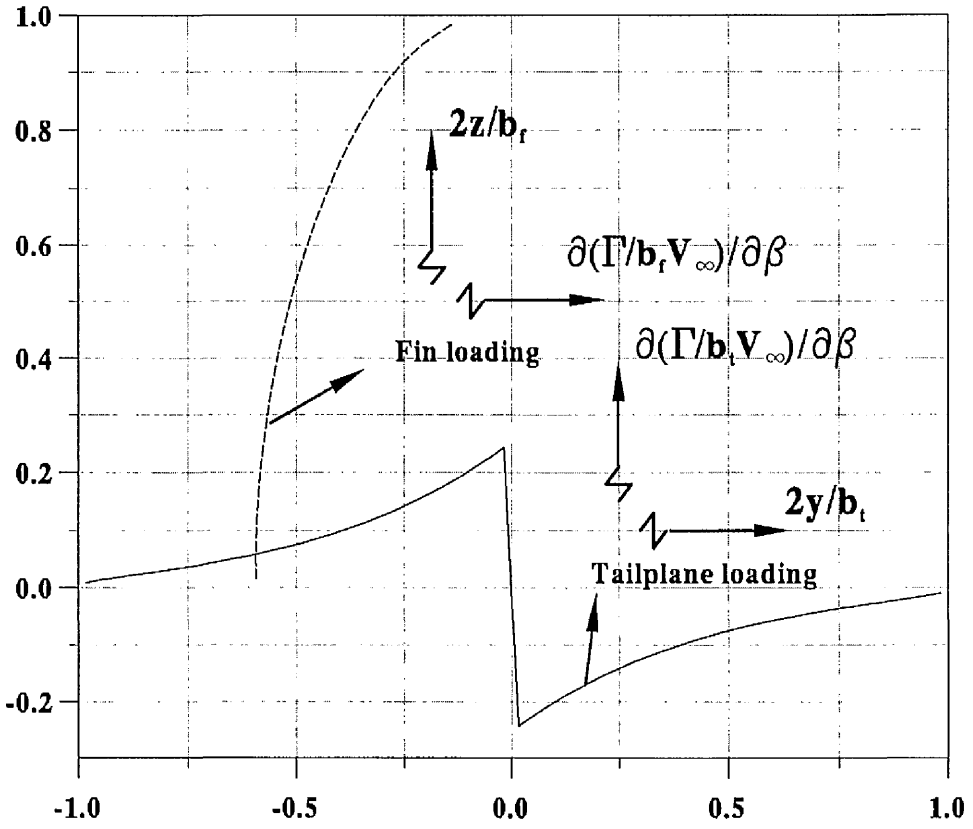

Figure 4.6: Circulation distribution over the tailplane and fin due to sideslip.

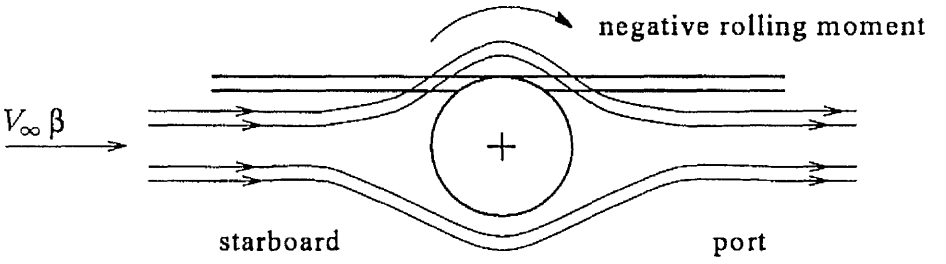

Figure 4.7: Flow around the fuselage of a high-wing.

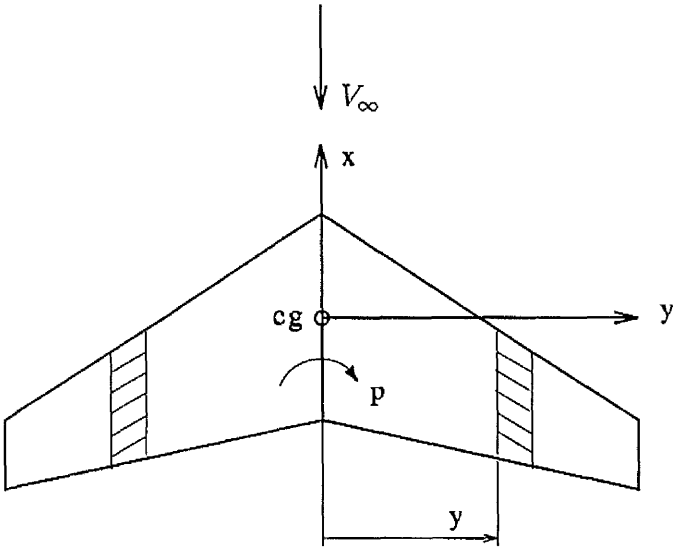

(a) Wing planform.

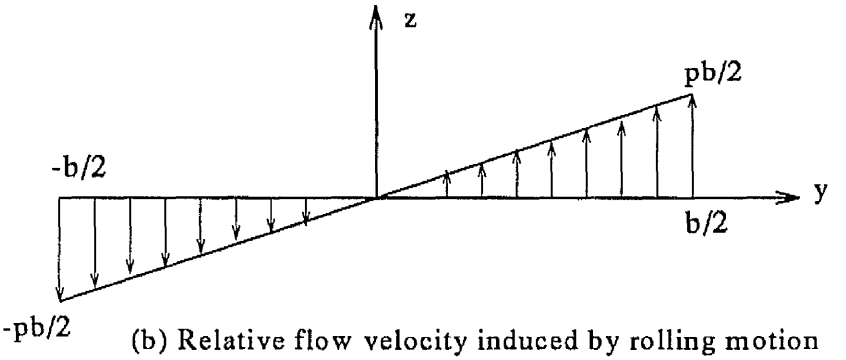

(b) Relative flow velocity induced by rolling motion

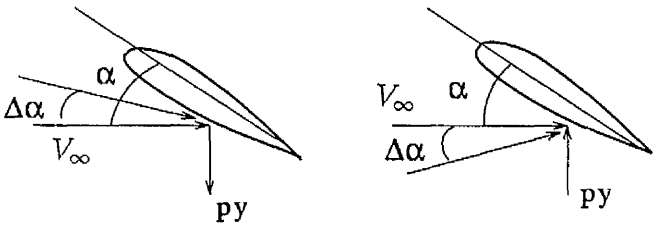

(c) Local flow direction of the starboard an port wings.

Figure 4.8: Aerodynamics of the rolling wing.

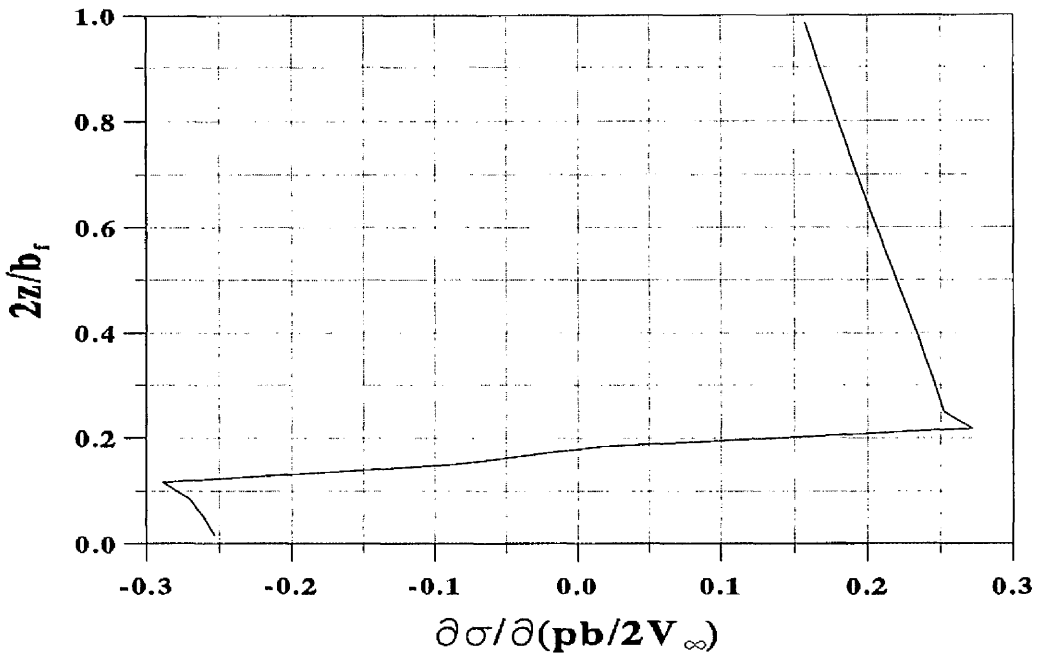

Figure 4.9: Sidewash induced by the rolling wing at the fin quarter-chord position.

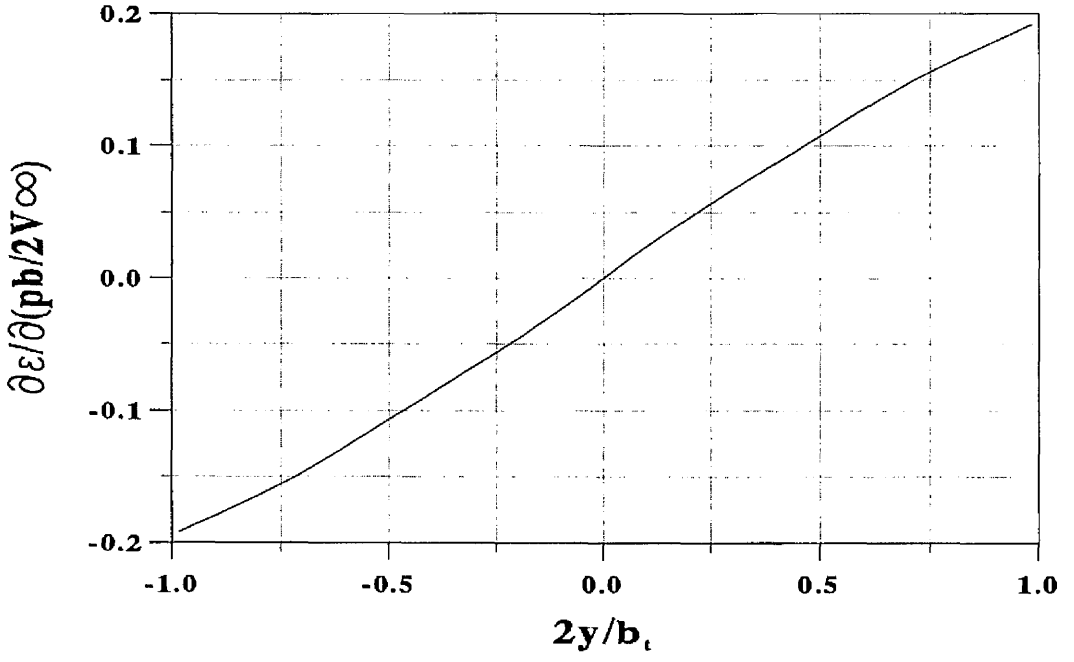

Figure 4.10: Downwash induced by the rolling wing at the tailplane quarter-chord position.

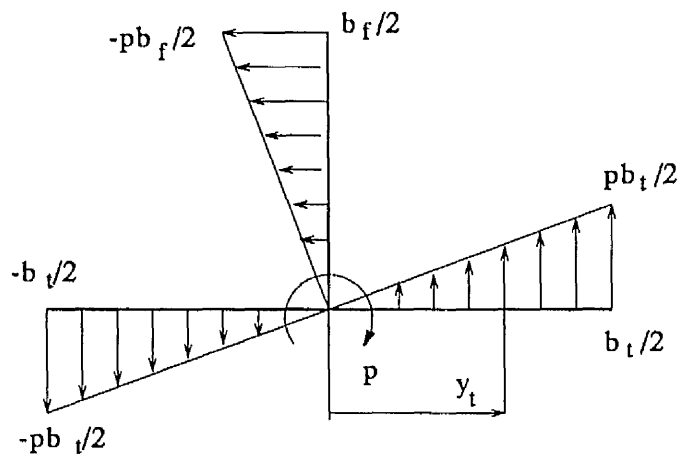

Figure 4.11: Velocities induced on tailplane and fin by the rolling motion of isolated tailplane-fin.

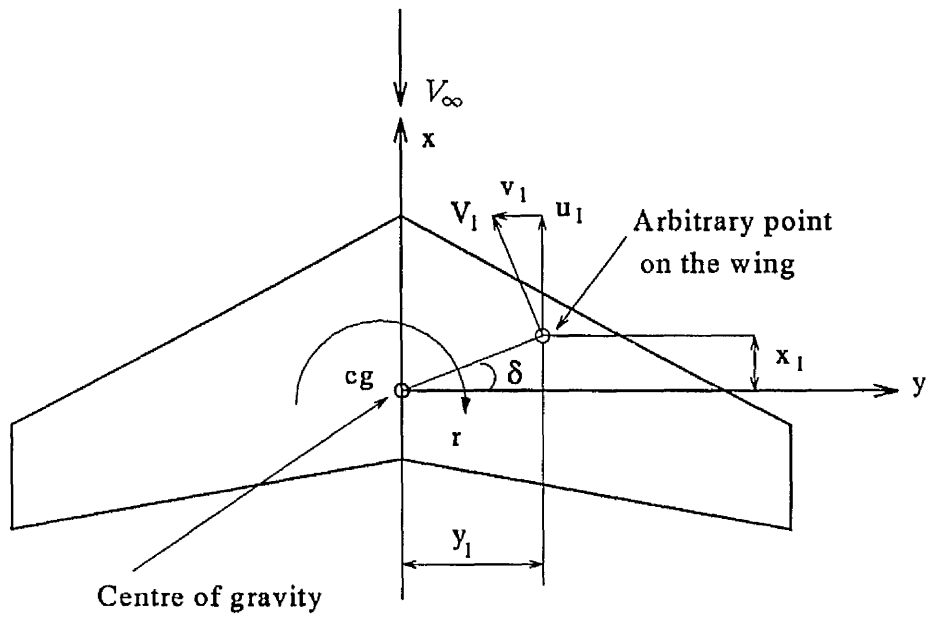

Figure 4.12: Velocities induced by the wing yawing motion.

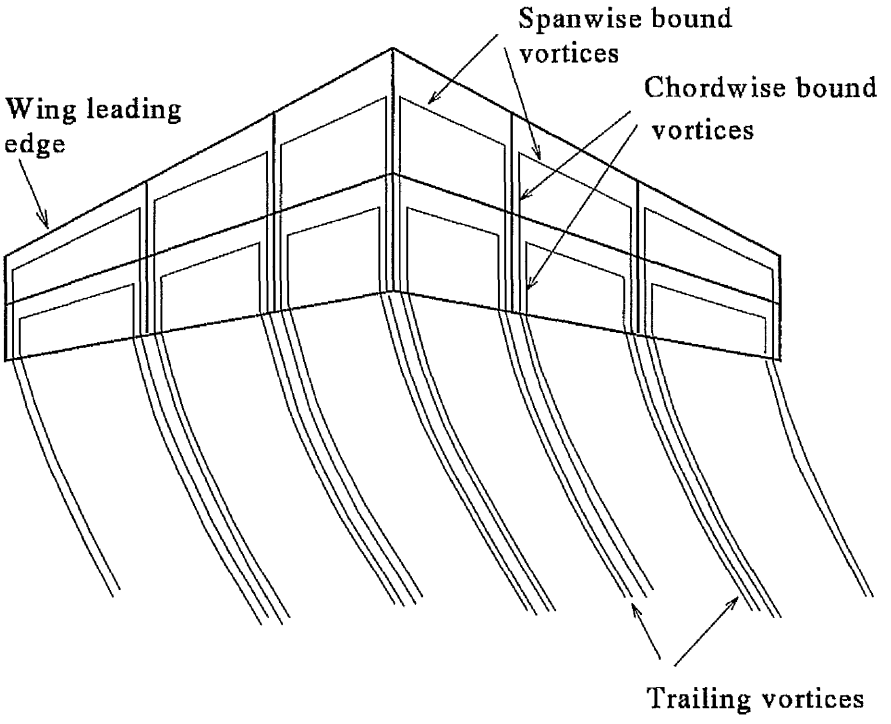

Figure 4.13: Vortex system for the yawing wing.

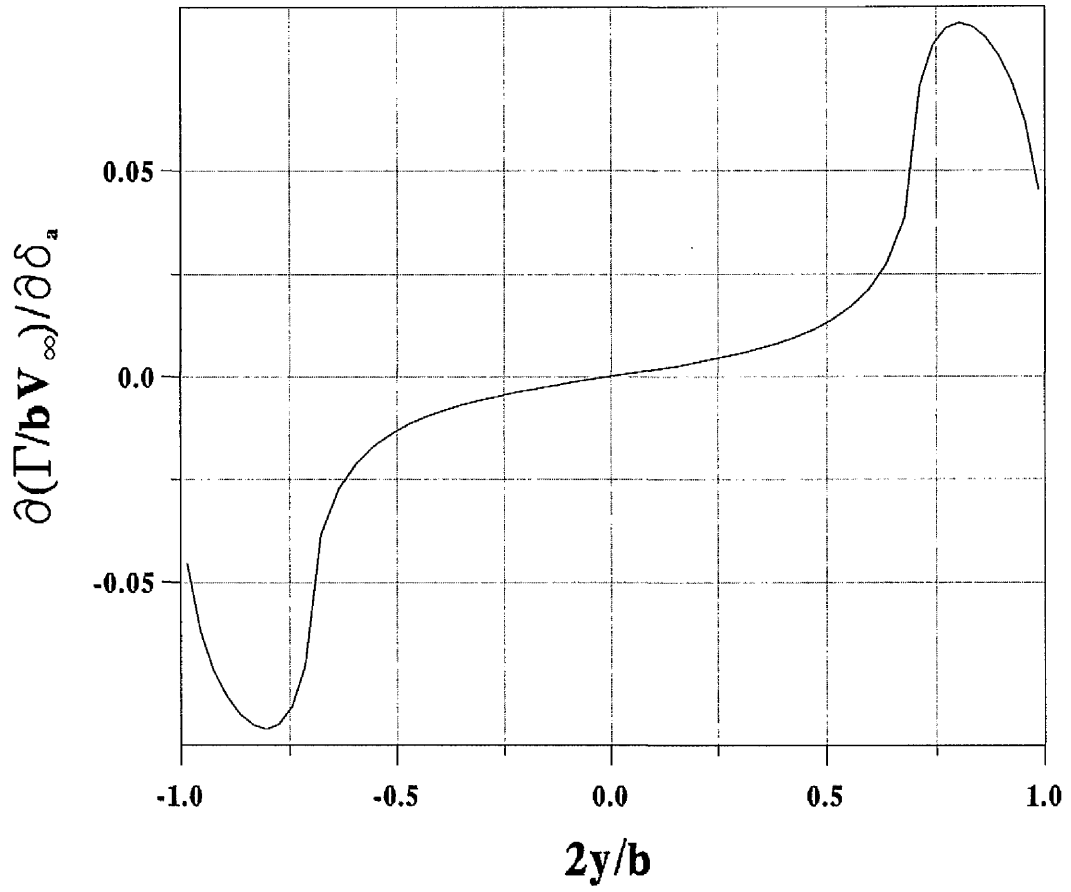

Figure 4.14: Circulation distribution over the wing due to aileron deflection.

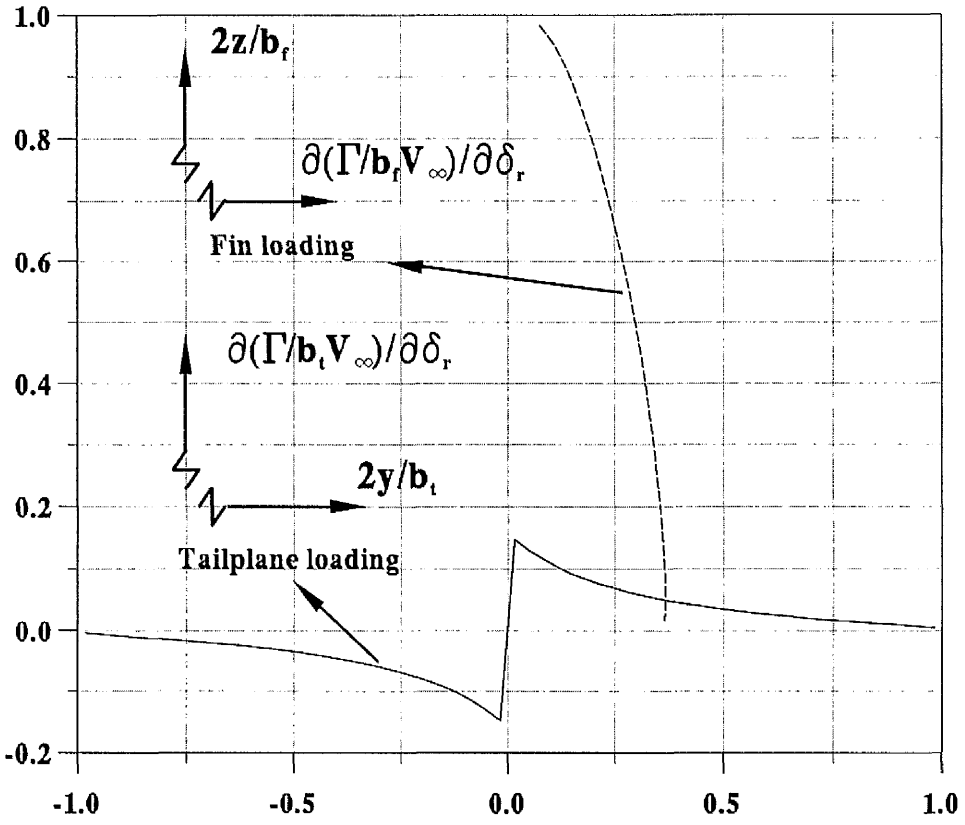

Figure 4.15: Circulation distribution over the tailplane and fin due to positive rudder deflection.

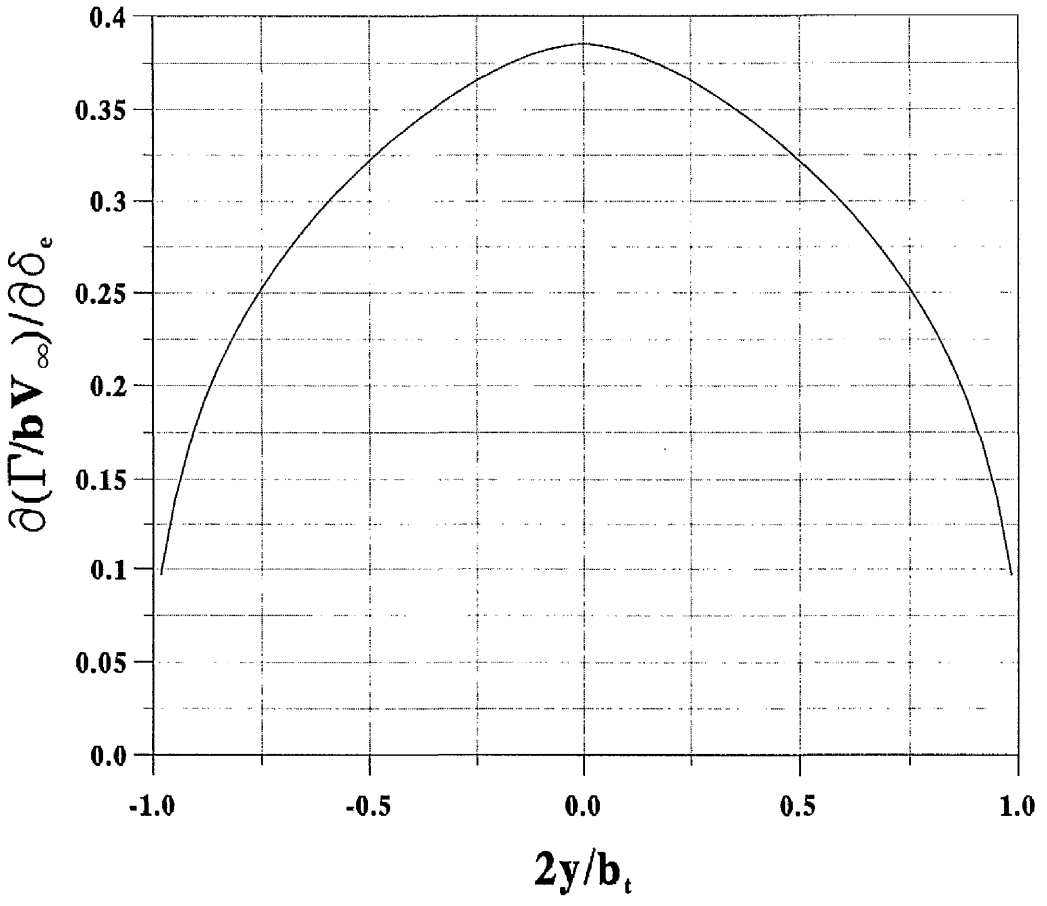

Figure 4.16: Circulation distribution over the tailplane due to elevator deflection.

Chapter 5

Lateral Aerodynamic Interference and Stability and Control in Air-to-Air Refuelling of Hercules from KC10 Tanker

This chapter analyses the lateral aerodynamic interference and stability and control of a Hercules MK3 receiver aircraft refuelling in flight from a KC10 tanker.

As described in chapter 1, during flight tests the Hercules receiver aircraft was found to be subjected to a directional wandering or lateral oscillation behind certain tanker aircraft such as the Tristar. Significant rudder activity was required to maintain the amplitude of the yawing oscillation low enough for a successful

refuelling. The directional wandering of the Hercules was judged to be unacceptable in flight behind heavy Tristar or KC10 tanker aircraft at low speed. The Hercules receiver aircraft also experienced a loss of directional stability, defined by rudder angle required to trim in a steady sideslip, which increased as the tanker lift coefficient increased.

The additional aerodynamic forces and moments produced on the Hercules receiver due to its position and attitude within the KC10 tanker vortex wake were determined using the aerodynamic models described in section 2.4. Small side, bank and yaw displacements from the datum position, which is with zero sideslip and wings level on the centre line of the tanker wing wake, were considered with the forces and moments expressed in terms of aerodynamic derivatives. For comparison these derivatives were obtained for both the flat vortex sheet and the vortex sheet with roll-up models of the tanker wing wake.

Next, in order to predict the loss of directional stability observed in flight tests, trim of the receiver in steady sideslip was considered in both free air and air-to-air refuelling with the nose of the receiver or its centre of gravity on the centre line of the tanker wake.

Finally, having obtained the aerodynamic derivatives of the Hercules in free air (see chapter 4) and the additional aerodynamic derivatives in air-to-air refuelling, the dynamic stability characteristics of the receiver were determined at a typical set of flight conditions using the linearised equations of motion. For comparison the dynamic stability characteristics of the receiver, which are expressed in terms of eigenvalues and eigenvectors, were determined for both free air and air-to-air

refuelling cases.

5.1 Flight Conditions and Aircraft Data

As described by Bradley [5] the flight envelopes of jet tanker aircraft and the Hercules turbo-prop aircraft have a relatively small overlap. Therefore the tanker is required to fly near its minimum speed with the receiver aircraft operating near its maximum speed. The Hercules receiver is considered refuelling in flight from the KC10 tanker at a typical altitude of 3.05 km (10,000 ft) and a flight Mach number of 0.347 corresponding to an equivalent airspeed of 97.8 m/s (190 knots). The tanker mass is taken as 1.76×10^5 kg (3.87×10^5 lb) giving a lift coefficient of 0.8. The mass of the Hercules receiver aircraft is taken as 0.48×10^5 kg (1.07×10^5 lb) corresponding to a lift coefficient of 0.5. Figure 5.1 shows the two aircraft at a typical horizontal separation distance of almost one tanker wing span as measured between the aircraft datum positions. The geometric data of the KC10 tanker wing and the Hercules receiver aircraft are obtained from references [55] and [6], respectively. Figures 5.2 and 4.2 in chapter 4 show the planforms of the KC10 wing and the Hercules wing, tailplane and fin used in the VLM computer program, respectively. All other relevant tanker and receiver aircraft data are given in table 5.1.

5.2 Aerodynamic Interference Model

The KC10 tanker aircraft is represented by its main wing with the trailing vortex wake modelled using either the 3-D roll-up or flat vortex sheet models. The tanker fuselage is not included in the aerodynamic model although the experimental results given by Bloy and Lea [56] indicate that its effect is small. Bloy and Lea measured the directional stability of a receiver aircraft model behind a tanker wing with and without the fuselage attached. When attached to the fuselage, the tanker wing was set low on the fuselage at a representative setting of 4°. Measurements taken by yawing the receiver with and without the tanker fuselage present show little difference.

The induced aerodynamic forces and moments on the receiver wing due to the tanker wing wake were estimated using the aerodynamic model described in section 2.4.1, with the tanker and receiver wings each represented by 60 spanwise and 4 chordwise panels whereas the induced aerodynamic loads on the receiver tailplane and fin were calculated using the aerodynamic model explained in section 2.4.2, with 30 spanwise and 4 chordwise panels used on the fin and each half of the tailplane. The distributed load along the receiver fuselage is modelled by forces and moments at the receiver centre of gravity position. These forces and moments were calculated using the ESDU data sheet for a fuselage in sideslip with a mean sideslip determined from components of the tanker induced downwash and sidewash at the receiver centre of gravity position as described below.

The effect of side displacement of the receiver from the centre line of the tanker

wake is to induce sidewash over the receiver aircraft. The interference between the tanker sidewash and the receiver high wing also induces additional sidewash at the receiver fin. Hence, the fuselage contributions to the side force, yawing and rolling moment due to side displacement derivatives are given by the following approximate expressions derived in appendix E

$$\left(C_{l_{y/b_R}}\right)_{Fuselage} = -\left(J_W - 1\right)\frac{\partial \sigma_T}{\partial\left(\frac{y}{b_R}\right)}\left(C_{l_\beta}\right)_{Fin} - \frac{\partial \sigma_T}{\partial\left(\frac{y}{b_R}\right)}\left(C_{l_\beta}\right)_{Fuselage} \tag{5.1}$$

$$\left(C_{n_{y/b_R}}\right)_{Fuselage} = -\left(J_W - 1\right)\frac{\partial \sigma_T}{\partial\left(\frac{y}{b_R}\right)}\left(C_{n_\beta}\right)_{Fin} - \frac{\partial \sigma_T}{\partial\left(\frac{y}{b_R}\right)}\left(C_{n_\beta}\right)_{Fuselage} \tag{5.2}$$

$$\left(C_{Y_{y/b_R}}\right)_{Fuselage} = -\left(J_W - 1\right)\frac{\partial \sigma_T}{\partial\left(\frac{y}{b_R}\right)}\left(C_{Y_\beta}\right)_{Fin} - \frac{\partial \sigma_T}{\partial\left(\frac{y}{b_R}\right)}\left(C_{Y_\beta}\right)_{Fuselage} \tag{5.3}$$

where the fin and fuselage contributions to the derivatives C_{l_β}, C_{n_β} and C_{Y_β} were determined in free air as described in chapter 4 and appendix C, respectively.

As in the side displacement case, the effect of the fuselage following a bank displacement is twofold. Firstly there is a side force on the fuselage due to the component of the tanker downwash along the lateral axis of the receiver and secondly this flow component acting on the high wing induces a sidewash at the fin. Thus, the fuselage contributions to the side force, yawing and rolling moment due to bank displacement derivatives are given by the following approximate expressions explained in appendix E.

$$\left(C_{l_\phi}\right)_{Fuselage} = -\left(J_W - 1\right)\epsilon_T\left(C_{l_\beta}\right)_{Fin} - \epsilon_T\left(C_{l_\beta}\right)_{Fuselage} \tag{5.4}$$

$$\left(C_{n_\phi}\right)_{Fuselage} = -\left(J_W - 1\right)\epsilon_T\left(C_{n_\beta}\right)_{Fin} - \epsilon_T\left(C_{n_\beta}\right)_{Fuselage} \tag{5.5}$$

$$\left(C_{Y_\phi}\right)_{Fuselage} = -\left(J_W - 1\right)\epsilon_T\left(C_{Y_\beta}\right)_{Fin} - \epsilon_T\left(C_{Y_\beta}\right)_{Fuselage} \tag{5.6}$$

The fuselage effect following a yaw displacement is determined by noting that the sidewash distribution along the fuselage is similar to that induced by yawing motion of the aircraft. This implies that the fuselage contribution to yawing moment due to yaw displacement derivative is related to the fuselage contribution to C_{n_r} by the following equation described in appendix E.

$$(C_{n_\psi})_{Fuselage} = -\frac{\partial \sigma_T}{\partial\left(\frac{2y}{b_R}\right)}(C_{n_r})_{Fuselage} \tag{5.7}$$

where the fuselage contribution to C_{n_r}, the yawing moment due to rate of yaw derivative, is found from the ESDU data sheet [44]. The associated side force and rolling moment derivatives due to yaw displacement are neglected.

In order to apply the 3-D roll-up model described in section 2.3 to the KC10 tanker wing wake, a number of parameters must be decided first. The parameters of interest are the downstream step size, number of trailing vortex legs, the use of equal strength or equally spaced trailing vortices and the smoothing factor. West [24] investigated the effects of these parameters on the behaviour of the vortex sheet model. In order to quantify the effects of varying step length, West determined the centreline displacement of the vortex sheet of the tapered wing used in chapter 3 at a specific downstream distance for various values of the step length. It was found that this displacement increased as the step length increased with the vertical displacement converging at a step length of $\bar{c}/8$. Typically 80 trailing vortex legs should be used in order to produce sufficient detail of roll-up in the wing tip vortices. The use of equal strength or equally spaced trailing vortices was found to give the same induced velocities with more detail of roll-up present in the wing tip spirals using the equal strength trailing vortices. For the smoothing factor, West [24]

suggested that an optimum value could be obtained in an empirical way by looking at the number of non-chaotic turns of the tip vortex spiral at a specific downstream station. Figure 5.3 shows slices through the KC10 wing vortex wake in the yz plane at a downstream position of x/b_T=4 for δ_k=0.02, 0.025, 0.03 and 0.05. A small smoothing factor produces instabilities in the calculations at a spanwise position of $y/b_T = 0.2$ and in the tip vortex core region as shown in figure 5.3a. Increasing the smoothing factor eliminates the instabilities but results in a reduction in the tip vortex spiral detail as shown in figures 5.3c and d. Based on the number of non-chaotic turns in the tip spiral, figure 5.3b gives the optimum smoothing factor δ_k=0.025 at the downstream position $x/b_T = 4$. The optimum value for the smoothing factor δ_k varies with downstream distance, increasing as the strength of the tip vortices increases. However West found that this variation of the smoothing factor for downstream distances relevant to air-to-air refuelling is insignificant and a constant value of δ_k is quite acceptable. The effect of the smoothing factor on the induced downwash and sidewash over the receiver wing is negligible as shown in figures 5.4 and 5.5, respectively. It follows that the calculated aerodynamic loads are also relatively insensitive to the value of δ_k.

The KC10 tanker wing is considered at a lift coefficient of 0.8 with the resulting spanwise circulation distribution as shown previously in figure 2.17. Typically 120 equal strength trailing vortices are used for the wing wake model. Figure 5.6 shows the development of the wake in the downstream direction using a smoothing factor of 0.025 and a downstream step size equal to 1/8th of the wing mean chord. The roll-up calculations are carried out to about $4\frac{1}{2}$ wing spans downstream since

this provides sufficient accuracy in the estimation of the induced velocities over the receiver aircraft [24]. The roll-up process is clearly illustrated and at a downstream distance of $x/b_T = 2.045$ the tip spirals are well defined. Once again the wing tip spirals can be seen to remain in the same horizontal plane while the centre of the vortex sheet is deflected downwards.

Figure 5.7 shows plan and side views of the KC10 wing vortex wake. It can be seen that at downstream distances greater than $x/b_T = 3.3$ and spanwise positions of $y/b_T = \pm 0.2$, there is evidence of the instability problem described by Krasny [40]. This instability was also observed to a much smaller degree for the tapered wing given in chapter 3. However the instability problem is not present to any degree in the region downstream of the tanker wing where the receiver is located, viz. 1.04 times the tanker wing span downstream. As described in chapter 3, figure 5.7a can be used to obtain an estimation of the relative distribution of vorticity between the tip spirals and the vortex sheet. Thus at a distance of one wing span downstream, it is estimated that 43% of the circulation at the centre line is rolled up in the tip spirals leaving 57% of the total circulation in the vortex sheet. Figure 5.8 shows a three-dimensional view of the KC10 tanker wing wake roll-up.

For comparison the tanker wing induced velocities over the receiver aircraft are determined from the flat vortex sheet, used previously by Bloy et al [19] and Hoganson [6], and the present vortex sheet with roll-up of the tanker wing wake. Typical distributions of downwash at the receiver wing and sidewash at the receiver fin using both models are shown in figures 5.9 and 5.10, respectively. The downwash

and sidewash obtained from the roll-up and flat vortex sheet models can be explained by comparing the wing wake used by the two models. The flat vortex sheet model assumes that the trailing vortices are all shed horizontally in the same plane. However, for the roll-up model the wing tip vortices remain practically in the same horizontal plane whereas the centre of the wing wake is deflected downwards as described above. The vertical displacement of the centre line of the KC10 wing wake was found to be $z/b_T = 0.128$ and $z/b_T = 0.158$ at the receiver wing and fin positions, respectively. Therefore, the flat vortex sheet model effectively increases the vertical separation between tanker wing wake and the receiver aircraft. Consequently the downwash and sidewash are higher for the roll-up model than for the flat vortex sheet model at values of the vertical separation below the rolled up wing wake.

5.3 Aerodynamic Interference Results

The induced lateral aerodynamic forces and moments on the receiver due to tanker wing wake depend on the side displacement and bank and yaw attitudes of the receiver. The rolling moment is mainly due to the change in downwash on the receiver wing following a side or bank displacement whereas the side force and yawing moment are mainly due to the sidewash at the receiver fin following a side or yaw displacement and the component of downwash normal to the fin following a bank displacement. The arrangements of tanker and receiver aircraft during positive side, bank and yaw displacements have been shown previously in figures 2.24a, b

and c, respectively.

During a typical refuelling operation, the displacements of the receiver aircraft from the datum refuelling position, which is approximately one tanker wing span behind the tanker and 1/4 tanker wing span below, are relatively small. The variation of the receiver aerodynamic forces and moments with small side, bank and yaw displacements from the datum position are essentially linear. This is illustrated in figures 5.11, 5.12 and 5.13 for side, bank and yaw displacements, respectively, at $z/b_T = 0.21$. This allows the aerodynamic loads to be expressed in terms of aerodynamic derivatives. There are nine of these derivatives due to the interference effect between tanker and receiver. As usual the aerodynamic derivatives are determined at the datum position.

For comparison, the additional aerodynamic derivatives of the receiver were obtained for both the roll-up and flat vortex sheet models of the tanker wing wake. The total values of the derivatives obtained from both models are then presented together with the breakdown of the receiver contributions due to wing, fin, tailplane and fuselage obtained from the more realistic roll-up model.

5.3.1 Side Displacement of the Receiver Aircraft

Rolling Moment Derivative $\partial C_l/\partial\,(y/b_R)$

The effect of positive side displacement is to increase the downwash on the port wing and tailplane and reduce the downwash on the starboard wing and tailplane. The resulting rolling moment due to side displacement is then negative and causes

the receiver to roll so that the lift vector in inclined to the port side, tending to return the receiver to the centreline position. This is a stable response. Figure 5.14 shows the variation of receiver rolling moment due to side displacement derivative with vertical separation. As described in chapter 3, this derivative depends on the downwash gradient in the spanwise direction (i.e. $d\epsilon/dy$) shown in figures 5.15a and b for both the roll-up and flat vortex sheet models, respectively. Figures 5.15a and b show that below the rolled up wake, the downwash gradient (i.e. $d\epsilon/dy$) is higher for the roll-up model than for the flat vortex sheet model resulting in a higher magnitude of the rolling moment derivative for the roll-up model. At a typical contact position during refuelling in the region of $z/b_T = 0.24$, the roll-up model gives a value of the derivative which is 55% higher in magnitude compared with that from the flat vortex sheet model.

Figure 5.14 indicates that the receiver fin, tailplane and fuselage contributions to the rolling moment derivative are very small compared to the wing contribution. The fin and fuselage contributions are destabilising acting in the opposite direction to the contributions from the wing and tailplane.

Side Force Derivative $\partial C_Y/\partial\,(y/b_R)$

The variation of receiver side force derivative with vertical separation is shown in figure 5.16. The side force is mainly due to the effect of the sidewash from the tanker wing wake at the receiver fin and fuselage with a small secondary contribution from the receiver wing. This latter contribution is associated with the modified lift distribution on the receiver wing in the presence of the tanker. The tanker wing

sidewash produces a maximum side force on the fin when the tip of the fin touches the tanker wing wake which agrees with the experimental data given in chapter 3. This is also in agreement with the experimental data given by Bloy and Lea [56]. Thus the position of the maximum value of the fin side force depends on the wake deflection. For the roll-up and flat vortex sheet models the maximum values of the fin side force were found to be in the regions of $z/b_T = 0.24$ and $z/b_T = 0.09$, respectively.

Figure 5.16 shows that the fuselage makes a significant contribution to the side force derivative. At a typical refuelling separation of $z/b_T = 0.24$, the fuselage contribution was found to be 18.6% of the total side force derivative. Below the tanker wing wake, the fin and fuselage contributions both act in a destabilising sense tending to increase the side displacement.

Yawing Moment Derivative $\partial C_n/\partial\,(y/b_R)$

Figure 5.17 shows the variation of receiver yawing moment due to side displacement derivative with vertical separation. This derivative is less significant than the rolling moment derivative. The main contributions to the yawing moment are due to the effect of the tanker sidewash on the receiver fin and fuselage with a small contribution due to the differential drag on the receiver wing which acts in a stabilising sense. The roll-up model can be seen to give a maximum value of the yawing moment which is almost the same as that for the flat vortex sheet model. Below the tanker wing wake, the yawing moment derivative is stabilising tending to point the nose of the receiver towards the tanker aircraft.

The fin and fuselage contributions to the yawing moment derivative are similar in form to those of the side force derivative. Again the fuselage produces a significant contribution which is in magnitude 37% of the fin contribution at the typical refuelling position of $z/b_T = 0.24$, with the two contributions acting in opposite directions.

5.3.2 Bank Displacement of the Receiver Aircraft

Rolling Moment Derivative $\partial C_l/\partial \phi$

Below the tanker wing wake, positive bank displacement has the same effect as a positive side displacement. The downwash over the port wing is increased as it moves up towards the tanker wing wake, while that over the starboard wing is reduced. This produces a negative stabilising rolling moment which tends to return the receiver to the level position. Figure 5.18 shows the variation of the rolling moment due to bank displacement derivative with vertical separation. This derivative depends mainly on the downwash gradient in the vertical direction i.e. $d\epsilon/dz$ which is shown in figures 5.19a and b for both the roll-up and flat vortex sheet models, respectively. Figure 5.19a indicates that this gradient changes sign from the centre line to the wing tip for low values of the vertical separation. This explains why the rolling moment derivative for the roll-up model changes sign at low values of z/b_T. Below the rolled up wake, the roll-up model predicts higher magnitudes of the gradient $d\epsilon/dz$ compared with the flat vortex sheet model as shown in figures 5.19a and b. Hence, higher values for the rolling moment derivative

are obtained from the roll-up model which gives a 34.5% increase in the magnitude of the derivative at a typical refuelling separation of $z/b_T = 0.24$.

As in the side displacement case, figure 5.18 indicates that the fin, tailplane and fuselage contributions to the rolling moment derivative are negligible compared with the wing contribution.

Side Force Derivative $\partial C_Y/\partial\phi$

The side force due to bank displacement derivative is produced by the receiver fin and fuselage. The fuselage contribution is due to the component of the tanker downwash along the lateral axis of the receiver as described in section 5.2 whereas the fin contribution is due to the components of the tanker sidewash and downwash acting normal to the receiver fin. The major contribution is from the component of tanker downwash normal to the fin. Therefore maximum side force due to bank displacement is obtained where the downwash is highest. Below the rolled up wake, the downwash is higher for the roll-up model than for the flat vortex sheet model as shown in figures 5.9a and b. This leads to higher values of the side force derivative for the roll-up model as shown in figure 5.20. The fuselage contribution is again significant and acts with the fin in a destabilising sense tending to move the receiver away from the tanker centreline.

Yawing Moment Derivative $\partial C_n/\partial\phi$

The variation of receiver yawing moment derivative with vertical separation is given in figure 5.21. This derivative is small compared with the rolling moment and side

force derivatives. It is mainly due to the receiver fin and fuselage with a small contribution from the differential drag on the receiver wing.

5.3.3 Yaw Displacement of the Receiver Aircraft

As described in chapter 3, receiver wing loading is practically unaffected by yawing the receiver. Therefore the forces and moments acting on the receiver aircraft following a yaw displacement are only due to the effect of the tanker wing wake on the receiver fin, tailplane and fuselage.

Side Force Derivative $\partial C_Y/\partial\psi$

The variation of receiver side force derivative with vertical separation is shown in figure 5.22. The side force is entirely due to the tanker induced sidewash at the receiver fin. Below the tanker wing wake, the side force is destabilising tending to increase the yaw displacement. However, as shown in figure 5.10a the sidewash at the receiver fin changes direction as the fin moves above the rolled up wing wake at low values of vertical separation. This produces a stabilising effect for z/b_T less than 0.13. The peak values of the side force derivative occur at $z/b_T = 0.24$ and $z/b_T = 0.09$ for the roll-up and flat vortex sheet models, respectively. These correspond to the tip of the fin touching the tanker wing wake as discussed in the side displacement case. Figure 5.22 shows that the roll-up model gives a peak value 14.5% less in magnitude than that obtained from the flat vortex sheet model.

Yawing Moment Derivative $\partial C_n/\partial\psi$

The receiver yawing moment due to yaw displacement derivative given in figure 5.23 is again due mainly to the fin. The yawing moment is only slightly affected by the receiver fuselage as shown in figure 5.23. This agrees with the experimental results given by Bloy and Lea [56]. Below the tanker wing wake, the yawing moment acts in a destabilising sense which results in a reduction in the directional stability of the receiver aircraft. The loss of directional stability in yaw was also observed by Bradley in flight tests. Figure 5.23 shows that the roll-up model gives a peak value 14.9% less than that obtained from the flat vortex sheet model.

Rolling Moment Derivative $\partial C_l/\partial\psi$

This derivative is negligible compared with the rolling moment due to side and bank displacement derivatives. It is due to the tanker induced sidewash and downwash on the receiver fin and tailplane, respectively. Figure 5.24 shows the variation of receiver rolling moment due to yaw displacement derivative. Below the rolled up wake, the tailplane and fin contributions are similar in magnitude and act in opposite directions.

5.4 Trim of Receiver Aircraft in Steady Sideslip

The trim of an aircraft in steady sideslip relates to its lateral and directional static stability and control characteristics. In both free air and air-to-air refuelling the

aircraft is banked and the ailerons and rudder are deflected to counteract the side forces, rolling and yawing moments due to sideslip.

In free air the trim of the receiver is given by the usual linearised equations which describe the balance of the side forces, rolling and yawing moments. These equations are given in non-dimensional form by [47]

$$\begin{bmatrix} C_{Y_\beta} & C_L & C_{Y_{\delta_a}} & C_{Y_{\delta_r}} \\ C_{l_\beta} & 0 & C_{l_{\delta_a}} & C_{l_{\delta_r}} \\ C_{n_\beta} & 0 & C_{n_{\delta_a}} & C_{n_{\delta_r}} \end{bmatrix} \begin{bmatrix} \beta \\ \phi \\ \delta_a \\ \delta_r \end{bmatrix} = \begin{bmatrix} 0 \end{bmatrix} \tag{5.8}$$

The values of the aerodynamic derivatives that appear in equations 5.8 are given previously in table 4.6. These derivatives are estimated at the flight conditions specified in section 5.1 by using linear VLM, ESDU data sheets and approximate methods as described in chapter 4.

In air-to-air refuelling the trim equations include additional terms due to the bank and yaw attitudes of the receiver and its lateral position in the vortex wake of the tanker. The trim of the receiver in steady sideslip behind the tanker is considered in two cases. Firstly the receiver centre of gravity is kept on the centre line of the tanker wake with the angle of yaw equal to minus the sideslip angle as shown in figure 5.25a. The corresponding trim equations in non-dimensional form are given

by

$$\begin{bmatrix} C_{Y_\beta} & C_{Y_\phi}+C_L & C_{Y_\psi} & C_{Y_{\delta_a}} & C_{Y_{\delta_r}} \\ C_{l_\beta} & C_{l_\phi} & C_{l_\psi} & C_{l_{\delta_a}} & C_{l_{\delta_r}} \\ C_{n_\beta} & C_{n_\phi} & C_{n_\psi} & C_{n_{\delta_a}} & C_{n_{\delta_r}} \end{bmatrix} \begin{bmatrix} \beta \\ \phi \\ \psi \\ \delta_a \\ \delta_r \end{bmatrix} = \begin{bmatrix} 0 \end{bmatrix} \tag{5.9}$$

where

$$\psi = -\beta$$

Secondly the nose of the receiver aircraft is assumed to remain on the centreline of the tanker wake as the receiver is yawed as shown in figure 5.25b. The yaw angle is again equal to minus the sideslip angle and the side displacement of the centre of gravity is equal to minus the yaw angle times the distance from the nose of the aircraft to the centre of gravity position. The relevant trim equations which include the additional side displacement terms are given in non-dimensional form by

$$\begin{bmatrix} C_{Y_\beta} & C_{Y_\phi}+C_L & C_{Y_\psi} & C_{Y_{y/b_R}} & C_{Y_{\delta_a}} & C_{Y_{\delta_r}} \\ C_{l_\beta} & C_{l_\phi} & C_{l_\psi} & C_{l_{y/b_R}} & C_{l_{\delta_a}} & C_{l_{\delta_r}} \\ C_{n_\beta} & C_{n_\phi} & C_{n_\psi} & C_{n_{y/b_R}} & C_{n_{\delta_a}} & C_{n_{\delta_r}} \end{bmatrix} \begin{bmatrix} \beta \\ \phi \\ \psi \\ y/b_R \\ \delta_a \\ \delta_r \end{bmatrix} = \begin{bmatrix} 0 \end{bmatrix} \tag{5.10}$$

where

$$\psi = -\beta \quad and \quad \frac{y}{b_R} = -\psi \frac{l_{cg}}{b_R}$$

where l_{cg} is the distance from the nose of the receiver aircraft to the centre of gravity position. The receiver additional aerodynamic derivatives that appear in equations 5.9 and 5.10, viz. C_{l_ϕ}, C_{Y_ϕ}, C_{n_ϕ}, C_{l_ψ}, C_{Y_ψ}, C_{n_ψ}, $C_{l_{y/b}}$, $C_{Y_{y/b}}$, and $C_{n_{y/b}}$, have been estimated in the previous section.

By solving equations 5.8, 5.9 and 5.10 for the angle of bank ϕ, aileron deflection δ_a and rudder deflection δ_r in terms of β, values for the gradients $\partial\phi/\partial\beta$, $\partial\delta_r/\partial\beta$ and $\partial\delta_a/\partial\beta$ can be obtained. These gradients are obtained over the range of vertical separation of interest. Figures 5.26a and b show the variations of the gradients $\partial\phi/\partial\beta$, $\partial\delta_r/\partial\beta$ and $\partial\delta_a/\partial\beta$ with vertical separation for both steady sideslip cases, where the receiver centre of gravity is considered on and off the centre line of the tanker wake, respectively. Compared with the free air case, the angle of bank in air-to-air refuelling is similar; the aileron angle is two to three times larger and the rudder angle is much less. For the steady sideslip case where the receiver centre of gravity is off the tanker wake centre line, the minimum value of the rudder angle in air-to-air refuelling is 21% of that required in free air. This implies a loss of directional stability of the receiver. The reduction in the required rudder angle is associated with the yawing moments due to yaw, bank and side displacements in steady sideslip which are equally significant acting in the same direction. The results are consistent with the flight test data given by Bradley [7]. In [7] the trim of a Hercules receiver aircraft in steady sideslip was considered in free air and when refuelling in flight from a Tristar tanker with 4° tanker flap deflection. Compared with the free air case, it was found that the rudder angle to trim is reduced by 100%; the aileron angle is 2.72 times higher and the bank angle is similar.

For both steady sideslip cases with the receiver centre of gravity off and on the tanker wake centre line, the variations of the gradients $\partial\phi/\partial\beta$, $\partial\delta_r/\partial\beta$ and $\partial\delta_a/\partial\beta$ with vertical separation are similar although displacing the receiver centre of gravity off the tanker wake centre line enhances the difference between the free air and air-to-air refuelling cases. The aileron angle is increased in magnitude and the rudder angle is decreased compared with the steady sideslip case where the receiver centre of gravity is on the tanker wake centre line.

5.5 Lateral Dynamic Stability

5.5.1 Linearised Equations of Motion

During air-to-air refuelling the receiver aircraft is kept close to the datum refuelling position with the wings almost level on the centre line of the tanker wing wake. It is therefore reasonable to use the linearised equations of motion for initially steady, straight horizontal flight to analyse the dynamic stability of the receiver.

The equations of motion in free air uncouple into two independent sets which describe the longitudinal and lateral motion. The lateral equations of motion, for fixed controls and with Ox initially horizontal, are given in non-dimensional form by [47]

$$\begin{bmatrix} (2\mu D - C_{Y_\beta}) & (-C_{Y_p}D - C_L) & (2\mu D - C_{Y_r}D) \\ -C_{l_\beta} & (i_A D^2 - C_{l_p}D) & (i_E D^2 - C_{l_r}D) \\ -C_{n_\beta} & (i_E D^2 - C_{n_p}D) & (i_C D^2 - C_{n_r}D) \end{bmatrix} \begin{bmatrix} \beta \\ \phi \\ \psi \end{bmatrix} = \begin{bmatrix} 0 \end{bmatrix} \quad (5.11)$$

These equations are based on the aerodynamic body axes, Oxyz, shown in figure 5.27.

The equations of motion in air-to-air refuelling include additional aerodynamic derivatives due to the position (x,y,z) and attitude (ϕ, θ, ψ) of the receiver within the tanker wake. The additional aerodynamic derivatives are C_{X_i}, C_{Y_i}, C_{Z_i}, C_{l_i}, C_{m_i} and C_{n_i}, where i represents x, y, z, ϕ, θ and ψ. Since the aircraft is symmetrical about its longitudinal plane Oxz, small symmetric disturbances (i.e. x, z and θ) can not produce asymmetric forces. Hence, the additional lateral derivatives C_{Y_i}, C_{l_i} and C_{n_i}, where i represents x, z and θ are all zero. As in the free air case, small asymmetric disturbances (i.e. y, ϕ and ψ) do not produce symmetric forces. Thus, the additional longitudinal derivatives C_{X_i}, C_{Z_i} and C_{m_i}, where i represents y, ϕ and ψ, are also zero.

Therefore, the equations of motion in air-to-air refuelling can be also uncoupled into two separate sets describing longitudinal and lateral motion. The lateral equations of motion, for fixed controls and with Ox initially horizontal, are given in non-dimensional form by

$$\begin{bmatrix} (2\mu D - C_{Y_\beta}) & (-C_{Y_p} D - C_L - C_{Y_\phi}) & (2\mu D - C_{Y_r} D - C_{Y_\psi}) & -C_{Y_{\frac{y}{b_R}}} \\ -C_{l_\beta} & (i_A D^2 - C_{l_p} D - C_{l_\phi}) & (i_E D^2 - C_{l_r} D - C_{l_\psi}) & -C_{l_{\frac{y}{b_R}}} \\ -C_{n_\beta} & (-i_E D^2 - C_{n_p} D - C_{l_\phi}) & (i_C D^2 - C_{n_r} D - C_{n_\psi}) & -C_{n_{\frac{y}{b_R}}} \\ -1 & 0 & -1 & 2D \end{bmatrix} \begin{bmatrix} \beta \\ \phi \\ \psi \\ \frac{y}{b_R} \end{bmatrix}$$

$$= \begin{bmatrix} 0 \end{bmatrix} \qquad (5.12)$$

5.5.2 Calculating the Characteristic Modes

In order to determine the aircraft characteristic modes, the equations of motion are written in first order form as the generalised eigenproblem

$$Ax = \lambda Bx \tag{5.13}$$

where A and B are real square matrices, λ is the eigenvalue and x is the eigenvector. The solution of equation 5.13 provides the aircraft characteristic modes in terms of eigenvalues and eigenvectors. The eigenvalues (or characteristic roots) give the magnitude of the modes while the eigenvectors (or mode shapes) indicate the nature or shape of the modes. Negative and positive real roots describe subsidence and divergent modes, respectively. Complex roots with negative and positive real parts correspond to damped and undamped oscillations, respectively. A typical oscillatory mode is given in the form

$$\lambda = -k \pm i\nu$$

where k is the damping index and ν is the damped frequency of the oscillation. The period and the time to half or double amplitude of an oscillatory mode are given by

$$Period = \frac{2\pi}{\nu}$$

$$Time = \frac{\ln 2}{\mid k \mid}$$

Thus, the equations of motion in both free air and air-to-air refuelling are solved by expressing them in the form given by equation 5.13, where the matrices A, B

and x, for the free air case, are given by

$$\left[A \right] = \begin{bmatrix} -C_{Y_\beta} & -C_{Y_p} & -C_L & (2\mu - C_{Y_r}) & 0 \\ -C_{l_\beta} & -C_{l_p} & 0 & -C_{l_r} & 0 \\ 0 & -1 & 0 & 0 & 0 \\ -C_{n_\beta} & -C_{n_p} & 0 & -C_{n_r} & 0 \\ 0 & 0 & 0 & -1 & 0 \end{bmatrix}$$

$$\left[B \right] = \begin{bmatrix} -2\mu & 0 & 0 & 0 & 0 \\ 0 & -i_A & 0 & i_E & 0 \\ 0 & 0 & -1 & 0 & 0 \\ 0 & i_E & 0 & -i_C & 0 \\ 0 & 0 & 0 & 0 & -1 \end{bmatrix}$$

$$\left[x \right] = \begin{bmatrix} \beta \\ \hat{p} \\ \phi \\ \hat{r} \\ \psi \end{bmatrix}$$

For the air-to-air refuelling case, the matrices A, B and x are given by

$$\left[A \right] = \begin{bmatrix} -C_{Y_\beta} & -C_{Y_p} & (-C_L - C_{Y_\phi}) & (2\mu - C_{Y_r}) & -C_{Y_\psi} & -C_{Y_{y/b_R}} \\ -C_{l_\beta} & -C_{l_p} & -C_{l_\phi} & -C_{l_r} & -C_{l_\psi} & -C_{l_{y/b_R}} \\ 0 & -1 & 0 & 0 & 0 & 0 \\ -C_{n_\beta} & -C_{n_p} & -C_{n_\phi} & -C_{n_r} & -C_{n_\psi} & -C_{n_{y/b_R}} \\ 0 & 0 & 0 & -1 & 0 & 0 \\ -1 & 0 & 0 & 0 & -1 & 0 \end{bmatrix}$$

$$\left[B \right] = \begin{bmatrix} -2\mu & 0 & 0 & 0 & 0 & 0 \\ 0 & -i_A & 0 & i_E & 0 & 0 \\ 0 & 0 & -1 & 0 & 0 & 0 \\ 0 & i_E & 0 & -i_C & 0 & 0 \\ 0 & 0 & 0 & -1 & 0 & 0 \\ 0 & 0 & 0 & 0 & 0 & -2 \end{bmatrix}$$

$$\left[x \right] = \begin{bmatrix} \beta \\ \hat{p} \\ \phi \\ \hat{r} \\ \psi \\ y/b_R \end{bmatrix}$$

The aerodynamic derivatives in free air are given in chapter 4 whereas the additional aerodynamic derivatives in air-to-air refuelling are described in section 5.3.

For both free air and air-to-air refuelling cases, the eigenvalues and eigenvectors were obtained using an appropriate NAG subroutine, viz. F02BJF.

5.5.3 Dynamic Stability Results

First the lateral characteristic modes of the Hercules are obtained in free air at the flight conditions given in section 5.1. These modes correspond to the Dutch roll oscillation, spiral and roll subsidence with eigenvalues and eigenvectors given in figure 5.28. Note that each eigenvector is normalised so that the component of

the largest modulus is real and the sum of the squares of the moduli equal one.

Next the lateral characteristic modes of the Hercules are determined in air-to-air refuelling at $z/b_T = 0.24$. This vertical separation corresponds to the condition of minimum directional stability discussed in section 5.4. The values of the additional aerodynamic derivatives of the Hercules at $z/b_T = 0.24$ are given in table 5.2. These derivatives were estimated in section 5.3 using the tanker wing wake roll up method. Figure 5.29 gives the eigenvalues and eigenvectors for the air-to-air refuelling case. Three oscillatory modes are present. These are the Dutch roll oscillation which is slightly less damped than in the free air case with a reduction in the damping index of 8.8%; a highly damped rolling oscillation and an undamped oscillation involving mainly bank and side displacement. The aircraft is therefore dynamically unstable with a divergent mode of period 12.7 s and a time to double amplitude of 3.12 s.

Since the divergent mode involves mainly bank and side displacement with relatively small variations in sideslip and yaw, an approximation to this mode can be obtained from the full lateral equations of motion, 5.12, by neglecting the yawing moment equation, sideslip and the terms ψC_{l_ψ} and rC_{l_r} in the rolling equation. The aerodynamic side forces and cross product of inertia can also be neglected. The equations of motion are then reduced to

$$\begin{bmatrix} -C_L & 2\mu D & 0 \\ (i_A D^2 - C_{l_p} D - C_{l_\phi}) & 0 & -C_{l_{\frac{y}{b_R}}} \\ 0 & -1 & 2D \end{bmatrix} \begin{bmatrix} \phi \\ \psi \\ \frac{y}{b_R} \end{bmatrix} = \begin{bmatrix} 0 \end{bmatrix} \qquad (5.14)$$

Equation 5.14 can be written in terms of y/b_R and ϕ as follows

$$\begin{bmatrix} -C_L & 4\mu D^2 \\ (i_A D^2 - C_{l_p} D - C_{l_\phi}) & -C_{l_{y/b_R}} \end{bmatrix} \begin{bmatrix} \phi \\ y/b_R \end{bmatrix} = \begin{bmatrix} 0 \end{bmatrix} \tag{5.15}$$

The resulting characteristic equation is

$$\lambda^4 - \frac{C_{l_p}}{i_A}\lambda^3 - \frac{C_{l_\phi}}{i_A}\lambda^2 - \frac{C_L C_{l_{y/b_R}}}{4\mu i_A} = 0 \tag{5.16}$$

The condition for stability requires that all the coefficients of equation 5.16, together with Routh's discriminant $R = C_L C_{l_p}^2 C_{l_{y/b_R}}/4\mu i_A^2$ to be positive [57]. Although all the coefficients are positive, Routh's discriminant is negative indicating dynamic instability. Solution of equation 5.16 resulted in $\lambda_{1,2} = -1.1 \pm 0.472i$ and $\lambda_{3,4} = 0.205 \pm 0.473i$ corresponding to the damped and undamped oscillations which are in good agreement with those obtained from the full lateral equations of motion.

Tanker Aircraft	
wing area	367.41 m^2
wing span	50.4 m
wing twist	3°
wing dihedral	4°
Receiver Aircraft	
wing area	161.81 m^2
wing span	40.41 m
wing twist	3°
wing dihedral	2.5°
inertia about Ox	2.6x10^6 kgm^2
inertia about Oz	3.8x10^6 kgm^2
product of inertia about Ox and Oz	-5.7x10^4 kgm^4

Table 5.1: KC10 tanker and Hercules receiver aircraft data.

$C_{l_{y/b_R}}$=-0.1055	$C_{n_{y/b_R}}$=-0.0291	$C_{Y_{y/b_R}}$=0.1392
$C_{l_\phi} = -0.0535\ rad^{-1}$	$C_{n_\phi} = -0.0119\ rad^{-1}$	$C_{Y_\phi} = 0.0536\ rad^{-1}$
$C_{l_\psi} = 0.0007\ rad^{-1}$	$C_{n_\psi} = 0.0183\ rad^{-1}$	$C_{Y_\psi} = -0.0507\ rad^{-1}$

Table 5.2: Hercules additional lateral aerodynamic derivatives in non-dimensional form at $z/b_T = 0.24$.

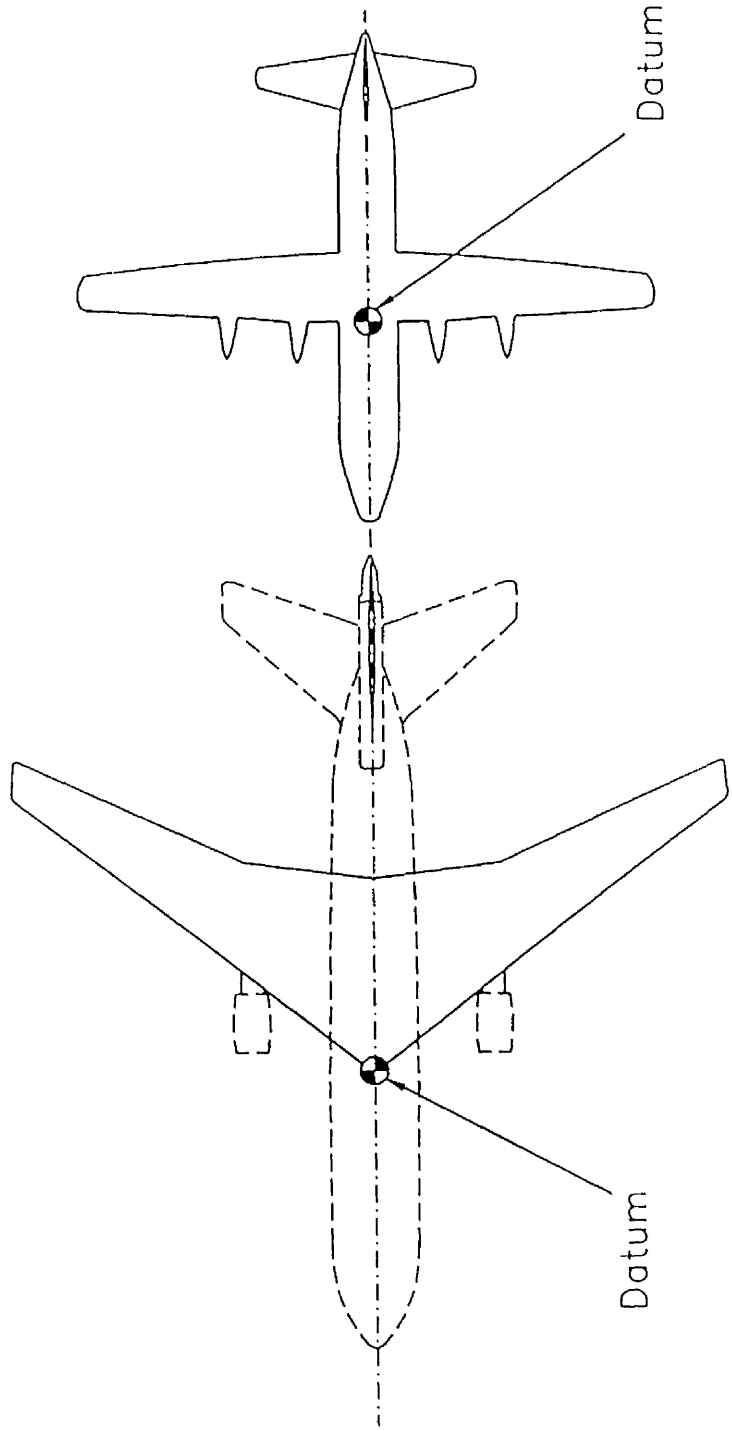

(a)

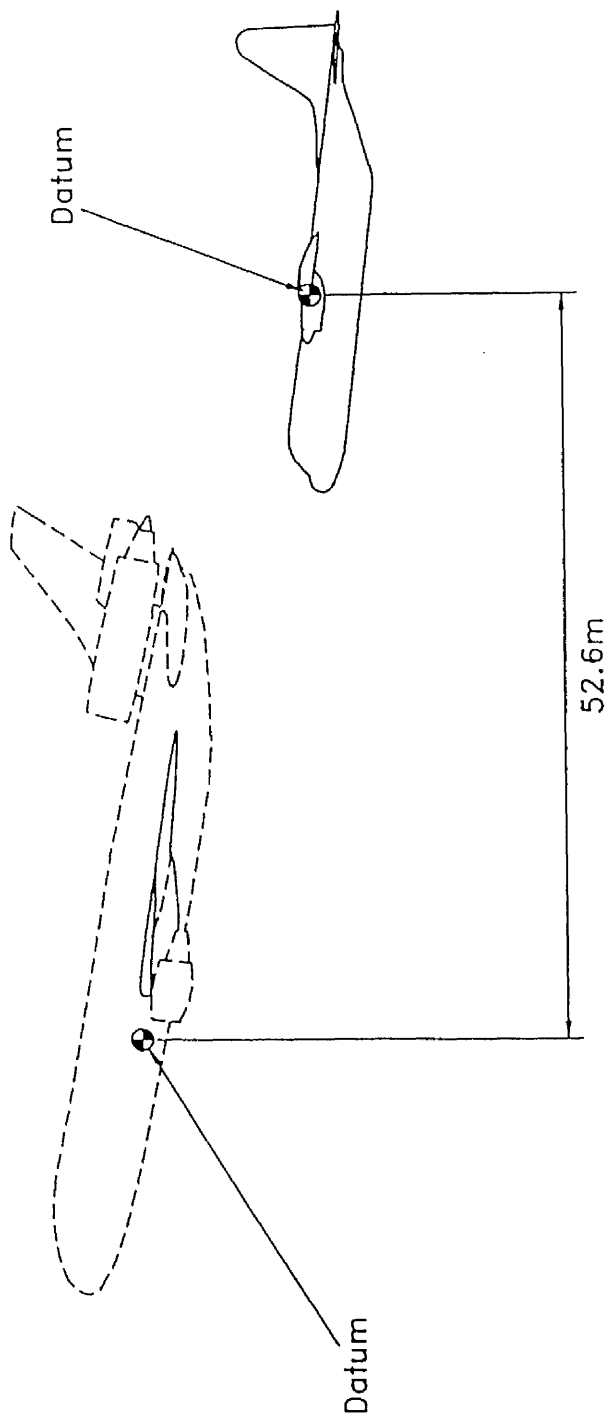

(b)

Figure 5.1: KC10 tanker/Hercules receiver aircraft.

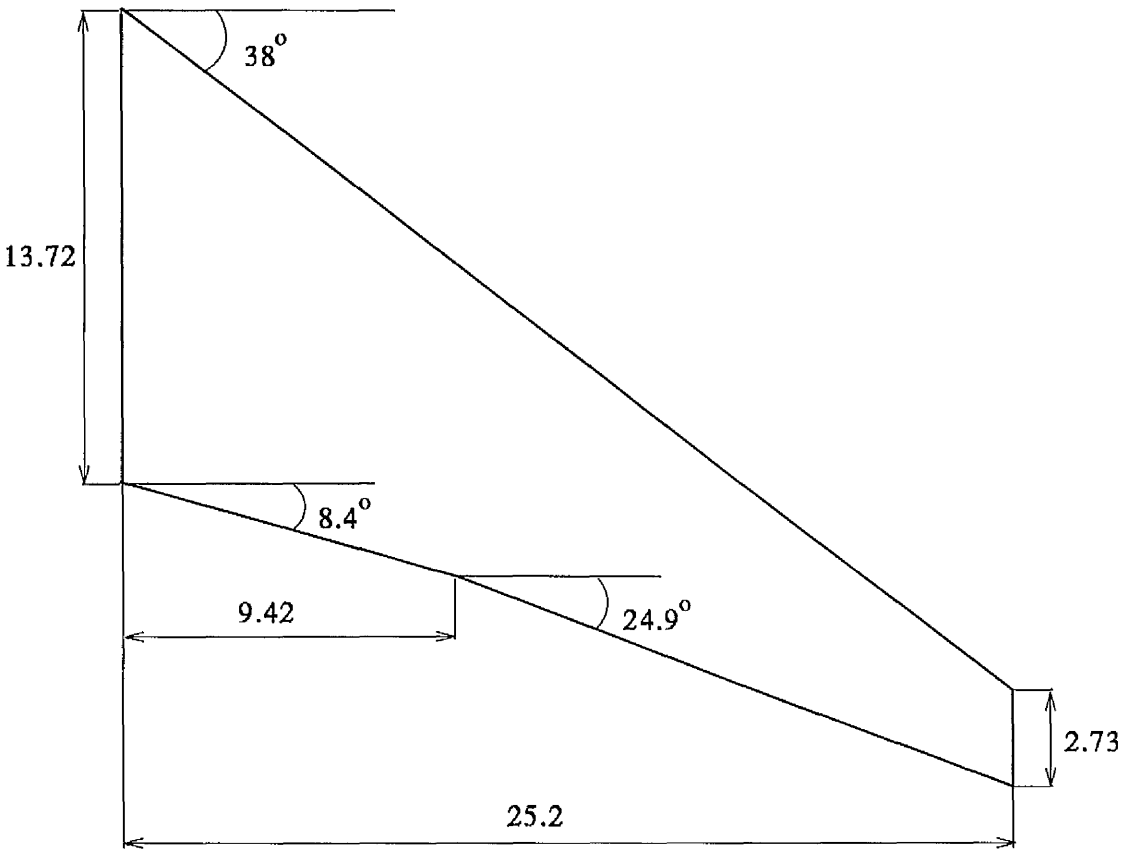

Figure 5.2: KC10 wing planform used in VLM computer program.

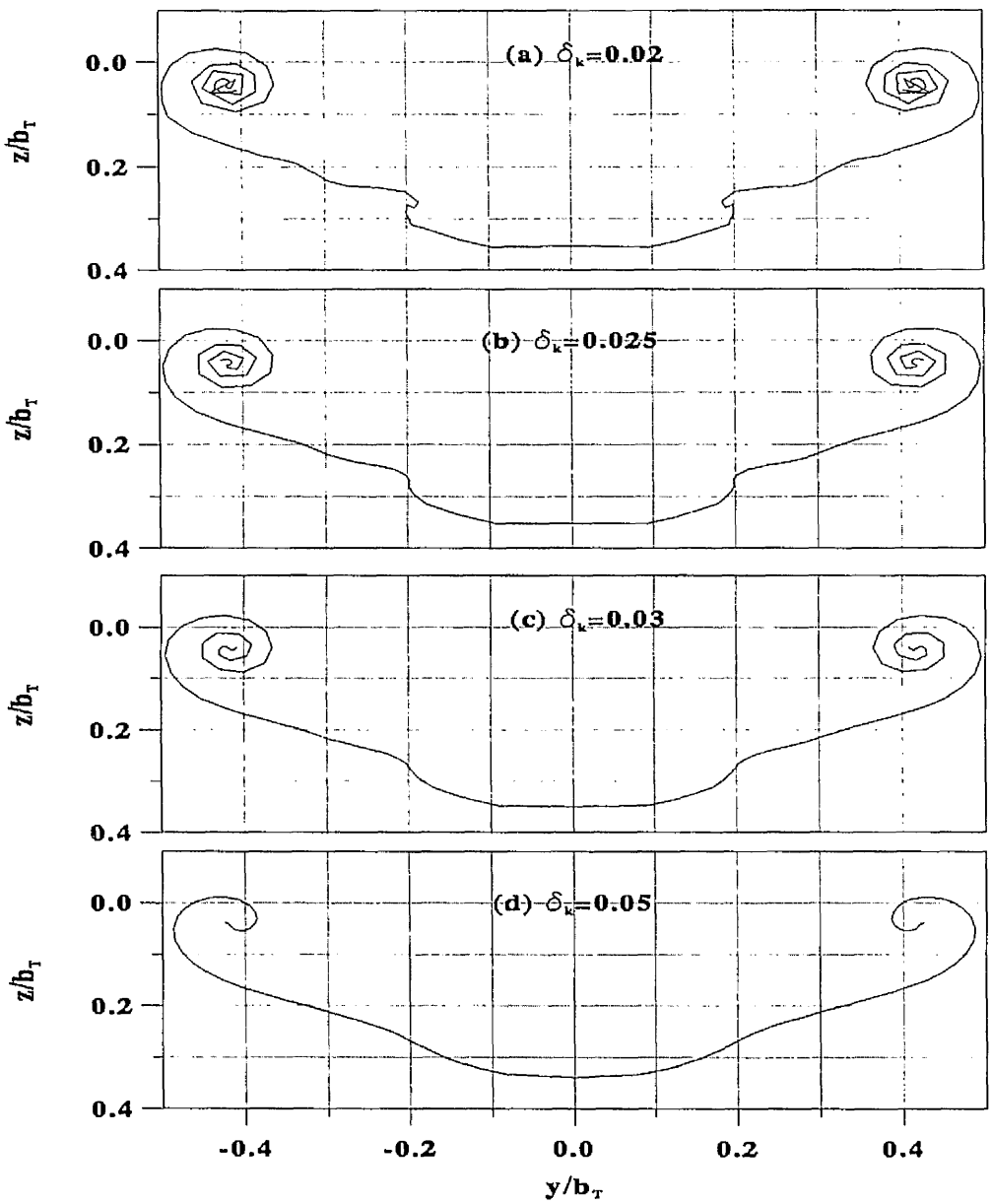

Figure 5.3: KC10 wing wake roll-up at $x/b_T = 4$ with various values of δ_k.

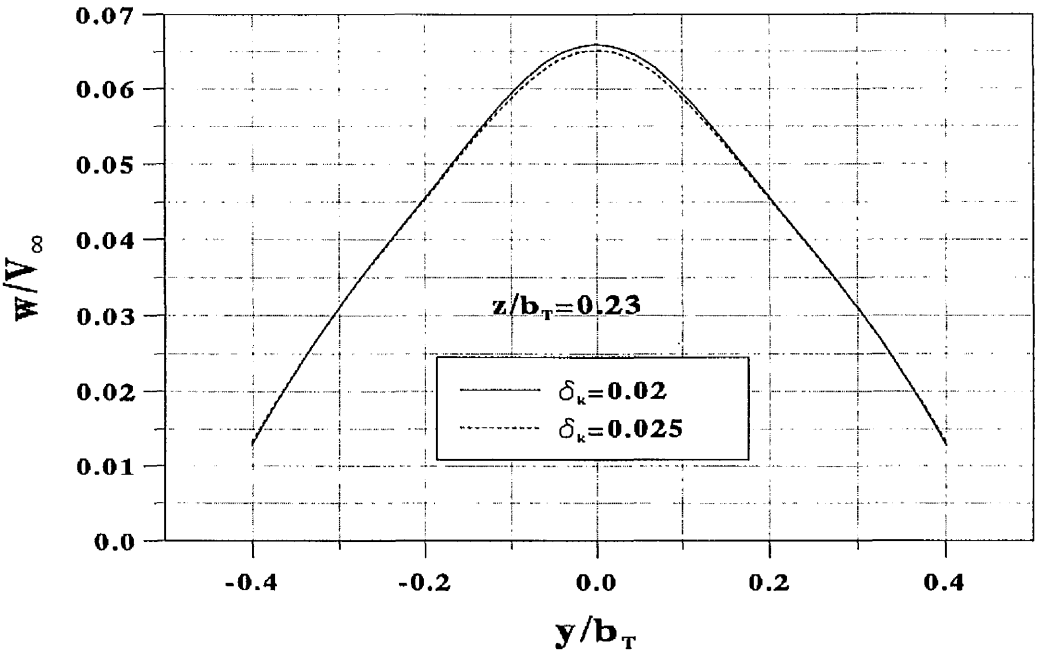

Figure 5.4: Effect of δ_k on the induced downwash over the receiver wing.

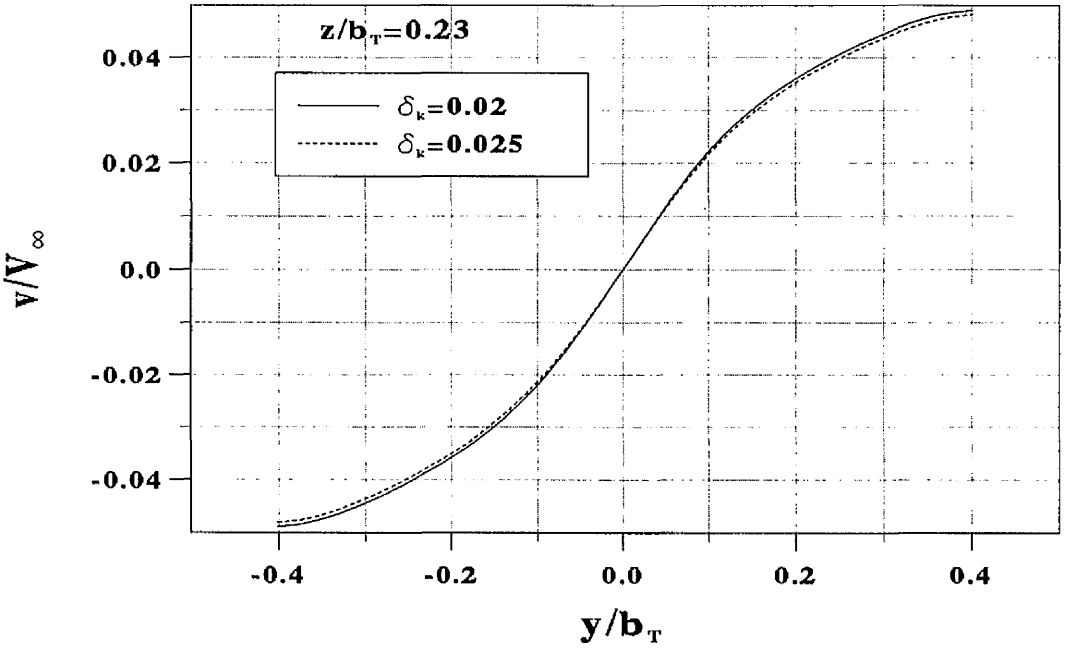

Figure 5.5: Effect of δ_k on the induced sidewash over the receiver wing.

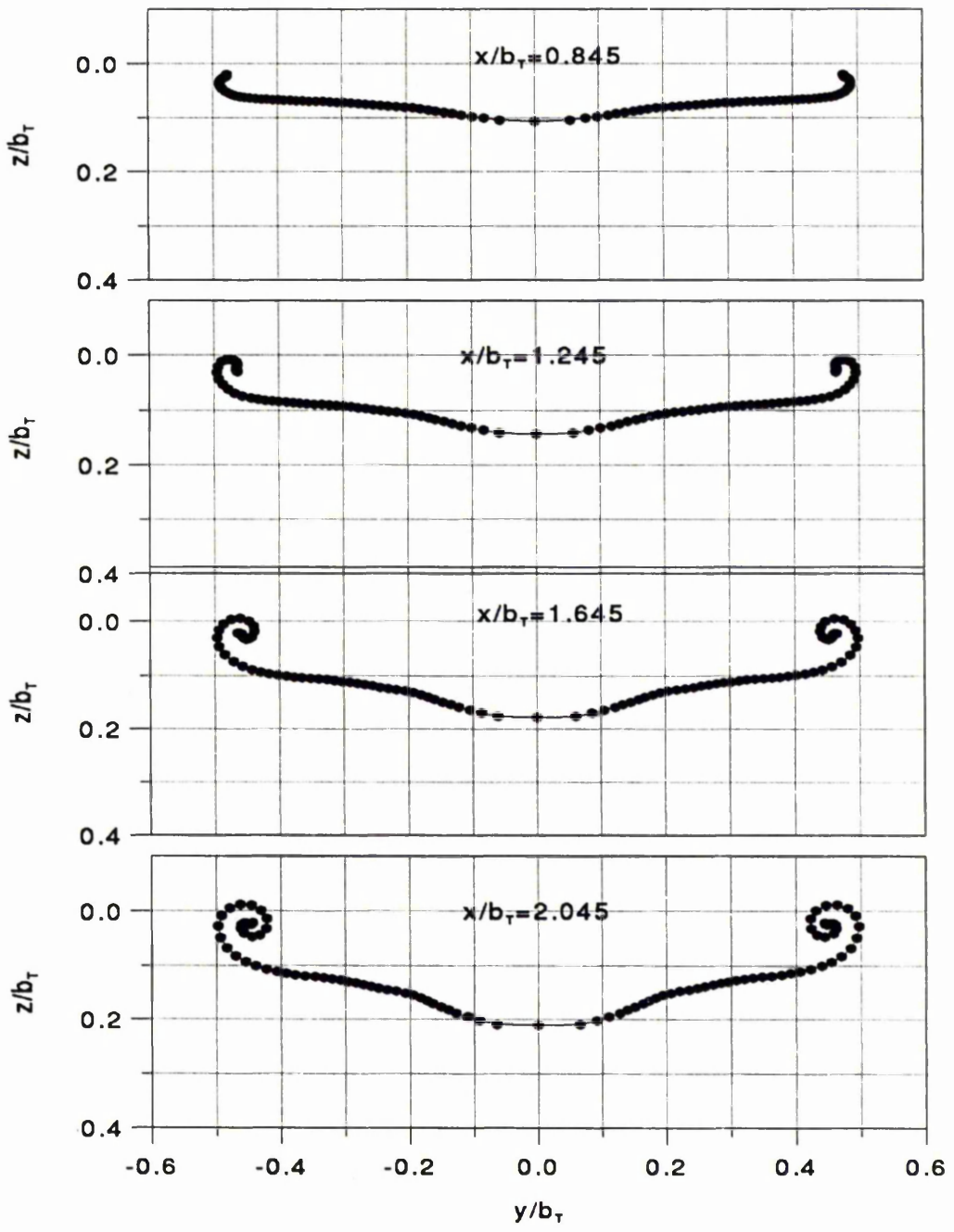

Figure 5.6: KC10 wing wake roll-up development in the downstream direction.

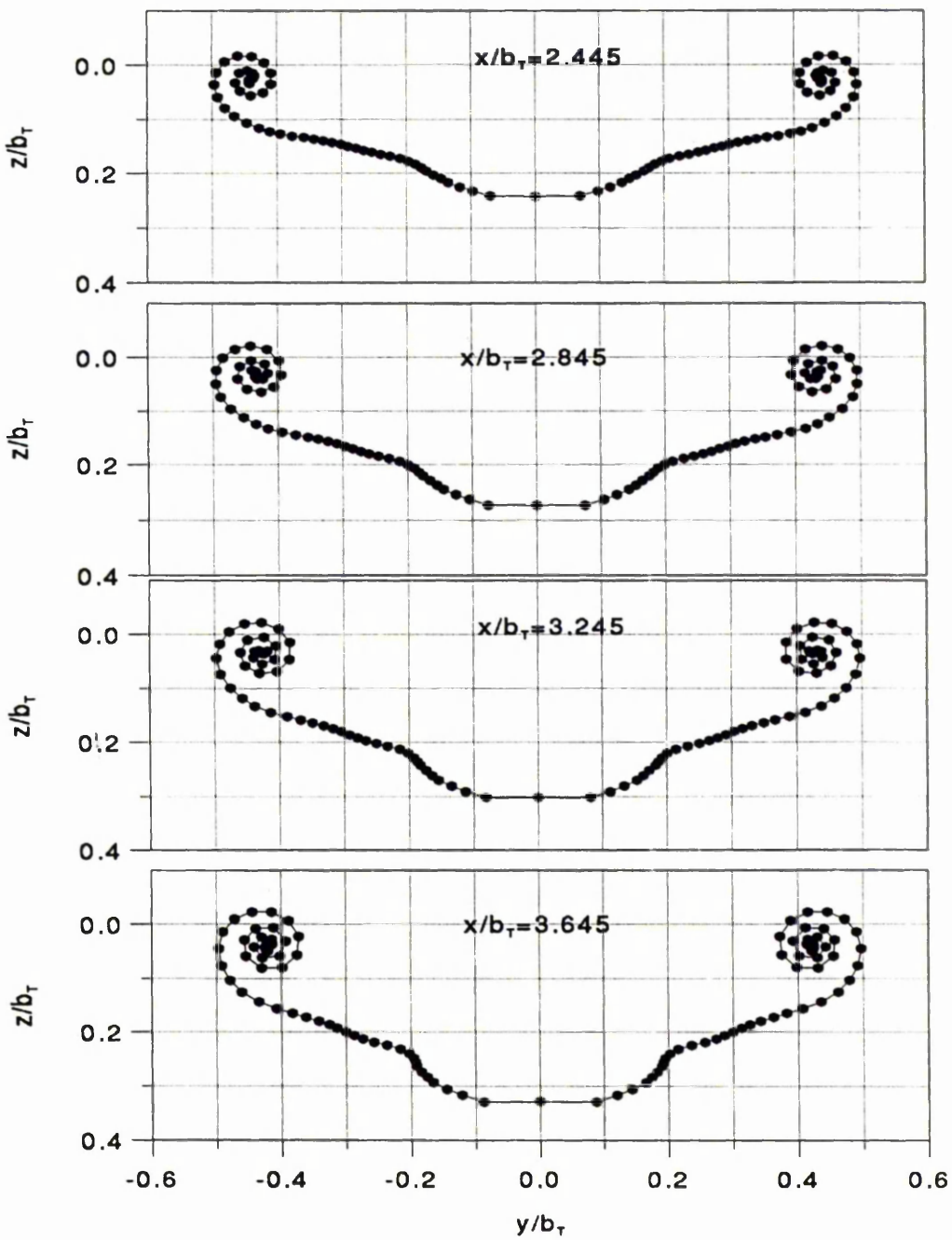

Figure 5.6: Continued

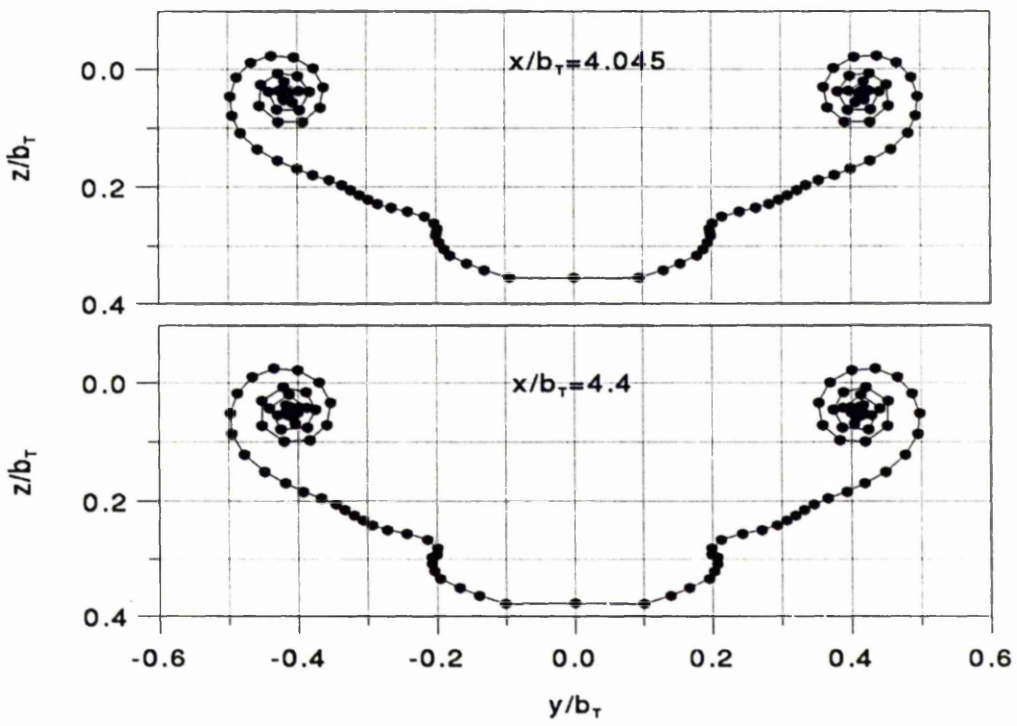

Figure 5.6: Continued

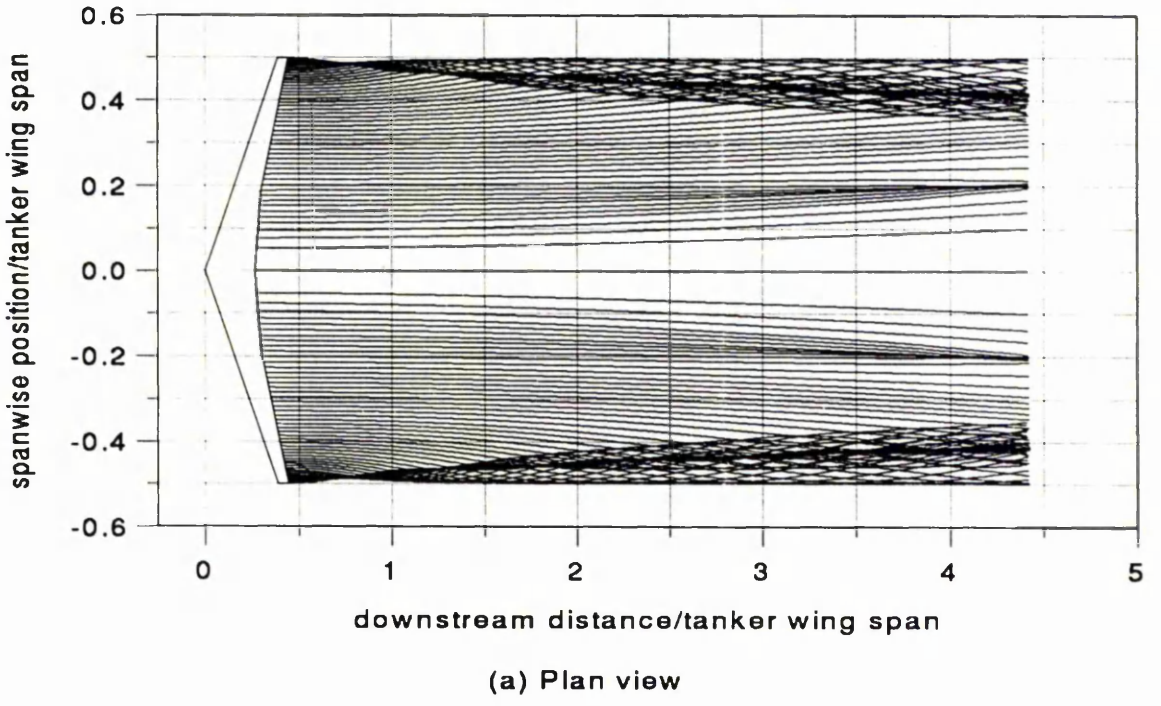

(a) Plan view

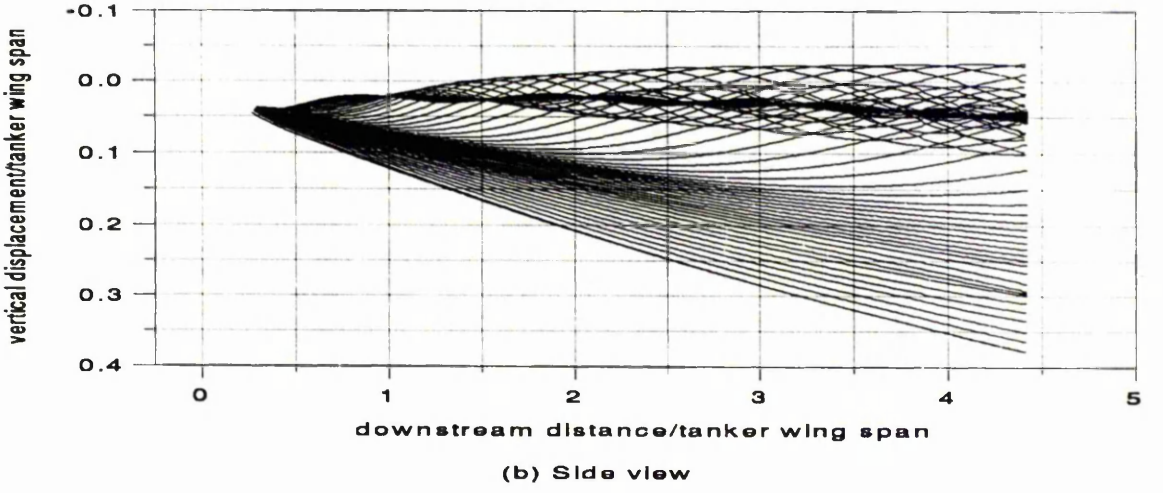

(b) Side view

Figure 5.7: Plan and side views of the KC10 wing wake roll-up.

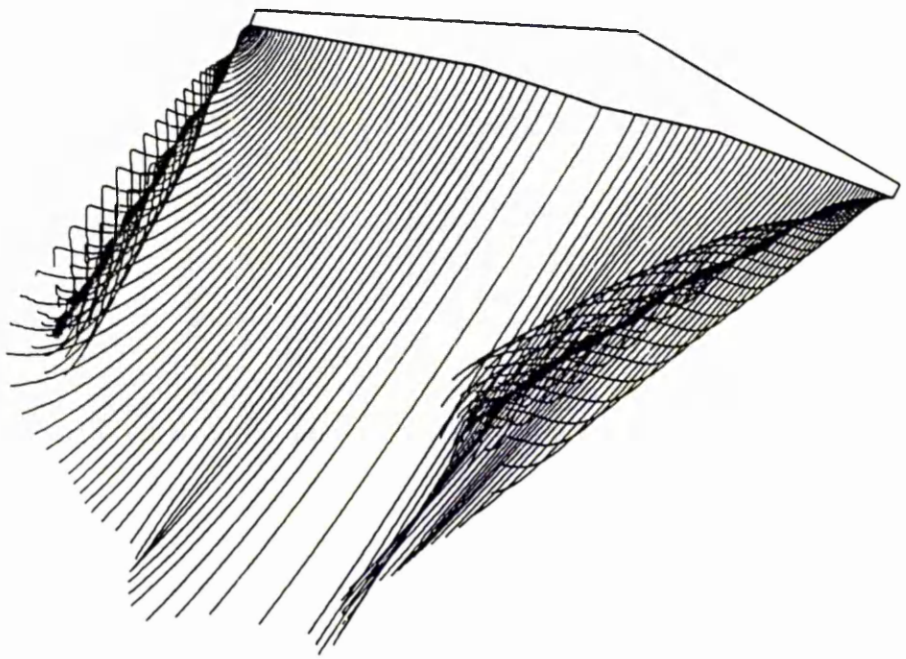

Figure 5.8: 3D view of the KC10 wing wake roll-up.

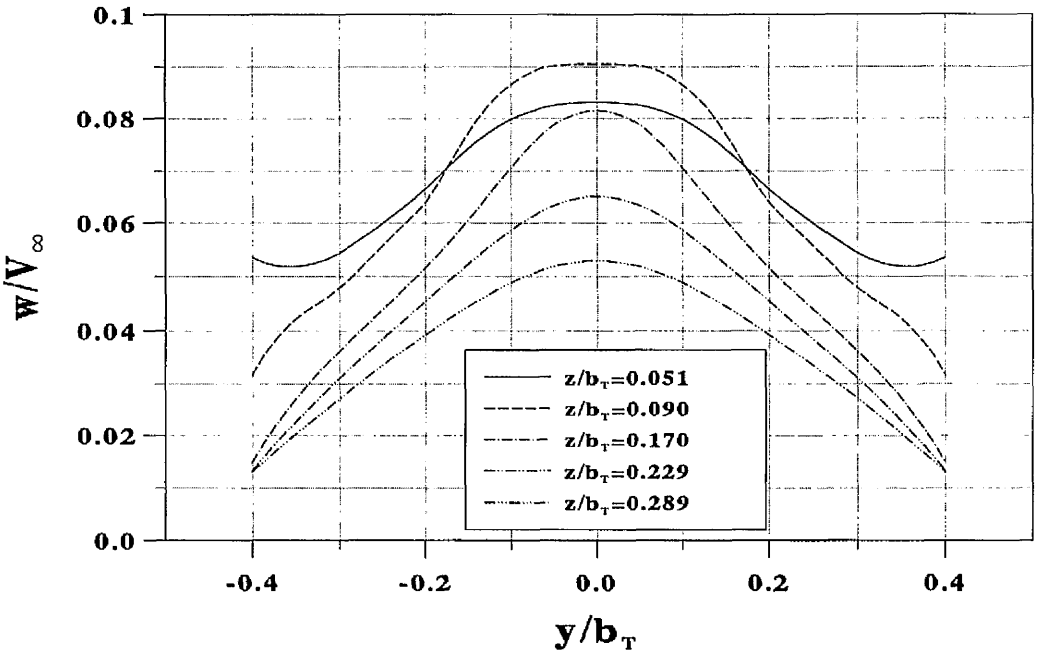

(a) Vortex sheet with roll-up

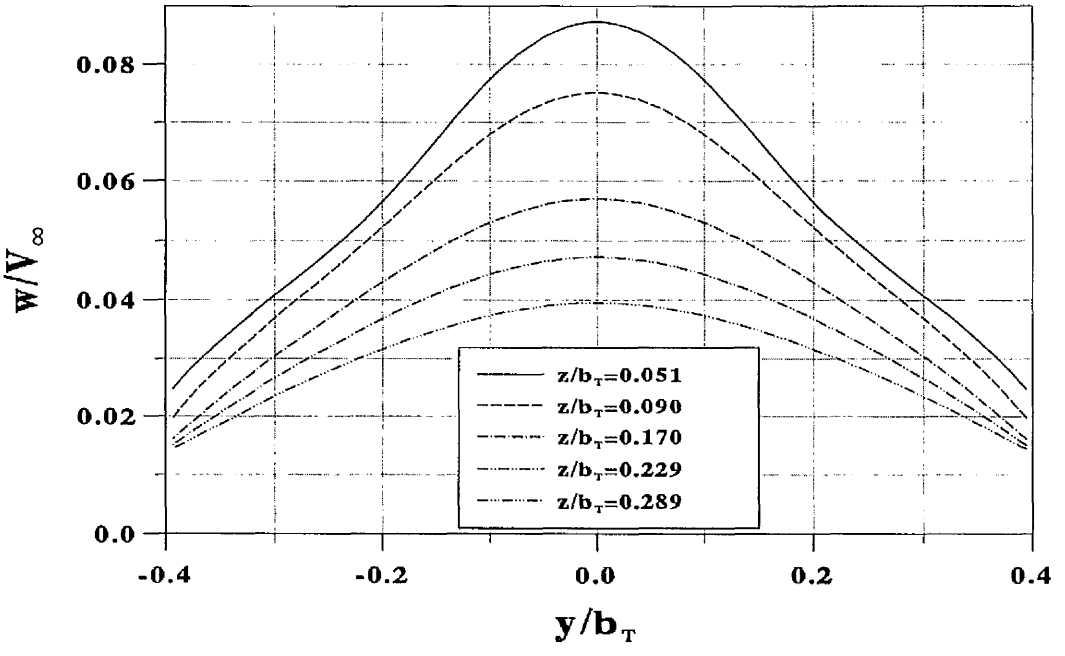

(b) Flat vortex sheet

Figure 5.9: Downwash induced by tanker wing at position of receiver wing.

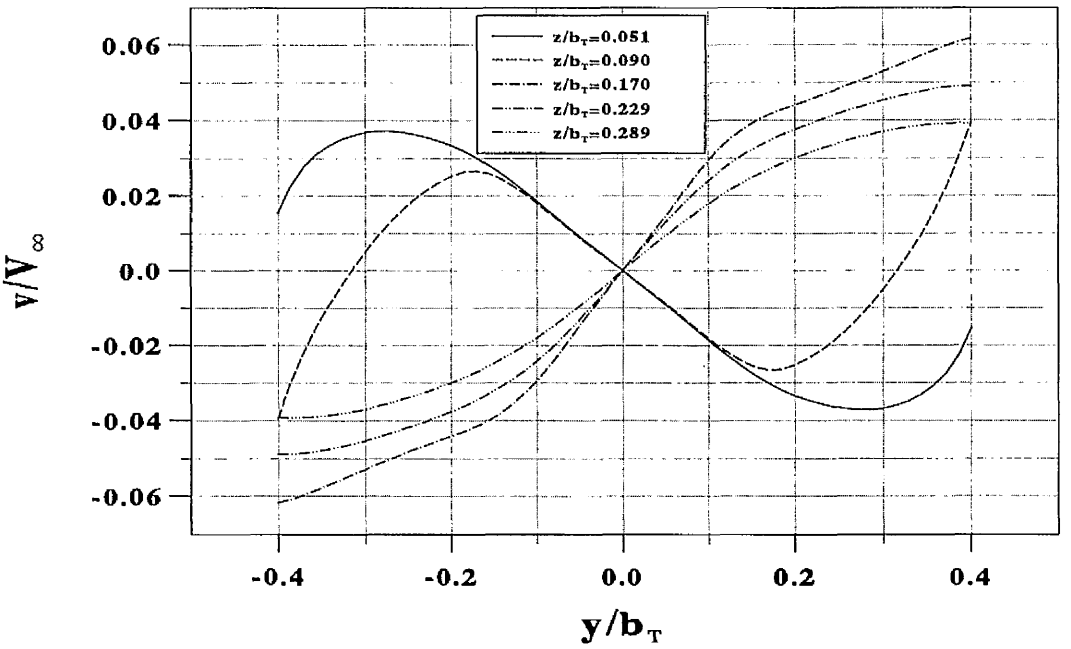

(a) Vortex sheet with roll-up

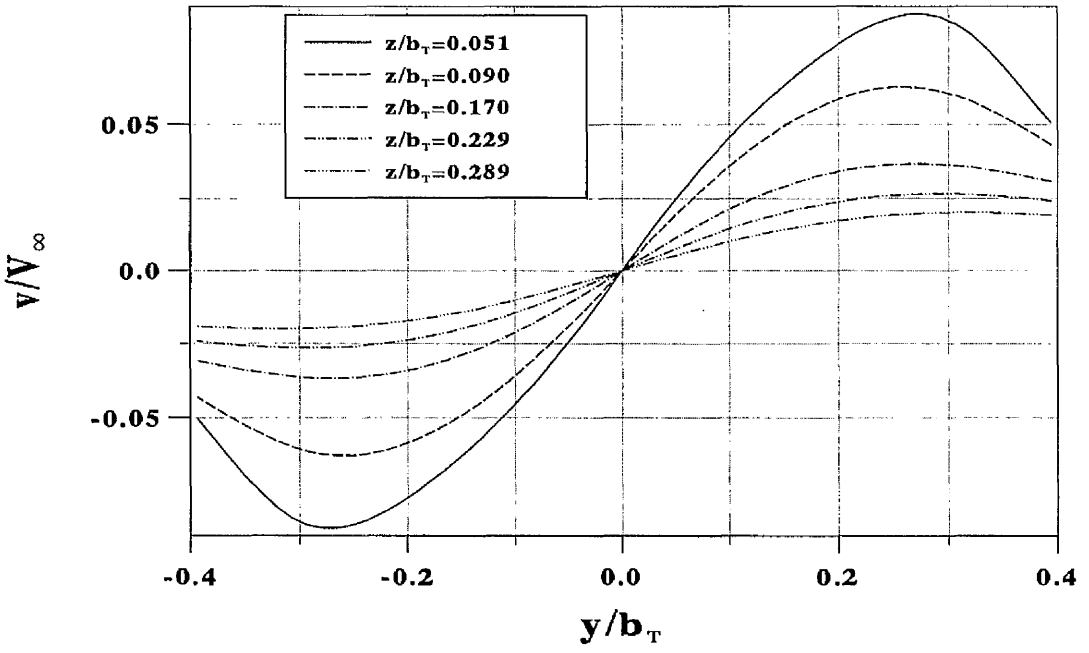

(b) Flat vortex sheet

Figure 5.10: Sidewash induced by tanker wing at position of receiver fin.

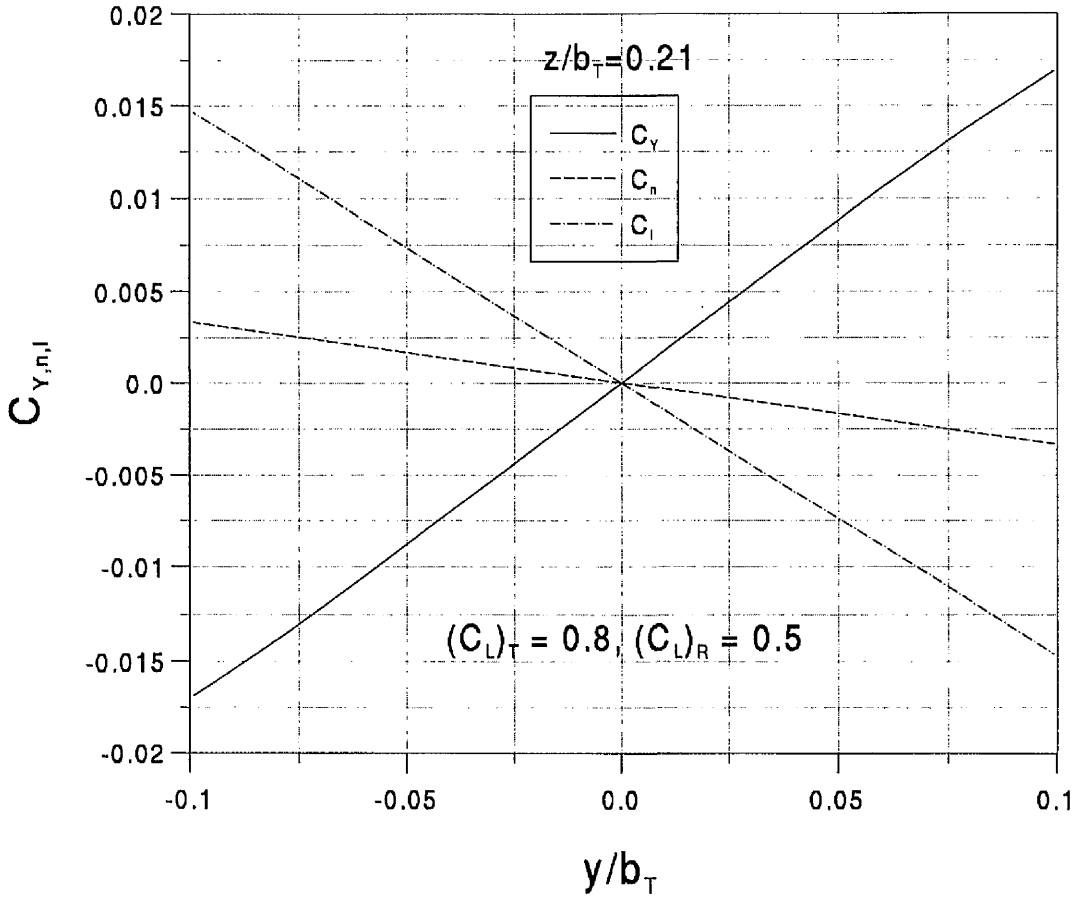

Figure 5.11: Receiver side force, yawing and rolling moments due to side displacement.

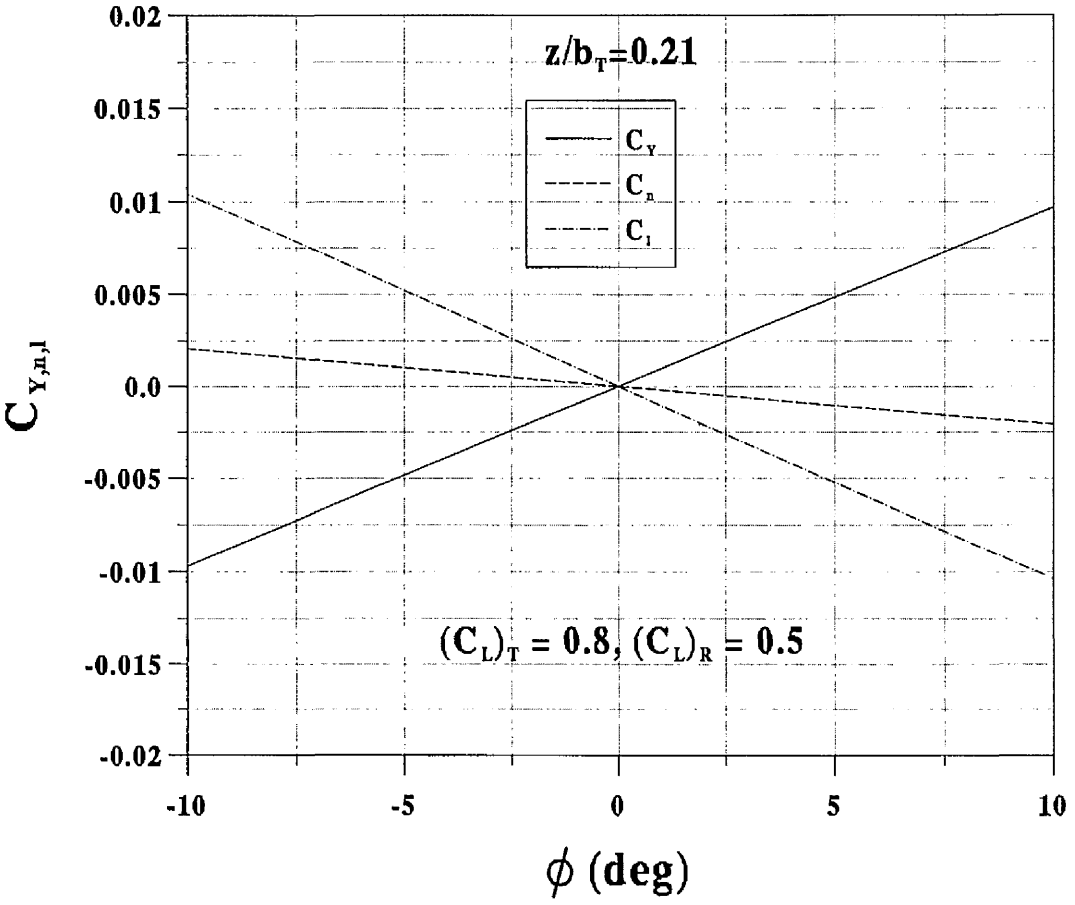

Figure 5.12: Receiver side force, yawing and rolling moments due to bank displacement.

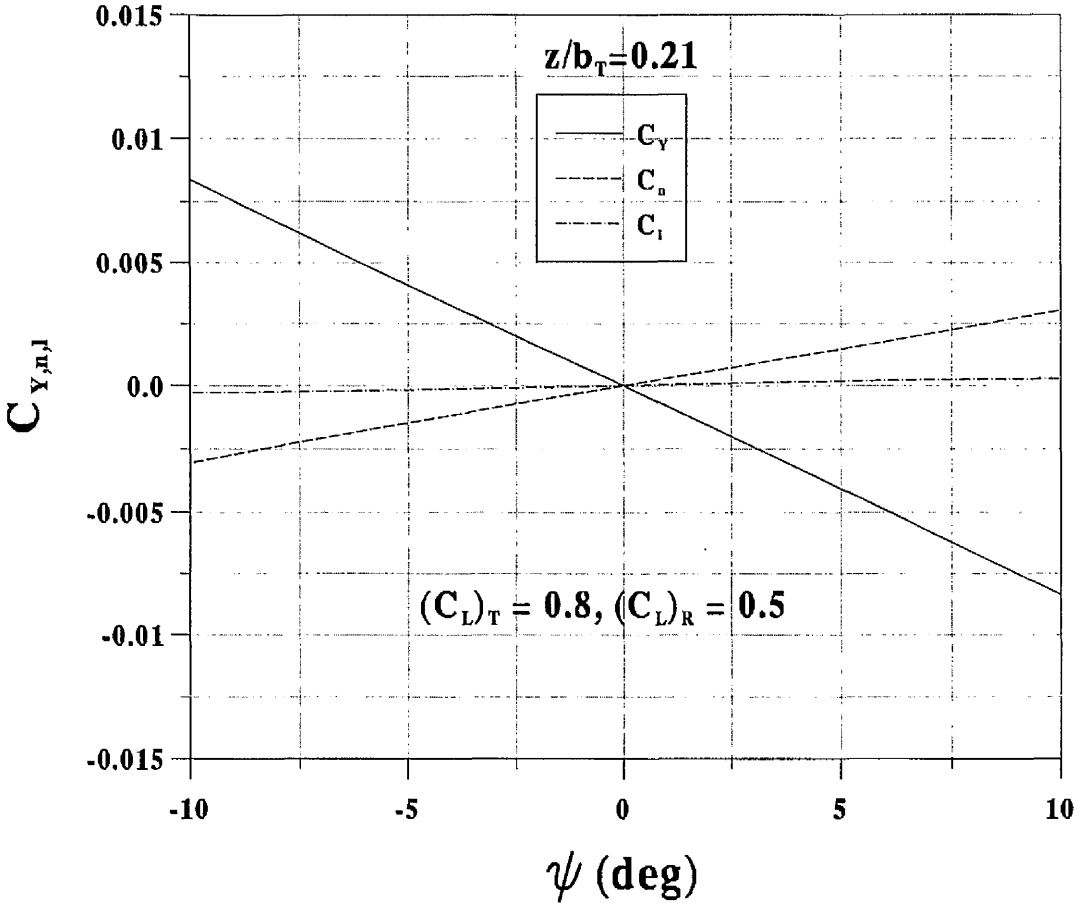

Figure 5.13: Receiver side force, yawing and rolling moments due to yaw displacement.

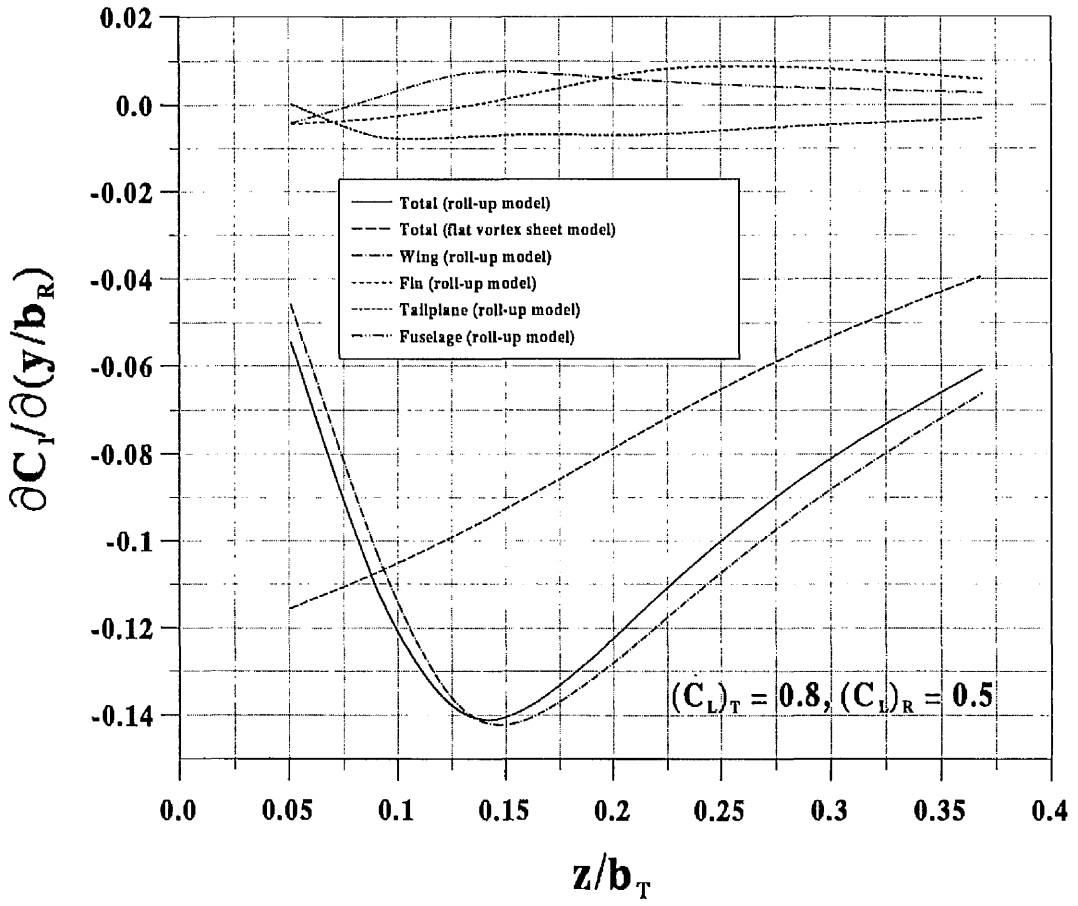

Figure 5.14: Variation of receiver rolling moment due to side displacement derivative with vertical separation.

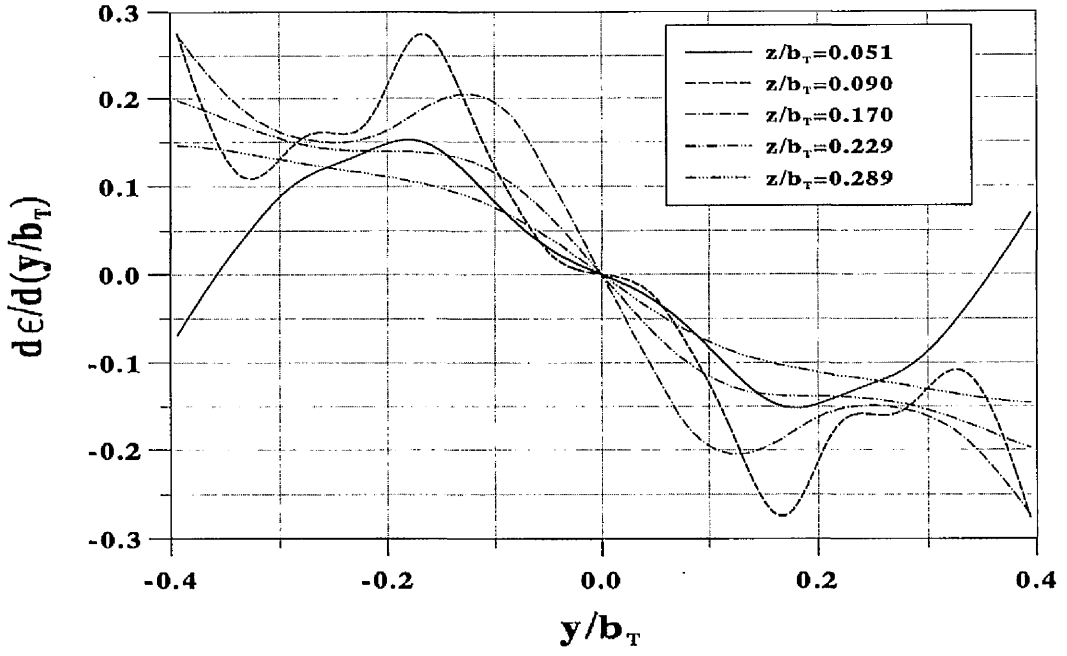

(a) Vortex sheet with roll-up

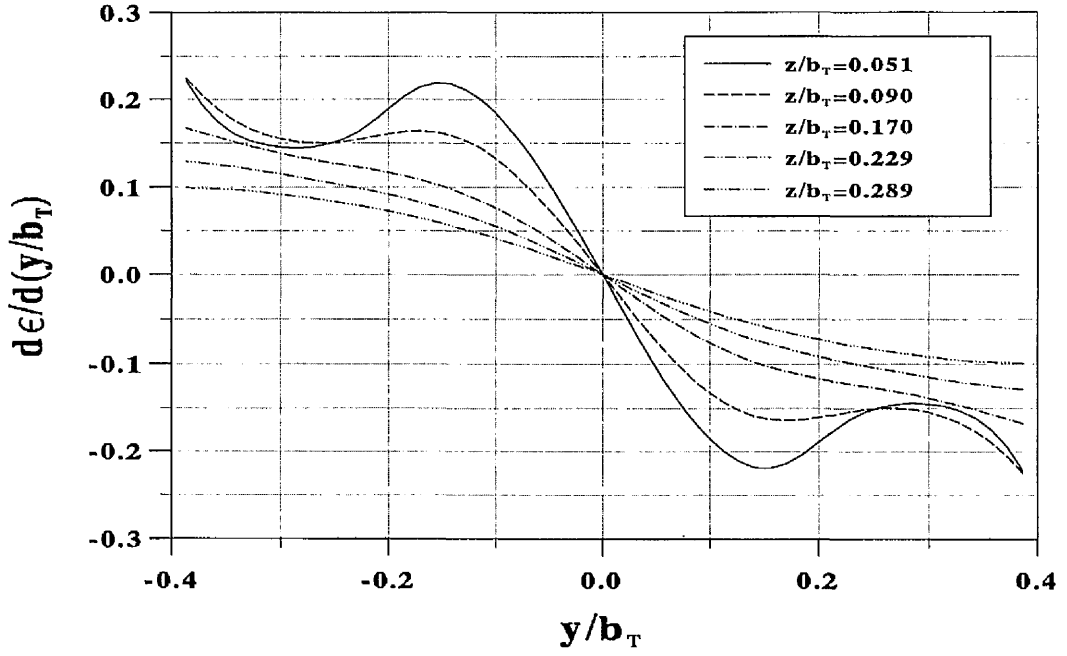

(b) Flat vortex sheet

Figure 5.15: Spanwise gradient of the downwash induced by tanker wing at position of receiver wing.

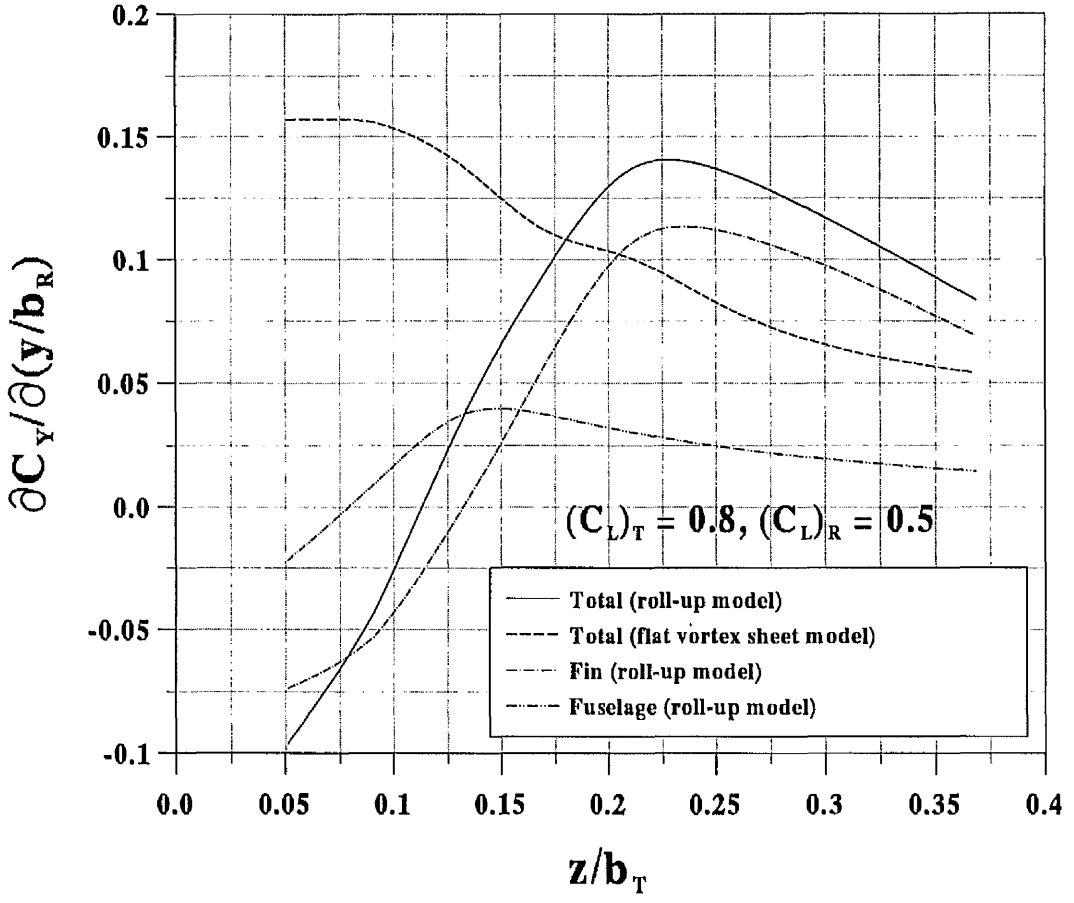

Figure 5.16: Variation of receiver side force due to side displacement derivative with vertical separation.

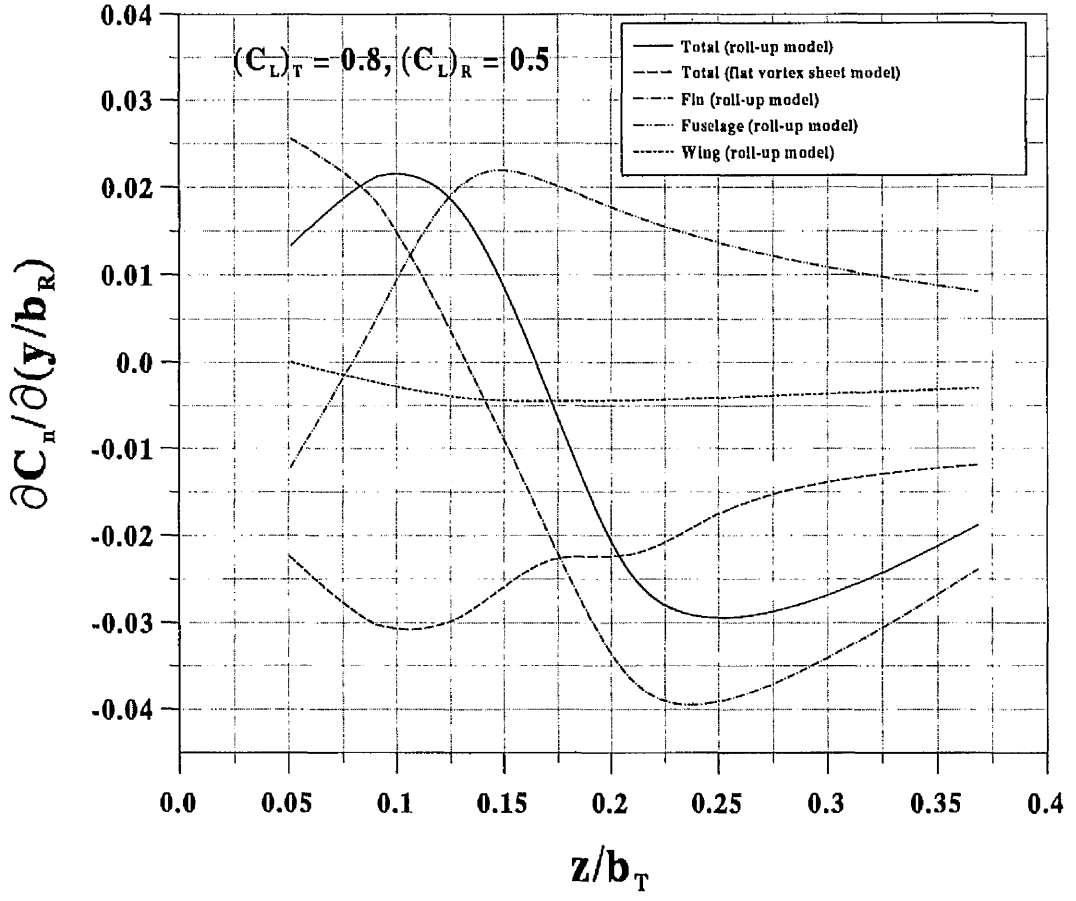

Figure 5.17: Variation of receiver yawing moment due to side displacement derivative with vertical separation.

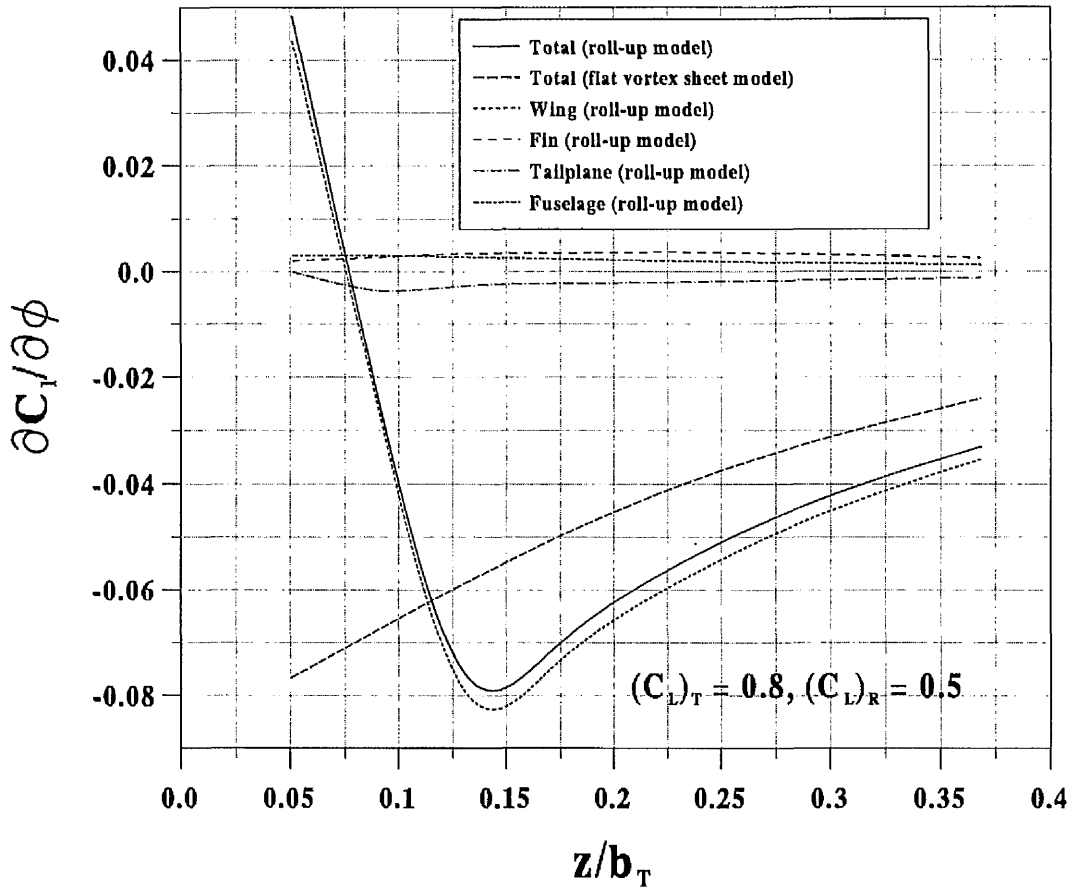

Figure 5.18: Variation of receiver rolling moment due to bank displacement derivative with vertical separation.

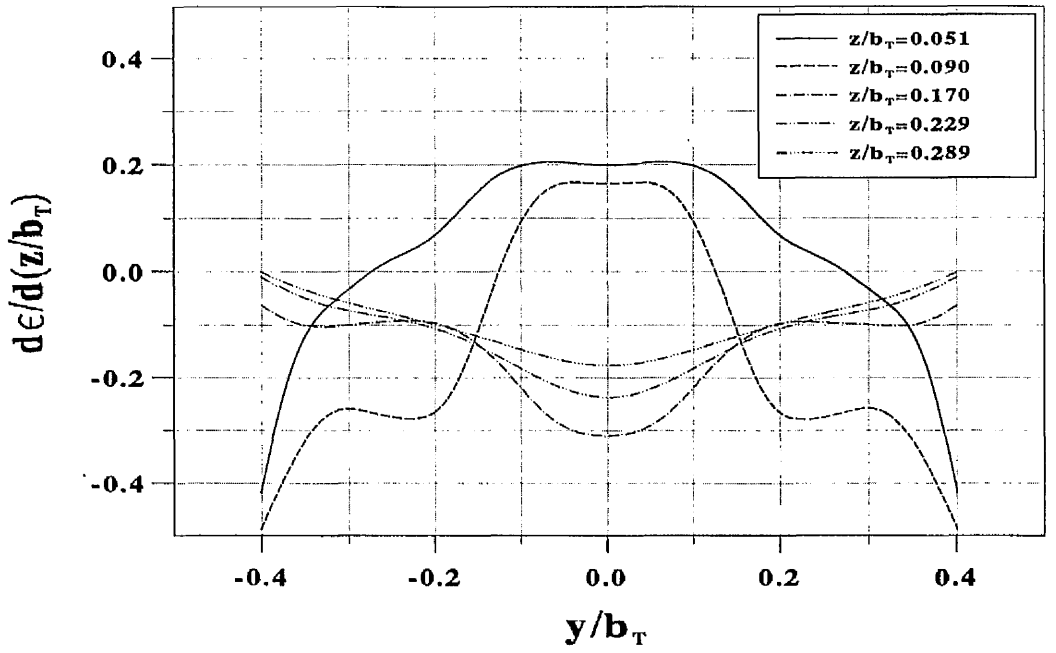

(a) Vortex sheet with roll-up

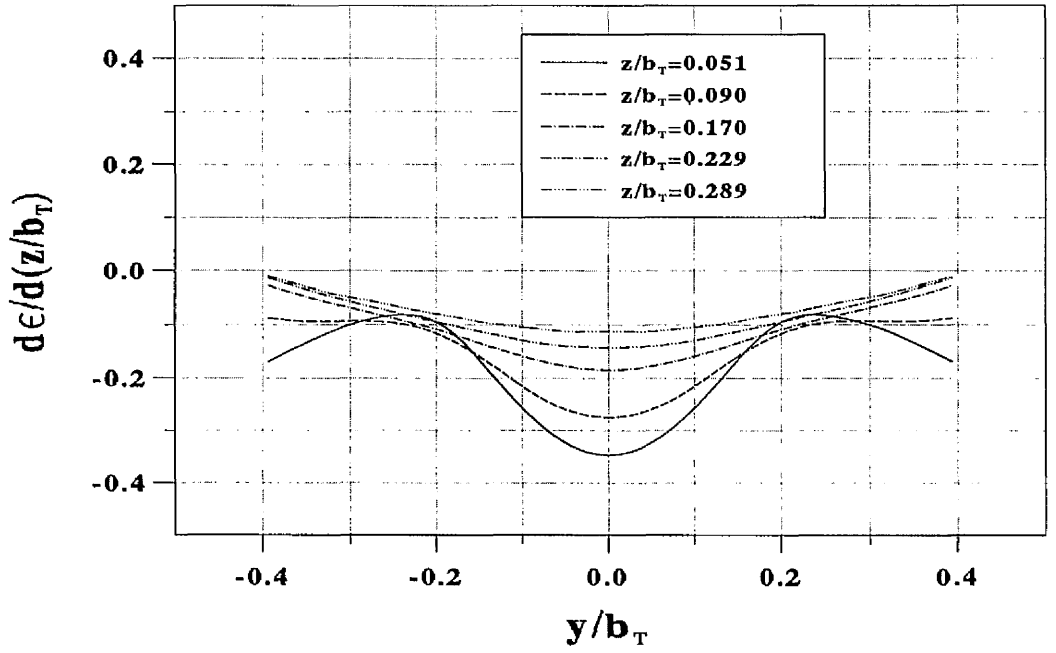

(b) Flat vortex sheet

Figure 5.19: Tanker downwash gradient in the vertical direction at position of receiver wing.

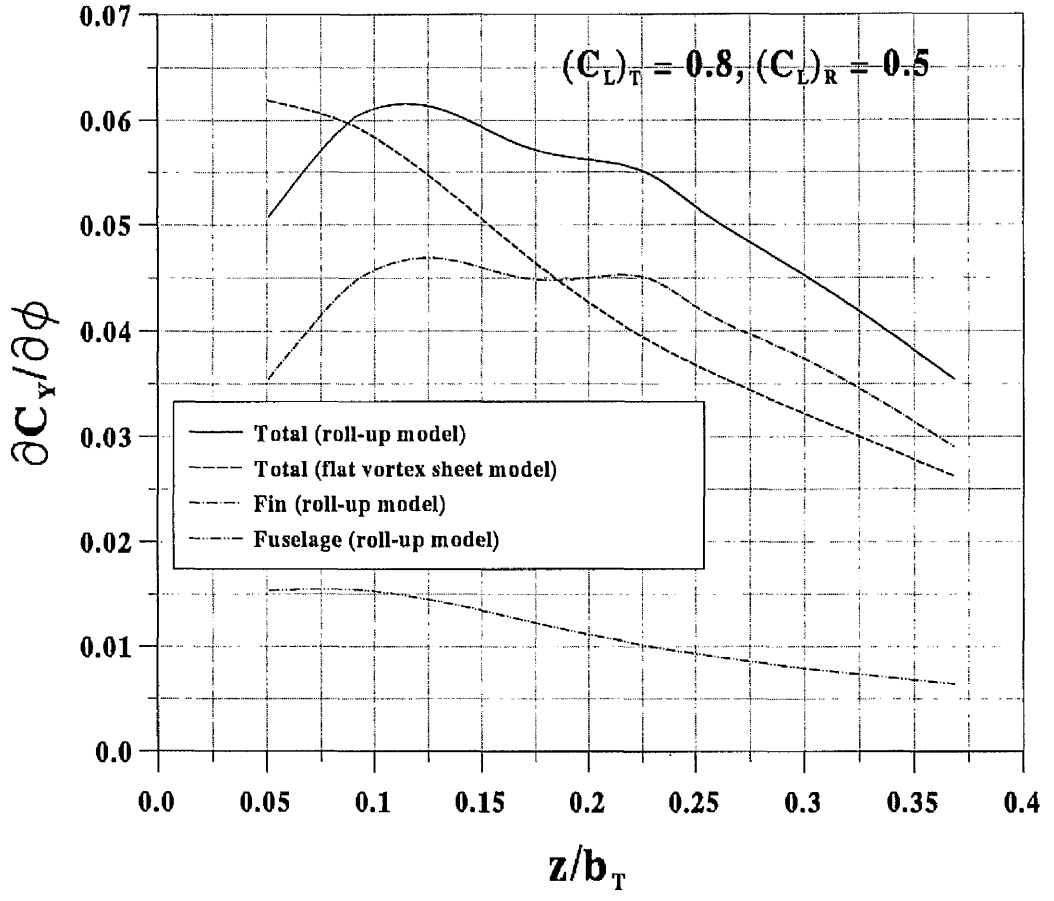

Figure 5.20: Variation of receiver side force due to bank displacement derivative with vertical separation.

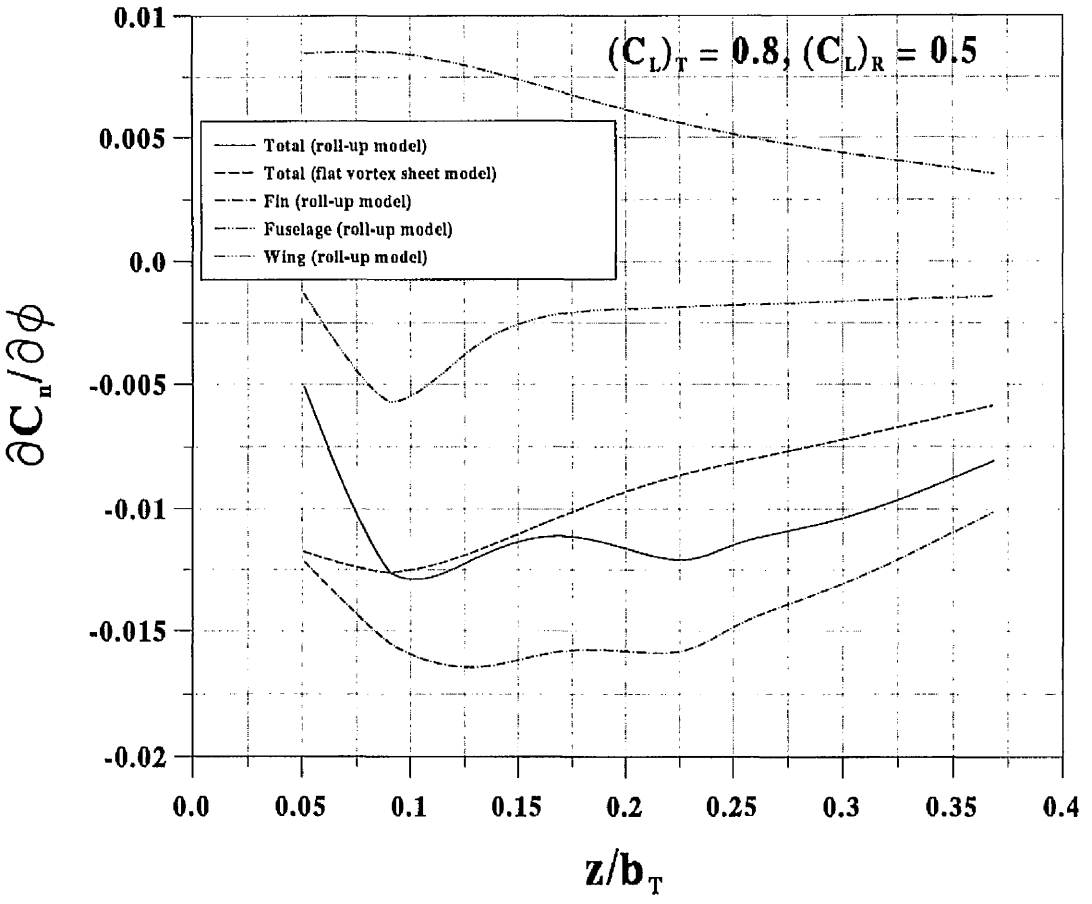

Figure 5.21: Variation of receiver yawing moment due to bank displacement derivative with vertical separation.

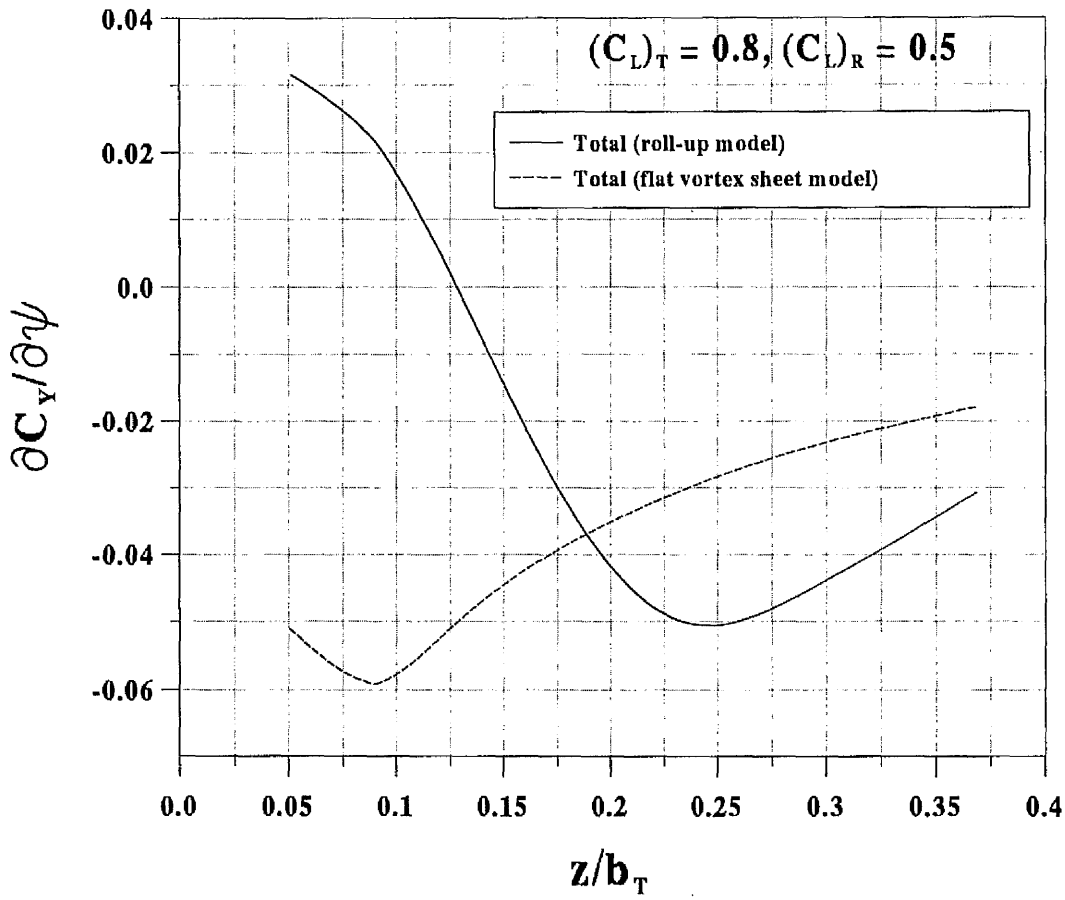

Figure 5.22: Variation of receiver side force due to yaw displacement derivative with vertical separation.

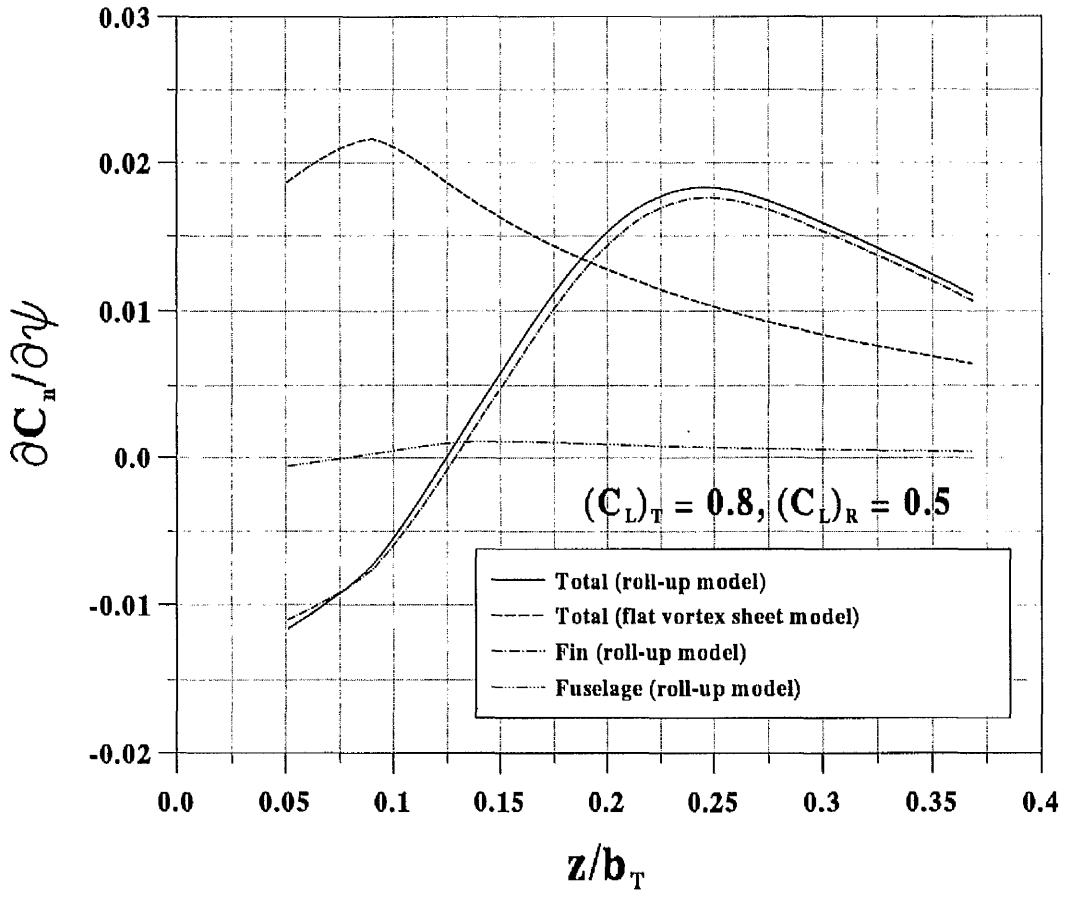

Figure 5.23: Variation of receiver yawing moment due to yaw displacement derivative with vertical separation.

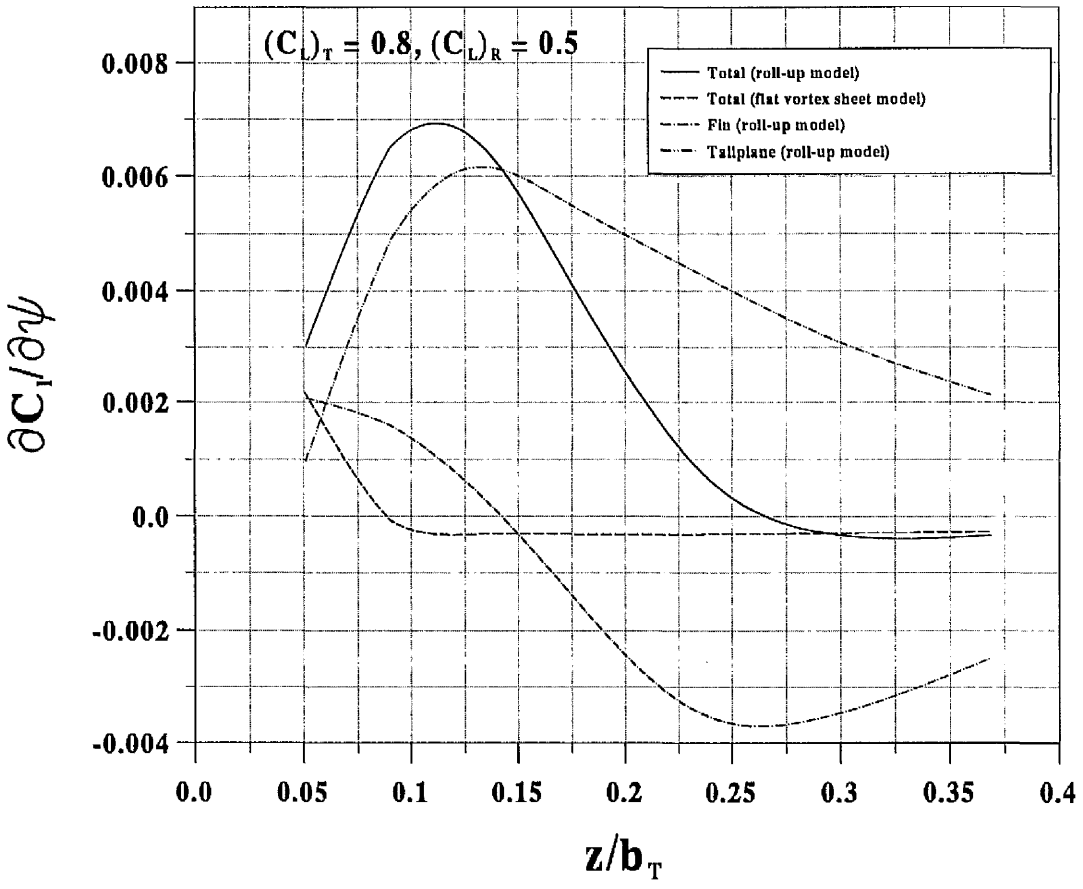

Figure 5.24: Variation of receiver rolling moment due to yaw displacement derivative with vertical separation.

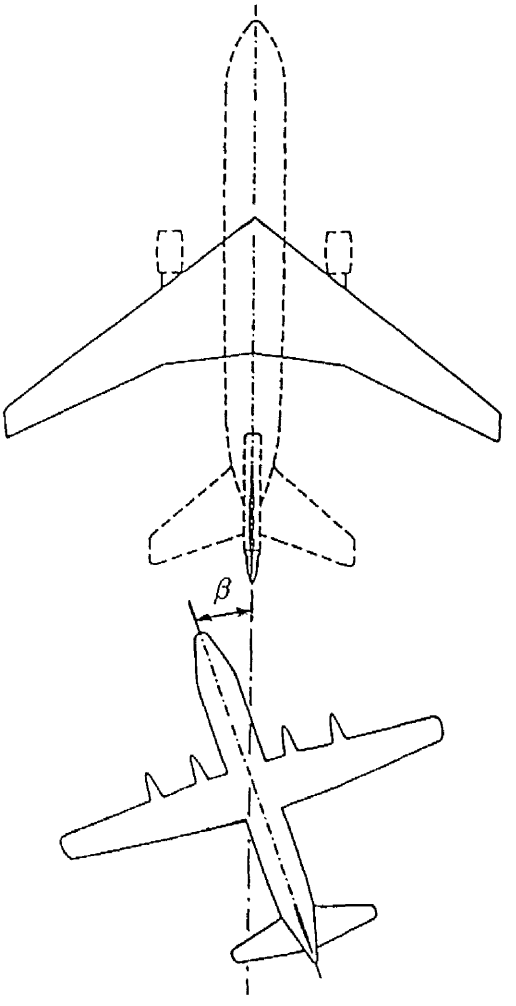

(a) Receiver c.g. on the centre line of tanker wake

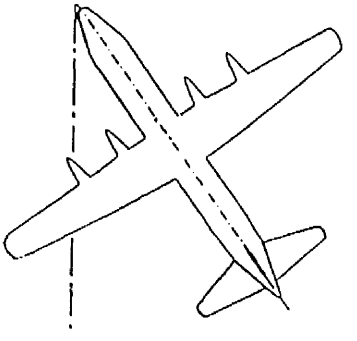

(b) Receiver nose on the centre line of tanker wake

Figure 5.25: Hercules receiver in steady sideslip behind KC10 tanker.

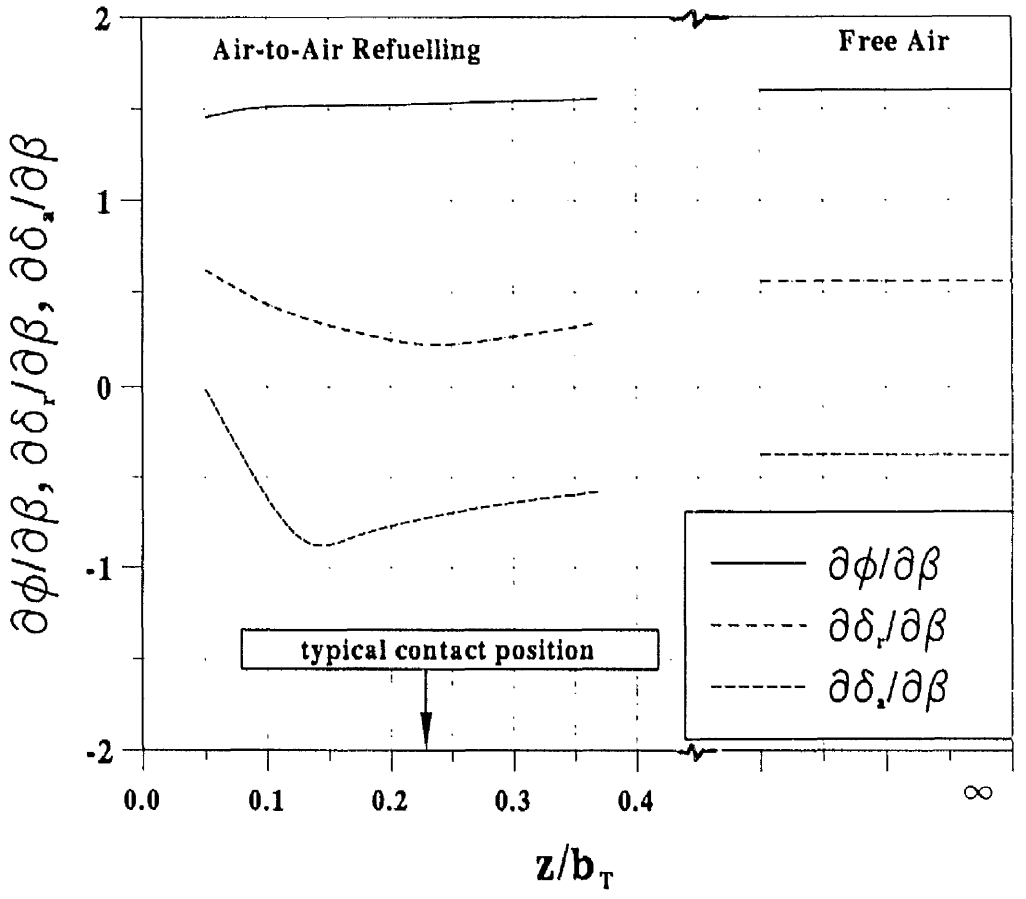

(a) Receiver c.g. on the centre line of tanker wake

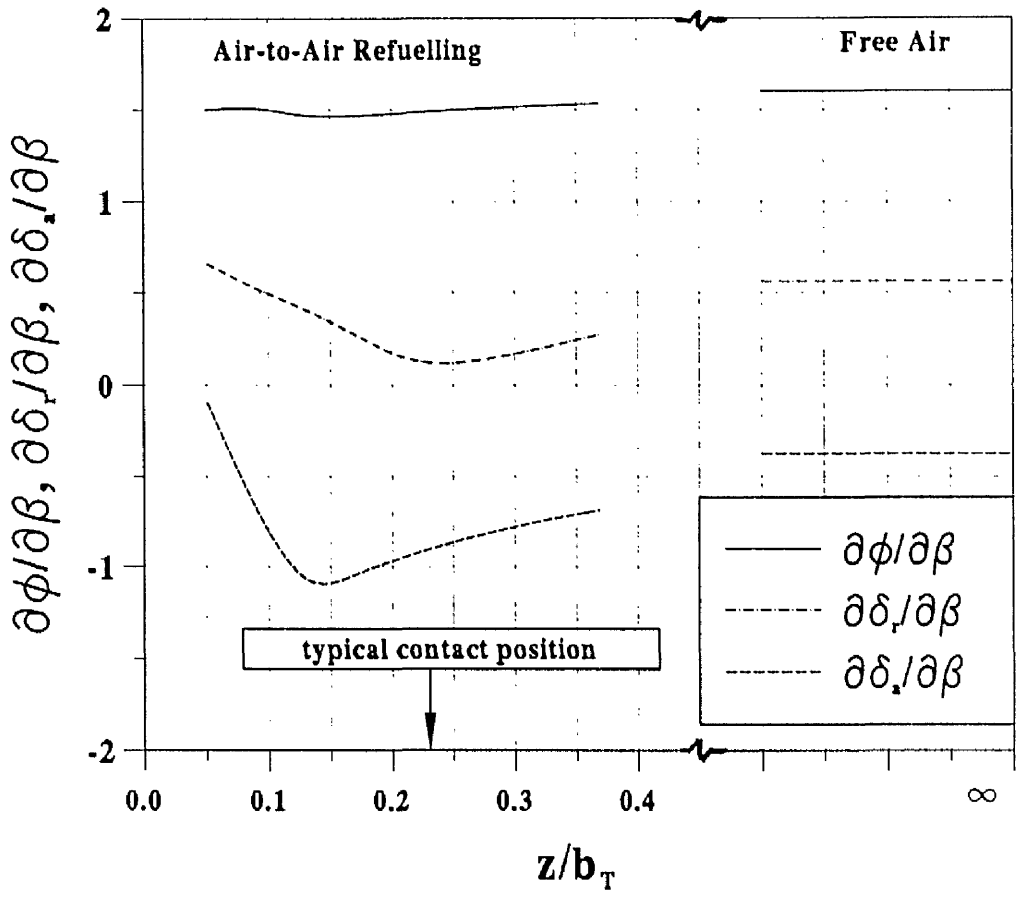

(b) Receiver nose on the centre line of tanker wake

Figure 5.26: Trim of receiver aircraft in steady sideslip.

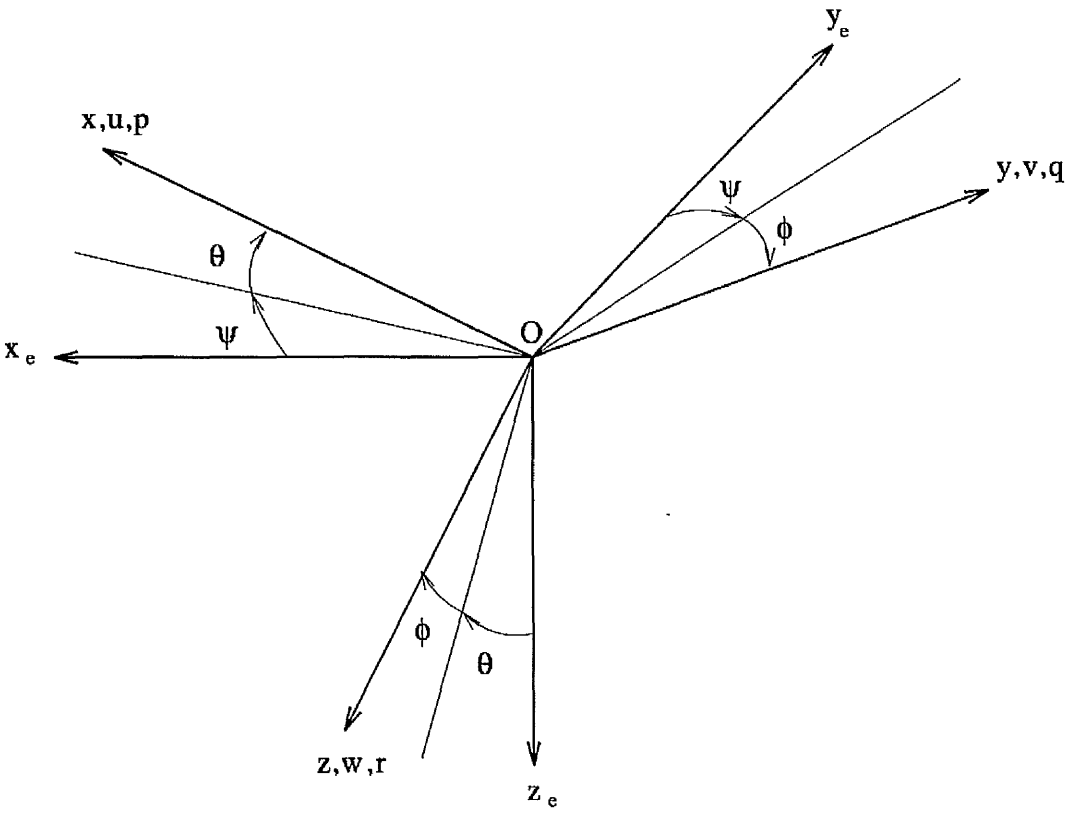

Figure 5.27: Aircraft body axes in datum and disturbed flight.

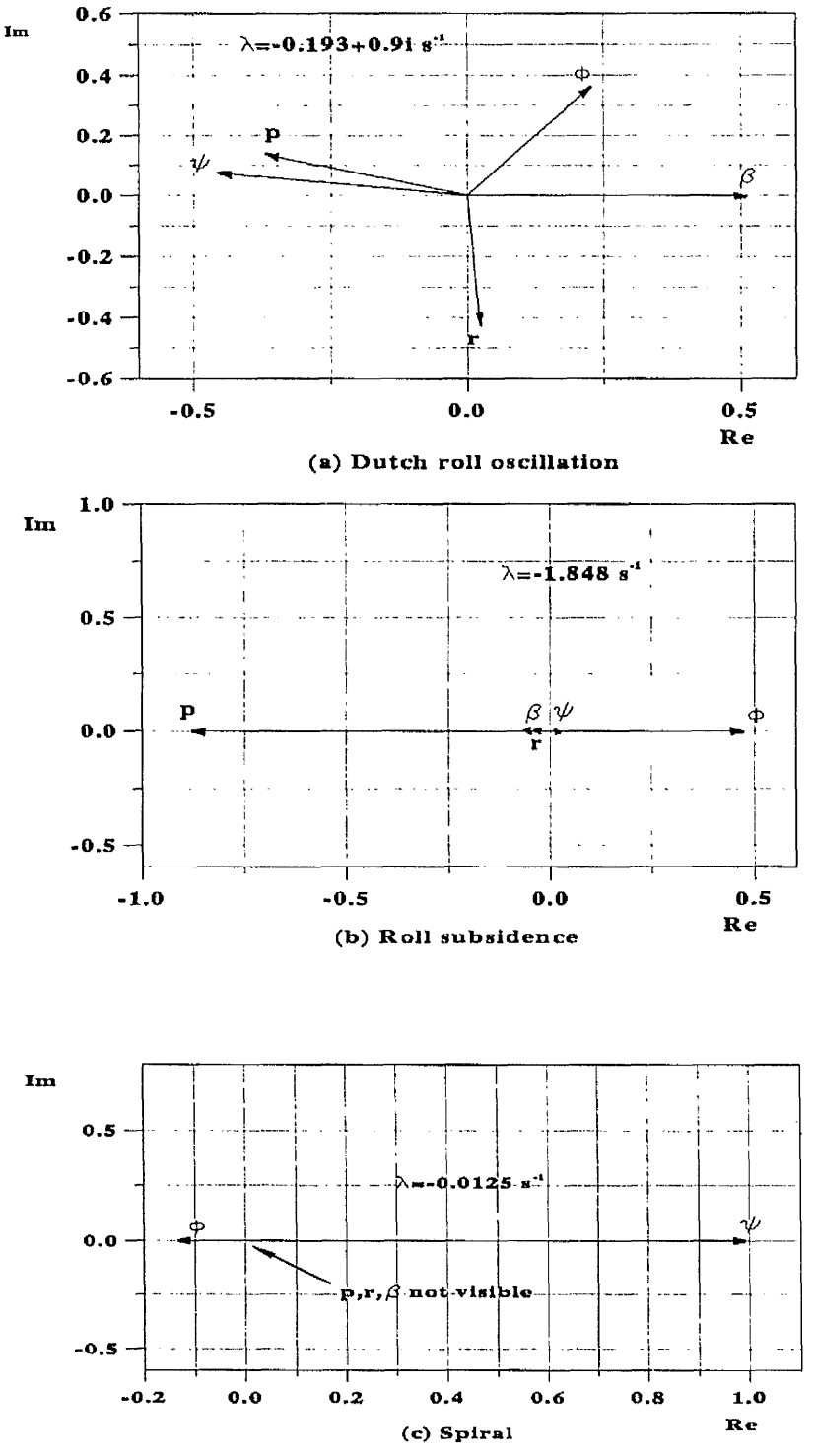

Figure 5.28: Eigenvalues and eigenvectors of lateral modes of Hercules aircraft in free air.

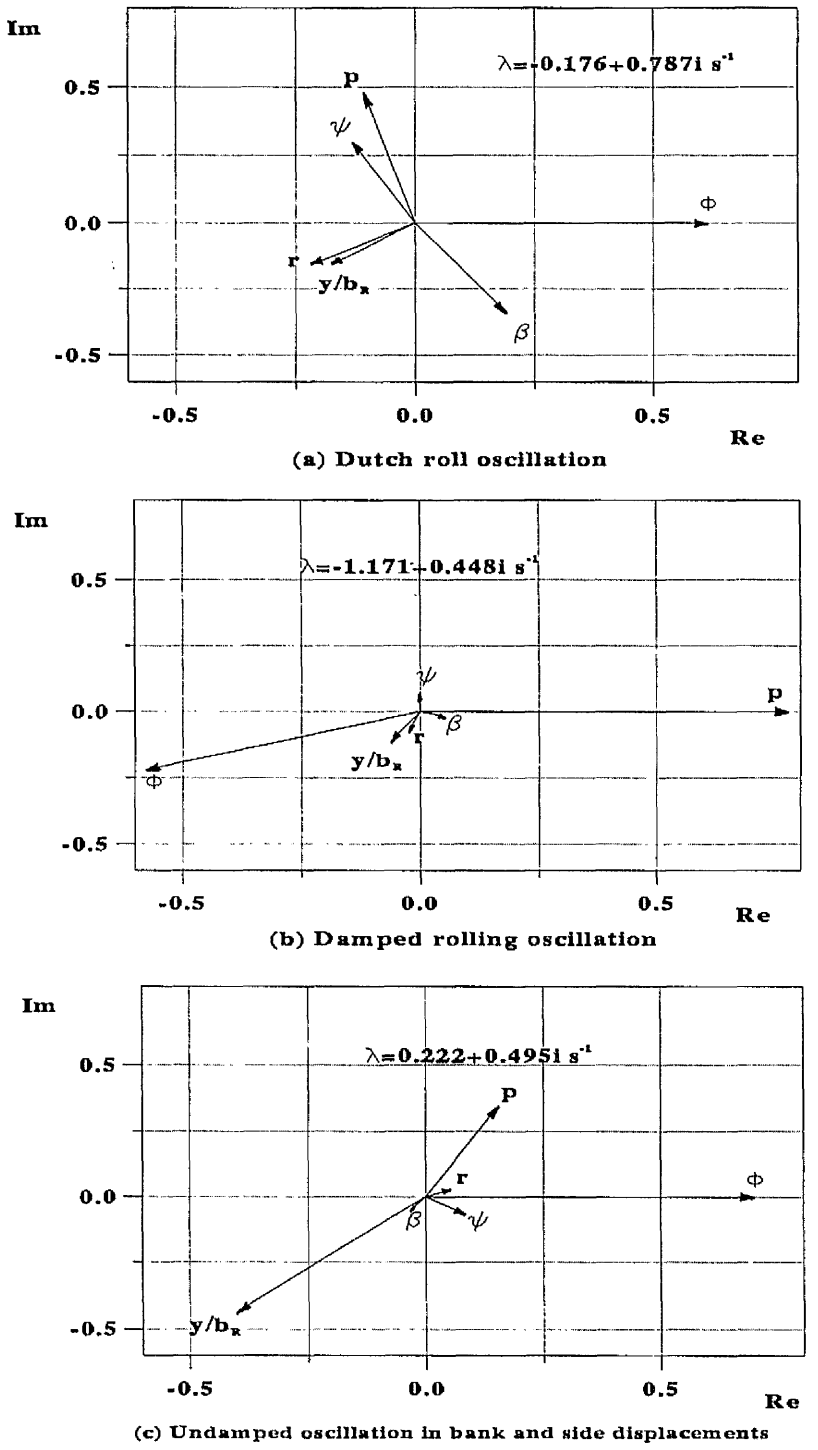

Figure 5.29: Eigenvalues and eigenvectors of lateral modes of Hercules aircraft in air-to-air refuelling at $z/b_T = 0.24$ and 3.05 km altitude.

Chapter 6

Trailing Vortex Effects of KC10 Tanker on Hercules Receiver Aircraft

This chapter investigates the effect of the KC10 tanker trailing vortex wake on the Hercules receiver aircraft over an envelope of the receiver positions and attitudes which covers that required for flight simulation.

In air-to-air refuelling, flight simulation is used both as a training aid and as a development tool. Bradley [7] has described the problem of the unacceptable lateral handling of the Nimrod receiver aircraft behind a heavy Tristar tanker. This problem was investigated on a simulator by assessing changes made to the yaw damper control laws although the simulation was not considered realistic enough to be useful in resolving the problem. The use of simulators in training offers major

savings in direct operating costs and aircraft fatigue life. The requirements for the flight simulation of air-to-air refuelling are described by Prothero [58]. It was stated that the process in achieving a successful contact between tanker and receiver and holding for long enough to achieve the necessary fuel transfer is the area in which a great deal of time is spent. Therefore, simulation of this flight phase requires good modelling of the aerodynamic interference between tanker and receiver aircraft.

In this research work, typical aerodynamic data of the interference between the KC10 tanker and Hercules receiver aircraft were obtained. The aerodynamic interference between the two aircraft was determined using the aerodynamic models described in section 2.4 which have previously been applied to the same tanker/receiver combination to estimate the additional lateral aerodynamic derivatives of the Hercules as described in chapter 5. The case of small lateral displacements of the receiver from a position on the centreline of the tanker wake with no bank or sideslip was considered in chapter 5 and the 9 lateral aerodynamic derivatives due to side, bank and yaw displacements were estimated. In this chapter the induced forces and moments on the receiver vary non-linearly with the position coordinates x, y, z of the receiver relative to the tanker. These forces and moments are usually illustrated by contour plots in the y, z plane at various downstream positions. Bank, yaw and pitch displacements also produce forces and moments.

Firstly, the aerodynamic forces and moments acting on the receiver aircraft due to its position and attitude were determined over an envelope of the receiver positions of interest. Next, the aerodynamic loads on the receiver due to its attitude within the tanker vortex wake viz. X, Y, Z, L, M and N due to ϕ, θ and ψ were expressed in

terms of aerodynamic derivatives since they vary almost linearly with displacement angles in the range $\pm 10°$. Then the receiver aerodynamic loads due to both its position and attitude, listed in table 6.1, were assessed relative to the receiver's aerodynamic characteristics in free air and presented by contour plots in the y, z plane at a typical downstream position.

6.1 Flight Conditions and Aircraft Data

Figure 5.1 in the previous chapter shows the KC10 tanker and Hercules receiver aircraft at a horizontal separation of 1.04 times the tanker wing span as measured between the datum positions which are taken at the wing apex of each aircraft. The tanker aircraft is again considered at a lift coefficient of 0.8 and flight Mach number of 0.347. However, the receiver aircraft is set at a fixed pitch angle of 6° to the horizontal which at the typical refuelling position gives a lift coefficient of 0.5 similar to that used in chapter 5. All other relevant tanker and receiver aircraft data are listed previously in table 5.1. The aerodynamic derivatives of the Hercules aircraft in free air conditions, estimated in chapter 4, are given in table 6.2.

6.2 Aerodynamic Model

The tanker aircraft induces downwash and sidewash over the receiver aircraft with the induced loads dependent on the position and attitude of the receiver. The aerodynamic model described in section 5.2 is used to determine the effect of the

KC10 tanker trailing vortex wake on the Hercules receiver aircraft. The contribution of the receiver fuselage to the pitching moment is estimated using the method of Multhopp [46]

$$(C_m)_{Fuselage} = \frac{1}{36.5S\bar{c}} \int_0^{l_{Fus}} W_{Fus}^2 \alpha_l dx$$

where α_l, in degrees, is the local angle of attack along the receiver fuselage which is given by

$$\alpha_l = \alpha_{Fuselage} - (\epsilon_T + \epsilon_R)$$

The integration is evaluated numerically using the same method described in section C.6. The contributions of the receiver fuselage to the lift and induced drag are neglected.

The variations of the side force, rolling and yawing moment coefficients with bank, yaw and pitch displacements at $z/b_T = 0.21$ and at two selected spanwise positions, viz. y/b_T=0.0 and 0.2, are shown in figures 6.1, 6.2 and 6.3, respectively. It can be seen that the variations are almost linear with ϕ and ψ in the range $\pm 10°$ and with θ in the range $\pm 5°$. Figures 6.4, 6.5 and 6.6 give the variations of the lift L (Z=-L), induced drag D_i (X=-D_i) and pitching moment coefficients with bank, yaw and pitch displacements at the same lateral and vertical separations mentioned above. The variations are also linear with the displacement angles in the range $\pm 10°$. This allows the induced forces and moments due to the receiver attitude to be represented by aerodynamic derivatives. These are also shown by contour plots. On the tanker wake centre line, the derivatives C_{l_θ}, C_{n_θ}, C_{Y_θ}, $C_{D_{i_\phi}}$, C_{L_ϕ}, C_{m_ϕ}, $C_{D_{i_\psi}}$, C_{L_ψ} and C_{m_ψ} are all zero.

The sidewash and downwash induced by the tanker wing at the position of the

receiver wing are shown in figures 6.7 and 6.8, respectively. The highest downwash occurs near the centreline of the tanker wing wake with upwash produced outboard of the wing tip. The highest sidewash is produced near the centre of the tip vortex which is in the region of $z/b_T = 0.43$ with the sidewash changing direction above the tanker wing wake.

6.3 Aerodynamic Results

Normally in air-to-air refuelling the receiver is positioned below the tanker wing wake although the fin may experience buffeting as it penetrates the tanker wake. All of the present results correspond to the receiver located downstream at a distance between the tanker and receiver datum points (which are located at the wing apex points) of 1.04 times the tanker wing span. The minimum vertical separation between the datum points is 0.15 times the tanker wing span which positions the receiver datum point just below the tanker wing wake. All the aerodynamic forces and moments acting on the receiver due to its position and attitude within the tanker wing wake are considered. As described above, the aerodynamic loads due to receiver attitude are given in terms of aerodynamic derivatives which consist of 18 terms, viz. X, Y, Z, L, M and N due to ϕ, θ and ψ. In order to assess the significance of the forces and moments on the receiver due to its position and attitude they are compared with the receiver's aerodynamic characteristics in free air. For example, the lift and induced drag coefficients are compared with C_{L_∞} and $C_{D_{i_\infty}}$, respectively. The receiver aerodynamic derivatives are compared with

the corresponding static stability derivatives due to angle of attack and sideslip. For example, the derivative C_{l_ϕ} is compared with C_{l_β}. This approach is valid if all the angles involved in any simulation viz. α, β, ϕ, θ and ψ are comparable in magnitude.

6.3.1 Contours of Forces and Moments due to Receiver position

Rolling Moment Parameter ($C_l/C_{l_{\delta_a}}$)

The induced rolling moment coefficient shown in figure 6.9 is essentially due to the downwash variation in the spanwise direction. Thus, the peak amplitudes of the rolling moment coefficient occur in the region $0.25 < y/b_T < 0.5$ where the highest spanwise downwash gradients are produced. The wing is the major contributor to the rolling moment coefficient with small contributions from the fin, tailplane and fuselage. The fin and fuselage contributions act in the opposite direction to the contributions from the wing and tailplane. The rolling moment coefficient is compared with the rolling moment coefficient due to aileron deflection in order to indicate the scale of this term. For a linear behaviour of the ailerons, this ratio gives the aileron deflection, in radians, required to balance the induced rolling moment since for trim $C_l = \delta_a C_{l_{\delta_a}}$. Figure 6.9 then shows the high rolling moment produced as the receiver is displaced outboard with the rolling moment acting in a stable sense tending to direct the lift vector towards the centreline of the tanker wake. As the receiver is displaced outboard of the tanker wing tip it experiences an

upwash over the inner wing which reverses the direction of the rolling moment. In flight tests, Bradley [5] found that it was not possible to refuel a Hercules receiver aircraft from a Tristar tanker wing refuelling station due to the large aileron and rudder deflections required to trim the receiver. This is consistent with the large aileron deflections shown in figure 6.9.

Yawing Moment Parameter ($C_n/C_{n_{\delta_r}}$)

The yawing moment coefficient depends mainly on the sidewash over the fin and fuselage with a small contribution due to the asymmetric loading on the receiver wing. Peak amplitudes then occur close to the centre of the tip vortex. Figure 6.10 shows the corresponding high value of the yawing moment coefficient compared with the yawing moment coefficient due to rudder deflection. This ratio gives the rudder deflection, in radians, required to balance the induced yawing moment which acts in a stable sense tending to yaw the nose of the receiver towards the centreline of the tanker wake. The large rudder deflections shown in figure 6.10 are again consistent with the flight test data [5] mentioned above.

Side Force Parameter (C_Y/C_{L_∞})

The side force coefficient, which is similar in form to the yawing moment coefficient, is also due mainly to the sidewash over the receiver fin and fuselage. Both the fin and fuselage contributions are destabilising tending to move the receiver away from the tanker wake centre line. Figure 6.11 shows the variation of the ratio of the side force coefficient C_Y to the lift coefficient in free air C_{L_∞} with the peak amplitudes

again occurring close to the centre of the tip vortex. This ratio is equivalent to the bank angle, in radians, required to prevent sideways drift of the receiver since $C_Y = \phi C_{L_\infty}$.

Induced Drag Parameter ($C_{D_i}/C_{D_{i_\infty}}$)

The change in the receiver induced drag at constant pitch attitude is due to the reduction in the angle of attack, and the backwards tilt of the lift vector. These components act in opposite directions and the net result is shown in figure 6.12 in comparison with the free air value. The wing is the major contributor to the receiver induced drag with a small contribution from the tailplane which is in the downwash of both tanker and receiver wings. The receiver induced drag increases as the tanker/receiver vertical separation is reduced. This is due to the increase in the tanker induced downwash on the receiver as it approaches the tanker from below. The highest changes in the receiver induced drag occur near the tanker wake centreline where the downwash is highest and reverse in sign in the upwash region outboard of the tanker wing tip. The induced drag coefficient is equal to $(-C_X)$.

Lift Force Parameter (C_L/C_{L_∞})

The change in the receiver lift coefficient, which is equal to $(-C_Z)$, is shown in figure 6.13 in comparison with the free air value. The contours of the lift and induced drag coefficients are similar in form since the changes in both coefficients depend on the tanker downwash. Since the angle of attack is equal to the pitch

angle θ minus the downwash angle ϵ, the receiver lift coefficient near the tanker wake centre line decreases as the vertical separation is reduced. The opposite applies in the upwash region outboard of the tanker wing tip vortex.

Pitching Moment Parameter ($C_m/C_{m_{\delta_e}}$)

Pitching moment coefficients on the receiver are associated with three effects. The major effect is the tanker downwash which reduces the receiver incidence and the inherent static stability of the aircraft produces a nose-up pitching moment. Secondly the mean tanker downwash over the wing is less than that over the tailplane producing a nose-up moment. Thirdly the tanker downwash changes the lift distribution over the receiver wing and consequently the downwash over the receiver tailplane. Figure 6.14 shows the contours of the resulting nose-up pitching moment coefficient compared with the pitching moment coefficient due to elevator deflection. This ratio gives the elevator deflection, in radians, required to balance the tanker induced pitching moment. Near the tanker wake centre line, a nose-up pitching moment is produced which increases in magnitude as the receiver approaches the tanker from below. The pitching moment changes direction in the upwash region where $y/b_T > 0.5$.

6.3.2 Contours of Forces and Moments due to Receiver attitude

Forces and Moments due to Bank Angle Displacement

Rolling Moment Derivative Ratio (C_{l_ϕ}/C_{l_β})

Near the centreline of the tanker wake the effect of banking the receiver produces a stabilising effect with the downgoing wing experiencing less downwash and the upgoing wing experiencing more downwash. The resulting rolling moment tends to maintain the wings level. Figure 6.15 shows the relative significance of the rolling moment derivative C_{l_ϕ} compared with the corresponding lateral static stability derivative C_{l_β}. The main contribution is from the receiver wing with negligibly small contribution from the fin, tailplane and fuselage. The highest values of the rolling moment derivative occur on the centre line of the tanker wake where the downwash gradient in the vertical direction is highest. In the upwash region outboard of the tanker wing tip, the rolling moment derivative is destabilising tending to increase the bank displacement.

Yawing Moment Derivative Ratio (C_{n_ϕ}/C_{n_β})

The effect of banking the receiver is to produce a component of the tanker downwash acting normal to the fin. This is the main term in the yawing moment and side force derivatives. Figure 6.16 shows the yawing moment derivative C_{n_ϕ} compared with the corresponding directional static stability derivative C_{n_β}. As the receiver

is displaced outboard of the tanker wing tip, the upwash component normal to the receiver fin reverses the direction of the yawing moment. Peak amplitudes occur on the tanker wake centreline where the downwash is highest. Although the values of C_{n_ϕ} are relatively small, the term ϕC_{n_ϕ} was considered significant when analysing trim in steady sideslip in air-to-air refuelling as described in chapter 5. This is because the angle of bank required to trim the receiver in steady sideslip is greater than the angle of sideslip.

Side Force Derivative Ratio (C_{Y_ϕ}/C_{Y_β})

Figure 6.17 shows the side force derivative C_{Y_ϕ} in comparison with the side force derivative due to sideslip C_{Y_β}. The derivative C_{Y_ϕ}, which is similar in form to C_{n_ϕ}, is relatively small. The peak amplitudes occur on the tanker wake centreline with the side force acting in stable sense outboard of the tanker wing tip.

Induced Drag, Pitching Moment and Lift Force Derivative Ratios ($C_{D_{i_\phi}}/C_{D_{i_\alpha}}$, C_{m_ϕ}/C_{m_α}, C_{L_ϕ}/C_{L_α})

The derivatives $C_{D_{i_\phi}}$, C_{m_ϕ} and C_{L_ϕ} compared with the corresponding derivatives due to incidence are shown in figures 6.18, 6.19 and 6.20, respectively. These derivatives, which exhibit a similarity, depend on the tanker downwash over the receiver wing and tailplane. It can be seen that the derivatives are relatively small with the ratios $C_{D_{i_\phi}}/C_{D_{i_\alpha}}$, C_{m_ϕ}/C_{m_α} and C_{L_ϕ}/C_{L_α} equal to zero on the centreline of the tanker wake and increasing to peak amplitudes less than 7% outboard of the wing tip.

Forces and Moments due to Yaw angle Displacement

Side Force, Yawing and Rolling Moment Derivative Ratios (C_{Y_ψ}/C_{Y_β}, C_{n_ψ}/C_{n_β}, C_{l_ψ}/C_{l_β})

Yawing the receiver changes the sidewash over the fin producing a side force and yawing moment with negligible rolling moment. The yawing moment, side force and rolling moment derivatives compared with the corresponding static stability derivatives are shown in figures 6.21, 6.22 and 6.23, respectively. Peak amplitudes occur on the centreline and outboard of the tanker wing tip where the spanwise gradients of sidewash are highest. Compared with the corresponding static stability derivatives due to sideslip, only the ratio C_{n_ψ}/C_{n_β} is significant. The prime contribution to the yawing moment is due to the effect of the tanker sidewash on the receiver fin with negligibly small contribution from the fuselage. Near the tanker wake centre line, the yawing moment acts in destabilising sense which leads to a reduction in the directional stability of the receiver aircraft.

Pitching Moment, Lift Force and Induced Drag Derivative Ratios (C_{m_ψ}/C_{m_α}, C_{L_ψ}/C_{L_α}, $C_{D_{i_\psi}}/C_{D_{i_\alpha}}$)

Yawing the receiver also changes the downwash over the tailplane resulting in a significant nose-up pitching moment as shown in figure 6.24 where the derivative C_{m_ψ} is compared with the derivative C_{m_α}. Peak amplitudes occur close to the centre of the tip vortex where the spanwise gradients of downwash are highest.

The derivatives C_{L_ψ} and $C_{D_{i_\psi}}$ associated with the changes in the tailplane lift and

drag are negligibly small as shown in figures 6.25 and 6.26 where the derivatives C_{L_ψ} and $C_{D_{i_\psi}}$ are compared with the derivatives C_{L_α} and $C_{D_{i_\alpha}}$, respectively.

Forces and Moments due to pitch angle Displacement

Pitching Moment, Lift Force and Induced Drag Derivative Ratios ($C_{m_\theta}/C_{m_\alpha}$, $C_{L_\theta}/C_{L_\alpha}$, $C_{D_{i_\theta}}/C_{D_{i_\alpha}}$)

Pitching the receiver aircraft nose-up moves the tailplane into a region of lower or higher downwash and results in a significant pitching moment as shown in figure 6.27 where the derivative C_{m_θ} is compared with C_{m_α}. Peak amplitudes are produced at the centreline where the downwash is highest with the pitching moment changing sign as the receiver aircraft moves into the region of upwash outboard of the tanker wing tip. Near the tanker wake centreline, the pitching moment acts in a stable sense tending to return the receiver to its original position.

The derivatives $C_{D_{i_\theta}}$ and C_{L_θ} associated with the tailplane drag and lift increments are negligibly small as shown in figures 6.28 and 6.29 where the ratios $C_{D_{i_\theta}}/C_{D_{i_\alpha}}$ and $C_{L_\theta}/C_{L_\alpha}$ are plotted, respectively.

Side Force, Yawing and Rolling Moment Derivative Ratios (C_{Y_θ}/C_{Y_β}, C_{n_θ}/C_{n_β}, C_{l_θ}/C_{l_β})

Pitching the receiver also alters the sidewash over the fin producing a significant yawing moment as shown by the contour plot of the ratio C_{n_θ}/C_{n_β} given in figure 6.30. The associated side force and rolling moment derivatives are relatively

small as shown in figures 6.31 and 6.32, respectively, where the derivatives C_{Y_θ} and C_{l_θ} are compared with the corresponding derivatives due to sideslip.

Finally, the peak amplitudes of the forces and moments acting on the receiver due to its position and attitude compared with the receiver's aerodynamic characteristics in free air are summarised in table 6.3. It can be concluded that for an air-to-air refuelling flight simulator of the KC10 tanker and Hercules receiver aircraft, all the receiver forces and moments due to its position are significant. However, some of the receiver longitudinal and lateral aerodynamic derivatives due to its attitude are relatively insignificant and can be neglected. These derivatives are $C_{L_{\theta,\phi,\psi}}$, C_{m_ϕ}, $C_{D_{i_{\theta,\phi,\psi}}}$, C_{l_ψ} and $C_{Y_{\phi,\psi}}$.

Receiver position and attitude	Tanker induced forces and moments and their derivatives in non-dimensional form					
x,y,z	C_X	C_Z	C_m	C_Y	C_n	C_l
θ	C_{X_θ}	C_{Z_θ}	C_{m_θ}	C_{Y_θ}	C_{n_θ}	C_{l_θ}
ϕ	C_{X_ϕ}	C_{Z_ϕ}	C_{m_ϕ}	C_{Y_ϕ}	C_{n_ϕ}	C_{l_ϕ}
ψ	C_{X_ψ}	C_{Z_ψ}	C_{m_ψ}	C_{Y_ψ}	C_{n_ψ}	C_{l_ψ}

Table 6.1: Hercules receiver forces and moments due to its position and attitude within KC10 tanker wing wake.

C_{Y_β}=-0.967 rad^{-1}	C_{n_β}= 0.0796 rad^{-1}	C_{l_β}=-0.103 rad^{-1}
C_{L_α}=6.235 rad^{-1}	C_{m_α}= -2.466 rad^{-1}	$C_{D_{i_\alpha}}$=0.2 rad^{-1}
$C_{l_{\delta_a}}$=-0.229 rad^{-1}	$C_{n_{\delta_r}}$=-0.103 rad^{-1}	$C_{m_{\delta_e}}$=-3.53 rad^{-1}
C_{L_∞}=0.783	$C_{D_{i_\infty}}$=0.0196	

Table 6.2: Hercules aerodynamic data in free air.

Receiver position and attitude	Peak amplitudes of tanker induced forces and moments and their derivatives in non-dimensional form		
x,y,z	$\mid C_l/C_{l_{\delta_a}} \mid = 0.14$	$\mid C_n/C_{n_{\delta_r}} \mid = 0.07$	$\mid C_Y/C_{L_\infty} \mid = 0.045$
	$C_{D_i}/C_{D_{i_\infty}} = 1.46$	$C_L/C_{L_\infty} = 0.6$	$\mid C_m/C_{m_{\delta_e}} \mid = 0.03$
ϕ	$\mid C_{l_\phi}/C_{l_\beta} \mid = 0.55$	$\mid C_{n_\phi}/C_{n_\beta} \mid = 0.12$	$\mid C_{Y_\phi}/C_{Y_\beta} \mid = 0.054$
	$\mid C_{D_{i_\phi}}/C_{D_{i_\alpha}} \mid = 0.073$	$\mid C_{L_\phi}/C_{L_\alpha} \mid = 0.028$	$\mid C_{m_\phi}/C_{m_\alpha} \mid = 0.03$
ψ	$\mid C_{l_\psi}/C_{l_\beta} \mid = 0.024$	$\mid C_{n_\psi}/C_{n_\beta} \mid = 0.18$	$\mid C_{Y_\psi}/C_{Y_\beta} \mid = 0.036$
	$\mid C_{D_{i_\psi}}/C_{D_{i_\alpha}} \mid = 0.016$	$\mid C_{L_\psi}/C_{L_\alpha} \mid = 0.012$	$\mid C_{m_\psi}/C_{m_\alpha} \mid = 0.12$
θ	$\mid C_{D_{i_\theta}}/C_{D_{i_\alpha}} \mid = 0.035$	$\mid C_{L_\theta}/C_{L_\alpha} \mid = 0.016$	$\mid C_{m_\theta}/C_{m_\alpha} \mid = 0.14$
	$\mid C_{l_\theta}/C_{l_\beta} \mid = 0.05$	$\mid C_{n_\theta}/C_{n_\beta} \mid = 0.25$	$\mid C_{Y_\theta}/C_{Y_\beta} \mid = 0.05$

Table 6.3: The peak amplitudes of the ratios of the KC10 tanker induced forces and moments on the Hercules and the corresponding aerodynamic characteristics of the Hercules in free air.

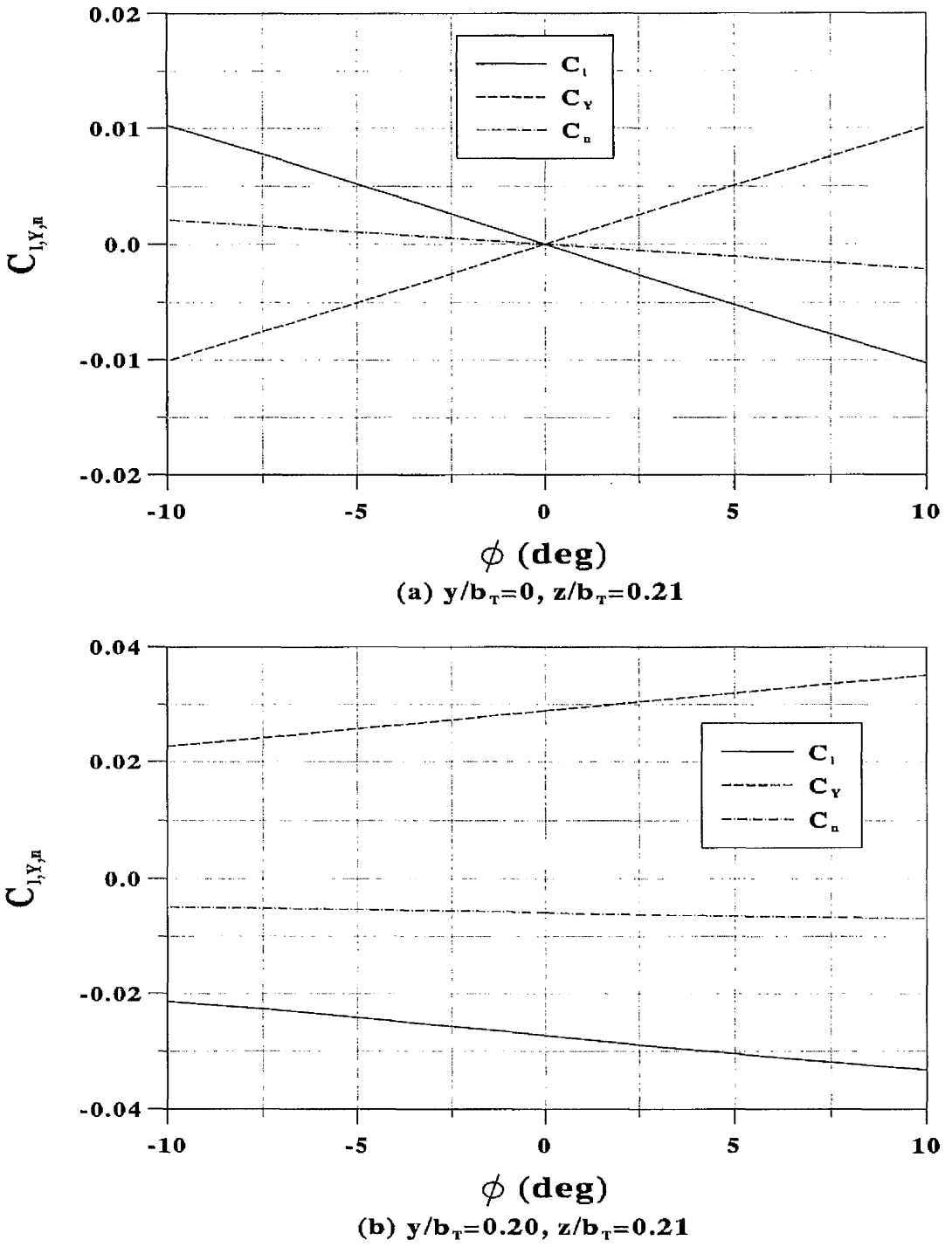

Figure 6.1: Receiver side force, rolling and yawing moments due to bank displacement.

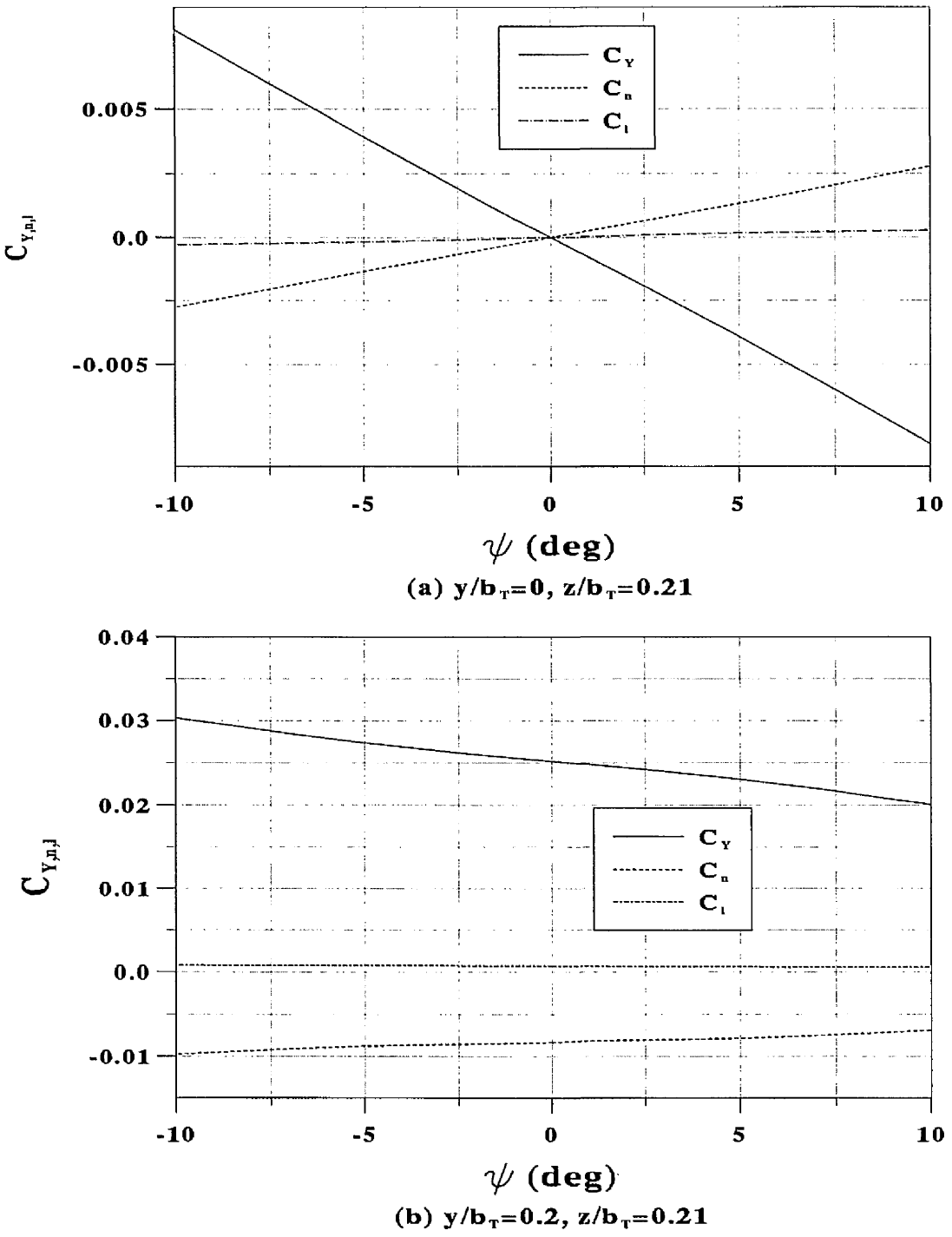

Figure 6.2: Receiver side force, rolling and yawing moments due to yaw displacement.

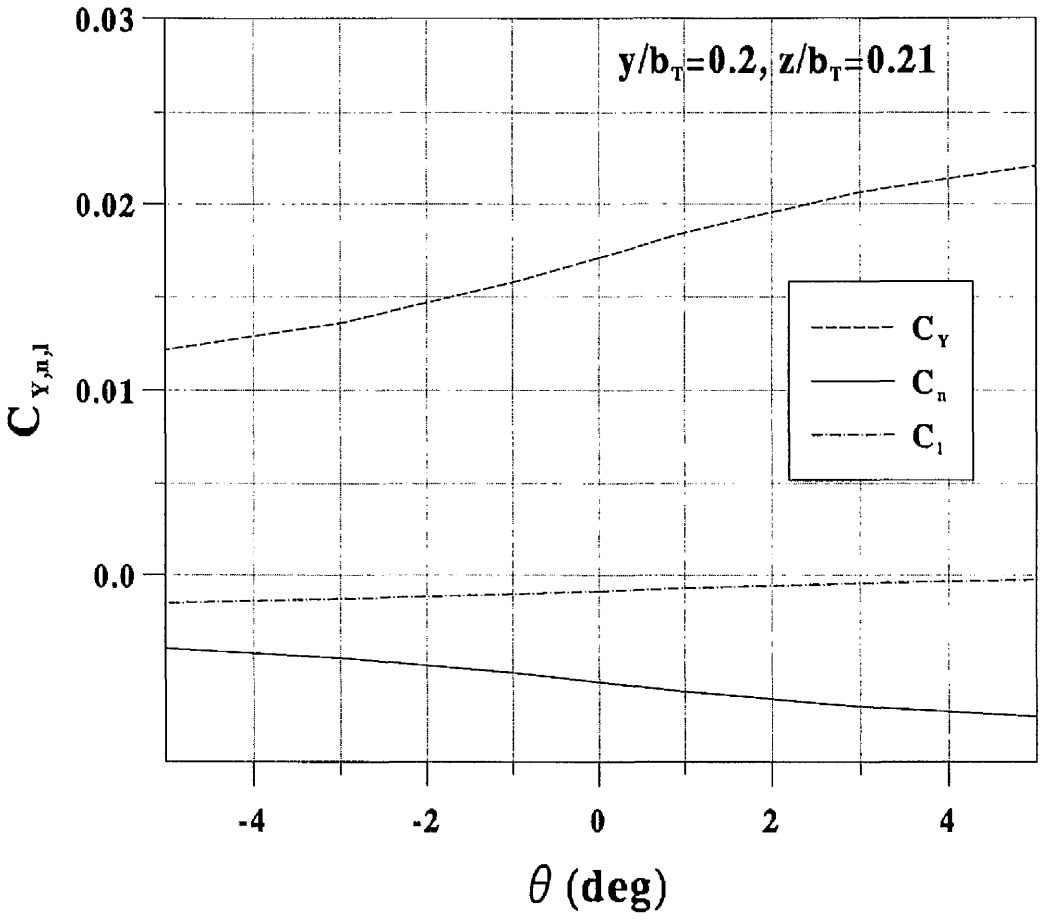

Figure 6.3: Receiver side force, yawing and rolling moments due to pitch displacement.

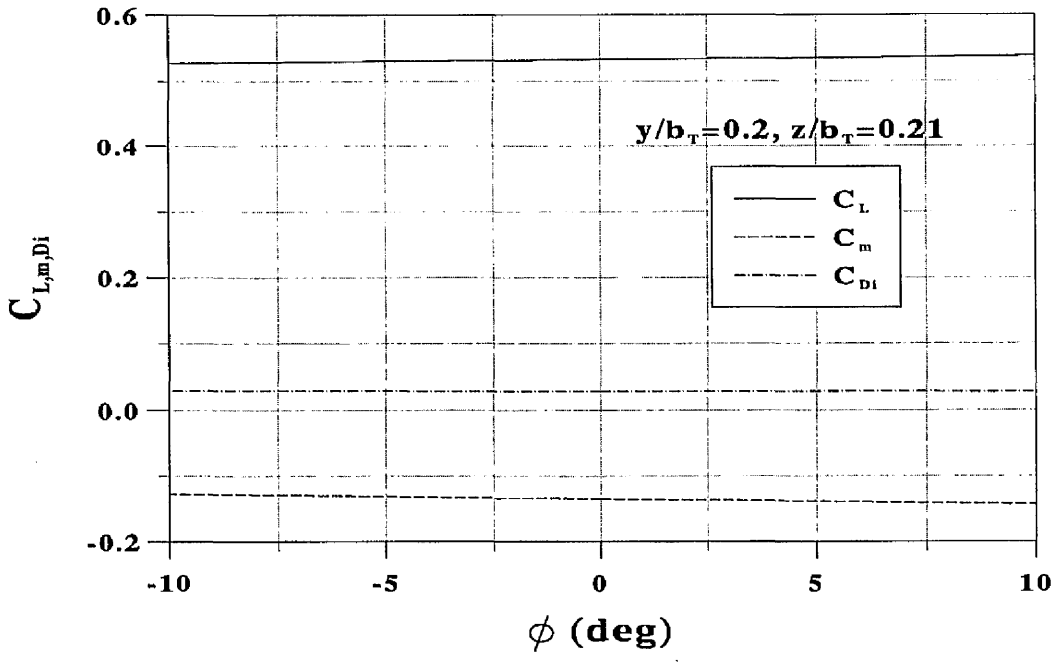

Figure 6.4: Receiver lift, induced drag and pitching moment due to bank displacement.

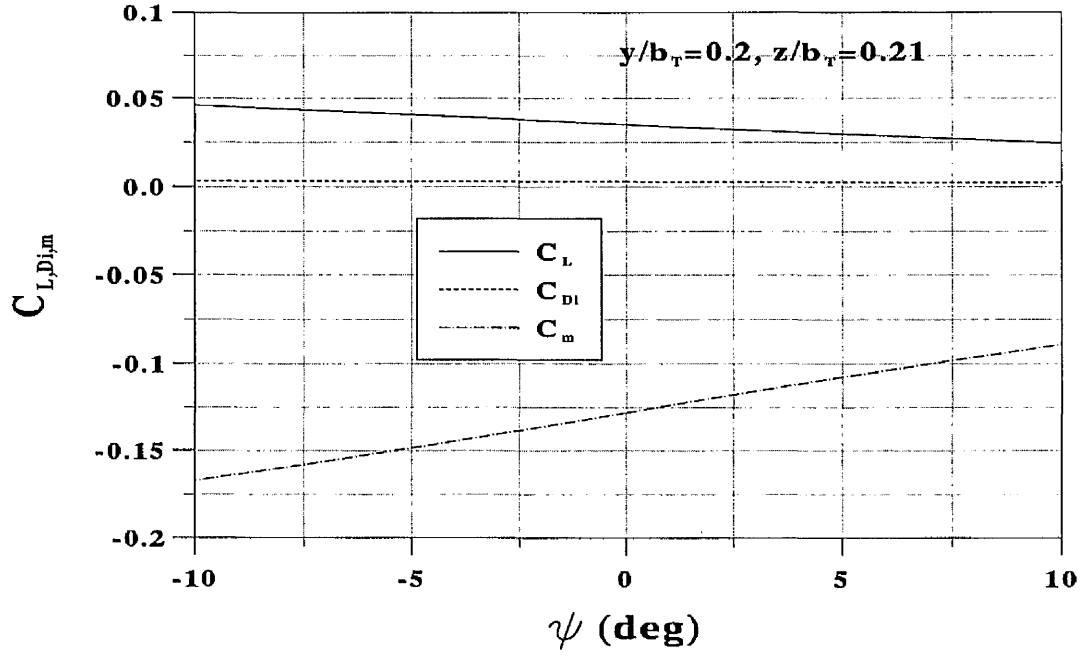

Figure 6.5: Receiver lift, induced drag and pitching moment due to yaw displacement.

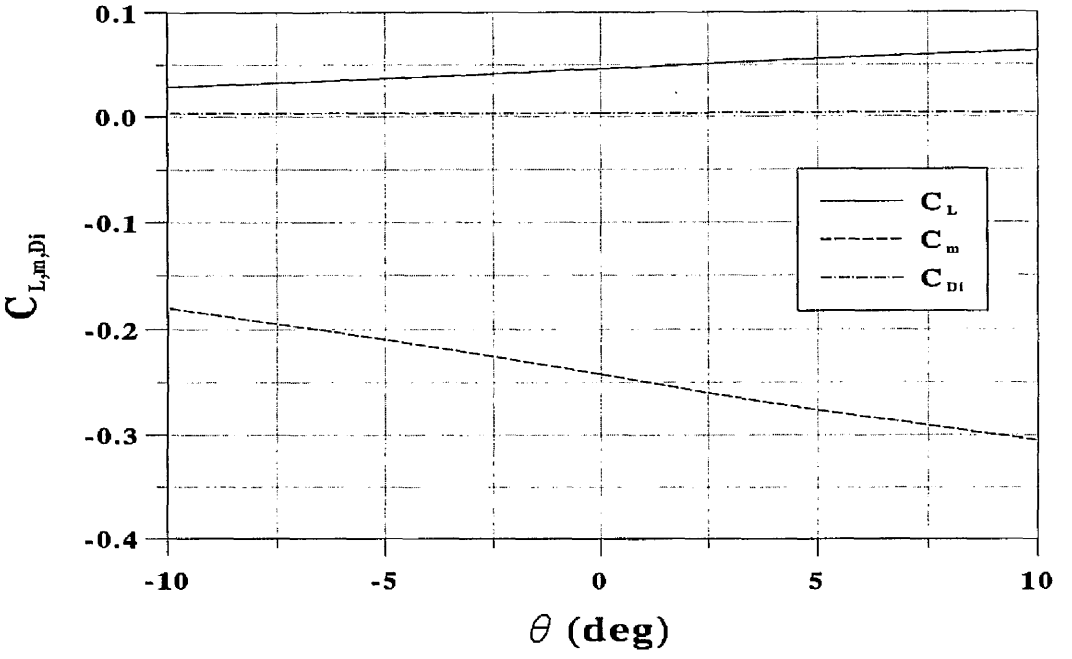

(a) $y/b_T=0$, $z/b_T=0.21$

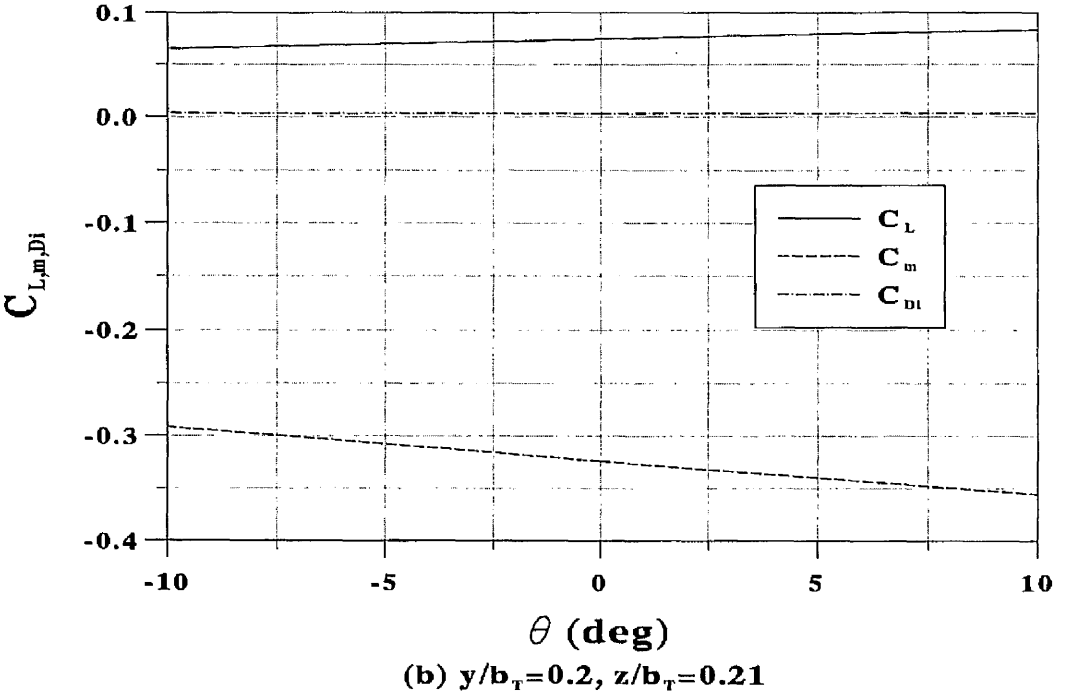

(b) $y/b_T=0.2$, $z/b_T=0.21$

Figure 6.6: Receiver lift, induced drag and pitching moment due to pitch displacement.

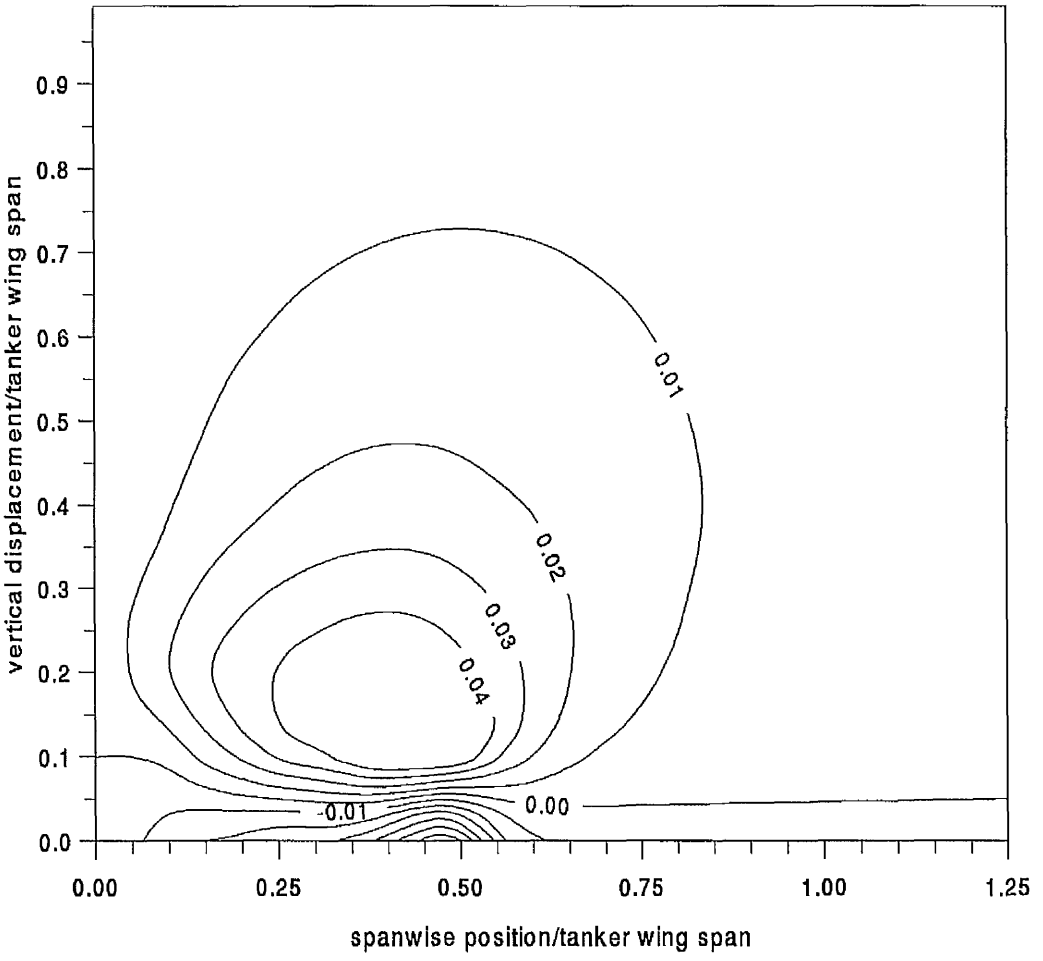

Figure 6.7: Contours of sidewash angle (rad) induced by tanker wing at position of receiver wing.

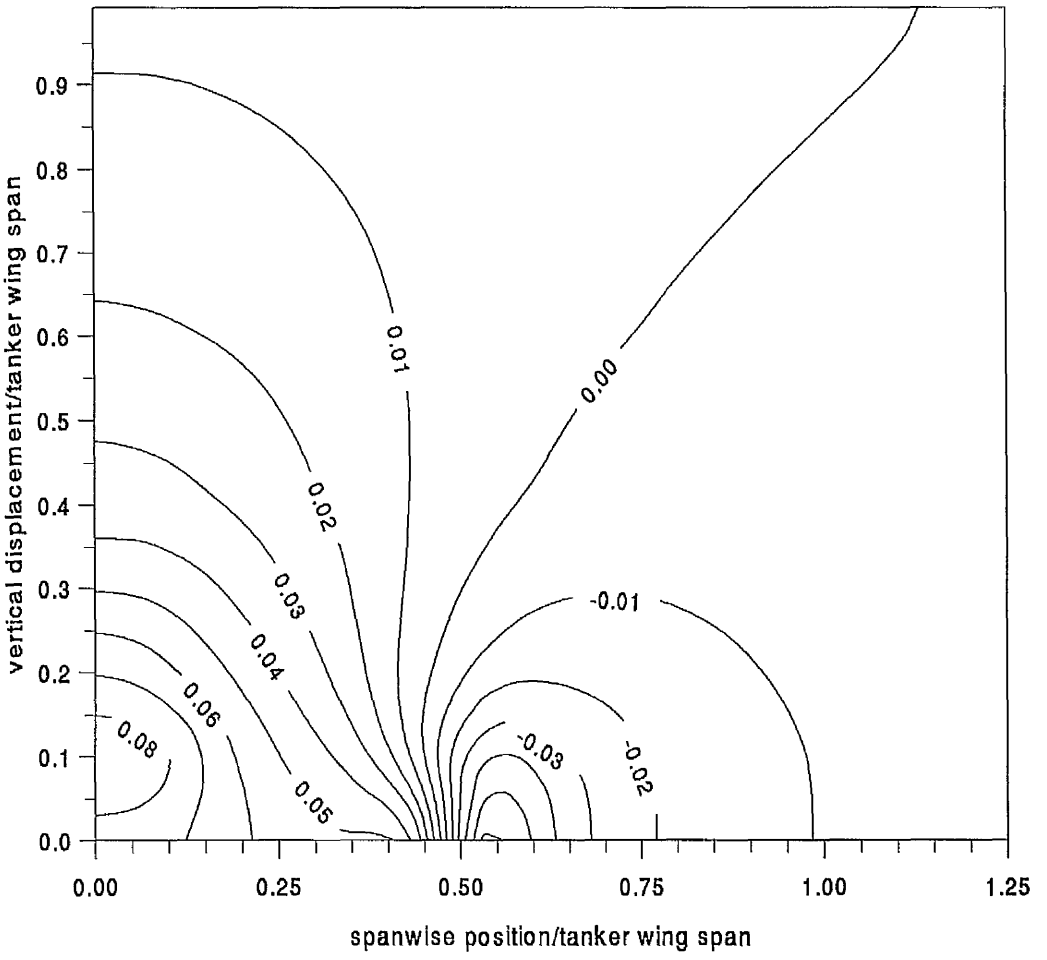

Figure 6.8: Contours of downwash angle (rad) induced by tanker wing at position of receiver wing.

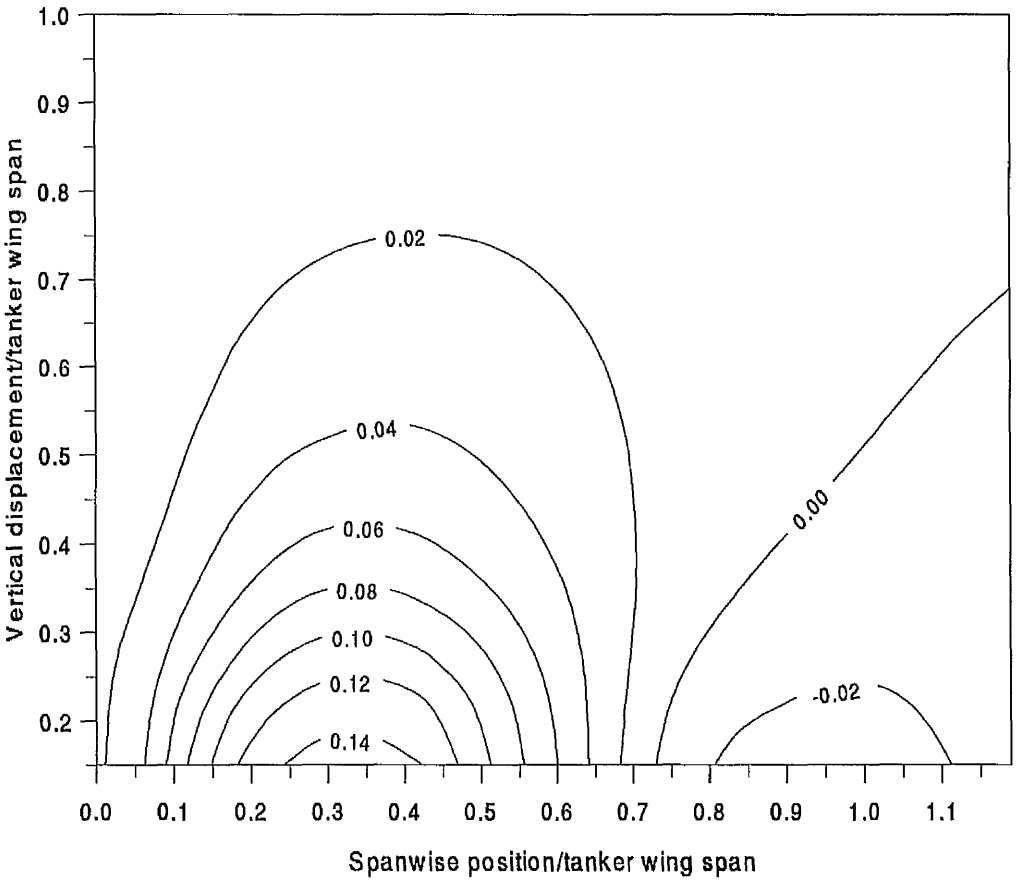

Figure 6.9: Contours of rolling moment parameter, $C_l/C_{l_{\delta_a}}$.

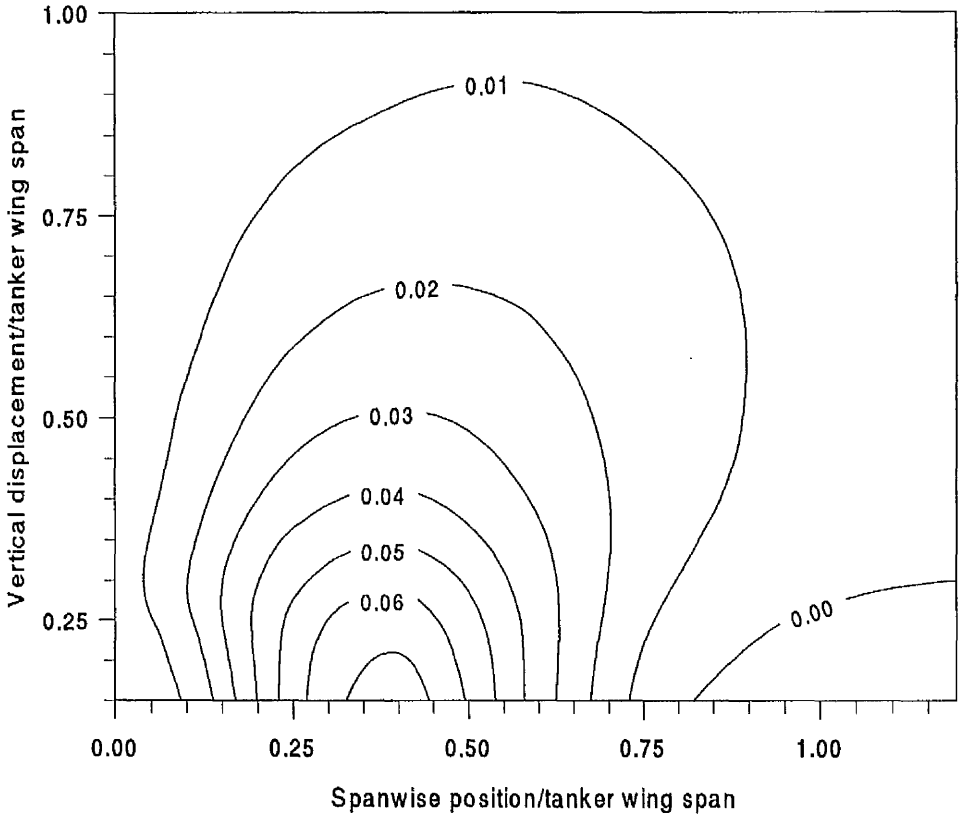

Figure 6.10: Contours of yawing moment parameter, $C_n/C_{n_{\delta_r}}$.

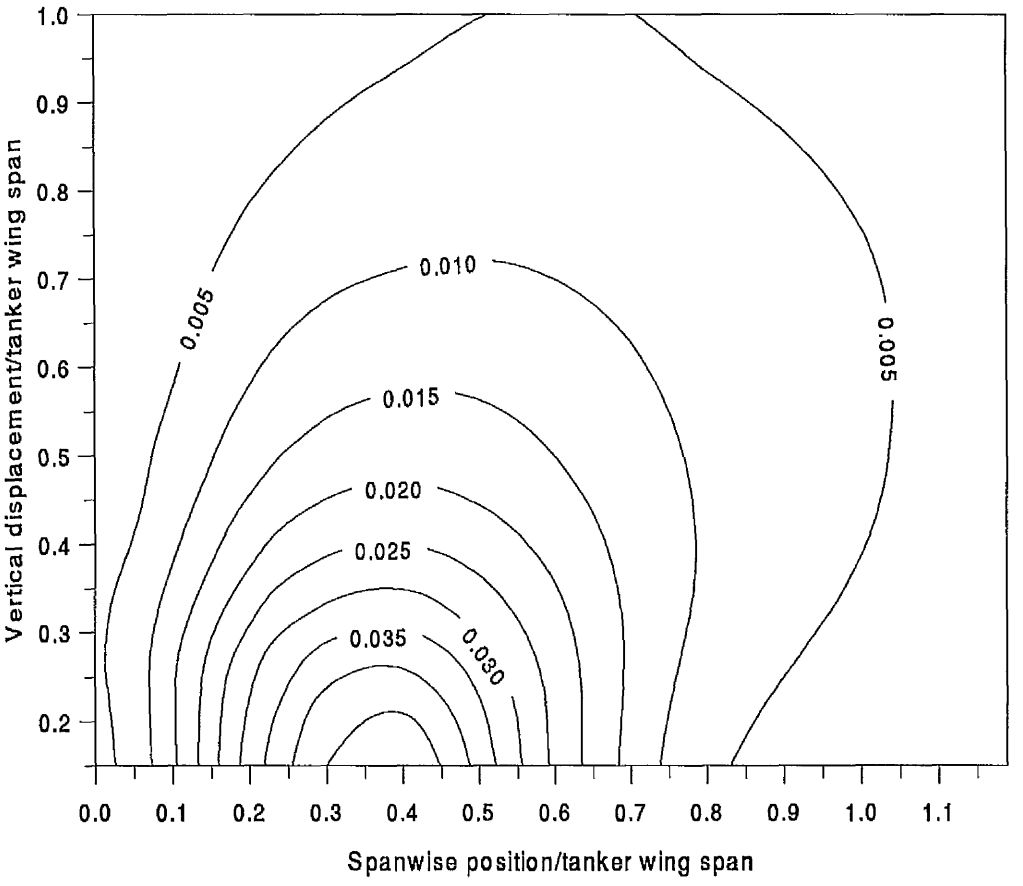

Figure 6.11: Contours of side force parameter, C_Y/C_{L_∞}.

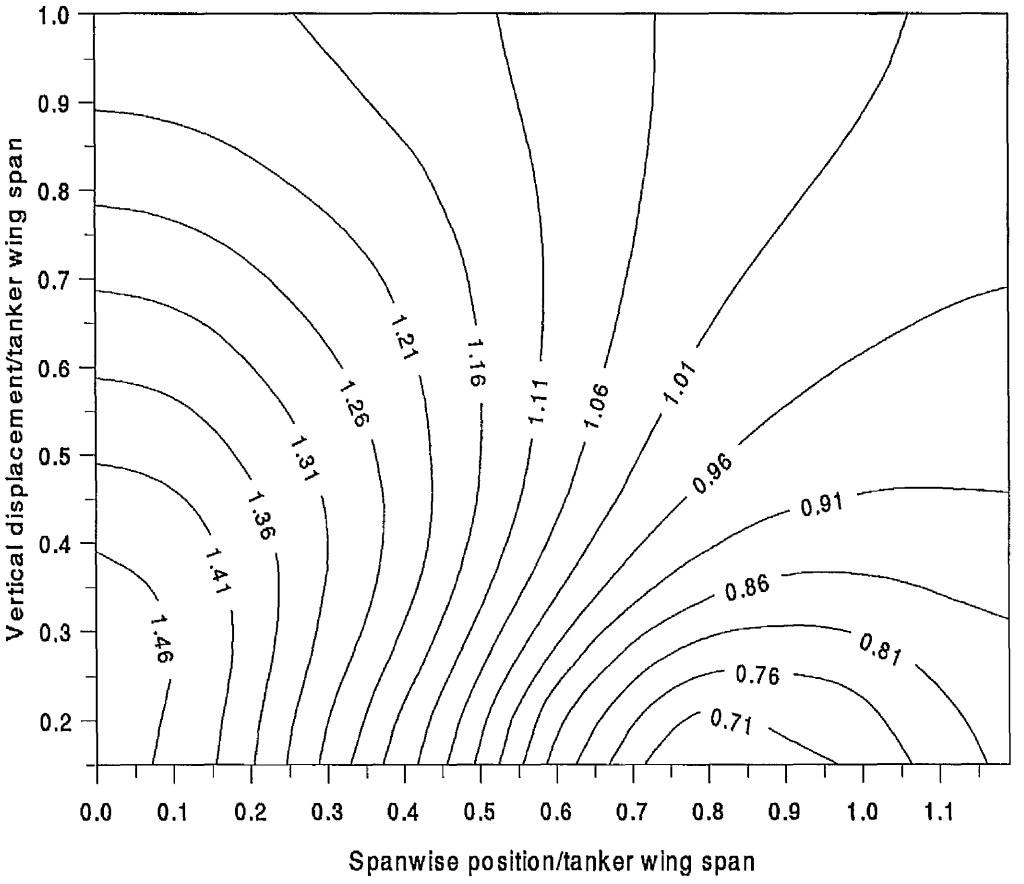

Figure 6.12: Contours of induced drag parameter, $C_{D_i}/C_{D_{i_\infty}}$.

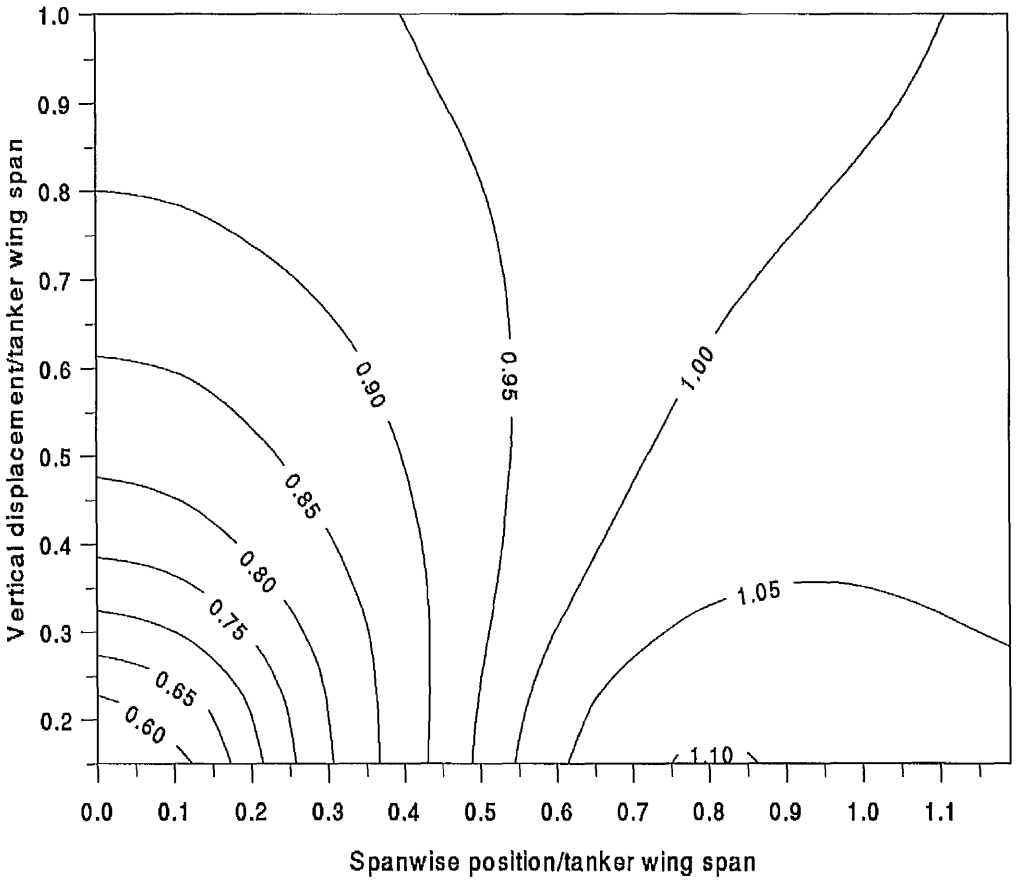

Figure 6.13: Contours of lift force parameter, C_L/C_{L_∞}.

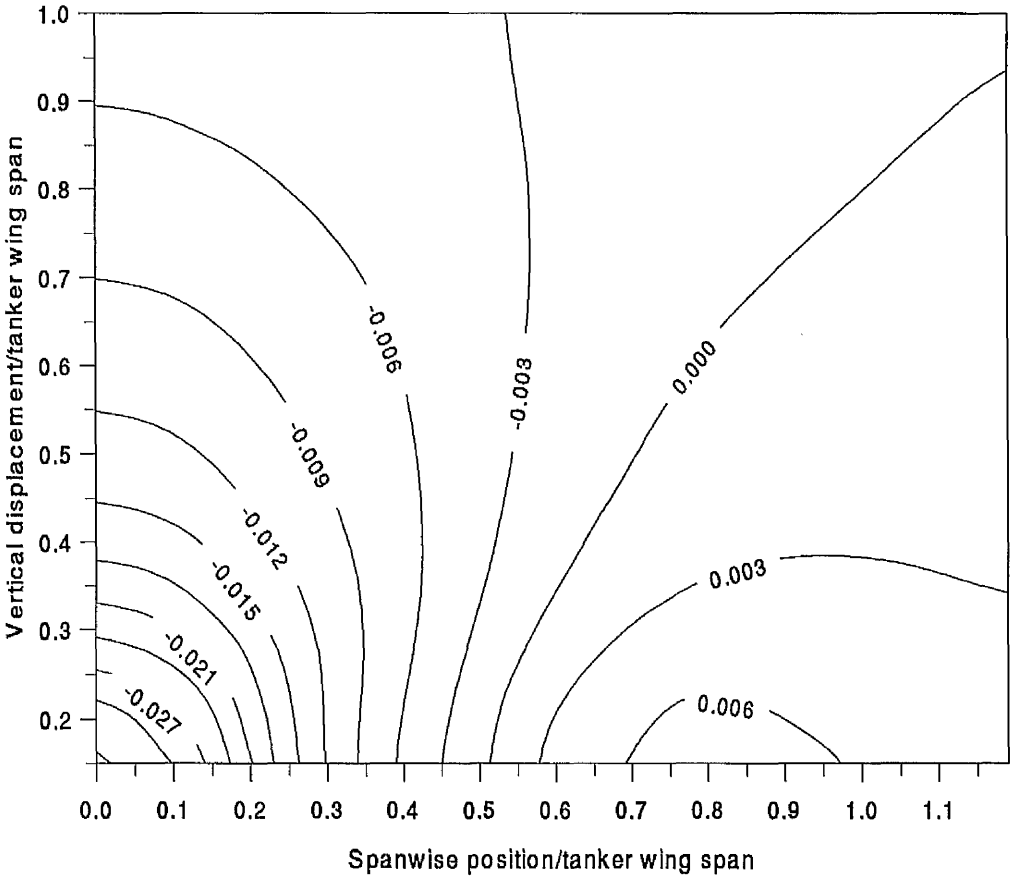

Figure 6.14: Contours of pitching moment parameter, $C_m/C_{m_{\delta_e}}$.

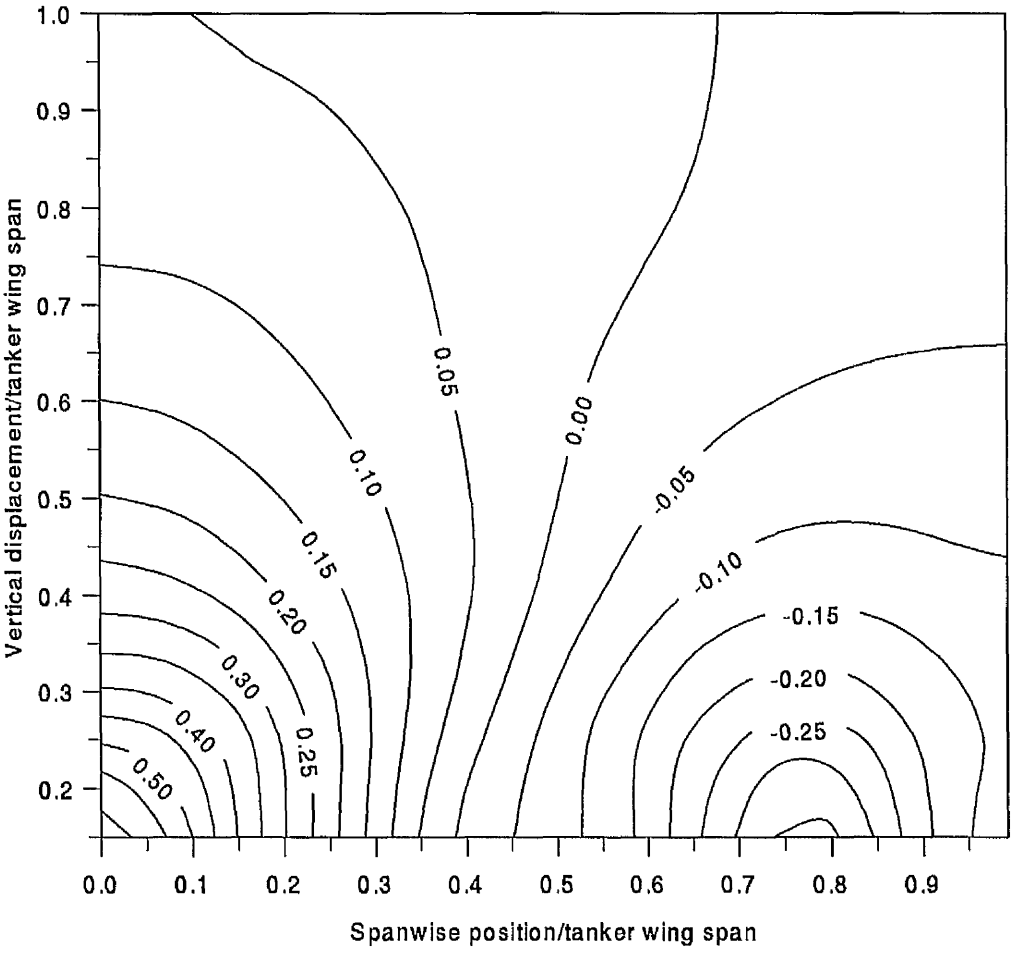

Figure 6.15: Contours of rolling moment due to bank angle ratio, C_{l_ϕ}/C_{l_β}.

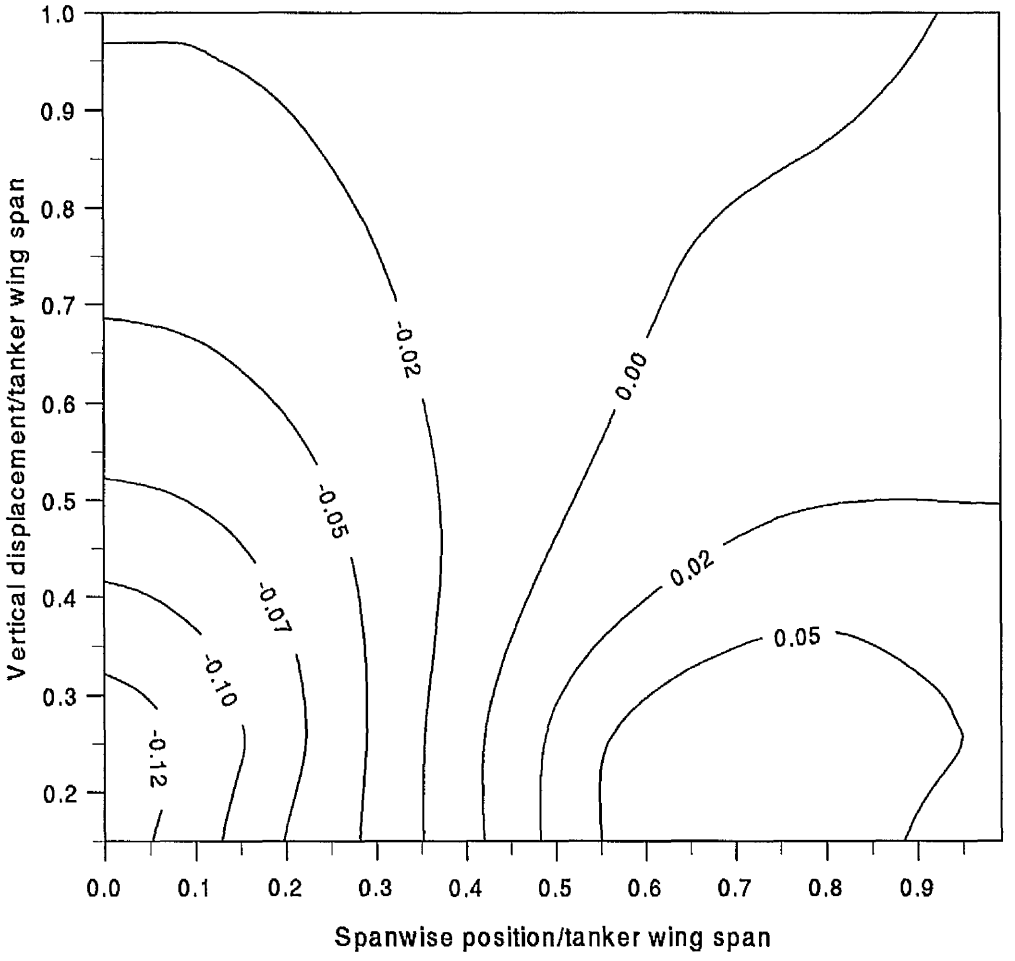

Figure 6.16: Contours of yawing moment due to bank angle ratio, C_{n_ϕ}/C_{n_β}.

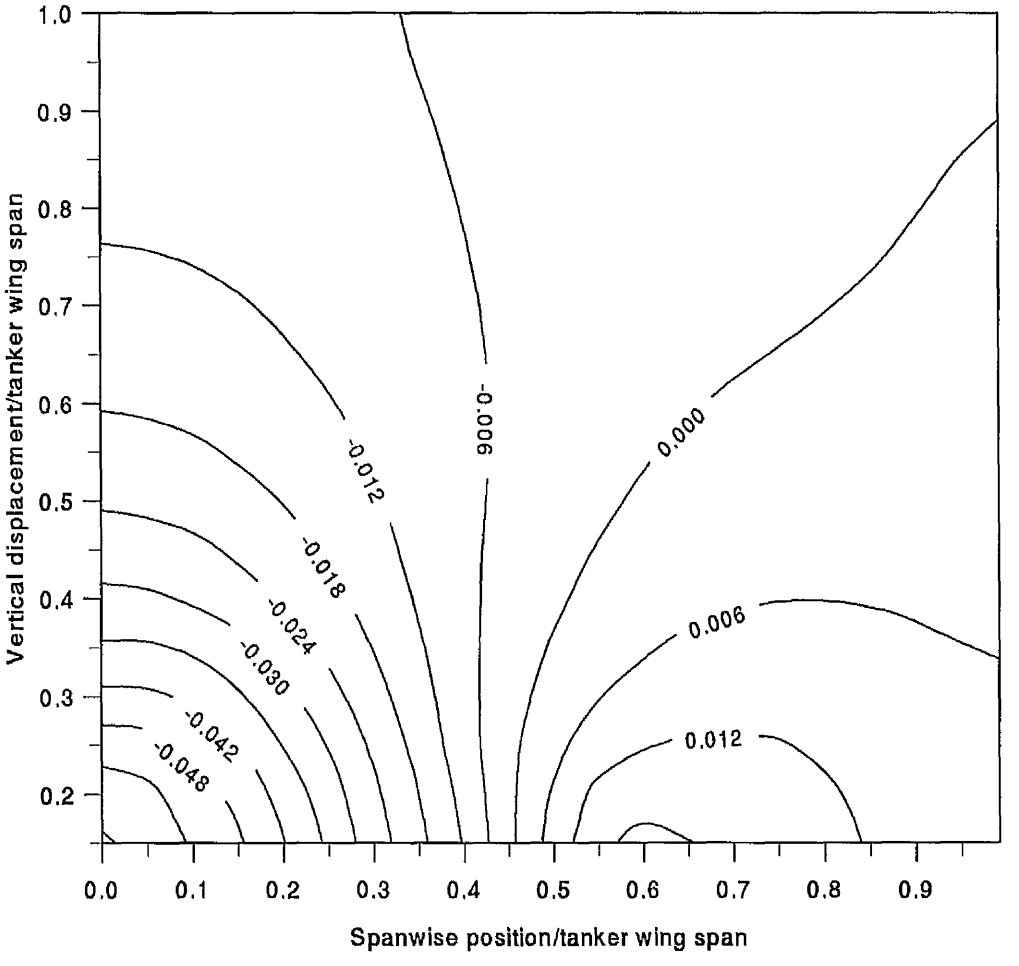

Figure 6.17: Contours of side force due to bank angle ratio, C_{Y_ϕ}/C_{Y_β}.

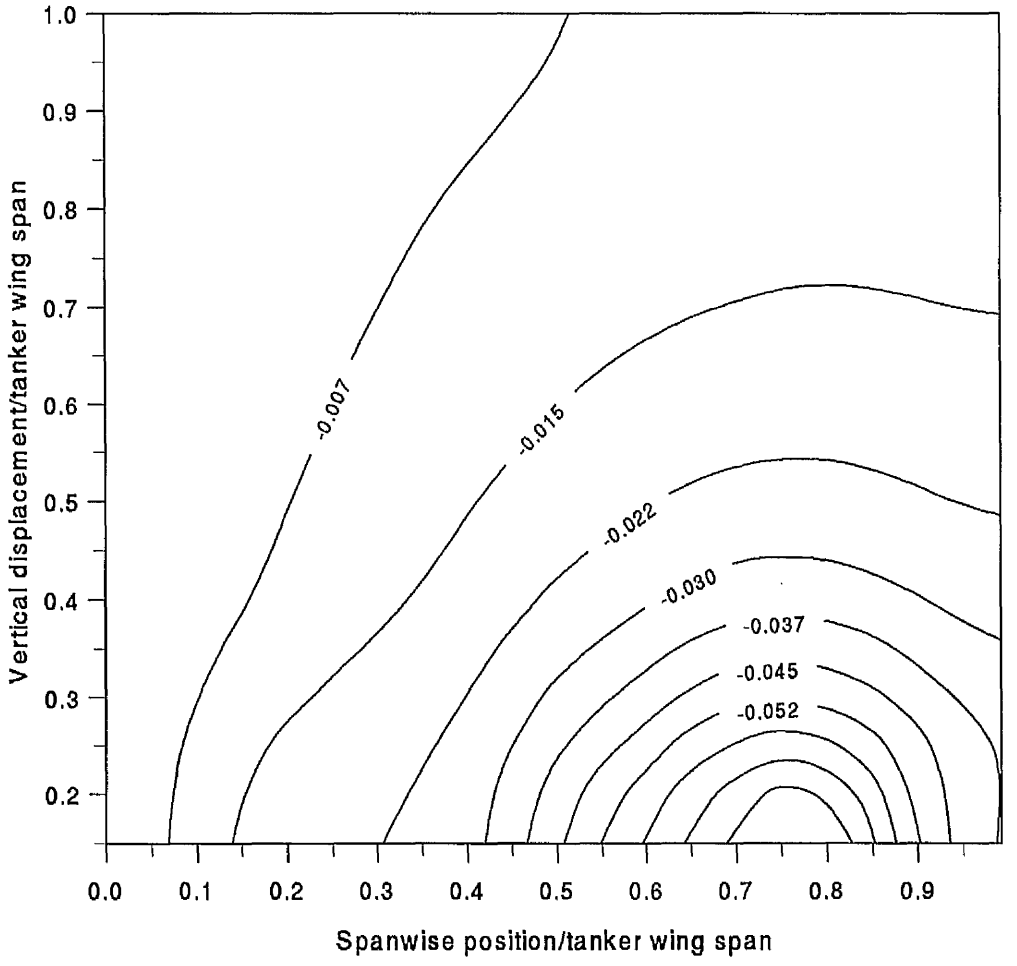

Figure 6.18: Contours of induced drag due to bank angle ratio, $C_{D_{i_\phi}}/C_{D_{i_\alpha}}$.

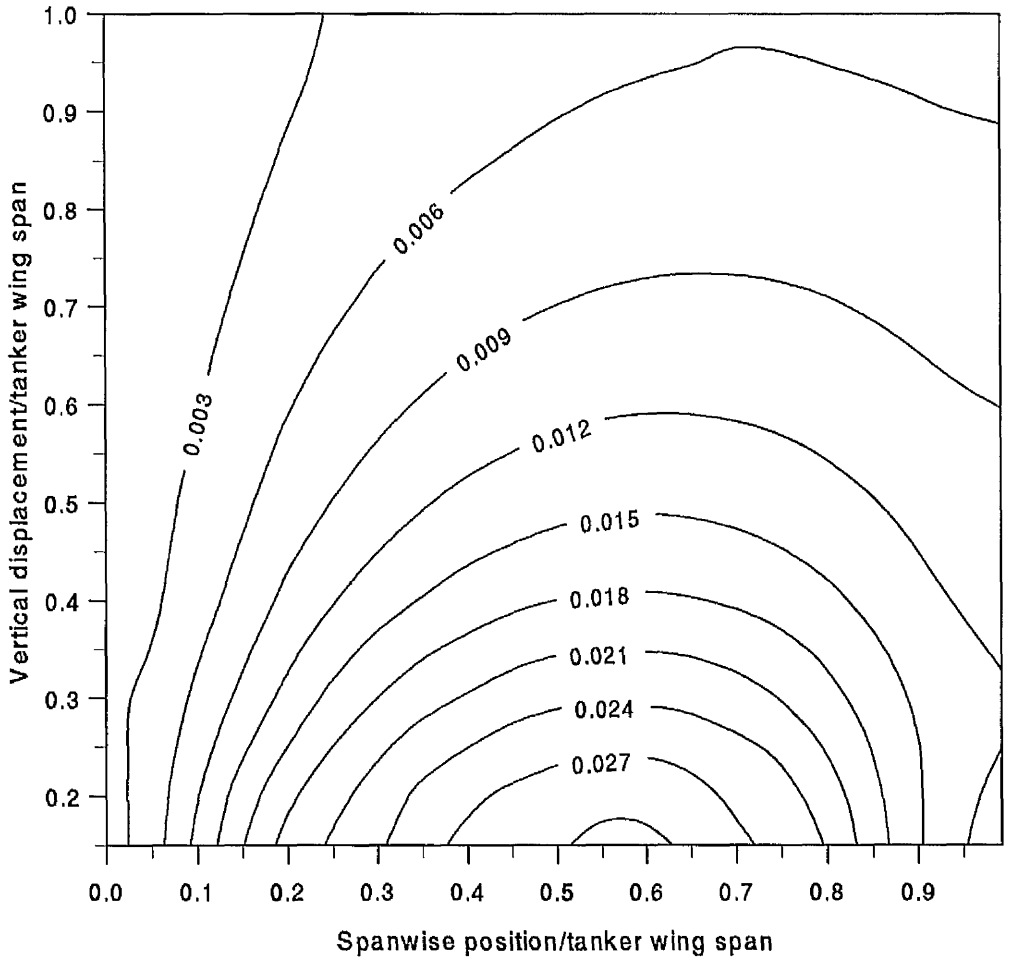

Figure 6.19: Contours of pitching moment due to bank angle ratio, C_{m_ϕ}/C_{m_α}.

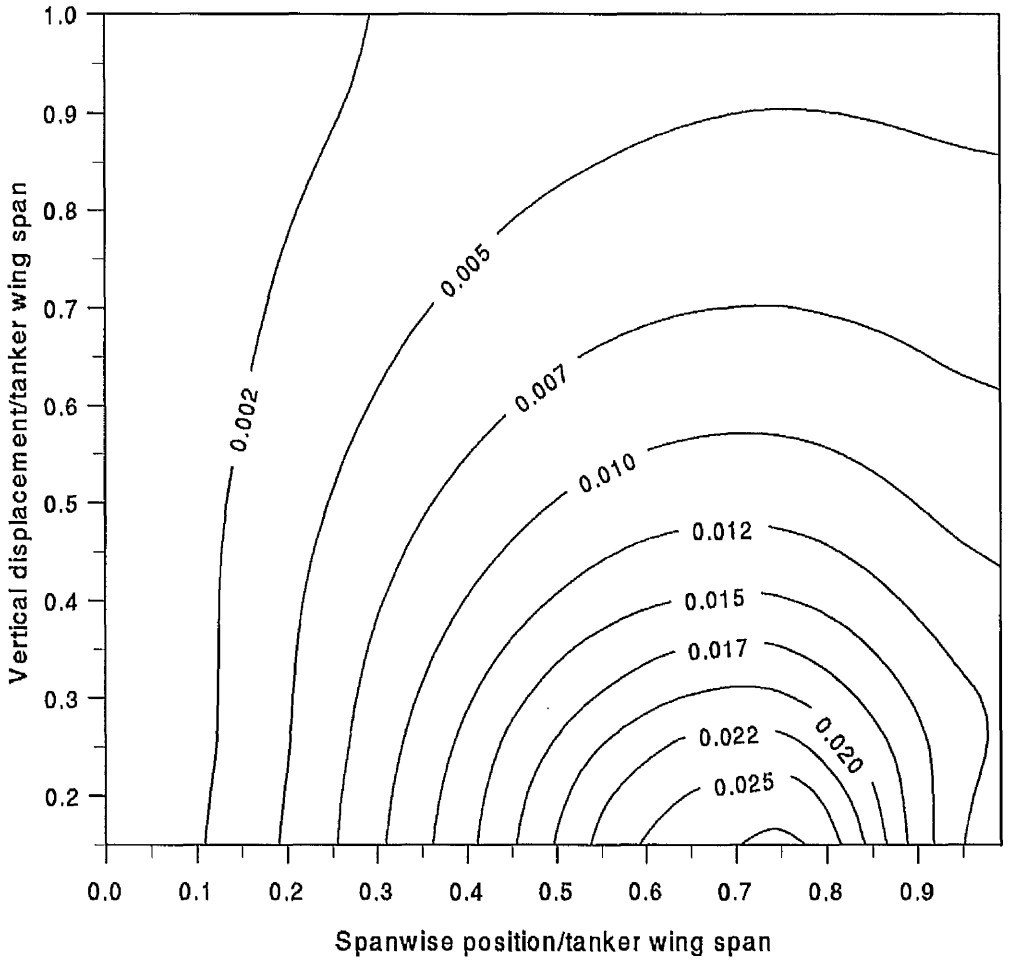

Figure 6.20: Contours of lift force due to bank angle ratio, C_{L_ϕ}/C_{L_α}.

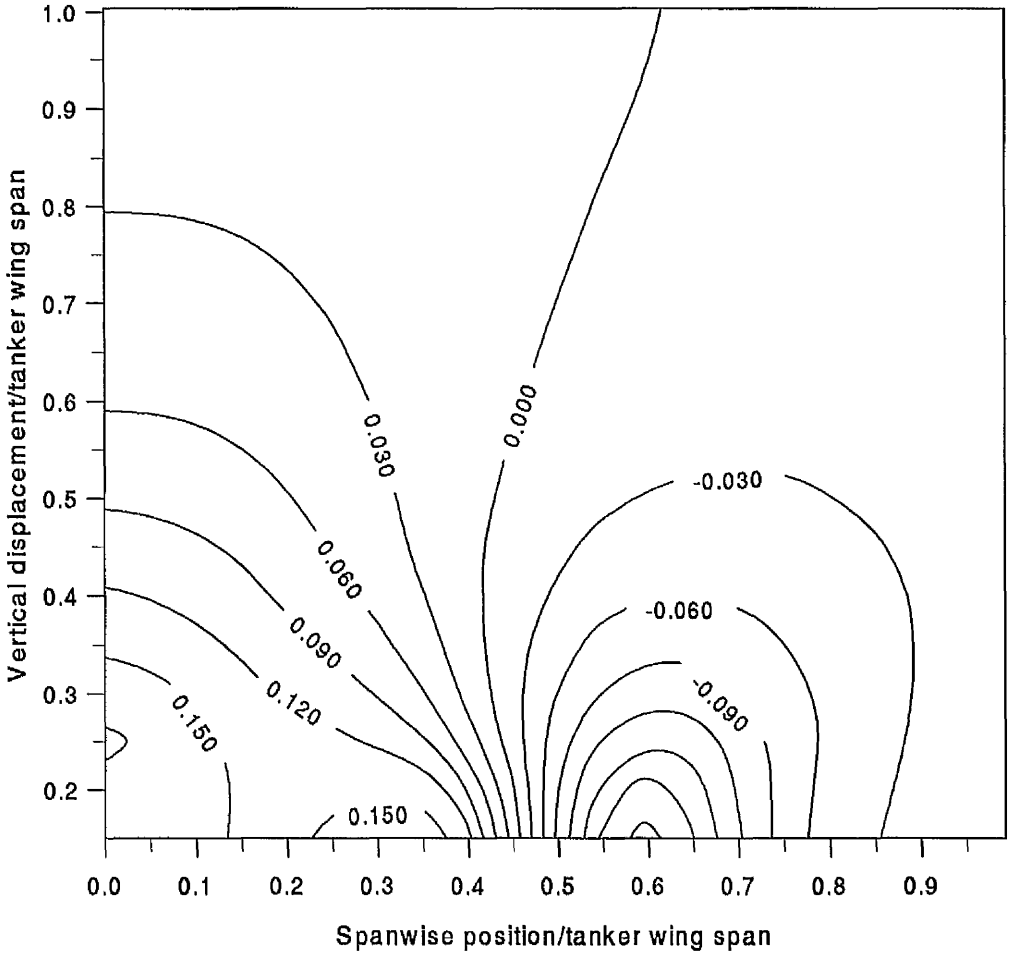

Figure 6.21: Contours of yawing moment due to yaw angle ratio, C_{n_ψ}/C_{n_β}.

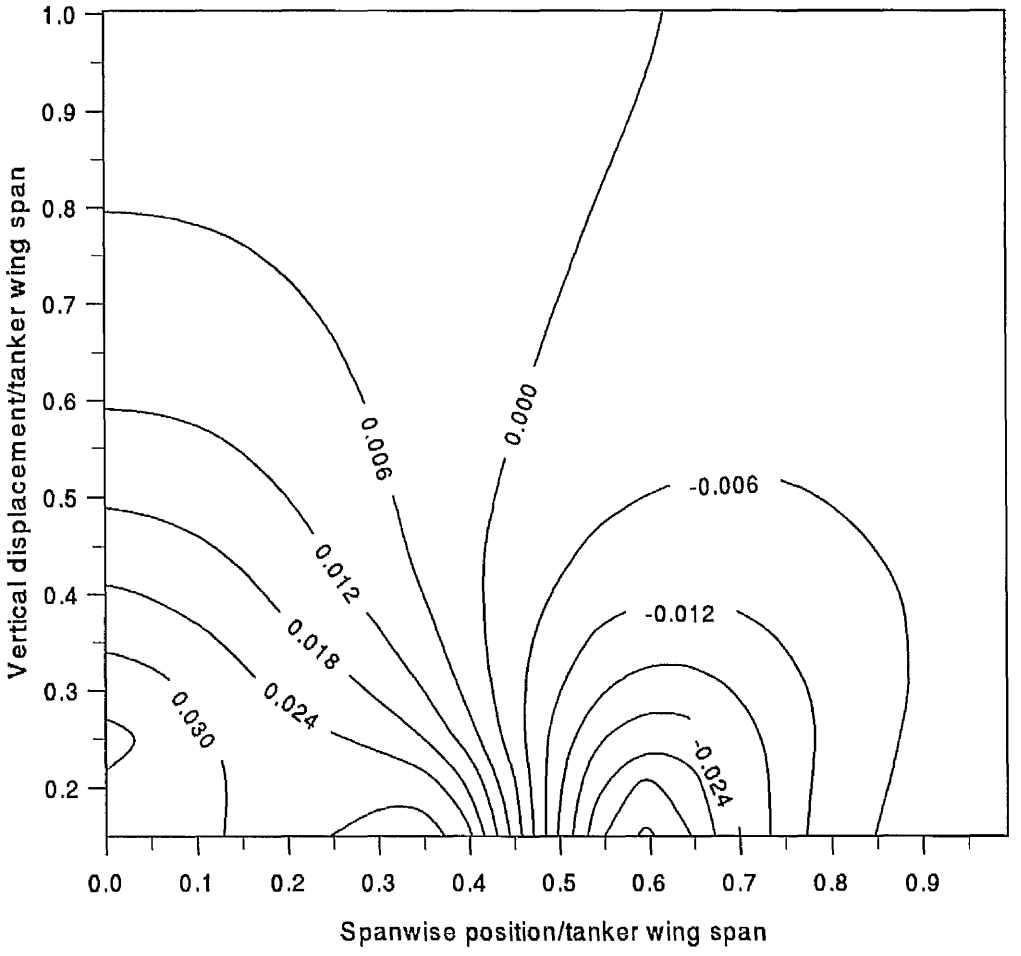

Figure 6.22: Contours of side force due to yaw angle ratio, C_{Y_ψ}/C_{Y_β}.

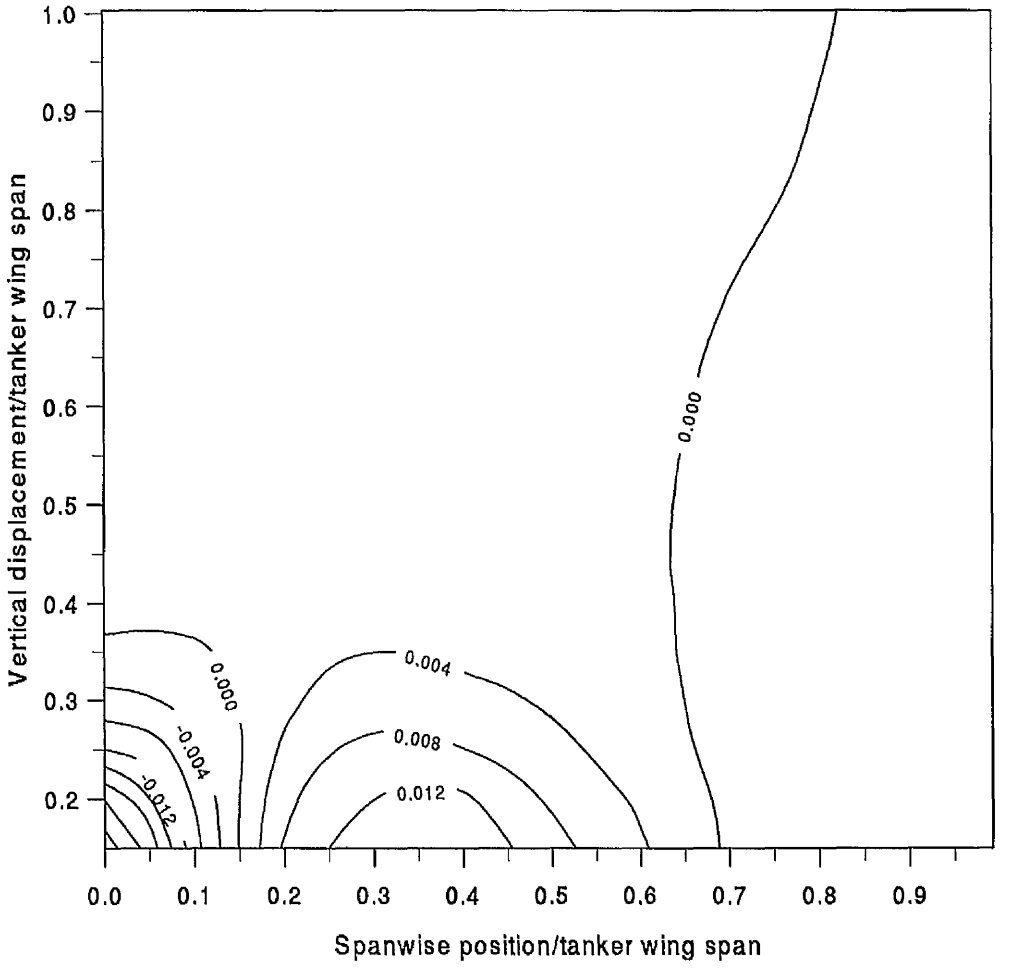

Figure 6.23: Contours of rolling moment due to yaw angle ratio, C_{l_ψ}/C_{l_β}.

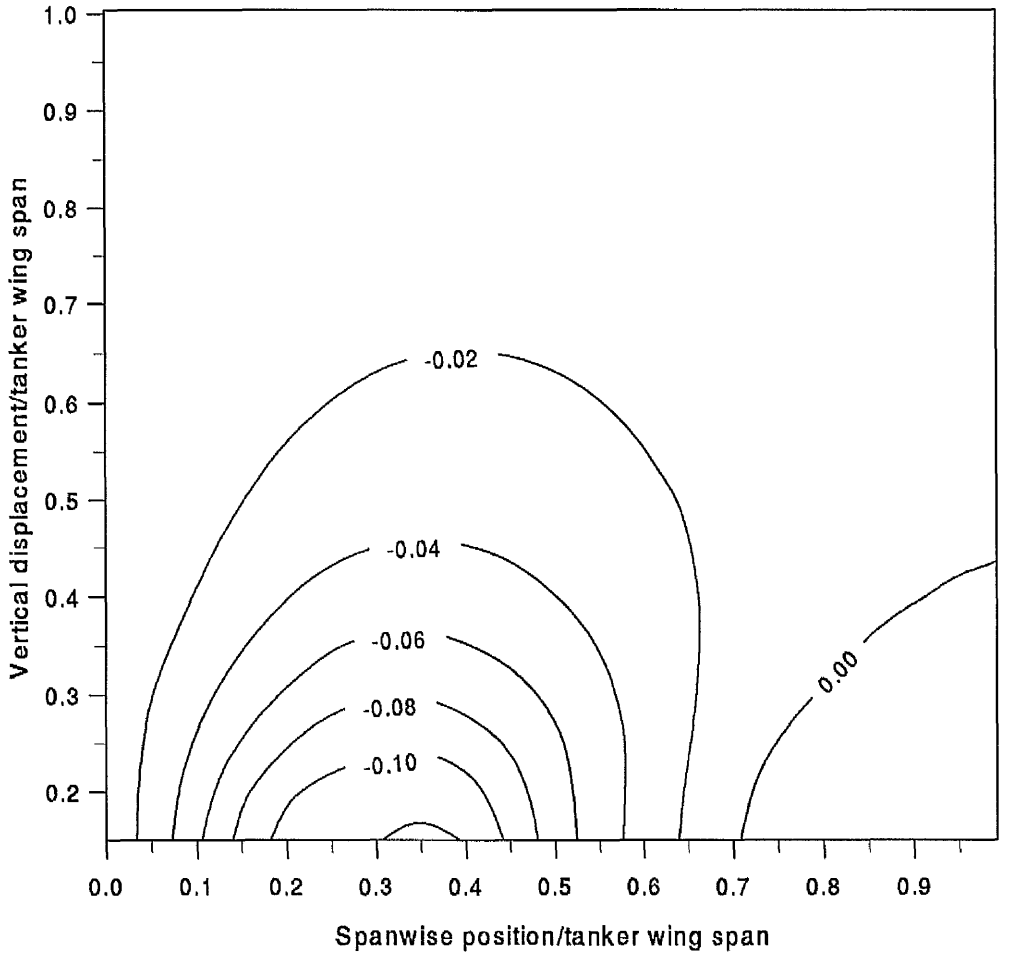

Figure 6.24: Contours of pitching moment due to yaw angle ratio, C_{m_ψ}/C_{m_α}.

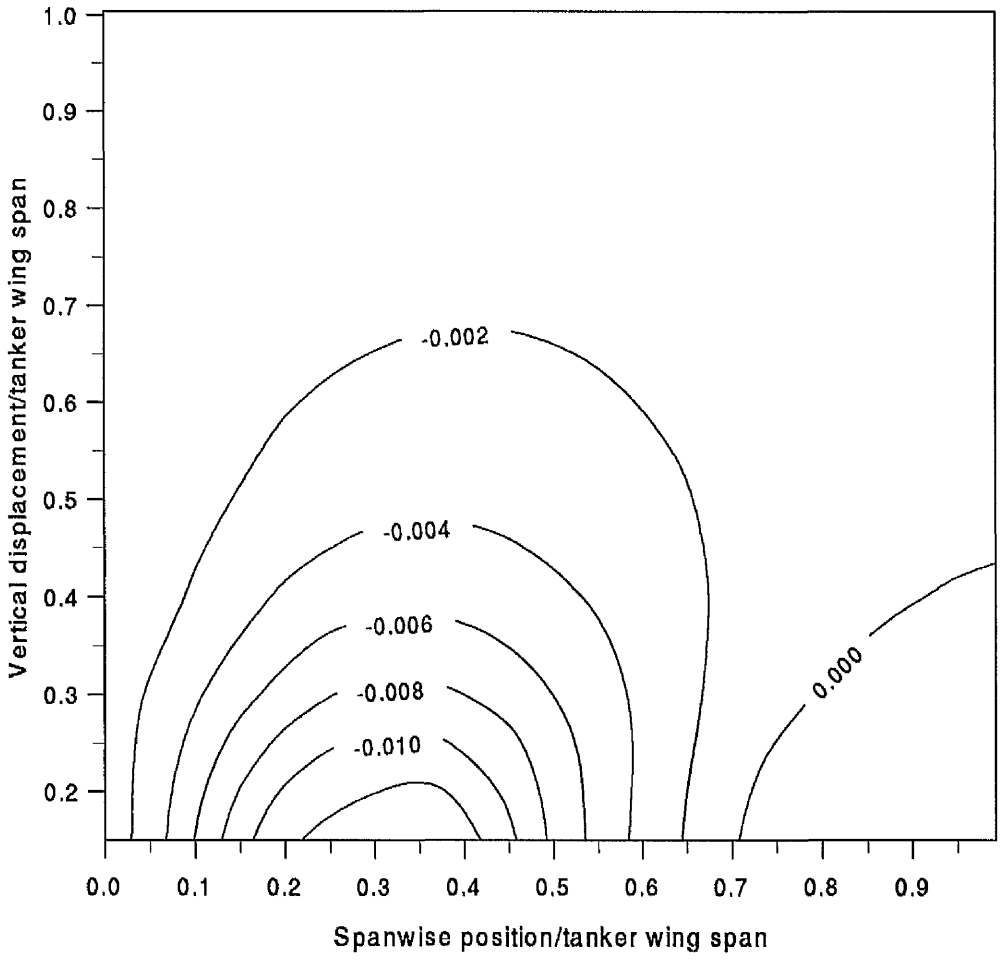

Figure 6.25: Contours of lift force due to yaw angle ratio, C_{L_ψ}/C_{L_α}.

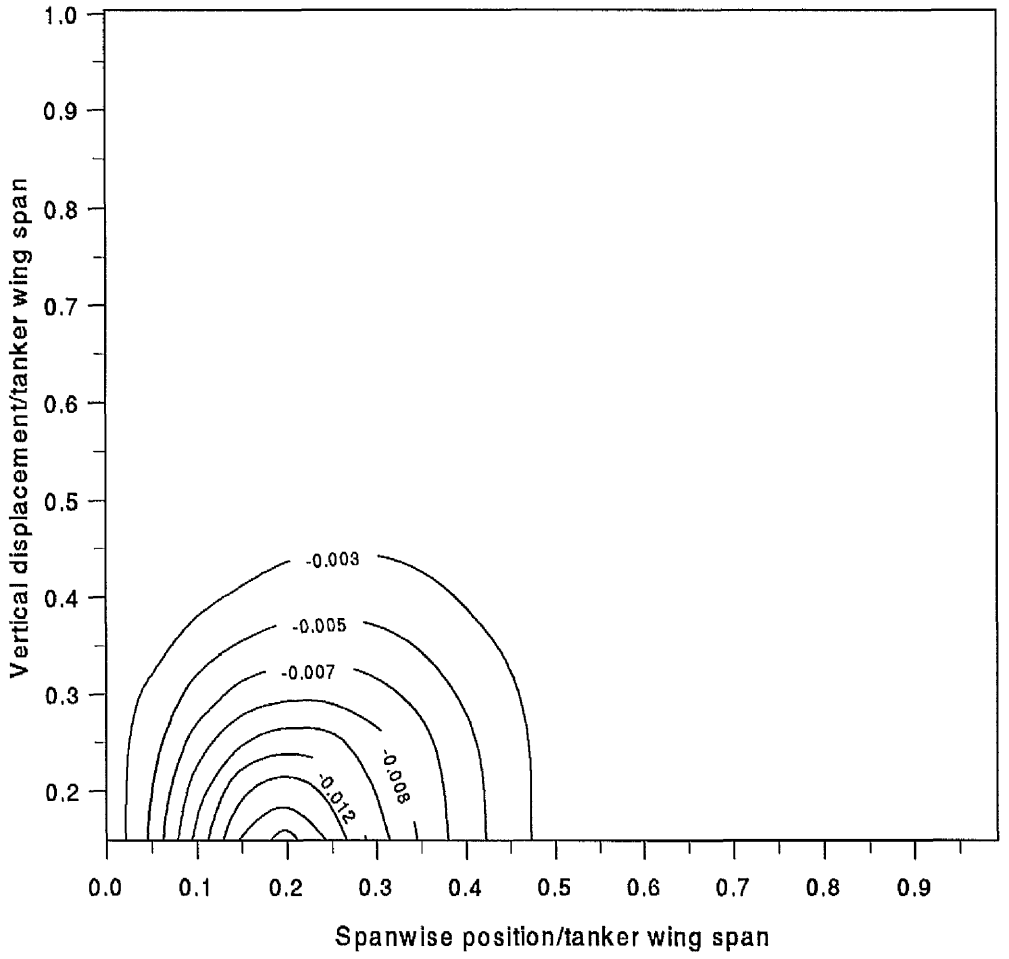

Figure 6.26: Contours of induced drag due to yaw angle ratio, $C_{D_{i_\psi}}/C_{D_{i_\alpha}}$.

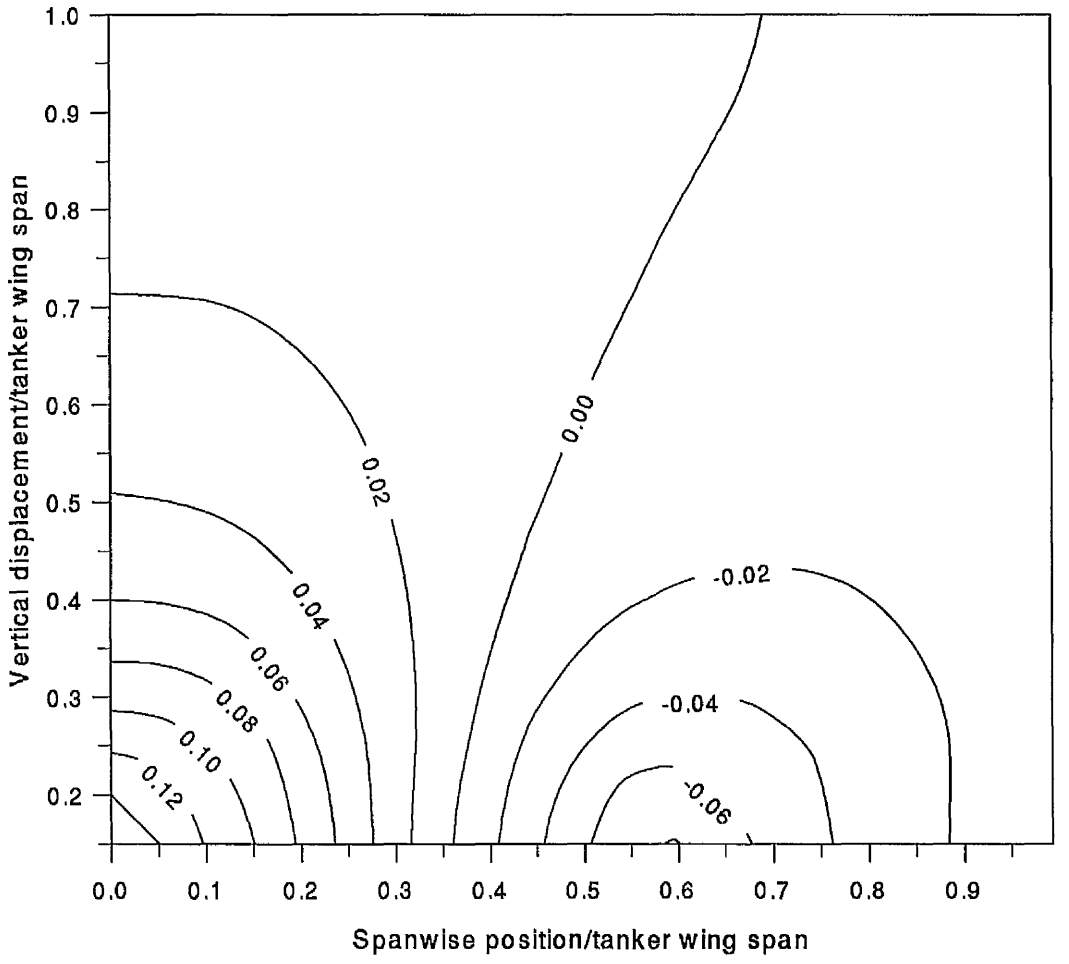

Figure 6.27: Contours of pitching moment due to pitch angle ratio, $C_{m_\theta}/C_{m_\alpha}$.

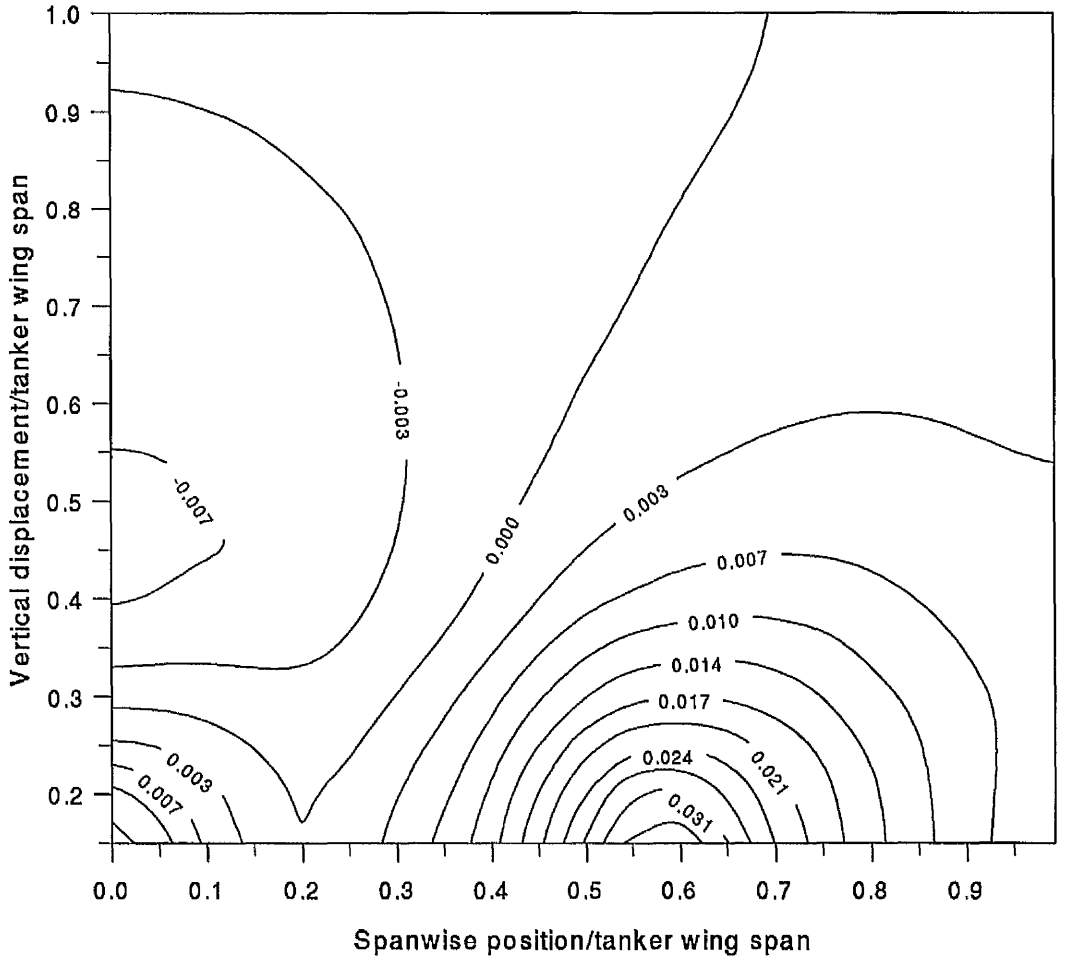

Figure 6.28: Contours of induced drag due to pitch angle ratio, $C_{D_{i_\theta}}/C_{D_{i_\alpha}}$.

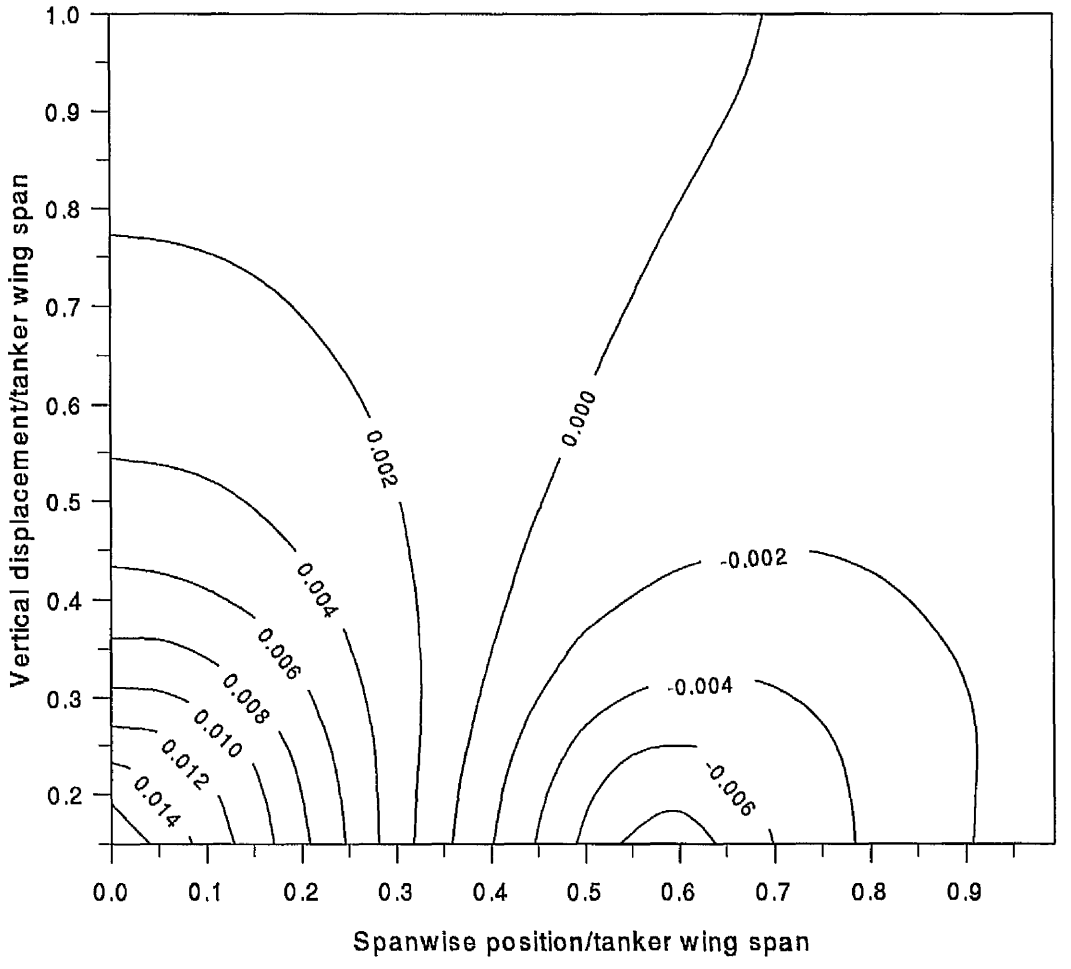

Figure 6.29: Contours of lift force due to pitch angle ratio, $C_{L_\theta}/C_{L_\alpha}$.

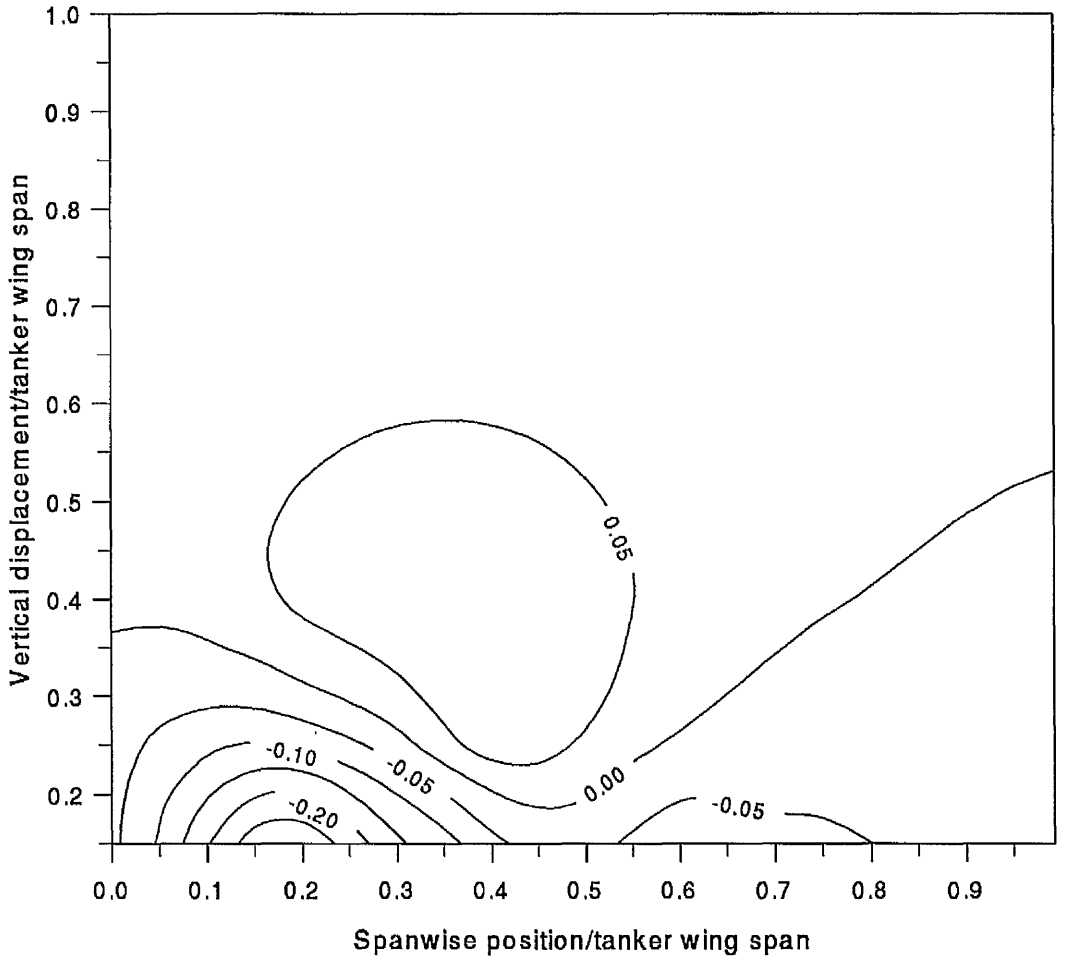

Figure 6.30: Contours of yawing moment due to pitch angle ratio, C_{n_θ}/C_{n_β}.

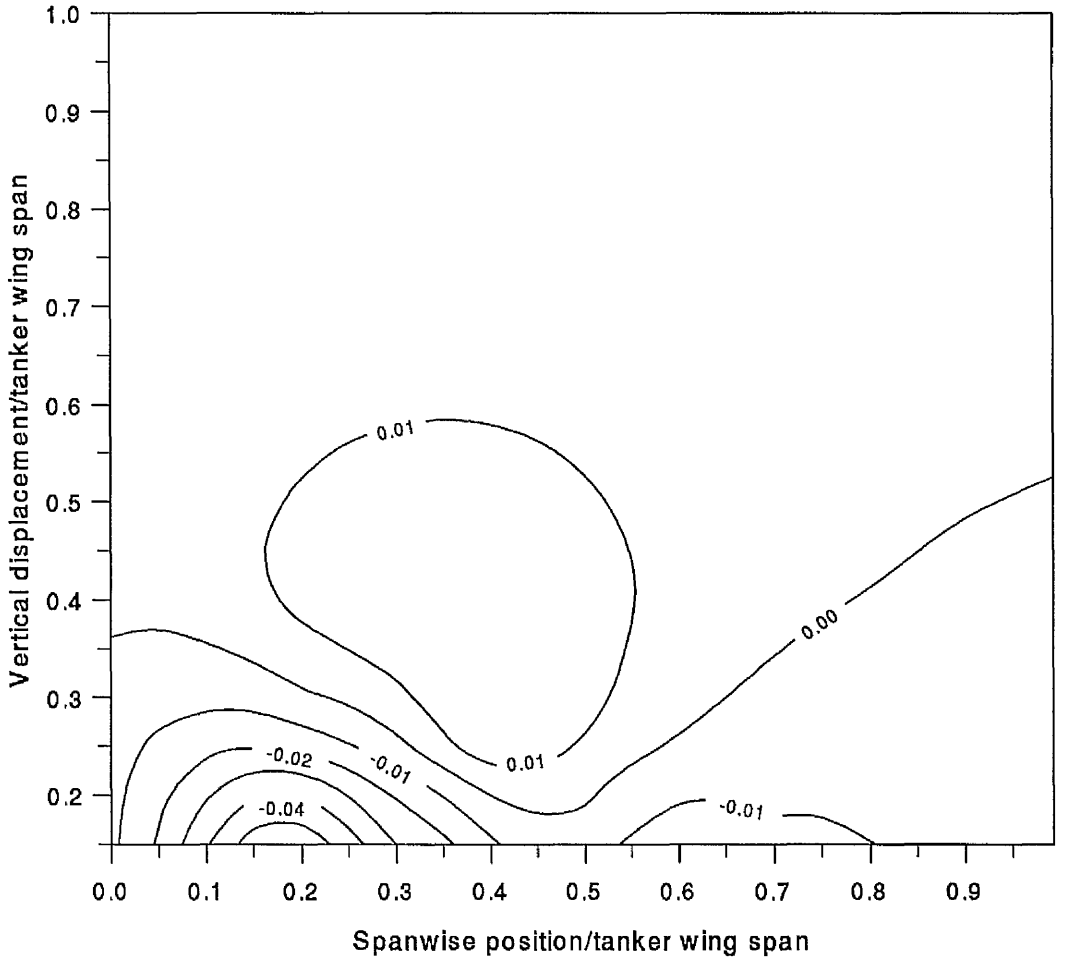

Figure 6.31: Contours of side force due to pitch angle ratio, C_{Y_θ}/C_{Y_β}.

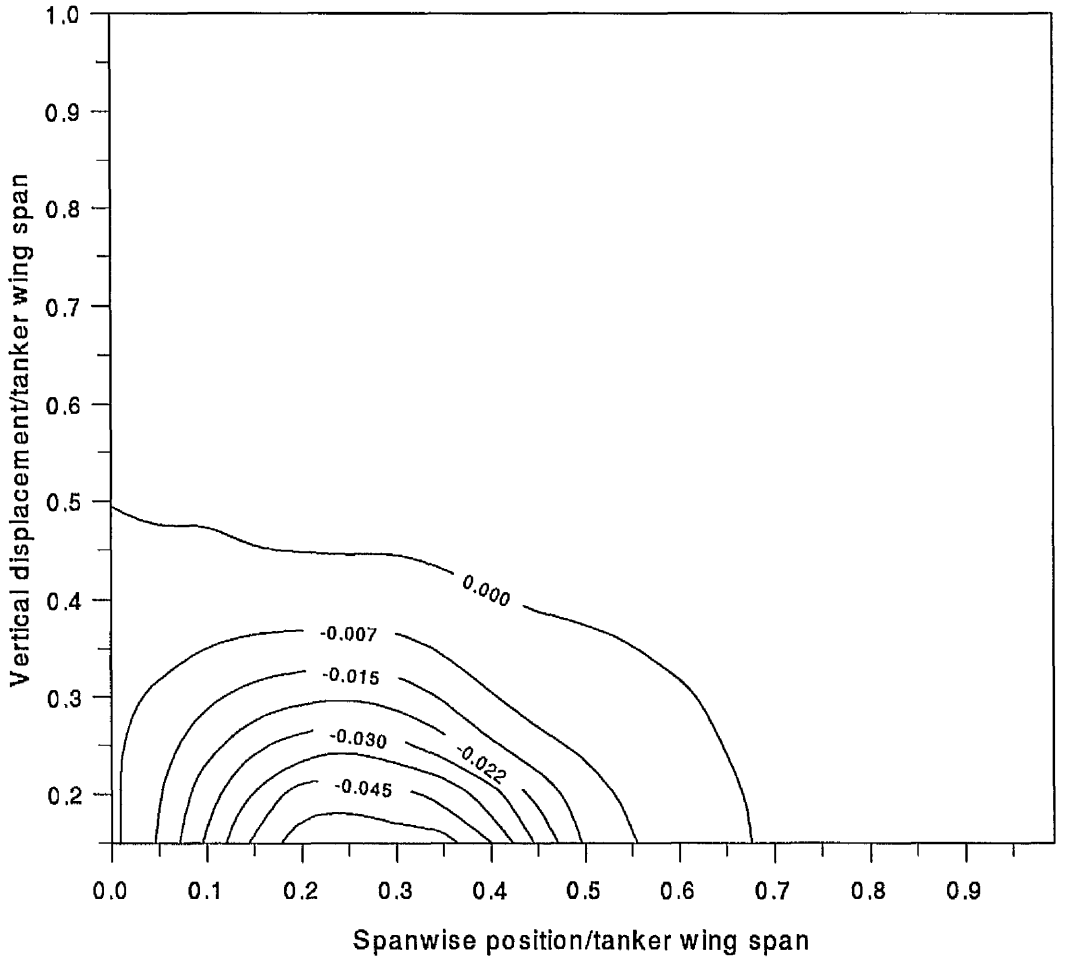

Figure 6.32: Contours of rolling moment due to pitch angle ratio, C_{l_θ}/C_{l_β}.

Chapter 7

Conclusions and Future Work

Conclusions

Theoretical models have been developed to determine the aerodynamic interference between typical tanker wing and large receiver aircraft during air-to-air refuelling.

Predictions from the theoretical models have been compared with existing open test section wind tunnel data. In the longitudinal case, the predictions of the receiver pitch angle, induced drag and pitching moment are found to follow the experimental trends with varying vertical separation z between the tanker wing and receiver aircraft model. However, the measured pitch angle and induced drag increments for the three tailplane positions are significantly higher than the predicted values due mainly to the significant wind tunnel boundary interference effect. The receiver pitching moment is strongly affected by the tailplane position on the fin and the theory compares favourably with experiment for both the low and high tailplane

cases.

In the lateral case, the side force, yawing and rolling moments are presented in derivative form since their variations with side, bank and yaw displacements are essentially linear. The most significant aerodynamic derivatives are the rolling moments due to side and bank displacements. The theoretical variations of these derivatives with vertical separation are shown to be in good agreement with the experiment. Both theory and experiment produce significant side force and yawing moment when the receiver fin is displaced from the centre line of the tanker wake. This leads to a significant loss in directional stability of the receiver aircraft.

The theoretical models have been used to determine the lateral aerodynamic interference and the stability and control characteristics of a Hercules receiver aircraft refuelling in flight from a KC10 tanker. The lateral aerodynamic interference results of the KC10 tanker and Hercules receiver aircraft show that significant aerodynamic loads are induced on the receiver. Since the variations of the receiver loads with small side, bank and yaw displacements are essentially linear, they are expressed in terms of aerodynamic derivatives. The Hercules fuselage makes significant contribution to the side force and yawing moment derivatives due to side and bank displacements. However the fuselage contribution to the yawing moment derivative due to yaw displacement is found to be very small which agrees with the experimental data given by Bloy and Lea [56]. A loss of directional stability is predicted for the Hercules receiver which is in agreement with flight test observations [7]. The minimum directional stability corresponds to the tip of the receiver fin intersecting the tanker wing wake which is consistent with experimental data [19, 56].

The application of the wake roll-up model to the KC10 tanker wing indicates that only half of the trailing vortex sheet from the tanker wing is rolled up into the tip vortex in the region of the Hercules receiver aircraft. Compared with the predictions from a flat vortex sheet model of the tanker wing wake, the predictions from the wake roll-up model indicate significantly higher values of the receiver rolling moment derivatives due to side and bank displacements. The roll-up model also produces better prediction of the side force and yawing moment derivatives.

The trim of the Hercules receiver in a steady sideslip behind the KC10 tanker has been determined with the receiver centre of gravity or the receiver nose on the tanker wake centre line. The induced loads due to the KC10 tanker wake greatly alter the trim of the Hercules receiver aircraft. Compared with the free air case, the rudder angle in air-to-air refuelling with the receiver nose on the tanker centre line is reduced by 79% for the typical flight conditions considered; the aileron angle is up to two to three times higher and the angle of bank is similar. These results agree qualitatively with flight test observations [7]. Displacing the receiver centre of gravity off the tanker centre line is found to increase the difference between the free air and air-to-air refuelling cases.

Solution of the linearised equations of motion gives three characteristic oscillatory modes for the Hercules receiver in air-to-air refuelling behind the KC10 tanker instead of the usual Dutch roll oscillation, spiral and roll subsidence in free air. The effect of the tanker wake is to slightly reduce the damping index of the Dutch roll oscillation. The roll subsidence is replaced by a highly damped rolling oscillation

and the third mode is a divergent oscillation involving mainly bank and side displacements. The time to double amplitude of the divergent mode is approximately 3.12 s and the period is 12.7 s.

Typical aerodynamic data of the interference between the KC10 tanker and Hercules receiver aircraft has been obtained over an envelope of the receiver positions and attitudes which covers that required for flight simulation. The forces and moments on the receiver due to its position and attitude within the tanker wing wake have been assessed by comparison with the aerodynamic characteristics of the receiver aircraft in free air.

In the longitudinal case, the tanker downwash produces large changes in the receiver lift, drag and pitching moment with varying vertical and lateral separations between tanker and receiver . Within the region between the tanker wing tip vortices, lift is reduced and lift dependent or induced drag is increased. A nose-up pitching moment is produced on the receiver due essentially to its static stability with respect to angle of attack.

In the lateral case the tanker sidewash produces high side force, yawing and rolling moments as the receiver moves towards the tanker wing tip vortices. The most important of these terms is the rolling moment due to sideways displacement.

Aerodynamic derivatives due to the receiver attitude are assessed by comparing with the corresponding aircraft derivatives due to angles of attack and sideslip. The most significant of these terms is the rolling moment due to bank angle derivative which has a peak value approximately equal to half the rolling moment due to

sideslip angle derivative. For the remaining longitudinal and lateral aerodynamic derivatives, only the yawing moment due to bank, pitch and yaw angles derivatives and the pitching moment due to pitch and yaw angles derivatives are significant.

Future Work

Further work is required to carry out the following investigations:

- The aerodynamic models developed in this research work are applicable to any tanker wing and any receiver aircraft. Therefore, these models can be applied to any tanker/receiver combination of interest such as those considered previously by Trochalidis [14].

- The wake roll-up model is also applicable to flapped tanker wings. Flaps are used on the tanker aircraft to allow the refuelling of turbo-prop aircraft such as the Hercules from heavy jet tanker aircraft. Thus, the effect of deflecting the KC10 wing flaps on the Hercules receiver aircraft should be determined and the results can be compared with the flight test data given by Bradley [7].

- A theoretical model should be developed for the receiver fuselage which makes a significant contribution to the side force and yawing moment due to side and bank displacement derivatives. This model should be used to examine the accuracy of the approximate methods used to determine the receiver fuselage effect.

- More accurate predictions of the aerodynamic interference between the tanker and receiver aircraft could be obtained by modelling simultaneously the roll-up of the wake shed from the tanker wing and the receiver wing, tailplane and fin. Hence, this should be investigated using the aerodynamic model developed by Lea [59].

- Finally, the effect of the KC10 tanker jet exhaust and the interaction between the Hercules receiver propellers and the KC10 tanker wing trailing vortex wake should be investigated.

Appendix A

Linearised Equations of Motion of Receiver Aircraft

A.1 Longitudinal Equations of Motion

For initially, steady, straight and horizontal flight, the longitudinal linearised equations of motion, for fixed controls, are given in concise form used in the U.K. by [14]

$$\begin{bmatrix} D+x_u & x_w & x_qD+g+x_\theta & x_x & x_z \\ z_u & (1+z_{\dot{w}})D+z_w & (-U_e+z_q)D+z_\theta & z_x & z_z \\ m_u & m_{\dot{w}}D+m_w & (D+m_q)D+m_\theta & m_x & m_z \\ -1 & 0 & 0 & D & 0 \\ 0 & -1 & U_e & 0 & D \end{bmatrix} \begin{bmatrix} u \\ w \\ \theta \\ x \\ z \end{bmatrix} = \begin{bmatrix} 0 \end{bmatrix}$$

A.2 Lateral Equations of Motion

For initially steady, straight and horizontal flight, the lateral linearised equations of motion, for fixed controls, are given in concise form by [14]

$$\begin{bmatrix} D+y_v & y_pD+y_\phi-g & (U_e+y_r)D+y_\psi & y_y \\ l_v & (D+l_p)D+l_\phi & (e_xD+l_r)D+l_\psi & l_y \\ n_v & (e_zD+n_p)D+n_\phi & (D+n_r)D+n_\psi & n_y \\ -1 & 0 & -U_e & D \end{bmatrix} \begin{bmatrix} v \\ \phi \\ \psi \\ y \end{bmatrix} = \begin{bmatrix} 0 \end{bmatrix}$$

Appendix B

Input Data for Wing and Tailplane-Fin VLM Computer Programs

B.1 Wing VLM Computer Program

This section describes the input data required for the wing VLM computer program. The axis system used in this program is described previously in section 2.1.3. A sample of the input data for the Hercules wing is shown in table B.1. All the input data need only be specified for the starboard wing, except for the geometric twist data which should be given for both the starboard and port wings. All the lengths and areas in the input data should be given in a consistent set of units. The input data are described in the order given in table B.1.

M Number of chordwise panels.

N Number of spanwise panels.

These are found in line 1.

CR Wing root chord.

$SREF$ Reference area used in forming aerodynamic coefficients.

$REFL$ Reference length used in forming aerodynamic moment coefficients.

xcg, zcg Distances between the wing apex and centre of gravity, measured parallel and perpendicular to the longitudinal body-axis.

These are found in line 2.

$ALFA$ Wing root chord angle of attack relative to the free stream, in degrees.

MIF Mach number.

These are found in line 3.

$\hat{y}(I)$ $\hat{y}$ coordinate of the Ith trailing vortex leg ($\hat{y}(1)$=0 and $\hat{y}(N+1)$=b/2).

$LE(I)$ Leading-edge sweep back angle of wing section to the right of the Ith trailing vortex leg, in degrees, (measured in $\hat{X}$-$\hat{Y}$ plane).

$TE(I)$ Trailing-edge sweep back angle of wing section to the right of the Ith trailing vortex leg, in degrees, (measured in $\hat{X}$-$\hat{Y}$ plane).

These are found in lines 4 to 13.

$TWS(I)$ Geometric twist angle of the wing section between Ith and (I+1)th

trailing vortex legs on the starboard wing, in degrees. This data must be input starting at the row near the root and proceeding to the row near the starboard tip.

$TWP(I)$ Geometric twist angle of the wing section between Ith and (I+1)th trailing vortex legs on the port wing, in degrees. This data must be input starting at the row near the root and proceeding to the row near the port tip.

These are found in lines 14 to 22.

$DIH(I)$ Dihedral angle of the wing section between Ith and (I+1)th trailing vortex legs, in degrees, positive upward. (measured in $\hat{Y}$-$\hat{Z}$ plane). This data must be input starting at the row near the root and proceeding to the row near the tip.

These are found in lines 23 to 31.

B.2 Tailplane-Fin VLM Computer Program

This section describes the input data required for tailplane-fin VLM computer program. The axis system used to describe the tailplane-fin geometry is shown previously in figure 2.11, with the origin is at the tailplane root chord leading edge. The input data required for the tailplane is given in the same manner as described for the wing in section B.1. A sample of this data for the Hercules tailplane is given in table B.2. A sample of the fin input data for the Hercules fin is given in

table B.3. This data is described in the order given in table B.3.

Line 1 is the same as that described in table B.1.

CRF Fin root chord.

$xfle$ $\hat{x}$-coordinate of the fin root chord leading edge relative to the axis system used to describe the tailplane-fin geometry.

These are found in line 2.

$BETA$ Sideslip angle, in degrees.

This is found in line 3.

Lines 4 to 9 are the same as those given in table B.1.

Line number	Hercules wing geometric data				
1	3	9			
2	4.88	161.84	40.41	1.22	1.591
3	3.686	0.347			
4	0.000	0.000	0.000		
5	1.891	0.000	0.000		
6	3.783	0.000	0.000		
7	5.674	2.355	-7.032		
8	8.096	2.355	-7.032		
9	10.518	2.355	-7.032		
10	12.940	2.355	-7.032		
11	15.361	2.355	-7.032		
12	17.783	2.355	-7.032		
13	20.205	2.355	-7.032		
14	2.860	2.860			
15	2.579	2.579			
16	2.298	2.298			
17	1.978	1.978			
18	1.618	1.618			
19	1.259	1.259			
20	0.899	0.899			
21	0.539	0.539			
22	0.180	0.180			
23	2.5				
24	2.5				
25	2.5				
26	2.5				
27	2.5				
28	2.5				
29	2.5				
30	2.5				
31	2.5				

Table B.1: Hercules wing input data for wing VLM computer program.

Line number	Hercules tailplane geometric data				
1	3 5				
2	4.428	161.84	40.41	15.776	1.591
3	3.686	0.347			
4	0.000	13.800	-6.010		
5	1.578	13.800	-6.010		
6	3.155	13.800	-6.010		
7	4.733	13.800	-6.010		
8	6.310	13.800	-6.010		
9	7.888	13.800	-6.010		

Table B.2: Hercules tailplane input data for tailplane-fin VLM computer program.

Line number	*Hercules fin geometric data*		
1	3 5		
2	5.95	-1.245	
3	1.0		
4	0.000	24.887	-11.106
5	1.342	24.887	-11.106
6	2.684	24.887	-11.106
7	4.026	24.887	-11.106
8	5.368	24.887	-11.106
9	6.710	24.887	-11.106

Table B.3: Hercules fin input data for tailplane-fin VLM computer program.

Appendix C

Contribution of Hercules Fuselage to the Aerodynamic Derivatives due to Sideslip, Rate of Yaw and angle of attack

C.1 Contribution of Fuselage to Rolling Moment due to Sideslip Derivative

Using ESDU data sheet [45], the Hercules fuselage contribution to the rolling moment due to sideslip derivative, $(C_{l_\beta})_{Fus}$, is estimated as follows

$$(C_{l_\beta})_{Fus} = (C_{l_\beta})_1 + (C_{l_\beta})_2$$

where $(C_{l_\beta})_1$ is the isolated fuselage contribution and $(C_{l_\beta})_2$ is the contribution due to the interference arising from the vertical position of wing on fuselage. $(C_{l_\beta})_1$ is determined from the expression

$$(C_{l_\beta})_1 = -0.014 \frac{l_{Fus}}{b} \frac{S_{Fus}}{S_W} \alpha_{Fus}$$

where

α_{Fus} is the fuselage incidence, in degrees, measured from the fuselage zero-lift value,

S_{Fus} is the maximum cross-sectional area of the fuselage ($S_{Fus} = 14.454$ m^2),

l_{Fus} is the overall fuselage length ($l_{Fus} = 34.37$ m),

b is the wing span (b=40.41 m),

S_W is the wing area ($S_W = 161.84$ m^2).

Thus

$$(C_{l_\beta})_1 = -0.0039 \quad rad^{-1}$$

$(C_{l_\beta})_2$ is given by

$$(C_{l_\beta})_2 = \frac{(C_{l_\beta})_2}{(1 + \frac{W}{H}) f(A)} \times (1 + \frac{W}{H}) f(A)$$

where

W is the width of the fuselage reference cross-section (W=4.29 m),

H is the height of ellipse equivalent to fuselage reference cross-section,

$f(A)$ is the aspect ratio correction factor.

For $A = 6$, the parameter $\frac{(C_{l_\beta})_2}{(1+\frac{W}{H})f(A)}$ is determined by using $\mid \frac{h}{H} \mid$ and $\frac{H}{b}$, where $\mid \frac{h}{H} \mid$ and $\frac{H}{b}$ are given by the following equations

$$\frac{H}{b} = \frac{4}{\pi W b} \times area\ of\ fuselage\ reference\ cross-section.$$

and

$$\frac{h}{H} = \frac{h_0}{H} - k\Gamma$$

where

h_0 is the vertical distance of quarter-chord point of wing centre-line chord from centroid of fuselage reference cross-section ($\mid h_0 \mid = 1.591$ m),

Γ is the wing dihedral angle, in degrees ($\Gamma = 2.5°$),

k is a factor determined by using $\mid \frac{h_0}{H} \mid$ and $\frac{H}{b}$ ($\mid \frac{h_0}{H} \mid = 0.371$, $\frac{H}{b} = 0.106$ and k=0.0102),

h is the wing vertical position relative to the fuselage ($\frac{h}{H} = -0.3965$).

Therefore

$$(C_{l_\beta})_2 = -0.033 \ \ rad^{-1}$$

Finally, the total fuselage contribution to the rolling moment due to sideslip derivative is given by the sum of $(C_{l_\beta})_1$ and $(C_{l_\beta})_2$ as

$$(C_{l_\beta})_{Fus} = -0.0039 - 0.033 = -0.0369 \ \ rad^{-1}$$

C.2 Contribution of Fuselage to Side Force due to Sideslip Derivative

Using ESDU data sheet [43], the Hercules fuselage contribution to the side force due to sideslip derivative, $(C_{Y_\beta})_{Fus}$, is given by the empirical relation

$$-(C_{Y_\beta})_{Fus} = [0.0714 + 0.674\frac{h^2}{S_{Fus}} + \frac{hbFF_W}{S_{Fus}}(4.95\frac{\mid z \mid}{h} - 0.12)]\frac{S_{Fus}}{S} + 0.006 \mid \Gamma \mid$$

where

h is the maximum height of fuselage section (h=4.29 m),

S_{Fus} is the area of side elevation of the fuselage ($S_{Fus} = 104.91$ m^2),

F is a function allowing for effects on side force derivative of wing height and wing span to fuselage width ratio (F=0.038),

F_W is a factor for applying corrections for wing planform to function F ($F_W = 0.86$),

z is the vertical position of quarter-chord point of wing root chord relative to the fuselage centre-line ($\mid z \mid = 1.591$ m),

S is the area of equivalent wing planform determined from ESDU data sheet [60] (S=165.192 m^2).

Therefore

$$(C_{Y_\beta})_{Fus} = -0.2332 \ \ rad^{-1}$$

C.3 Contribution of Fuselage to Yawing Moment due to Sideslip Derivative

Using ESDU data sheet [43], the yawing moment derivative about a yaw axis through the mid-point of the fuselage, $[(C_{n_\beta})_{mid}]_{Fus}$, is given by the empirical relation

$$-[(C_{n_\beta})_{mid}]_{Fus} = [0.2575 + \frac{l^2{}_{Fus}}{S_{Fus}}\{0.0008\frac{l^2{}_{Fus}}{S_{Fus}} - 0.024\}][1.39(\frac{h_1}{h_2})^{\frac{1}{2}} - 0.39][\frac{S_{Fus}l_{Fus}}{Sb}]$$

where

h_1, h_2 are the fuselage section heights, at $0.25l_{Fus}$ and $0.75l_{Fus}$, respectively, ($h_1 = 3.875$ m and $h_2 = 2.491$ m)

l_{Fus}, S_{Fus}, S and b are the same as defined in sections C.1 and C.2. Therefore

$$[(C_{n_\beta})_{mid}]_{Fus} = -0.08372 \ \ rad^{-1}$$

The fuselage yawing moment derivative about a yaw axis through the centre of gravity, $(C_{n_\beta})_{Fus}$, is given by

$$(C_{n_\beta})_{Fus} = [(C_{n_\beta})_{mid}]_{Fus} + \frac{l_{cg} - 0.5l_{Fus}}{b}(C_{Y_\beta})_{Fus}$$

where l_{cg} is the distance between the fuselage nose and the centre of gravity. Thus

$$(C_{n_\beta})_{Fus} = -0.0724 \ \ rad^{-1}$$

C.4 Contribution of Fuselage to Side Force due to Rate of Yaw Derivative

Using ESDU data sheet [44], the Hercules fuselage contribution to the side force due to rate of yaw derivative, $(C_{Y_r})_{Fus}$, is given by the approximation

$$(C_{Y_r})_{Fus} = -0.08\frac{l_{Fus}S_{Fus}}{bS_W}$$

where l_{Fus}, S_{Fus}, b and S_W are the same as defined in section C.1. Thus

$$(C_{Y_r})_{Fus} = -0.045 \ \ rad^{-1}$$

C.5 Contribution of Fuselage to Yawing Moment due to Rate of Yaw Derivative

Using ESDU data sheet [44], the Hercules fuselage contribution to the yawing moment due to rate of yaw derivative, $(C_{n_r})_{Fus}$, is given by the approximation

$$(C_{n_r})_{Fus} = -0.02\frac{l^2{}_{Fus}S_{Fus}}{b^2S_W}$$

where l_{Fus}, S_{Fus}, b and S_W are the same as those used in section C.1. Therefore

$$(C_{n_r})_{Fus} = -0.0095 \ \ rad^{-1}$$

C.6 Contribution of Fuselage to Pitching Moment due to Angle of Attack Derivative

Multhopp [46] proposes the following formula to estimate the fuselage contribution to the pitching moment due to angle of attack derivative

$$(C_{m_\alpha})_{Fus} = \frac{57.3}{36.5S\bar{c}} \int_0^{l_{Fus}} W_{Fus}^2 \frac{\partial \alpha_l}{\partial \alpha} dx \tag{C.1}$$

The integration is evaluated numerically by dividing the Hercules fuselage into 20 sections as shown in figure C.1. Equation C.1 can be then approximated by

$$(C_{m_\alpha})_{Fus} = \frac{57.3}{36.5S\bar{c}} \sum_{i=1}^{i=20} W_{Fus_i}^2 \left(\frac{\partial \alpha_l}{\partial \alpha}\right)_i \Delta x_i \tag{C.2}$$

where

W_{Fus_i} is the average width of the fuselage sections,

Δx_i is the length of the fuselage sections,

l_{Fus} is the overall fuselage length,

α_l is the local angle of attack of the fuselage sections (i.e. the geometric angle of attack minus the local induced angle due to the wing upwash or downwash).

The change in local flow angle with angle of attack, $\frac{\partial \alpha_l}{\partial \alpha}$, along the fuselage is determined using the wing flat vortex sheet model. It is assumed that the fuselage portion between the wing leading edge and trailing edge is not affected by the wing flow field (i.e. $\frac{\partial \alpha_l}{\partial \alpha} = 0$) [53, 54].

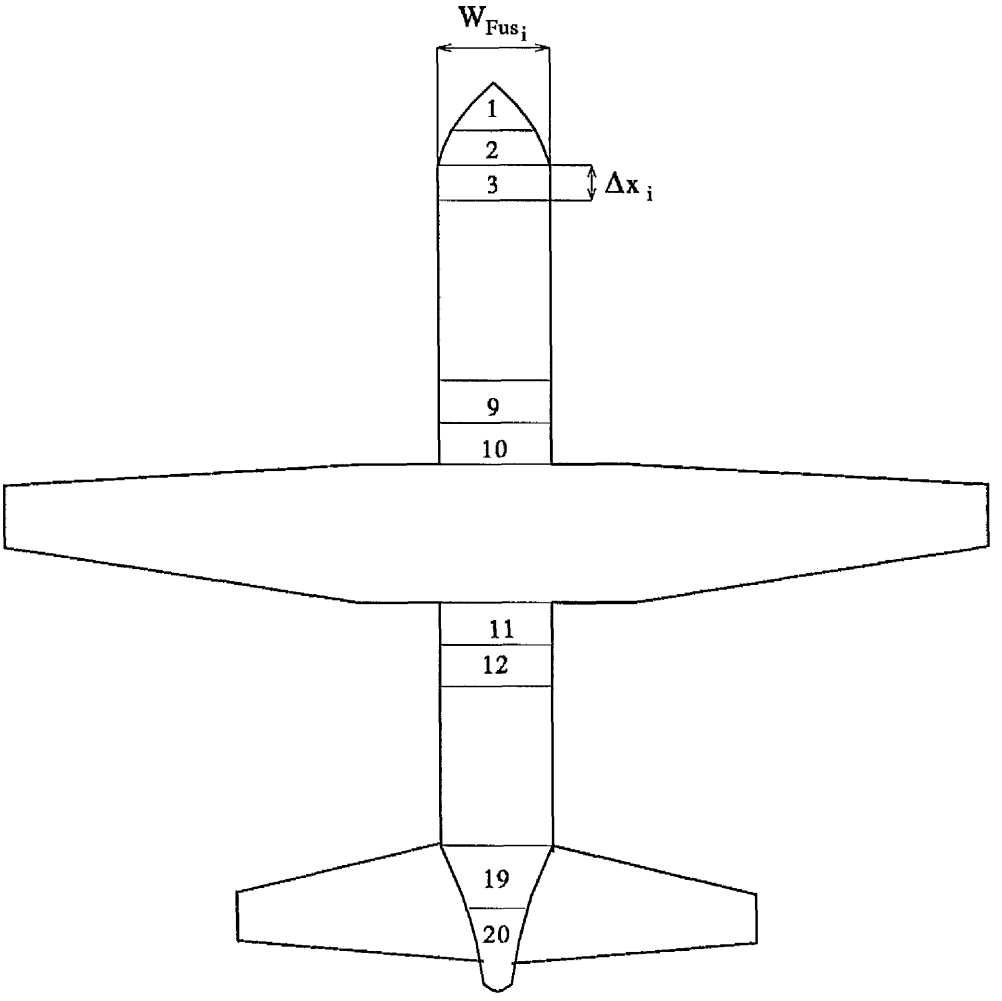

Figure C.1: Diagram showing fuselage sections used to estimate $(C_{m_\alpha})_{Fus}$

Appendix D

Contribution of Hercules Propellers and Nacelles to the Lateral Aerodynamic Derivatives due to Sideslip

D.1 Contribution of Propellers to Side Force and Yawing Moment due to Sideslip Derivatives

$(C_{Y_\beta})_{Pro}$ and $(C_{n_\beta})_{Pro}$ are estimated using the method of reference [51] which is given in reference [47]. The contribution of n propellers to the side force due to

sideslip derivative, $(C_{Y_\beta})_{Pro}$, is determined as follows

$$(C_{Y_\beta})_{Pro} = -n\frac{\partial(N_{Pro}/qS_{Pro})}{\partial\alpha_{Pro}}\frac{S_{Pro}}{S_W} \tag{D.1}$$

where

S_{Pro} is the cross section area of the propeller ($S_{Pro} = 12.5664$ m^2),

S_W is the wing area ($S_W = 161.84$ m^2),

n is the number of propellers (n=4),

N_{Pro} is the propeller normal force,

α_{Pro} is the propeller angle of attack , the angle between the propeller thrust line and the free-stream.

$\frac{\partial(N_{Pro}/qS_{Pro})}{\partial\alpha_{Pro}}$ is given as a function of number of blades and the nominal blade angle at 0.75 of the blade radius. For the Hercules aircraft, the number of blades of one propeller is 4 and the nominal blade angle is taken to be 37°, hence

$$\frac{\partial(N_{Pro}/qS_{Pro})}{\partial\alpha_{Pro}} = 0.27 \ \ rad^{-1}$$

and

$$\left(C_{Y_\beta}\right)_{Pro} = -0.084 \ \ rad^{-1}$$

The corresponding yawing moment derivative due to sideslip, C_{n_β}, for n propellers, is

$$(C_{n_\beta})_{Pro} = \frac{x_{Pro}}{b}(C_{Y_\beta})_{Pro}$$

where

x_{Pro} is the distance between the the propeller and the centre of gravity, measured parallel to the longitudinal body-axis.

thus

$$(C_{n_\beta})_{Pro} = -0.0075 \ \ rad^{-1}$$

D.2 Contribution of Nacelles to Side Force and Yawing Moment due to Sideslip Derivatives

ESDU data sheet [43] is used to estimate the contribution of the Hercules nacelles to side force and yawing moment due to sideslip derivatives, $(C_{Y_\beta})_{Nac}$ and $(C_{n_\beta})_{Nac}$. With $\frac{W_{Nac}^2}{s^2} = 0.005$, $(C_{Y_\beta})_{Nac}$ and $(C_{Y_\beta})_{Nac}$ for four nacelles are

$$(C_{Y_\beta})_{Nac} = -0.1884 \ \ rad^{-1}$$

$$(C_{n_\beta})_{Nac} = -0.012 \ \ rad^{-1}$$

where

W_{Nac} is the maximum width of nacelle ($W_{Nac} = 1.4$ m),

s is the wing semi-span (s=20.205 m).

Appendix E

Contribution of Hercules Fuselage to the Additional Lateral Aerodynamic Derivatives

E.1 Contribution of Fuselage to Side Displacement Derivatives

The relation between $C_{Y_{y/b_R}}$ and C_{Y_β} can be derived as follows:

$$C_{Y_{y/b_R}} = \frac{\partial C_Y}{\partial (y/b_R)} = \frac{\partial C_Y}{\partial \beta} \frac{\partial \beta}{\partial (y/b_R)} = C_{Y_\beta} \frac{\partial \beta}{\partial (y/b_R)}$$

where

$$\beta = -\frac{v}{V_\infty}$$

and v is the tanker sidewash induced at the receiver centre of gravity. Thus

$$C_{Y_{y/b_R}} = -\frac{\partial\left(v/V_\infty\right)}{\partial\left(y/b_R\right)} C_{Y_\beta} \tag{E.1}$$

The side force acting on the receiver fuselage following a side displacement has two components. Firstly there is a side force on the fuselage due to tanker sidewash and secondly there is a side force on the fin due to the interference between the tanker sidewash and the receiver high wing. Based on equation E.1, the fuselage contribution to $C_{Y_{y/b_R}}$ due to tanker sidewash is given by

$$\left(C_{Y_{y/b_R}}\right)_{Fus1} = -\frac{\partial\sigma_T}{\partial\left(y/b_R\right)} \left(C_{Y_\beta}\right)_{Fus} \tag{E.2}$$

where σ_T is the tanker wing sidewash angle at the receiver centre of gravity position.

The fin contribution to the side force due to side displacement derivative, $(C_{Y_{y/b_R}})_{Fin}$, produced by the interference between the tanker sidewash and receiver high wing, is determined using ESDU data sheet [50] as follows

$$\left(C_{Y_\beta}\right)_{Fin} = J_W \left(C_{Y_\beta}\right)_{Fin,VLM} \tag{E.3}$$

where

J_W	is the high wing-fin interference factor,
$(C_{Y_\beta})_{Fin,VLM}$	is the fin contribution to C_{Y_β} obtained from linear VLM,
$(C_{Y_\beta})_{Fin}$	is the fin contribution to C_{Y_β} including the interference between the receiver high wing and fin.

Equation E.3 can also be written as

$$\left(C_{Y_\beta}\right)_{Fin} = \left(C_{Y_\beta}\right)_{Fin,VLM} + \Delta C_{Y_\beta} \tag{E.4}$$

where ΔC_{Y_β} is the contribution due to the interference between the high wing and fin. By substituting equation E.3 into equation E.4, ΔC_{Y_β} can be expressed as

$$\Delta C_{Y_\beta} = (J_W - 1)\left(C_{Y_\beta}\right)_{Fin} \tag{E.5}$$

Based on equations E.1 and E.5, $(\Delta C_{Y_{y/b_R}})_{Fin}$, the contribution due to the interference between the high wing and fin, can be written as

$$\left(\Delta C_{Y_{y/b_R}}\right)_{Fin} = -(J_W - 1)\frac{\partial \sigma_T}{\partial (y/b_R)}\left(C_{Y_\beta}\right)_{Fin} \tag{E.6}$$

Finally, the total fuselage contribution to $C_{Y_{y/b_R}}$ is obtained by summing equations E.2 and E.6

$$\left(C_{Y_{y/b_R}}\right)_{Fus} = -\frac{\partial \sigma_T}{\partial (y/b_R)}\left(C_{Y_\beta}\right)_{Fus} - (J_W - 1)\frac{\partial \sigma_T}{\partial (y/b_R)}\left(C_{Y_\beta}\right)_{Fin} \tag{E.7}$$

Similarly, the total fuselage contributions to $C_{n_{y/b_R}}$ and $C_{l_{y/b_R}}$ can be written as

$$\left(C_{n_{y/b_R}}\right)_{Fus} = -\frac{\partial \sigma_T}{\partial (y/b_R)}\left(C_{n_\beta}\right)_{Fus} - (J_W - 1)\frac{\partial \sigma_T}{\partial (y/b_R)}\left(C_{n_\beta}\right)_{Fin} \tag{E.8}$$

$$\left(C_{l_{y/b_R}}\right)_{Fus} = -\frac{\partial \sigma_T}{\partial (y/b_R)}\left(C_{l_\beta}\right)_{Fus} - (J_W - 1)\frac{\partial \sigma_T}{\partial (y/b_R)}\left(C_{l_\beta}\right)_{Fin} \tag{E.9}$$

E.2 Contribution of Fuselage to Bank Displacement Derivatives

The C_{Y_ϕ} derivative can be related to the C_{Y_β} as follows:

$$C_{Y_\phi} = \frac{\partial C_Y}{\partial \phi} = \frac{\partial C_Y}{\partial \beta}\frac{\partial \beta}{\partial \phi} = C_{Y_\beta}\frac{\partial \beta}{\partial \phi}$$

where β is due to tanker induced flow along the lateral axis of the receiver.

$$\beta = -\frac{w}{V_\infty}\phi$$

Thus,

$$\frac{\partial \beta}{\partial \phi} = -\frac{w}{V_\infty}$$

and

$$C_{Y_\phi} = -\frac{w}{V_\infty}C_{Y_\beta} \tag{E.10}$$

As in the side displacement case, the side force acting on the receiver following a bank displacement has also two components. Firstly there is a side force on the fuselage due to the component of the tanker downwash along the lateral axis of the receiver and secondly the interference of this flow component with the receiver high wing produces a side force on the fin. The derivation of the fuselage contribution to the derivative C_{Y_ϕ} is similar to that described for the side displacement case. Thus, from equations E.10 and E.7, the fuselage contribution to the side force due to bank displacement derivative can be written as

$$\left(C_{Y_\phi}\right)_{Fus} = -\epsilon_T \left(C_{Y_\beta}\right)_{Fus} - \left(J_W - 1\right)\epsilon_T \left(C_{Y_\beta}\right)_{Fin} \tag{E.11}$$

where ϵ_T is the tanker wing downwash angle at the receiver centre of gravity position.

Similarly, the fuselage contributions to C_{n_ϕ} and C_{l_ϕ} can be expressed as

$$\left(C_{n_\phi}\right)_{Fus} = -\epsilon_T \left(C_{n_\beta}\right)_{Fus} - (J_W - 1)\,\epsilon_T \left(C_{n_\beta}\right)_{Fin} \tag{E.12}$$

$$\left(C_{l_\phi}\right)_{Fus} = -\epsilon_T \left(C_{l_\beta}\right)_{Fus} - (J_W - 1)\,\epsilon_T \left(C_{l_\beta}\right)_{Fin} \tag{E.13}$$

E.3 Contribution of Fuselage to Yawing Moment due to Yaw Displacement Derivative

The relation between the C_{n_ψ} derivative and the C_{n_r} derivative can be derived as follows:

$$N_\psi = \frac{\partial N}{\partial \psi}$$

The yawing moment due to yaw ψN_ψ is proportional to the local sideslip angle along the fuselage given by

$$\delta\beta = -\frac{\ell\psi}{V_\infty}\left(\frac{\partial v}{\partial y}\right)_{y=0}$$

where ℓ is the fin yawing moment arm and v is the tanker induced sidewash.

Similarly, The yawing moment due to yaw rate rN_r depends on the induced sideslip angle given by

$$\delta\beta = \frac{\ell r}{V_\infty}$$

Since the constant of proportionality is identical to that in the yaw case it follows that

$$\frac{\psi N_{\psi}}{r N_r} = -\frac{\frac{\ell\psi}{V_\infty}\left(\frac{\partial v}{\partial y}\right)_{y=0}}{\frac{\ell r}{V_\infty}} \tag{E.14}$$

Hence

$$\frac{(N_{\psi})_{Fus}}{(N_r)_{Fus}} = -\frac{\partial v}{\partial y} \tag{E.15}$$

In non-dimensional form, equation E.15 can be expressed as

$$(C_{n_\psi})_{Fus} = -\left(\frac{\partial\left(v/V_\infty\right)}{\partial\left(2y/b_R\right)}\right)_{y=0} (C_{n_r})_{Fus} \tag{E.16}$$

References

[1] Gardner B. The story of air-to-air refuelling. Airextra, Aug.-Sept. 1985.

[2] McCormick, J.E. In-flight refuelling and the world of the eighties. Aeronautical Journal, Vol. 82, Aug. 1978.

[3] MacGregor, P.S. Refuelling in flight. Aircraft Engineering, Vol. 36, Sep. 1964.

[4] Miller, J.A. A history of the development of flight refuelling. Aeronautical J. November 1960, pp 687-691.

[5] Bradley, J. Handling and performance trials needed to clear an aircraft to act as a receiver during air-to-air refuelling. AGARD Conf. Proc. No. 373, Flight Test Techniques, 1984, paper 9.

[6] Hoganson, E.H. A study of aerodynamic interference effects during aerial refuelling. M.Sc Thesis, AD-A136895, Air Force Inst. of Tech., Wright-Patterson AFB, Ohio, 1983.

[7] Bradley, J. Handling and performance considerations when conducting air-to-air refuelling of a large aircraft by the probe and drogue system. Society of Flight Test Engineering 21st Annual Symposium, 1990, paper 3.

[8] Abu-Assaf, H.A.S. Flight control problems associated with air-to-air refuelling. M.Sc. Thesis, University of Manchester, May 1990.

[9] Bloy, A.W., Lamont, P.J., Abu-Assaf, H.A., and Ali, K.A.M. The lateral dynamic stability and control of a large receiver aircraft during air-to-air refuelling. Aeronautical Journal, Vol. 90, June-July 1986, pp 237-243.

[10] Kucheman, D. A simple method for calculating the span and chordwise loading on straight and swept wings of any given aspect ratio at subsonic speeds. R.A.E. R. Aero 2476, A.R.C. R & M 2935, 1952.

[11] Bloy, A.W., Ali, K.A.M. and Trochalidis, V. The longitudinal dynamic stability and control of a large receiver aircraft during air-to-air refuelling. Aeronautical Journal, Vol. 91, Feb. 1987, pp 64-71.

[12] Ali, K.A.M. Aircraft stability and control during air-to-air refuelling and microcomputer flight simulation. M.Sc. Thesis, University of Manchester, June 1986.

[13] Margason, R.J. and Lamar, J.E. Vortex-lattice Fortran program for estimating subsonic aerodynamic characteristics of complex planforms. NASA TN D-6142, Feb. 1971.

[14] Trochalidis, V.T. Aircraft aerodynamics and stability and control during air-to-air refuelling. Ph.D Thesis, University of Manchester, May 1990.

[15] Bloy, A.W., and Trochalidis, V. The performance and longitudinal stability and control of large receiver aircraft during air to air refuelling. Aeronaut. J.,

Vol. 93, December 1989, pp 367-378.

[16] Bloy, A.W. and Trochalidis, V. The aerodynamic interference between tanker and receiver aircraft during air-to-air refuelling. Aeronautical Journal, Vol. 94, May 1990, pp 165-171.

[17] Bloy, A.W. and Trochalidis, V. and West, M.G. The aerodynamic interference between a flapped tanker aircraft and a receiver aircraft during air-to-air refuelling, Aeronaut. J., Oct. 1991, Vol. 95, pp 274-282.

[18] Donaldson, C. DU P., Snedeker, R.S. and Sullivan, R.D. Calculation of aircraft wake velocity profiles and comparison with experimental measurements, J. Aircraft, 1974, 11, pp 547-555.

[19] Bloy, A.W., West, M.G., Lea, K.A. and Jouma'a, M. Lateral aerodynamic interference between tanker and receiver in air-to-air refuelling. J. Aircraft, 1993, 30, 705-710.

[20] Jouma'a, M. Lateral aerodynamic interference during air-to-air refuelling. M.Sc Thesis University, of Manchester, October 1992.

[21] Spreiter, J.R., Sacks, A.H. The rolling-up of the trailing vortex sheet and its effect on the downwash behind wings. Journal of Aeronautical Sciences, 1951, pp 21-32.

[22] El-Ramly, Z. and Rainbird, W.J. Flow survey of the vortex wake behind wings, J. Aircraft, 1977, 14, pp 1102-1108.

[23] Grow, T.L. Effect of a wing on its tip vortex. Journal of Aircraft, Vol. 6, January-February 1969, pp 37-41.

[24] West, M.G. Aerodynamic interference during air-to-air refuelling. Ph.D. Thesis, University of Manchester, May 1993.

[25] Bloy, A.W. and West, M.G., Interference between tanker wing wake with roll-up and receiver aircraft. Journal of Aircraft, Vol. 31, No. 5, 1994, pp 1214-1216.

[26] Mendenhall, M.R., Spangler, S.B., Nielsen, J.N. and Goodwin, F.K. Calculation of the longitudinal aerodynamic characteristics of wing-flap configurations with externally blown flaps. NASA CR 2705, Sept. 1976.

[27] Mendenhall, M.R., Spangler, S.B., Nielsen, J.N. and Goodwin, F.K. A computer program to calculate the longitudinal aerodynamic characteristics of wing-flap configurations with externally blown flaps. NASA CR 2706, Sept. 1976.

[28] Smith, W.G. and Lazzeroni, F.A. Experimental and theoretical study of a rectangular wing in a vortical wake at low speed. NASA TN D-339, October 1960.

[29] McMillan, O.J., Schwind, R.G., Niesen, J.N., and Dillenius, M.F.E. Rolling Moments in a trailing vortex flow field. NASA CR-151961, Feb. 1977.

[30] Barrows, T.M. Simplified methods of predicting aircraft rolling moments due to vortex encounters. J Aircraft, May 1977, Vol. 14, No. 5, pp 434-439.

[31] Heaslet, M.A. and Spreiter, J.R. Reciprocity relations in aerodynamics. NACA Rept. 1119, 1953.

[32] Iversen, J.D. and Bernstein, S. Trailing vortex effects on following aircraft. Journal of Aircraft, Vol. 11, No. 1, 1974, pp 60-61.

[33] Iversen, J.D. and Bernstein, S. Dynamic simulation of an aircraft under the effect of vortex wake turbulence. Annales de ℓ'Association pour le Calcul Analogique, Vol. 14, 1972, pp.136-144.

[34] Yates, A.H. Note on the effect of the trailing vortex system on the control of aeroplanes in close formation. R.A.E. Technical Note 1292. Sept. 1943.

[35] Bertin, John J. and Smith, M.L. Aerodynamics for engineers. Prentice-Hill, Englewood Cliffs, NJ, 1979.

[36] Laschka, B. Interfering lifting surfaces in subsonic flow. Z. Fleigwiss, 1970, pp 359-369.

[37] Alford, W.J. Theoretical and experimental investigation of the subsonic-flow fields beneath swept and unswept wings with tables of vortex-induced velocities. NACA Report 1327, 1957.

[38] Butter, D.J. and Hancock, G.J. A numerical method for calculating the trailing vortex system behind a swept wing at low speed, Aeronaut. J., Aug. 1971, Vol. 75, pp 564-568.

[39] Moore, D.W. A numerical study of the roll-up of a finite vortex sheet. Journal of Fluid Mechanics, Vol. 184, 1987, pp 123-155.

[40] Krasny, R. Computation of vortex sheet roll-up in the Trefftz plane. J. Fluid Mechanics, 1987, 184, pp 123-155.

[41] Maziat, R. Aerodynamic characteristics of bodies and multi-wing configurations in coning motion. Ph.D. Thesis to be submitted to the University of Manchester.

[42] William, H.R. and Alan, P. Low-speed wind tunnel testing. 2nd ed., John Wiley & Sons, 1984.

[43] Anon. Wing-body yawing moment and side force derivatives due to sideslip: N_V and Y_V. Engineering Sciences Data Unit, Item No. 79006, 1979.

[44] Anon. Contribution of body to yawing moment and side force derivatives due to rate of yaw, $(N_r)_B$, $(Y_r)_B$. Engineering Sciences Data Unit, Item No. 83026, 1983.

[45] Anon. Effects of isolated body and wing-body interference on rolling moment due to sideslip. Engineering Sciences Data Unit, Item No. 73006, 1981.

[46] Multhopp, H. Aerodynamics of the fuselage. NACA TM-1036, December 1942.

[47] Etkin, B. Dynamics of flight - stability and control. John Wiley and Sons, 1982.

[48] Queijo, M.J. Theory for computing span loads and stability derivatives due to sideslip, yawing, and rolling for wings in subsonic compressible flow. NASA TN D-4929, 1968.

[49] Queijo, M.J. Theoretical span load distribution and rolling moments for sideslipping wings of arbitrary plan form in incompressible flow. NACA Report 1269, 1956.

[50] Anon. Contribution of fin to side force, yawing moment and rolling moment derivatives due to sideslip, $(Y_V)_F$, $(N_V)_F$, $(L_V)_F$, in the presence of body, wing and tailplane. Engineering Sciences Data Unit, Item No. 82010, 1982.

[51] Ribner, H. S. Formulas for propellers in yaw and charts of the side force derivative. NACA Rept. 819, 1945.

[52] Anon. Contribution of fin to side force, yawing moment and rolling moment derivatives due to rate of yaw, $(Y_r)_F$, $(N_r)_F$, $(L_r)_F$. Engineering Sciences Data Unit, Item No. 82017, June 1982.

[53] Nelson, R.C. Flight stability and automatic control. McGraw-Hill, 1989.

[54] Smetana, F.O. Computer assisted analysis of aircraft performance stability and control. McGraw-Hill, 1984.

[55] Jane's All the world's aircraft. 1987-88.

[56] Bloy, A.W. and Lea, K.A. Directional stability of a large receiver aircraft in air-to-air refuelling. J. Aircraft, Vol. 32, No. 2, March-April 1995, pp 453-455.

[57] Babister, A.W. Aircraft dynamic stability and response. Pergamon. 1980.

[58] Prothero, R. Air-to-air refuelling simulation-rapid progress reveals novel problem. Proceedings of the International Conference on Advances in Flight Simulation Visual and Motion Systems, The Royal Aeronautical Society, London,

1986, pp.2.1-2.10.

[59] Lea, K.A. The aerodynamics of air-to-air refuelling for a large receiver aircraft. Ph.D. Thesis, University of Manchester, September 1995.

[60] Anon. Geometrical properties of cranked and straight tapered wing planforms. Engineering Sciences Data Unit, Item No. 76003, 1981.